

THERMODYNAMIC SYNTHESIS OF LADDER-TYPE
FUNCTIONAL ORGANIC MATERIALS

A Dissertation

by

JONGBOK LEE

Submitted to the Office of Graduate and Professional Studies of
Texas A&M University
in partial fulfillment of the requirements for the degree of

DOCTOR OF PHILOSOPHY

Chair of Committee,	Lei Fang
Committee Members,	Donald J. Darensbourg
	Karen L. Wooley
	Jodie L. Lutkenhaus
Head of Department,	Simon W. North

August 2018

Major Subject: Chemistry

Copyright 2018 Jongbok Lee

ABSTRACT

Conjugated ladder-type macromolecules with coplanar, sp^2 atom-rich backbones represent a captivating class of materials on account of their well-defined rigid structures, intriguing syntheses, and promising potential in optoelectronic applications. The ladder-type backbones possess an intrinsically rigid conformation and limit possible torsional disorder. The unique architecture of conjugated ladder-type material leads to extended π -conjugation length, longer exciton diffusion length, and enhanced stability. In contrast, conventional conjugated polymers have intrinsic torsional disorder which partially break the conjugation pathways of the polymers and could be detrimental to the material properties.

Several preliminary literature examples have demonstrated the synthesis of ladder-type materials. However, it is still challenging to synthesize well-defined ladder polymers with a minimum level of structural defects because of the poor product solubility and limited synthetic methods. In order to overcome these obstacles, a highly efficient synthetic method and a rationally designed structural characteristic that enables solubility need to be accomplished simultaneously.

We envisioned that thermodynamically controlled ring-closing olefin metathesis (RCM) held the promise for a highly efficient and synthesis of conjugated ladder polymers with minimum levels of structural defects due to the strong thermodynamic driving force of aromatization and its reversible nature between starting material and side products. Moreover, the mild reaction conditions allow a wider scope of substrates and excellent

functional group tolerance. This efficient and versatile synthetic strategy successfully afforded various fused polycyclic heteroarenes, a series of extended ladder-type oligomers, and conjugated ladder polymers with minimum levels of structural defects in excellent yields. Furthermore, RCM demonstrated an excellent ring annulation efficiency with electron deficient acceptor units. Due to the good solubility of the ladder-type materials originating from orthogonally adopted α -branched solubilizing group, the properties of the desired materials were rigorously investigated in solution and the solid-state, such as photophysical properties, solid-state conformation and morphology, effective conjugation length, formation of charge transfer complexes, and crystallization dynamics. This research provides a well-established synthetic strategy to construct a fully conjugated ladder-type material and a fundamental understanding of ladder-type functional organic materials for potential future applications in electronic and optoelectronic devices.

DEDICATION

To my family

ACKNOWLEDGEMENTS

First and foremost, I would like to express gratitude to my advisor Dr. Lei Fang for his insightful and invaluable guidance, support, patience, and encouragement during my journey towards my Ph D degree at Texas A&M University. He led me to be an independent researcher, who did not have any background and knowledge on the subject I had worked during my graduate study. He always trusted me with full freedom to pursue my research. The power of his trust and patience made this work possible. I was really lucky to have him as my advisor because I fully understand how difficult to have such a nice boss. As one of his first graduate students, I was fully satisfied and couldn't be happier during my graduate study. I also really appreciate his full of understanding to take care of my family.

I also thank my committee members, Dr. Donald J. Darensbourg, Dr. Karen L. Wooley, and Dr. Jodie L. Lutkenhaus for their guidance and precious time spent for me. It was a great honor to have you on my committee during my graduate study.

I would like to thank my collaborator, Mohammed Al-Hashimi, at Texas A&M University at Qatar for his helpful support, Dr. Alexander Ayzner and William R. Holligsworth at the University of California, Santa Cruz for their photophysical analysis of the ladder polymer, Dr. Yuebing Zheng and Bharath B. Rajeeva at the University of Texas at Austin for the investigation of the ladder polymer self-assembly behavior by STM, and Dr. Hanying Li, Huanbin Li at Zhejiang University, China for their efforts to fabricate OFET devices with ladder-type oligomers.

I have great pleasure in acknowledging my gratitude to past and current group members in the Fang group: Dr. Yang Zou, Dr. Zi-Hao Guo, Congzhi Zhu, Alex Kalin, Tianyu Yuan, Chenxu Wang, Sai Che, Mariela Vazquez, Xiaozhou Ji, Anthony Mu, Bailey Phillips, Che-Hsuan Chang, Yirui Cao, and Bo-Ji Peng. It was a great opportunity to work with them and an unforgettable moment in my life. I really appreciate your attitude to make a wonderful laboratory environment. Here's wishing you SUCCESS and HAPPINESS in everything you do! Good Luck.

I must express my heartfelt gratitude to my Korean friends in the Department of Chemistry at Texas A&M University: Dr. Soon-Mi Lim, Dr. Youngbok Lee, Dr. Gyu seong Heo, Dr. Yerok Park, Dr. Sangho Cho, Dr. Dr. Doyong Kim, Dr. Jihye Park, Dr. Sinhye Ahn, Yewon Kim, and Jihyun Kim, who kept me going on my path successfully.

My acknowledgement would not be complete without thanking my family, the biggest source of my strength. My parents are always patient, very supportive, and trust in me. Their hard work in every aspect of life gave me an example and that has taught me how to deal with any obstacle. I am absolutely very proud of them, and I have the greatest respect for them. Without their lessons, I would have given up this long journey. I love you, dad and mom. I am indebted to my parents-in-law who are always kind, give me the full trust, and treat me as their son. I love you as much as my wife loves you. I also thank my brother who is by my parents while I am gone. Remember, I am always proud of you! I am grateful to my sister-in-law and brother-in-law for their kindness and respect. Last but not least, I must express my sincere gratitude to my wife Hyejin Lee for her sacrifice, full support, and big love. I could easily forget about concerns in my research because you

are always stand by me. That you have done for me during five years in foreign country is beyond description. I love you so much! Dear my son Jayden, for some day you grow enough to read this, daddy wants to say thank you for coming to us and becoming our precious child. You made us always happy, and we are very proud of you. We love you very much.

CONTRIBUTORS AND FUNDING SOURCES

Contributors

This work was supervised by a dissertation committee consisting of Professor Lei Fang [advisor] of the Departments of Chemistry and Materials Science and Engineering; Professor Donald J. Darensbourg [committee member] of the Department of Chemistry; Professor Karen L. Wooley [committee member] of the Departments of Chemistry, Chemical Engineering, and Materials Science and Engineering; and Professor Jodie L. Lutkenhaus [committee member] of the Departments of Chemical Engineering. In Chapter II, X-ray single crystal structures were collected by Dr. Nattamai Bhuvanesh of the Department of the Chemistry. In Chapter III, X-ray single crystal structures were collected by Dr. Nattamai Bhuvanesh of the Department of the Chemistry. Fluorescence quantum yield was measured by Dr. Xu Zhou, Fang-Dong Zhuang, and Dr. Jian Pei from Peking University, China. GIWAXS measurement was supported by Dr Joseph Strzalka from Argonne National Laboratory. STM measurement was performed by Bharath Bangalore Rajeeva and Dr Yuebing Zheng from The University of Texas at Austin. In Chapter IV, GIWAXS measurement was supported by Dr Joseph Strzalka from Argonne National Laboratory. In Chapter V, X-ray single crystal structures were collected by Dr. Nattamai Bhuvanesh of the Department of the Chemistry. GIWAXS measurement was supported by Dr Joseph Strzalka from Argonne National Laboratory. OFET measurement was performed by Huanbin Li and Dr. Hanying Li from Zhejiang University, China.

Funding Sources

The work for Chapter I was supported by the National Priorities Research Program award (NPRP7-285-1-045) from the Qatar National Research Fund and the Welch Foundation (A-1898). For Chapter II, this work was supported by the National Priorities Research Program award (NPRP7-285-1-045) from the Qatar National Research Fund. For Chapter III, this work was supported by the National Priorities Research Program award (NPRP7-285-1-045) from the Qatar National Research Fund. Use of the Advanced Photon Source at Argonne National Laboratory was supported by the U. S. Department of Energy, Office of Science, Office of Basic Energy Sciences, under Contract No. DEAC02-06CH11357. The National Priorities Research Program award (NPRP7-285-1-045) from the Qatar National Research Fund for financial support of the work for Chapter IV. This research used resources of the Advanced Photon Source, a U.S. Department of Energy (DOE) Office of Science User Facility operated for the DOE Office of Science by Argonne National Laboratory under Contract No. DE-AC02-06CH11357. The work for Chapter V was supported by Welch Foundation (A-1898), and the Laboratory for Molecular Simulation at Texas A&M University provided software support and computer time (National Science Foundation Award CHE-0541587). This research used resources of the Advanced Photon Source, a U.S. Department of Energy (DOE) Office of Science User Facility operated for the DOE Office of Science by Argonne National Laboratory under Contract No. DE-AC02-06CH11357.

NOMENCLATURE

A-D-A	Acceptor-donor-acceptor
AFM	Atomic force microscopy
AIBN	2,2'-Azobis(2-methylpropionitrile)
BBL	Poly(benzimidazole benzophenanthroline)
BHT	2,6-Di- <i>t</i> -butyl-4-methylphenol
Boc	<i>t</i> -Butoxycarbonyl
BTD	Benzothiadiazole
BTp	Benzo[<i>k</i>]tetraphene
cLPs	Conjugated ladder Polymers
CP-MAS	Cross polarization magic-angle spinning
CTC	Charge transfer complex
D-A	Donor-acceptor
DFT	Density functional theory
DLS	Dynamic light scattering
DP	Degree of polymerization
DSC	Differential scanning calorimetric
ECL	Effective conjugation length
F ₄ TCNQ	2,3,5,6-Tetrafluoro-7,7,8,8-tetracyanoquinodimethane
FT-IR	Fourier-transform infrared spectroscopy
GIWAXS	Grazing incidence wide-angle X-ray diffraction

GIXD	Grazing incidence X-ray diffraction
GNRs	Graphene nanoribbons
HMPA	Hexamethylphosphoramide
HOMO	Highest occupied molecular orbital
HOPG	Highly-ordered pyrolytic graphite
HPLC	High performance liquid chromatography
HR-MALDI	High-resolution Matrix-assisted laser desorption/ionization
ICT	Intramolecular charge transfer
LPPPs	Ladder-type poly(para-phenylene)s
LR-APCI	Low-resolution atmospheric pressure chemical ionization
LUMO	Lowest unoccupied molecular orbital
M_n	Number averaged molecular weight
M_w	Weight averaged molecular weight
NDI	Naphthalene diimide
NMR	Nuclear magnetic resonance
NOESY	Nuclear overhauser effect spectroscopy
OFET	Organic field-effect transistor
OLED	Organic light-emitting diode
OPVs	Organic Photovoltaics
PDI	Polydispersity index
PDI _s	Perylene diimides
PL	Photoluminescence

POL	Poly(phenoaxazine)
PQL	Polyquinoxaline
PTL	Poly(phenthiazine)
RCM	Ring-closing olefin metathesis
RMS	Root mean square
SANS	Small-angle neutron scattering
SAXS	Small-angle X-ray scattering
SEC	Size exclusion chromatography
S/N	Signal to noise ratio
STM	Scanning tunneling microscopy
TDDFT	Time-dependent density functional theory
TFA	Trifluoroacetic acid
TGA	Thermogravimetric analysis
TIPS	Triisopropylsilyl
TLC	Thin-layer chromatography

TABLE OF CONTENTS

	Page
ABSTRACT	ii
DEDICATION	iv
ACKNOWLEDGEMENTS	v
CONTRIBUTORS AND FUNDING SOURCES.....	viii
NOMENCLATURE.....	x
TABLE OF CONTENTS	xiii
LIST OF FIGURES.....	xv
LIST OF SCHEMES.....	xix
CHAPTER I INTRODUCTION AND BACKGROUND.....	1
1.1. Fully Conjugated Ladder Polymers.....	1
1.2. Conjugated Ladder-Type Oligomers.....	31
CHAPTER II EXTENDED FUSED POLYCYCLIC HETEROARENES VIA THERMODYNAMICALLY CONTROLLED RING-CLOSING OLEFIN METATHESIS.....	41
2.1. Introduction	41
2.2. Results and Discussion.....	42
2.3. Experimental Section	51
2.4. Conclusion.....	52
CHAPTER III THERMODYNAMIC SYNTHESIS OF SOLUTION PROCESSABLE LADDER POLYMERS.....	53
3.1. Introduction	53
3.2. Results and Discussion.....	55
3.3. Experimental Section	68
3.4. Conclusion.....	71

CHAPTER IV	DONOR-ACCEPTOR CONJUGATED LADDER POLYMER VIA AROMATIZATION-DRIVEN THERMODYNAMIC ANNULATION	73
4.1.	Introduction	73
4.2.	Results and Discussion.....	75
4.3.	Experimental Section	86
4.4.	Conclusion.....	89
CHAPTER V	EXTENDED LADDER-TYPE BENZO[<i>K</i>]TETRAPHENE- DERIVED OLIGOMERS	91
5.1.	Introduction	91
5.2.	Results and Discussion.....	93
5.3.	Experimental Section	102
5.4.	Conclusion.....	109
CHAPTER VI	CONCLUSIONS.....	111
REFERENCES	115
APPENDIX A	136
APPENDIX B	171
APPENDIX C	193
APPENDIX D	202

LIST OF FIGURES

		Page
Figure 1.1	Graphical representation of conjugated ladder polymer (cLP) and conventional conjugated polymer with free torsional motions.....	2
Figure 1.2	Graphical synthetic approaches to construct a ladder polymer. (a) Single-step ladderization and (b) post-polymerization modification: ladderization.....	5
Figure 1.3	Chemical structures of <i>trans</i> and <i>cis</i> poly(benzimidazole benzophenanthroline) (BBL) 1 , polyquinoxaline (PQL) 2 , poly(phenthiazine) (PTL) 3 , and poly(phenooxazine) (POL) 4	7
Figure 1.4	Defects common in cLPs. (a) Conjugation breaking torsional defects formed by incomplete ladderization or postsynthetic degradation, (b) regioisomeric structures created during nonregioselective syntheses, and non-conjugation breaking emissive defects (c) as a result of non-ladderized chain end groups, and (d) internally in the polymer chain...	21
Figure 1.5	(a) Proposed illustration using cleavable side chains in cLPs processing to obtain a well-ordered, solvent resistant film from an easily processed material. (b) Schematic representation of Boc cleavage of 22 by thermal annealing in the solid state. (c) GIXD of the as-cast film of 22 (blue) in comparison with that of the annealed thin film (red). Reproduced from ref. 51 with permission from Elsevier	25
Figure 1.6	(a) STM images of cLP 27 on HOPG. (b) section profile along the arrow line drawn in (a). (c) STM images of the graphene nanoribbon on HOPG from ref. 68. (d) section profile along the blue line in (c). Reproduced from ref. 7 and 68 with permission from The Royal Society of Chemistry and Nature Publishing Group, respectively	29
Figure 1.7	Sequential oligomerization–annulation synthesis of ladder-type oligomers. Discrete oligomers are synthesized through multistep iterative couplings, then subsequently endcapped and annulated to give the fully fused oligomer	33
Figure 2.1	X-ray single crystal structures (left) and packing structures (right) of (a) DBCz , (b) DBTDCz , (c) DBICz , (d) DBTDICz , and (e) DTICz . Hydrogen atoms (left) and alkyl side chains (right) have been omitted for clarity. Colors indicate different layers of packing structures.	46

Figure 2.2	(a) UV-vis absorption spectra and (b) Fluorescence emission spectra of fused polycyclic heteroarenes in CHCl ₃	49
Figure 2.3	UV-vis-NIR spectra of <i>p</i> -doped fused polycyclic heteroarenes with F ₄ TCNQ. The spectra were observed at 2.5 × 10 ⁻³ M concentration in 1,2-dichlorobenzene.....	50
Figure 3.1	(a) A general retrosynthetic analysis for the designed ladder polymer; (b) Structural formula of the carbazole-derived monomer 1	56
Figure 3.2	(a) Solid-state structure of compound 3 obtained from single-crystal X-ray diffraction; (b) UV-vis absorption spectra of compound 2 (black) and 3 (red) in CHCl ₃ , with the TDDFT calculated electronic transitions of 3 shown as blue bar; (c) Fluorescent emission spectra of 2 (black) and 3 (red) with absolute intensity scale. Inset is the same spectra with normalized intensity.....	59
Figure 3.3	(a) Partial ¹ H NMR spectra of 2 and 3 . Dotted lines represent the change of chemical shift of each resonance peak after RCM reaction. Proton resonance peaks for <i>c</i> , <i>c'</i> , <i>f</i> and <i>g</i> in the box all disappeared after converting 2 into 3 ; (b) Partial ¹ H NMR spectra of CP and LP showing the similar change of chemical shift. Proton resonance peaks for the terminal vinyl groups <i>c</i> , <i>c'</i> , <i>f</i> , and <i>g</i> in the box all disappeared after the RCM reaction; (c) ¹³ C NMR spectra of CP* (S/N = 94 after 413 scans) and LP* (S/N = 367 after 17816 scans). The carbons labeled with “*” are 99% ¹³ C isotope enriched. ¹³ C resonance peaks for the terminal vinyl carbon β in the box disappeared after the RCM reaction	60
Figure 3.4	(a) UV-vis absorption spectra of CP (black) and LP (red) in CHCl ₃ and as thin films; (b) Fluorescence emission spectra of CP (black) and LP (red) in CHCl ₃ with absolute intensity scale. Inset is the same spectra with normalized intensity. Graphical illustration of the conformational change of (c) CP and (d) LP between in solution and in the solid state	63
Figure 3.5	Film morphology comparison of 3 and LP . The thin films were deposited on UV-Ozone cleaned silicon wafers by spin-casting solutions (2 mg/ml in toluene) at a rate of 2000 rpm. (a) Optical microscope image of 3 with observed microcrystals (1 ~ 3 μm) and (b) that of LP with no optical feature; (c) AFM images of microcrystals of 3 (RMS = 5.39 nm) and (d) amorphous morphology of LP (RMS = 0.45 nm); (e) GIWAXS patterns of 3 and (f) LP . Both samples were measured at an incident angle of 0.2° and 30 second exposure time, and both images have the same color scale	65

Figure 3.6	(a) STM image of LP on highly-ordered pyrolytic graphite; (b) Section profile along the arrow line drawn in (a). The STM image was obtained with a tunneling current set point of 0.9 nA and sample bias of 50 mV. The distance between consecutive convex spots along the X-axis is 1.27 nm, and average distance between peaks along the Y-axis is 0.70 nm. (c) Theoretical dimensions of an oligomeric model LP backbone from DFT calculation (B3LYP/6-311G)	67
Figure 4.1	General retrosynthesis of (a) a D-A type ladder polymer and (b) a D-A type conjugated polymer. The curved arrows indicate free torsional motions.....	75
Figure 4.2	Partial ¹ H NMR spectra of DACP and DALP . Dotted lines represent the change of chemical shifts of each resonance peak after RCM. Proton resonance peaks for the vinyl groups in the box all disappeared after RCM	79
Figure 4.3	(a) UV-vis absorption and fluorescence emission spectra of DACP and DALP in toluene. (b) UV-vis absorption and fluorescence emission spectra of DALP in different solvents	81
Figure 4.4	UV-vis-NIR spectra of (a) <i>p</i> -doped LP with F ₄ TCNQ (24.9 wt%, MR = 0.4, black solid line) and (b) DALP with F ₄ TCNQ (11.5 wt%, MR = 0.3, red solid line) and control spectra of CP (black dashed line, MR = 0.4) and DACP (red dashed line, MR = 0.3) with F ₄ TCNQ. The structure of CP can be found in Figure B.7. The spectra were observed at 2.5 × 10 ⁻³ M concentration in 1,2-dichlorobenzene.....	83
Figure 4.5	GIWAXS image of (a) DALP after annealing at 250 °C and (b) after alkyl chain cleavage at 500 °C. Both samples were measured at an incident angle of 0.14° and 30 second exposure time, and both images have the same color scale. (c) TGA trace of DACP and DALP . Decomposition temperature of DACP (T _d , 5 % weight loss) was 361 °C with a 34 % carbonization yield at 900 °C, and that of DALP (T _d , 5 % weight loss) is 342 °C with a 42 % carbonization yield at 900 °C....	85
Figure 5.1	Structures of [9]benzo[<i>k</i>]tetraphene and its constitutional isomers, [9]acene and [9]phenacene, superimposed on a piece of armchair graphene. Clar's aromatic sextets are shown with circles	92
Figure 5.2	The aromatic regions of ¹ H NMR spectra (500 MHz) of BTp-5~13 , color-coded by corresponding groups of protons. BTp-5~11 : CDCl ₃ , 298K; BTp-13 : C ₂ D ₂ Cl ₄ , 373K	96

Figure 5.3 (a) UV-vis absorption of **BTp** derivatives in CHCl_3 . Boxes indicate the characteristic α - (black), p - (yellow) and β -bands (green); (b) Expanded view of the α -bands; (c) Correlation plots and exponential fits of **BTp** derivatives between the absorption maxima of the p -band ($\lambda_{a, \text{max}}$, ■) and the fluorescence emission maxima ($\lambda_{e, \text{max}}$, ●) vs number of benzene rings (n)..... 98

Figure 5.4 GIWAXS images of (a) **BTp-5**, (b) **BTp-7**, (c) **BTp-9**, and (d) **BTp-11** thin films as-cast and after annealing. (e) Correlation chart between intermolecular interaction and molecular mobility based on the relative size of building block to the alkyl chain. Low solubility of **BTp-13** prevented processing of thin films of adequate quality for GIWAXS .. 101

LIST OF SCHEMES

		Page
Scheme 1.1	Synthesis of ladder polymer 7 by Diels-Alder reaction followed by dehydrogenation	8
Scheme 1.2	Synthesis of ladder polymer 8 by self-assembled intramolecular N-H interaction	9
Scheme 1.3	Synthesis of poly(<i>p</i> -phenylene) ladder polymers (LPPPs) 11 and 12 by Friedel-Craft ring annulation.....	11
Scheme 1.4	Synthesis of spiro-bridged LPPP 14 by Friedel-Craft ring annulation.....	12
Scheme 1.5	Synthesis of carbazole-fluorene-based ladder polymer 15 by Bischler-Napieralski cyclization	13
Scheme 1.6	Synthesis of D-A type ladder polymer 16 by Friedel-Craft ring annulation	13
Scheme 1.7	Synthesis of poly(<i>p</i> -phenacene)s 17 and 18 by carbonyl olefination and electrophile-induced cyclization, respectively	14
Scheme 1.8	Synthesis of ladder polymer 20 by electrochemical oxidation and D-A type ladder polymer 21 by photochemical oxidation	15
Scheme 1.9	Metal catalyst-free synthesis of quinacridone derived ladder polymers 22 and 23	16
Scheme 1.10	Synthesis of imine-bridged LPPP 24 and D-A type ladder polymer 25 by thermodynamically controlled imine condensation	18
Scheme 1.11	Synthesis of carbazole-based ladder polymer 27 by thermodynamically controlled ring-closing olefin metathesis	19
Scheme 1.12	Representative kinetically controlled ladderization reactions through (a) electrophilic aromatic annulation followed by demethylation and removal of TIPS, (b) the Scholl reaction, (c) alkyne benzannulation, and (d) Buchwald coupling followed by removal of TIPS	34

Scheme 1.13	Examples of thermodynamic ladderization reactions through (a) RCM, (b) dehydration of carboxylic acids, and (c) imine condensation.....	38
Scheme 2.1	Synthesis of extended fused polycyclic heteroarenes DBCz , DBTDCz , DBICz , DBTDICz , and DTICz	43
Scheme 3.1	(a) Synthesis of small molecular model compound 3 ; (b) synthesis of ladder polymer LP . Reaction conditions: <i>i</i>) Pd(PPh ₃) ₄ , K ₂ CO ₃ , aliquat 336, BHT, PhMe, H ₂ O, 100 °C, 24 h. <i>ii</i>) Grubbs' 2 nd generation catalyst, PhMe, reflux, 6 h. <i>iii</i>) Pd(PPh ₃) ₄ , K ₂ CO ₃ , aliquat 336, BHT, PhMe, H ₂ O, 100 °C, 24 h; then 2-bromostyrene and 2-vinylphenylboronic acid.....	57
Scheme 4.1	Synthesis of D-A ladder polymer DACP and DALP . (i) Pd(PPh ₃) ₄ , K ₂ CO ₃ , aliquat 336, BHT, PhMe, H ₂ O, 100 °C, 24 h; then 2-bromostyrene and 2-vinylphenylboronic acid. (ii) Grubbs' 2 nd generation catalyst, PhMe, reflux, 6 h.....	78
Scheme 5.1	Structural formula and synthesis of vinyl-functionalized <i>p</i> -phenylene derivatives 1~5 . (i) 1 , Pd(PPh ₃) ₄ , K ₂ CO ₃ , aliquat 336, BHT, PhMe, H ₂ O, 100 °C, 24 h. (ii) B ₂ pin ₂ , Pd ₂ dba ₃ , SPhos, KOAc, BHT, Dioxane, 70 °C, 18 h.....	93
Scheme 5.2	(a) Synthesis of ladder-type oligomers BTp-5~13 . (i) Pd(PPh ₃) ₄ , K ₂ CO ₃ , aliquat 336, BHT, PhMe, H ₂ O, 100 °C, 24 h. (ii) Grubbs' 2 nd generation catalyst, PhMe, reflux, 6 h (<i>o</i> -DCB at 130 °C was used for BTp-13). (b) HOMOs and (c) LUMOs of BTp-5~13 , calculated by DFT at B3LYP/6-311G(d,p) level of theory.....	94

CHAPTER I

INTRODUCTION AND BACKGROUND*

1.1. Fully Conjugated Ladder Polymers

1.1.1. Introduction

Fully conjugated ladder polymers (cLPs) are an intriguing subset of macromolecules. Their development has relied on a wide scope of synthetic strategies to obtain a host of unique structures and materials useful for their physical, optical, and chemical properties.¹⁻³ In general, ladder polymers are multiple stranded polymers with periodic linkages connecting the strands, resembling the rails and rungs of a ladder, and giving an uninterrupted sequence of adjacent rings that share two or more atoms.⁴ *Conjugated* ladder polymers (cLPs) are a specific subtype of ladder polymers in which all the fused rings in the backbone are π -conjugated. In addition, they are distinct from conventional conjugated polymers in that the fused-ring constitution restricts the free torsional motion in between the aromatic units along the backbone.

Stemming from the fused backbone, cLPs exhibit extraordinary thermal, chemical, and mechanical stability.^{3, 5-7} Because of the diminished torsional defects, cLPs with fully coplanar backbones promise coherent π -conjugation,⁸ fast intra-chain charge transport,⁹ long exciton diffusion length,¹⁰ and strong π - π stacking interactions.¹ In contrast, the

*Reprinted with permission from “Fully Conjugated Ladder Polymers” by Jongbok Lee, Alexander J. Kalin, Tianyu Yuan, Mohammed Al-Hashimi, and Lei Fang, *Chem. Sci.*, **2017**, *8*, 2503-2521. Copyright 2017 The Royal Society of Chemistry.

*Reprinted with permission from “Annulation Reactions for Conjugated Ladder-Type Oligomers” by Alexander J. Kalin, Jongbok Lee, and Lei Fang, *Synlett*, **2018**, *29*, 993-998. Copyright 2018 Thieme.

aromatic repeating units of conventional conjugated polymers tend to adopt non-zero dihedral angles either because of torsional strain or thermal fluctuation (Figure 1.1). Such torsional defects partially break the conjugation along the polymer backbone, resulting in decreased electronic delocalization, widened band gaps, increased numbers of trapped charges, and less effective intermolecular coupling.^{8, 11}

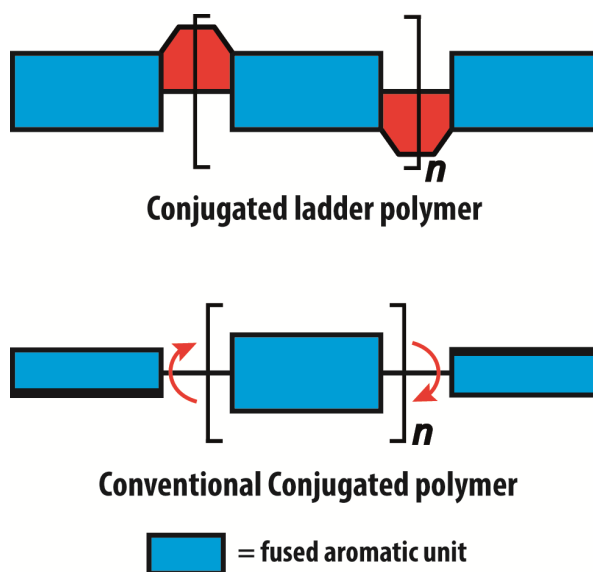


Figure.1.1. Graphical representation of conjugated ladder polymer (cLP) and conventional conjugated polymer with free torsional motions.

Since the synthesis of poly(benzimidazole benzophenanthroline) (BBL) **1** in the 1960s,¹² many different cLPs have been prepared and investigated for various applications.²⁻³ Despite numerous reported syntheses of cLPs, the field has seen inherent synthetic challenges limiting the scope of usable precursors and reaction designs. Limitations are mainly related to several issues; (i) there are relatively few synthetic strategies available to efficiently construct defect-free structures; and (ii) poorly soluble

products caused by backbone rigidity and coplanarity. In order to construct a well-defined cLP, the conversion of the ring annulation reaction must be nearly quantitative without undesired side reactions such as intermolecular cross-linking. Due to the lack of backbone rotation, at least one of the building blocks' reaction sites should possess C_{2h} symmetry in order for the rigid backbone to extend linearly. Furthermore, adequate solubilizing groups on the backbone of the cLPs are required to allow the reaction to complete while still obtaining soluble products for the subsequent characterization and processing.

From initial synthesis, through to characterization, analysis, and finally as potential end-user applications, cLPs face a number of unique challenges not found in other organic materials, originating from their rigid ribbon-like structures.^{3, 13} The low solubility and backbone rigidity of the polymers limit the effectiveness of common polymer analysis techniques such as structural elucidation by NMR or molecular weight estimation by size exclusion chromatography (SEC). The low solubility also impedes simple solution processing methods in some cases. In this context, unique methods have been developed to circumvent these barriers, leading to more straightforward syntheses and widespread uses of cLPs.

Despite the aforementioned challenges in cLPs, their exceptional stability and promising electronic properties have prompted exploration in various optical and electronic applications, such as OLEDs^{2, 5, 14-16} and OFETs,¹⁷⁻²¹ among others. In a large number of examples, cLP optoelectronic properties surpassed that of their non-ladder type counterparts.

In this perspective, our focus will center on the general synthetic strategies and specific examples of cLPs followed by discussion of chemical and engineering challenges associated with these materials. The demonstrated functions and potential applications of cLPs on multiple fronts are also discussed and outlined. Please note that conjugated step-ladder polymers³ (conjugated polymers composed of oligomeric ladder-type building blocks connected by single-stranded σ bonds) are not discussed in this perspective. Fused-ring π -conjugated oligomers are also excluded from this perspective due to the limitation on the page and reference number.

1.1.2. Review/Discussion

1.1.2.1. General Synthetic Strategies

The synthesis of a well-defined cLP must fulfill several criteria; (i) reasonable solubility and (ii) quantitative conversion in the ring-closing reactions. In addition, the issues impacting the degree of polymerization and polydispersity must also be taken into consideration. Therefore, the development of an efficient and versatile synthetic strategy is indispensable to explore the potential for a functional cLP. In general, two distinct approaches can be employed to construct a fully conjugated ladder-type structure (Figure 1.2). One is single-step “ladderization” that constructs two strands of bonds simultaneously, such as polycondensation of tetra-functional monomers or repetitive Diels-Alder cycloaddition. The other approach relies on post-polymerization annulation. In this two-step approach, a pre-functionalized single-stranded conjugated polymer is first prepared, followed by the ladderization steps in which the functional groups cyclize to

form the second strand of bonds. This stepwise approach provides a wider scope of applicable synthetic methods and monomeric building blocks. For this strategy, however, it is essential to ensure high conversion of the post-polymerization annulation reaction, while keeping good solubility of the reaction intermediate to achieve a well-defined ladder polymer with minimum levels of structural defects. Herein, we introduce the backgrounds and features of important cLP syntheses, discuss developments in the last decade, and offer synthetic perspective on cLPs.

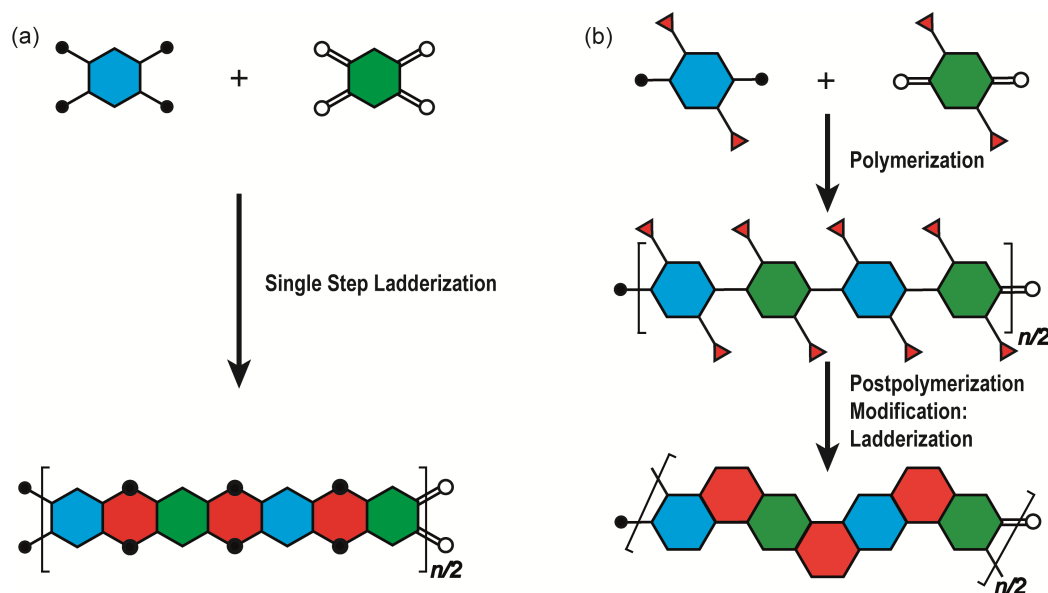


Figure 1.2. Graphical synthetic approaches to construct a ladder polymer. (a) Single-step ladderization and (b) post-polymerization modification: ladderization.

1.1.2.2. Single-Step Ladderization

In the late 1960s, Van Deusen reported the synthesis of BBL **1** for the purpose of thermally stable organic materials (Figure 1.3).¹² BBL **1** now represents one of the most

extensively studied cLPs to date. The synthesis of BBL **1** was achieved by a single-step polycondensation of two tetrafunctional monomers (1,2,4,5-tetraaminobenzene and 1,4,5,8-tetracarboxynaphthalene) in polyphosphoric acid (PPA) solution. It can be viewed as a statistical copolymer of *cis* and *trans* isomeric repeating units. In parallel, one of these tetrafunctional monomers, 1,2,4,5-tetraaminobenzene, was also used in the construction of other cLPs with different comonomers by Stille *et al.*²² Their first trial to prepare a polyquinoxaline (PQL) ladder polymer **2** with hydroxyketone and tetraamine monomers provided incomplete ladder formation resulting in low thermal stability due to the low reactivity of the hydroxyl group.²² By replacing the hydroxyketone monomer with a tetraketone monomer, *e.g.* 1,2,6,7-tetraketopyrene, where tautomerization is restricted, thermally stable PQL **2** was afforded in hexamethylphosphoramide (HMPA) solution at 180 °C.²³ It is noteworthy to mention that the key monomer (tetraaminobenzene) for the synthesis of BBL **1** and PQL **2**, is not stable to air oxidation. Therefore, oxidative side-reactions may cause structural defects of the cLP product if the reaction was not handled in a rigorously oxygen free condition. Similar synthetic strategy was employed in exploring the synthesis of poly(phenthiazine) (PTL) **3** and poly(phenoaxazine) (POL) **4** by Kim in the 1980s.²⁴ These single-step polycondensed cLPs, however, can usually only be suspended in strong acids such as PPA or sulfuric acid, and are insoluble in common organic solvents. As a result, common solution phase characterization techniques (NMR and SEC) were not feasible to fully elucidate these structures.

Nonetheless, a promising synthetic approach was reported by Schlüter and coworkers in the mid 1990s.²⁵⁻²⁶ The fully unsaturated ladder polymer backbone was

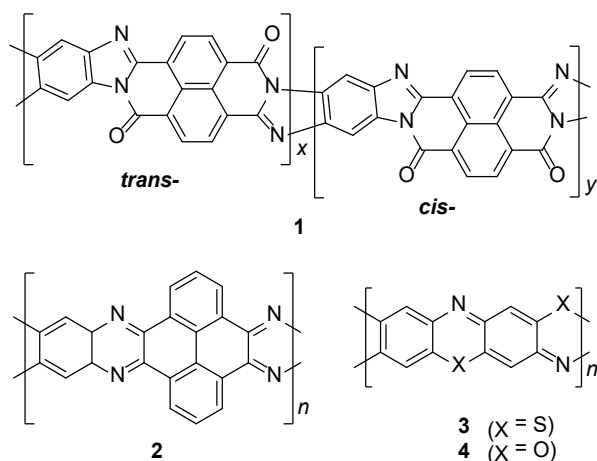
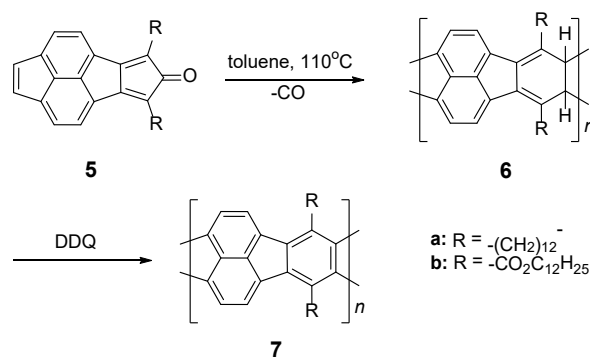


Figure 1.3. Chemical structures of *trans* and *cis* poly(benzimidazole benzophenanthroline) (BBL) **1**, polyquinoxaline (PQL) **2**, poly(phenthiazine) (PTL) **3**, and poly(phenoaxazine) (POL) **4**.

achieved by using Diels-Alder reaction followed by dehydrogenation (Scheme 1.1). These two reactions both gave high conversions on small molecule model compounds. cLP **7a** was synthesized through an AB+AB step growth polymerization using one single monomer containing both diene and dienophile functionalities. The product was analyzed by elemental analysis, UV-vis spectroscopy, and cross polarization magic-angle spinning (CP-MAS) ^{13}C NMR spectroscopy.²⁵ The carbon resonance peak corresponding to saturated carbons in the backbone of **7a** disappeared after dehydrogenation. Compound **7a** was insoluble in common organic solvents even with a long looped alkyl solubilizing group. Furthermore, film formation was not possible even when using the low molecular weight fraction ($M_n = 2 - 7$ kg/mol by SEC). A different solubilizing group was also installed to improve the molecular weight of intermediate **6**.²⁶ When an ester-linked dodecyl alkyl chain was used as the solubilizing group and the reaction was performed in an airtight ampoule, M_n of **6b** was relatively improved (34 kg/mol by SEC and 85 kg/mol

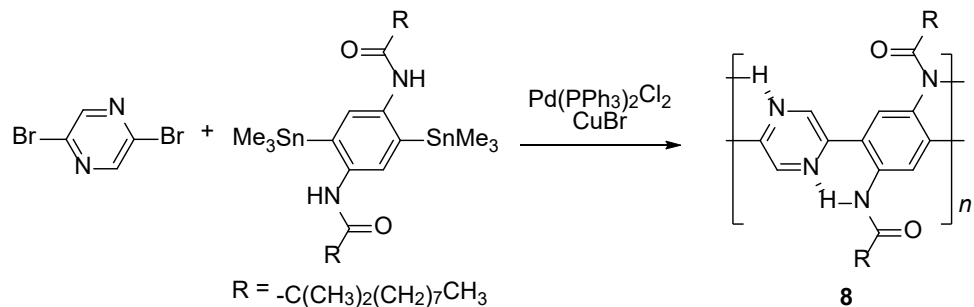
by osmometry). After dehydrogenation, CP-MAS ^{13}C NMR spectrum of product **7b** showed complete disappearance of the sp^3 carbon on the polymer backbone. Product **7b**, however, was still insoluble in several organic solvents, preventing its analysis by solution-phase ^1H NMR spectroscopy. Although single-step ladderization has been investigated for over 50 years, the methods have not been widely adopted as a general approach for cLP synthesis due to the limited availability of ideal multifunctional monomers and their related solubility issues.



Scheme 1.1. Synthesis of ladder polymer **7** by Diels-Alder reaction followed by dehydrogenation.

By using intramolecular non-covalent bonds, ladder-like conjugated backbones can be constructed through the formation of only one strand of covalent bonds. This strategy could also be considered as an interesting one-step approach to cLP-mimicking polymers. Through this approach, one strand of covalent bonds is formed through polymerization while another strand of non-covalent bonds can be generated simultaneously because of the dynamic and spontaneous nature of the non-covalent bonds.

This approach was demonstrated in 1996, when Meijer and coworkers synthesized²⁷ a ladder-like polymer using intramolecular hydrogen bonding between the nitrogen on 2,5-dibromopyrazine and an adjacently attached amide functionality (Scheme 1.2). In this case, although the intramolecular hydrogen bonding feature was observed by ¹H NMR and IR spectroscopy, the synthesized polymer **8** was not able to adopt a fully coplanar structure along the backbone, due to the 2,2' H-H steric repulsion on the neighboring benzene and pyrazine units.²⁸ It is imperative that no steric effect should be present between neighboring rings in order to approach backbone coplanarity by using non-covalent interactions. Intramolecular dynamic bond-assisted coplanarization has been also reported using various kinds of non-covalent/coordination interactions such as N-H, S-N, and B-N interactions.²⁹⁻³³ In principle, these dynamic yet simultaneous bonding could be used in the future for a one step construction of cLPs. In general, pre-organized non-covalent interactions could provide an alternative method to construct a coplanar ladder-like polymer without the concerns of the ladderization efficiency or intermolecular cross-linking during a ladderization step. Furthermore, the dynamic nature of intramolecular



Scheme 1.2. Synthesis of ladder polymer **8** by self-assembled intramolecular N-H interaction.

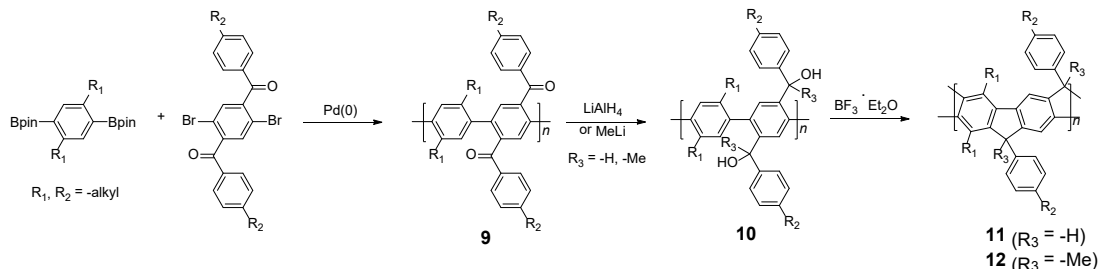
bonding could allow a simple approach to actively control the torsional conformation and intermolecular packing while processing these polymers into the solid-state.

1.1.2.3. Two Step Approach: Polymerization Followed by Ladderization

1.1.2.3.1. Kinetic Ring Annulation

A widely used, Friedel-Crafts method to construct ladder-type poly(para-phenylene) structures was reported by Müllen and coworker in 1991.³⁴ The fused-ring backbones are achieved by transition metal-mediated polymerization followed by electrophilic cyclization. The synthesis of ladder-type poly(para-phenylene)s (LPPPs) started with Suzuki polymerization of benzenebisboronic ester and aromatic ketone-functionalized dibromobenzene (Scheme 1.3). The ketone functional groups on the single-stranded intermediate **9** were reduced by lithium aluminum hydride or alkyllithium reagents. Eventually, Lewis acid-mediated Friedel-Crafts ring annulation afforded the double-stranded LPPP products. Due to the rigid coplanar backbone of LPPPs, their UV-vis spectra possess a well-resolved vibronic progression with a very small Stokes shift (4 nm).³⁵⁻³⁶ In addition, MeLPPP ($R^3 = \text{Me}$) **12** showed identical photoluminescence (PL) spectra in solution and the thin film state, indicating that the molecular conformation does not change from the solvated state into the solid state.² The key factor in this synthetic strategy is the steric hindrance on the bridgehead. It is essential that substituents on $-\text{CR}^2\text{R}^3\text{OH}$ possess moderate steric hindrance (*i.e.*, $R^3 = \text{H}$ or alkyl).² Less hindered substituents can lead to intermolecular cross-linking during the reaction, resulting in insoluble by-products. On the other hand, a bulkier substituent could prevent the ring

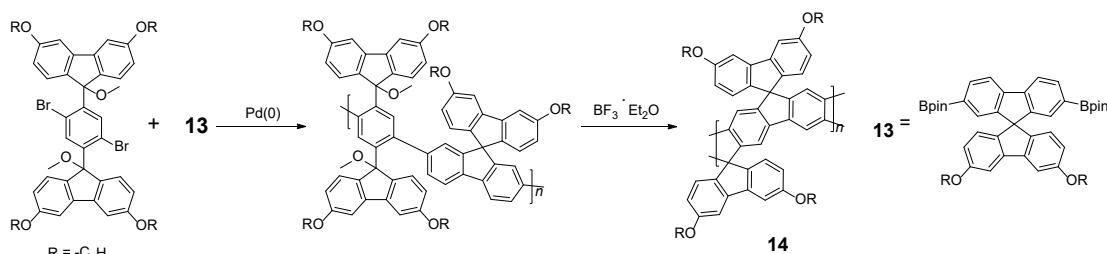
annulation from completing. Later on, this synthetic strategy was expanded to prepare a number of different types of ladder polymers.³⁷⁻⁴¹



Scheme 1.3. Synthesis of poly(*p*-phenylene) ladder polymers (LPPPs) **11** and **12** by Friedel-Craft ring annulation.

Although ¹H NMR and FT-IR spectroscopy detected no defect in LPPP polymers, careful investigations on the structure-property relationship of these polymers were performed to reveal small amounts of structural defects on their backbones which can be detrimental to the properties of the desired cLP materials.⁴² These defects were mainly caused by incomplete reduction of ketones that afforded monoalkylated fluorene backbones.⁴³⁻⁴⁴ As a result, these defect sites can be subsequently oxidized into fluorenones. The synthetic method was modified by Ma and coworkers to give a lower level of structural defects and thus better thermal stability.⁴⁵ This method was further improved by Bo and coworkers,⁵ who introduced methoxy functional groups, replacing the hydroxyl groups to avoid keto defects (Scheme 1.4). In this case, a spiro-bridged solubilizing group was installed to minimize aggregation between the polymer chains. The bromide end groups of the conjugated polymer were end-capped using the monoboronic ester of **13** to afford a well-defined ladder-type structure. As a result, the synthesized spiro-

bridged LPPP **14** showed typical properties of a rigid cLP – no obvious chromatic shift in the UV-Vis and PL spectra between solution and the solid state was seen. In addition, the polymer exhibited a small Stokes shift of 2 nm, and excellent thermal and optical stability.

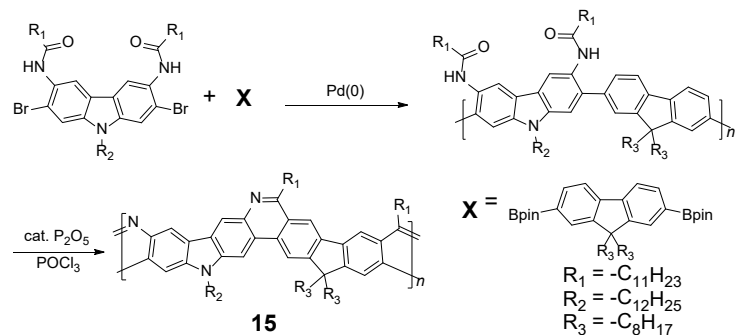


Scheme 1.4. Synthesis of spiro-bridged LPPP **14** by Friedel-Craft ring annulation.

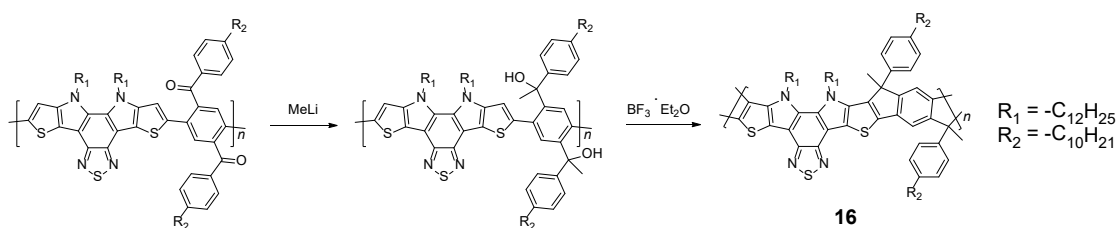
The remarkable thermal stability was also demonstrated by the unchanged PL spectrum after annealing at 110 °C for 24 h in air.

Bo and coworkers. also reported the synthesis of a soluble imine-bridged ladder polymer **15** by Bischler-Napieralski cyclization (Scheme 1.5).⁴⁶ The carbazole-fluorene conjugated polymer with dodecanamides was cyclized by POCl₃ in the presence of P₂O₅ to form the imine bridge. It is interesting to note that the repeating units of the synthesized ladder polymer **15** lack a C_{2h} symmetry, resulting in a backbone which possesses an angular structure and does not extend in a straight manner. More recently, Scherf and coworkers. reported a donor-acceptor (D-A) alternating ladder polymer **16**, fusing electron rich thiophene units and electron deficient benzothiadiazole (BTD) units in the backbone. The synthesis was achieved by reduction of the ketones followed by the ring-closing reaction in the presence of boron trifluoride (Scheme 1.6).³⁶ The key to this successful

synthetic design was the ability to pre-fuse the electron deficient BTD unit with thiophene, which avoided electrophilic cyclization on an already electron deficient aromatic unit.



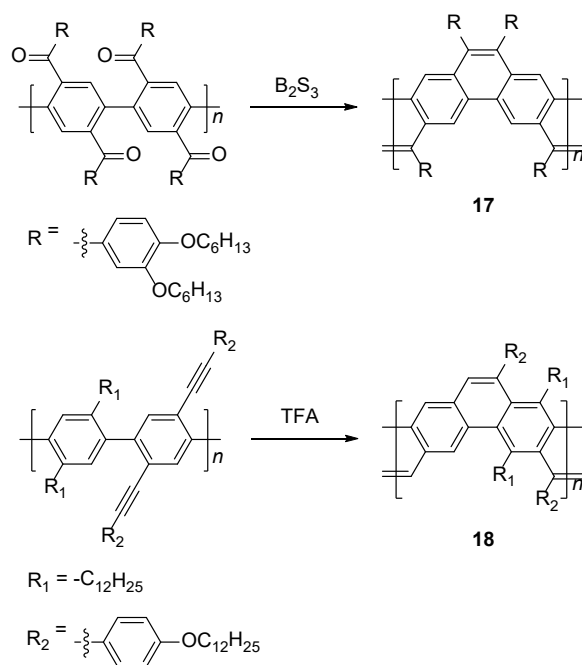
Scheme 1.5. Synthesis of carbazole-fluorene-based ladder polymer **15** by Bischler-Napieralski cyclization



Scheme 1.6. Synthesis of D-A type ladder polymer **16** by Friedel-Craft ring annulation.

Scherf and coworkers also reported⁴⁷ the synthesis of ladder type poly(*p*-phenacene) derivatives by using Yamamoto coupling of a diketo-functionalized monomer, followed by carbonyl olefination in the presence of B_2S_3 . Alternatively, the ladderization step could be also carried out by the McMurry reaction. In this report, polymer **17** with a linear side chain (4-decyloxyphenyl) resulted in a polymer which was marginally soluble, so that the product was soluble only at a low molecular weight (*ca.* 4 kg/mol). The solubility and molecular weight of ladder type poly(*p*-phenacene) derivative **17** was improved by replacing the linear side chain with bulkier (3,4-dihexyloxy)phenyl units.⁴⁸

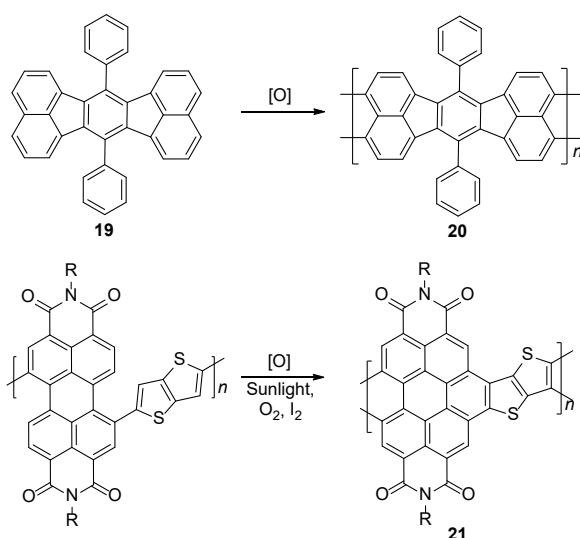
A similar ladder-type backbone was also prepared by Swager and coworkers using electrophile-induced cyclization (Scheme 1.7).⁴⁹ The acetylenic functional group on the conjugated polymer was cyclized in the presence of trifluoroacetic acid (TFA) to form aromatic rings to afford the ladder polymer **18**.



Scheme 1.7. Synthesis of poly(*p*-phenacene)s **17** and **18** by carbonyl olefination and electrophile-induced cyclization, respectively.

Electrochemical and photochemical oxidation reactions could also be employed to prepare cLPs (Scheme 1.8). Bard and coworkers described an electrochemical oxidation polymerization of precursor **19** to afford the postulated ladder polymer **20** deposited on the electrode surface. Because of the uncertain regioselectivity of the oxidative coupling process and the insolubility of **20**, the precise structure cannot be characterized by solution-phase analysis.⁵⁰ Xiong and coworkers reported photocyclization of a conjugated

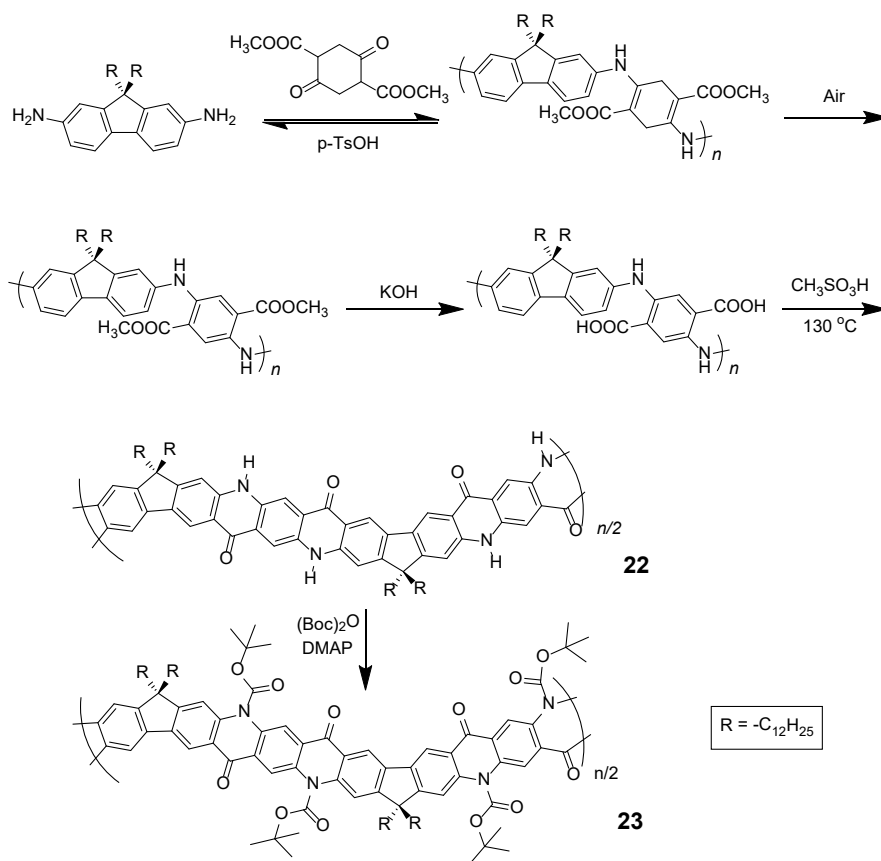
polymer precursor under sunlight,³⁵ to afford D-A ladder polymer **21** with a highly rigid and coplanar aromatic core. Due to the electron deficient nature of its perylene diimide components, **21** exhibited a low LUMO energy level of -3.98 eV, promising good *n*-type semiconducting behavior. Although the ladder polymer **21** had moderate solubility in common organic solvents at room temperature, structural characterization of the ladder backbone proved to be difficult.



Scheme 1.8. Synthesis of ladder polymer **20** by electrochemical oxidation and D-A type ladder polymer **21** by photochemical oxidation.

In the cases discussed above, metal catalyzed cross-coupling reactions were employed prevalently to construct the conjugated polymer precursors. A synthetic method free of precious metal catalyst, however, would suit better for scalable production of cLPs. Recently, Fang and coworkers reported a 3-step, metal-free synthesis of conjugated ladder polymer **22** derived from quinacridone (Scheme 1.9).⁵¹ Relying on imine

polycondensation and a subsequent *in situ* oxidation in air, a conjugate backbone was constructed. The ring annulation was achieved through a kinetic process mediated by methanesulfonic acid. Although **22** was not soluble in common organic solvent, the structural elucidation was achieved indirectly by characterizing its soluble derivative **23**, which is functionalized with *t*-butoxycarbonyl (Boc) groups.



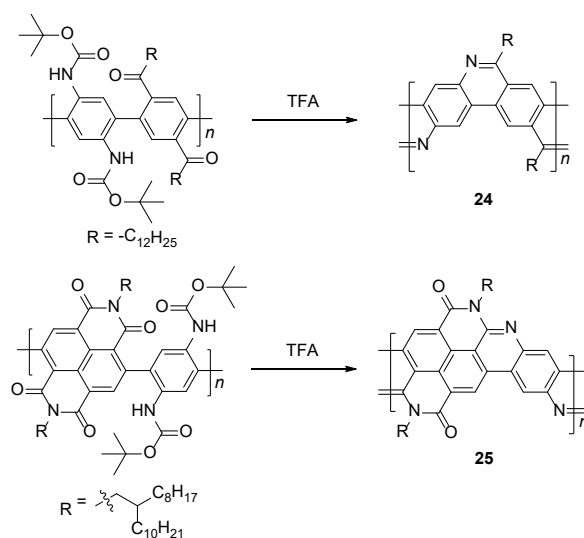
Scheme 1.9. Metal catalyst-free synthesis of quinacridone derived ladder polymers **22** and **23**.

1.1.2.3.2. Thermodynamic Ring Annulation

Distinct from kinetically controlled annulations, which require a careful selection of reagents and conditions for the efficient production of a single product due to the irreversibility of the reactions, thermodynamically controlled annulations, in principle, allow “error-checking” and “proof-reading” to push the reversible equilibrium to the most stable state.⁵² Because the goal in the synthesis of cLPs is usually to construct stable aromatic rings, thermodynamically controlled reactions should afford the desired product with higher yield and fewer structural defects such as unreacted sites or inter-chain crosslinking.

In the 1990s, Tour *et al.* reported a thermodynamically controlled reaction for post-polymerization modification that afforded cLP **24**.⁵³ Imine-bridged LPPP **24** was synthesized by imine condensation of a conjugated polymer precursor (Scheme 1.10). To avoid unwanted imine condensation between free amines and ketones during the polymerization step, the amino group was protected by Boc group before the polymerization. In several small molecule model reactions, this method afforded fused aromatic ring formation and showed nearly quantitative conversions. The conjugated polymer was converted into imine-bridged cLP **24** by deprotection of the Boc group in the presence of TFA. However, **24** was only soluble in TFA, which can result in the protonation of the nitrogen atoms along the polymer chains and could partially dissociate the C=N bond; therefore, the structural analysis of unmodified **24** remained unclear. Luscombe and coworkers also reported solution processable imine-bridged ladder polymer **25** containing naphthalene diimide (NDI) building blocks, synthesized using the

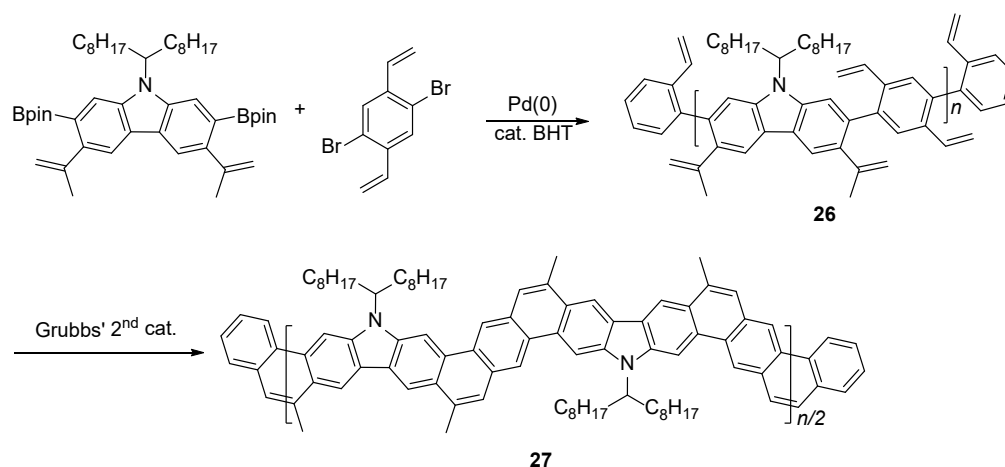
same method as **24** (Scheme 1.10).¹⁷ The β -branched 2-octyldodecyl alkyl side chain on the NDI nitrogens provided sufficient solubility for ladder polymer **25** in common organic solvents. It is worthy to note that the SEC-measured molecular weight of **25** ($M_n = 14$ kg/mol) was overestimated due to the increased hydrodynamic radius of the rigid, ribbon-like backbone, giving a higher M_n than the precursor conjugated polymer (7.2 kg/mol).



Scheme 1.10. Synthesis of imine-bridged LPPP **24** and D-A type ladder polymer **25** by thermodynamically controlled imine condensation.

Another method that has recently been recognized as an efficient strategy to construct fused-ring aromatic systems is the thermodynamically controlled ring-closing olefin metathesis (RCM) method.⁵⁴ The dynamic nature of the RCM reaction can avoid the formation of cross-metathesis side-products and drives the reaction equilibrium to the desired fused-ring product, which sits in a deep energy sink because of additional aromaticity. Fang and coworkers reported the synthesis of carbazole-derived ladder

polymer **27** by RCM from vinyl pendant precursor polymer **26** (Scheme 1.11).⁷ The single-stranded conjugated polymer **26** was prepared by Suzuki polymerization and endcapped using styrene derivatives. The reaction was conducted in the presence of a catalytic amount of butylated hydroxytoluene (BHT) as a radical scavenger, to avoid radical crosslinking of the styrene-like derivatives. Because of the strong solubilizing effect of the α -branched 1-octylnonyl group on carbazole, cLP **27** showed good solubility in common organic solvents at room temperature, allowing for solution analysis and processing. ¹³C NMR analysis of ¹³C isotope-enriched **27** revealed that the average number of possible unreacted vinyl groups in a single polymer chain was less than one (Defect < 1% and DP^{SEC} = 23-27). Due to the minimum levels of unreacted defects, the polymer conformation was maintained in solution and the solid state giving nearly identical UV-Vis spectra in both states with Stokes shift of only 1 nm.



Scheme 1.11. Synthesis of carbazole-based ladder polymer **27** by thermodynamically controlled ring-closing olefin metathesis.

Overall, the development of both single-step ladderization and stepwise polymerization followed by ladderization methods has steadily progressed in the past decade. Although the single-step approach is limited in reaction scope, the strategy of using simultaneous dynamic bonds should provide promising advancement for cLP synthesis. For the stepwise approach, various synthetic methods have been explored to expand the selection of kinetic ring annulation. Furthermore, recent examples of thermodynamic ring annulation have widened the scope of the synthesis of well-defined cLPs. As synthetic methods to develop a wider range of cLPs have improved, similar progress has occurred in their analytical and characterization techniques. Though the challenges originating from cLPs' highly rigid structures have prompted the rise of many new techniques, continued innovation of more advanced approaches is still a potentially impactful opportunity.

1.1.3. Challenges and Issues

1.1.3.1. Structural Defects

In conventional conjugated polymers, the planar aromatic repeating units tend to adopt non-zero dihedral angles between each building block due to torsional strain and thermodynamic fluctuation.⁵⁵ Such torsional defects partially break the coherent π -conjugation of the backbone, shorten the effective conjugated lengths along the polymer chain, and decrease carrier mobilities.^{8, 56} The torsional defects also perturb the intermolecular packing of the polymer materials, resulting in a higher energy barrier for the charge carriers and excitons to transport throughout the bulk material.^{11, 57} These

combined factors cause a much lower electronic performance of polymers compared to the theoretical value of a conjugated polymer chain.⁹ Unlike conventional conjugated polymers, ideal conjugated ladder polymers are torsional defect-free, maximizing π -electron delocalization. As a result, cLPs with a perfect structure should show increased electronic performance over conventional conjugated polymers. Such a defect-free cLP, however, is challenging to synthesize and characterize, as described above. Most of the reported cLPs are likely decorated with structural defects resulting from unreacted sites or side-reactions.

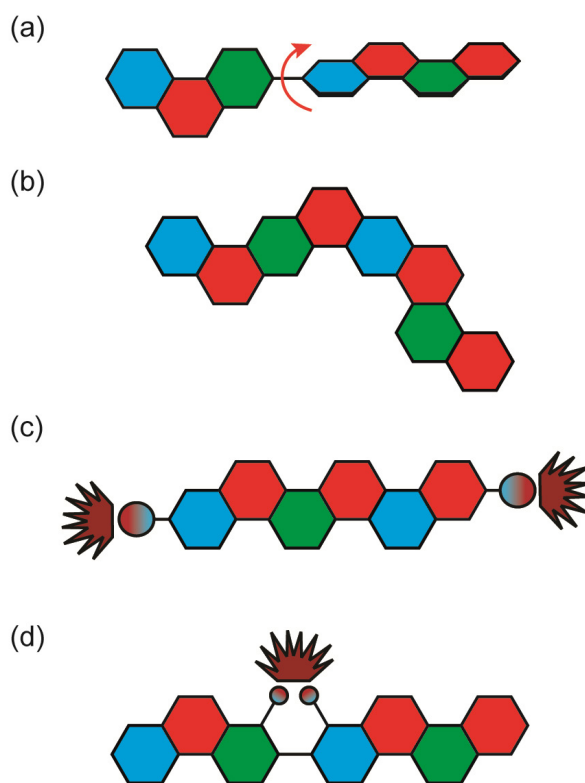


Figure 1.4. Defects common in cLPs. (a) Conjugation breaking torsional defects formed by incomplete ladderization or postsynthetic degradation, (b) regioisomeric structures created during nonregioselective syntheses, and non-conjugation breaking emissive defects (c) as a result of non-ladderized chain end groups, and (d) internally in the polymer chain.

Because of the significant impacts that polymer defects could impose on the material's properties, methods to remove or prevent these defects on cLPs are valuable. There are multiple ways in which defects can occur in a ladder polymer, including impurities in starting materials, incomplete or inefficient ladderization reactions, or a loss of solubility en route to the desired product (Figure 1.4a and b). This leads to the demand of quantitative ladderization reactions, because even a small decrease in conversion from single-stranded conjugated polymer to cLP can cause multiple defects per strand if the molecular weight is high.

An alternative way to achieve low level of defect in cLP is to remove defect-containing macromolecules. In the case of cLP **27**, the small amount of polymer chains containing unreacted pendant vinyl groups was reacted in solution with azobisisobutyronitrile (AIBN) to initiate the free radical cross-linking of these vinyl groups. This reaction only takes place on the polymers containing vinyl defects, giving insoluble products that can be easily removed by filtration, leaving behind the pure defect free macromolecules in solution. In general, the defect removal process depends heavily on identifying reactions that selectively react with defect sites. For soluble cLPs, cross-linking the unwanted polymer chains through defect site reactions may be developed into a useful method for purification.

The end groups are also considered defects, because undesired end groups can affect the properties of the polymer by both acting as a charge trap as well as affecting long range packing in some conjugated polymers (Figure 1.4c).⁵⁸⁻⁶⁰ In this context, end-

capping a cLP during synthesis is sometimes necessary to lower the defect level for a better material performance.

In addition, some cLPs may develop defects after synthesis. The defect-property correlations have been investigated thoroughly in LPPP derived cLPs, by taking advantage of the large difference in emission characteristics between the pristine polymer and those with defects. For example, LPPPs **11** and **12** undergo oxidative degradation that can either break one of the strands of bonds and create a torsional defect or be oxidized into an emissive ketone defect. Both LPPPs **11** and **12** and alkylated polyfluorenes, which are photooxidized into fluorenones, have been studied to illustrate the effects of these emissive defects (Figure 1.4d).⁶¹ After these oxidative defects are formed, both systems show a broad, low energy emission, sometimes called the Green Band. Though originally thought to be caused by excimers or other intermolecular interactions, more recent research has shown that it was solely the effect of ketonic defects acting as emissive traps.⁶² Such oxidation is much more likely to take place if the bridgehead carbon contains a hydrogen, as illustrated in HLPPP ($R^3 = H$) **11**, which has a much stronger low-energy band than MeLPPP **12**. It is also possible for residual impurities to play a significant role in the degradation of cLPs. Ma's group showed that $Pd(PPh_3)_4$, a common aryl coupling catalyst, could trigger the oxidation of fluorene moieties into their fluorenone forms as well, demonstrating the critical role residual impurities could play in defect formation.⁶³ PL lifetime measurements of defect formation were recently investigated by Lupton and coworkers using poly(9,9-dioctylfluorene) as a model system,⁶⁴ showing evidence that the Green Band is not a single broad band but instead consists of multiple emitters, each at a

discrete wavelength. Scherf and coworkers showed that these emissive properties are still maintained in the absence of any intermolecular interactions, further suggesting the lack of excimer involvement in emissions.⁶⁵ To rectify this problem, the previously discussed spiro-LPPP **14** was synthesized through a slightly different, but defect-resistant synthetic scheme, and consequently showed a stable emission.^{5, 66} These studies illustrated that defects can often impose significant impacts on the optical properties of cLPs.

1.1.3.2. Solubility and Processing

The features of rigid backbones enhance the strong π - π interactions of cLPs and often result in their limited solubility caused by these strong intermolecular attractions.^{1, 67-68} A notable example of a fully fused aromatic system is graphite, which is composed of π -stacked graphene layers and is apparently insoluble in any organic solvent. In addition, the presence of heteroaromatic repeating units may cause other interchain attractive interactions, *e.g.* hydrogen bonds and dipole-dipole interactions. Limited solubility of many cLPs due to these properties imposes challenges in processability and therefore in many practical applications.

A typical method to improve the solubility of cLPs is to introduce to the backbone flexible yet bulky side chains, which cause enough steric hindrance between chains to disrupt interchain aggregation.¹⁷ For example, in LPPPs **11** and **12**, the two alkyl groups installed on the quaternary sp^3 carbon center can be viewed as a branched alkyl group. As the branching point is moved farther from the polymer chain, interchain π - π distance decreases, leading to a general trend of decreasing solubility but increasing charge carrier

mobility in bulk.⁶⁹⁻⁷⁰ In addition, as alkyl chains grow longer, the amount of space taken up by nonconductive hydrocarbons increases, further separating conductive pathways. Therefore, a balance must be struck between solubility and device performance for a cLP that is designed for applications associated with electronic performances.^{69, 71-74} In order to address this dilemma, side-chain engineering in terms of chemical structures, linkages to the backbone, and conformations need to be investigated extensively to best achieve the desired processability and properties of the cLP materials.

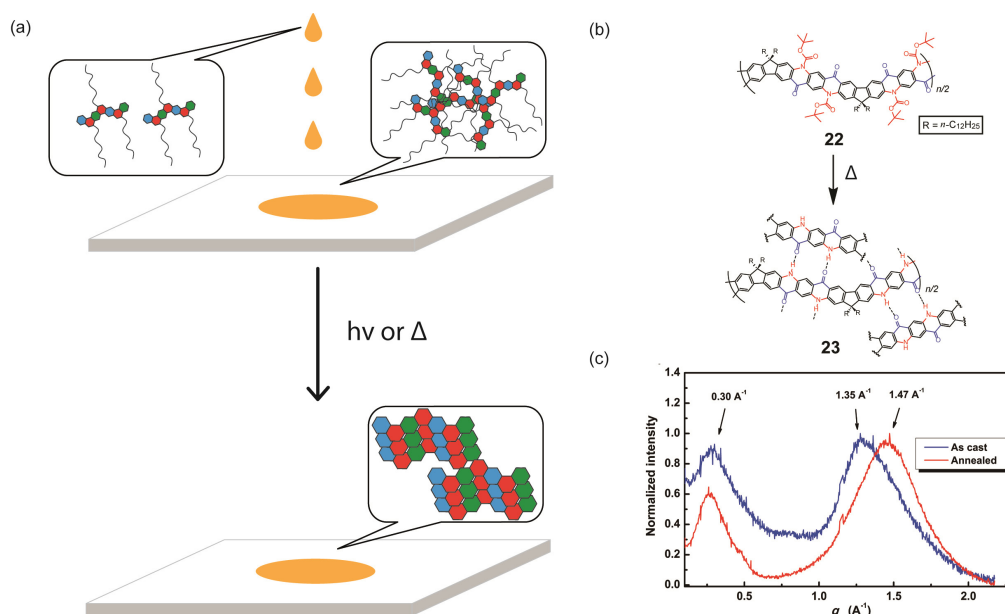


Figure 1.5. (a) Proposed illustration using cleavable side chains in cLPs processing to obtain a well-ordered, solvent resistant film from an easily processed material. (b) Schematic representation of Boc cleavage of **22** by thermal annealing in the solid state. (c) GIXD of the as-cast film of **22** (blue) in comparison with that of the annealed thin film (red). Reproduced from ref. 51 with permission from Elsevier.

A promising strategy to address the aforementioned challenge is the employment of cleavable side-chains. Cleavable solubilizing groups enable solution processability of the cLP materials and can also be easily removed after processing to potentially allow for efficient packing in the solid state (Figure 1.5a). In addition, these polymers should possess significant solvent resistance after processing and side-chain cleavage,⁷⁵⁻⁷⁶ providing additional advantages for processing and operation in harsh conditions. In the example reported by Fang and coworkers, quinacridone derived ladder polymer **22** was rendered soluble by the incorporation of bulky Boc protecting groups that inhibit intermolecular hydrogen bonds (Fig. 5b).⁵¹ These Boc groups were then thermally cleaved to regenerate the hydrogen bonds and to produce thin films with remarkable solvent resistance. Grazing incidence X-ray diffraction (GIXD) measurements of the thermally annealed polymer thin films showed a decrease in the π - π stacking distance as a result of removal of the bulky Boc group (Figure 1.5c).

1.1.3.3. Characterization of Conformation and Molecular Weight

Because of the inherent rigid nature of cLPs, their conformations and dynamics in solution are expected to differ from prevailing non-rigid polymers significantly. Quantitatively, this difference should give a much higher Mark-Houwink exponent ($0.8 < a < 2.0$) for cLPs than that of flexible polymers ($0.5 < a < 0.8$). Correlation between hydrodynamic volumes and molecular weights for cLPs is therefore also drastically different from that of flexible polymers. As a result, traditional solution characterization techniques, such as SEC calibrated by polystyrene standards, cannot provide accurate

depictions of the conformation and molecular weight for cLPs. Research has illustrated that when using multiple methods of analyzing molecular weights,⁷⁷⁻⁷⁹ the measured values vary between the different methods used. To date, a number of different methods have been applied to solve these issues, with varying levels of effectiveness.

Small angle X-ray and neutron scattering (SAXS and SANS) have been applied to characterize the conformations and gain accurate molecular weights of rigid polymers. X-rays interact with the electron cloud of the molecule, while neutrons are scattered by elastic collisions with the nuclei of the material. The scattering intensity for various values of concentration (c) and scattering angle (θ) is plotted in a Zimm plot. Upon extrapolation to $c=0$ and $\theta=0$, the intersection of the two lines is equal to $1/M_w$ and can therefore be used to determine accurate molecular weights. In addition, the slope of the $\theta=0$ line is proportional to the 2nd virial coefficient. SANS in particular provides a unique method of characterization on partially deuterated sample in order to provide a higher contrast variation without largely changing the sample itself, due to the differences of neutron scattering between hydrogen and deuterium.⁸⁰ Alternatively, a hydrogenated sample in deuterated solvent can also provide the needed contrast. These techniques were used, for example, to study the conformation of LPPP **12** in solution.⁷⁸ The use of both methods showed a persistence length of approximately 6.5 nm, indicative of a 3D ribbon-like structure instead of a one-dimensional rigid rod. However, the complexity of the instrumentation and radiation sources necessary for these forms of measurement make it challenging to perform routine measurements on other cLP systems.

Simpler light scattering methods have also been utilized to characterize rigid polymers, including dynamic light scattering (DLS), which measures the anisotropic diffusion coefficients of the materials in solution and can be used to estimate the length of an idealized rigid rod.⁸¹ Because of the simplicity and accuracy of measurement, DLS has been used for other rod-like structures and represents an accessible method for the conformational analysis of cLPs.⁸²⁻⁸³

Other methods to characterize molecular weights of rigid ladder polymers include the use of osmometry or viscometry.⁸⁴⁻⁸⁵ These methods rely on the change in chemical potential of a solution of ladder polymers compared to a pure, non-theta solvent. Osmometry measures the osmotic pressure of a solution by change in volume through a semipermeable membrane (membrane osmometry) or of vapor pressure in a closed system (vapor phase osmometry). Viscometry measures the change in viscosity of varying concentrations of a polymer solution in order to find the polymer's intrinsic viscosity, and via the Mark-Houwink equation, the polymer's molecular weight. However, unreliable results may be obtained at either sufficiently high or low molecular weights depending on the method used. In addition, diffusion across the membrane of the osmometer can take extended time to reach an equilibrium.

In order to calculate the molecular weight and polydispersity index (PDI) of cLPs in a more rigorous manner, several advanced methods can be used. These include SEC with viscometer-assisted universal calibration⁸⁶⁻⁸⁷ or SEC coupled with multi-angle light scattering detectors.⁸⁸⁻⁸⁹ The employment of these methods for the characterization of cLPs, however, has not yet been well-established.

Structural elucidation has been another major challenge for the investigation of rigid cLPs. Both ^1H and ^{13}C NMR spectroscopy suffer from broad and low intensity signals, due largely to the limited solubility of the cLP samples and aggregation. This problem can be circumvented by the use of isotope labeling or alternative isotope measurements,⁷ in particular ^{13}C or ^{19}F , although the drawback for this method is sometimes tedious chemical synthesis. NMR analysis at higher temperature could also be employed to improve data quality by increasing the solubility and breaking up any aggregation. The incorporation of distinctive side chain or end-capping groups is another simple method to facilitate easier characterization. Alternatively, using the effects that rigid macromolecules have on NMR linewidths can also offer unique information of the polymers, such as the nature of solution aggregation or solid-state crystallinity.⁹⁰⁻⁹²

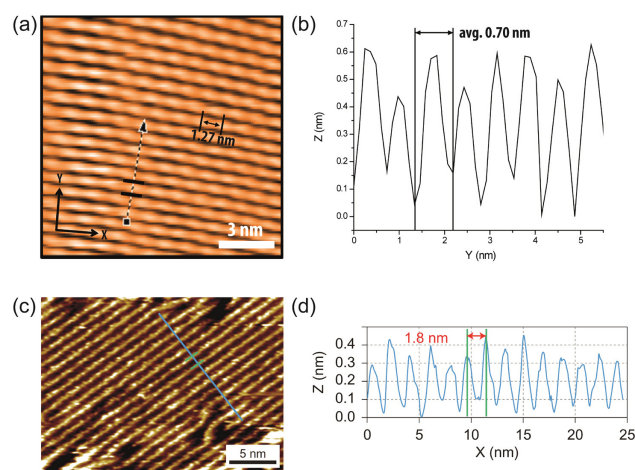


Figure 1.6. (a) STM images of cLP 27 on HOPG. (b) section profile along the arrow line drawn in (a). (c) STM images of the graphene nanoribbon on HOPG from ref. 68. (d) section profile along the blue line in (c). Reproduced from ref. 7 and 68 with permission from The Royal Society of Chemistry and Nature Publishing Group, respectively.

Surface probe microscopy can also be used to visualize the conformation of cLPs (Figure 1.6). In particular, due to the conjugated and semiconducting nature of the backbones, individual polymer chains of some cLPs can be visualized by scanning tunneling microscopy (STM). STM analysis of cLP **27** on highly-ordered pyrolytic graphite (HOPG) showed the rigid and linear shape of the polymers with repeating units that aligned well with calculated dimensions of an oligomeric model.⁷ In addition, STM has found extended use in the visualization of graphene nanoribbons with improved resolution due to the extended conjugated system's favorable interaction with graphite substrates.^{68, 93}

In general, though many accurate techniques have been adopted for cLP characterization, the most common method remains the use of non-rigid SEC standards. Therefore, the widespread application of a universally accurate method would help standardize measurements across the breadth of the field, increasing the quality and efficiency of related research.

1.2. Conjugated Ladder-Type Oligomers

1.2.1. Introduction

As an intriguing subset of functional organic materials, fully conjugated ladder-type oligomers and polymers have drawn intense research attention because of their promising physical and chemical properties.^{2, 94-95} Multiple strands of bonds in the backbone of these macromolecules lock the torsional conformation, hence leading to coherent conjugation within the coplanar pi-system and strong intermolecular interactions. These features promote their potential utility as active materials for applications that desire the optical and electronic character afforded by the fused aromatic backbones.

Though ladder-type polymers have recently become an area of increasing focus, the study of oligomers may well be equally instructive. Due to the polydispersity of the molecular weights of polymers, it is challenging to correlate specific properties to molecular size in a precise manner; in contrast, the investigation of a series of linearly extended oligomers can provide the basis for conclusive evidence for size-dependent properties. The trends discerned from these oligomers can inform rational design and predict the resulting properties of their polymeric analogues, whose properties and performances are improved by ladderization.⁹⁶⁻⁹⁷ The tunable properties derived from these precisely designed and controlled oligomers can then be imparted into semiconducting conjugated polymers by utilizing the oligomers as polymer precursors.^{3, 98-99} Additionally, within the oligomeric regime, length-dependent properties begin to emerge that are not apparent in small molecules, but are controllable via their precise

length in contrast to polydisperse polymers. Therefore, oligomers may allow for access to a unique set of properties unavailable in either small molecules or polymers.

The synthesis of ladder-type oligomers is contingent on successfully constructing the fused-ring backbone, which may be accomplished through two different approaches: (1) simultaneously constructing multiple strands of bonds in one transformation,¹⁰⁰⁻¹⁰⁴ or (2) sequentially synthesizing a conventional oligomeric precursor connected with one strand of bonds, followed by a “ladderization” step in which an intramolecular annulation forms the second strand of bonds (sequential oligomerization–annulation, Figure 1.7), which will be the principal focus of this essay. Discrete oligomeric precursors are obtained either by a step-growth polymerization to give a mixture of oligomers which are then separated on the basis of their lengths,¹⁰⁵⁻¹⁰⁷ or a stepwise synthesis in order to directly access the desired oligomer length, where different oligomers are synthesized in parallel procedures rather than simultaneously. Due to the higher inherent purity given by the stepwise approach, the latter has been employed extensively as the primary synthetic strategy even with the cost of the extra steps. In nearly all examples discussed herein, transition metal-catalyzed coupling reactions are used to construct the single-stranded oligomer precursors, before the intramolecular annulation reactions.

Our discussion will focus on the various available methods of ladderization for the sequential oligomerization–annulation strategy. The syntheses and properties of ladder-type polymers,^{2, 94-95} graphene nanoribbons,^{93, 108-109} and other large pi-conjugated

systems,¹¹⁰⁻¹¹³ have been covered in other reviews and therefore are not discussed in detail in this essay.

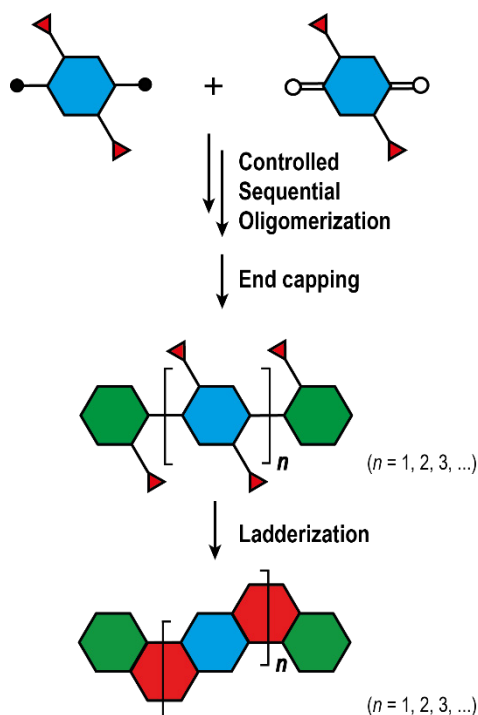
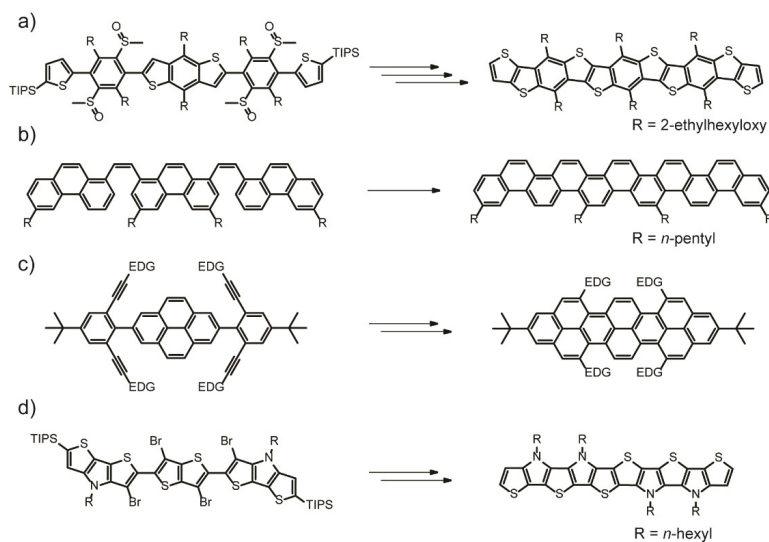


Figure 1.7. Sequential oligomerization-annulation synthesis of ladder-type oligomers. Discrete oligomers are synthesized through stoichiometrically controlled couplings which then can be endcapped and annulated to give the fully fused oligomers.

1.2.2. Kinetic Annulations

During the key ladderization step, the majority of the annulation reactions are irreversible and so give a kinetic product, making the precursor and reaction design instrumental to achieve the desired high efficiency. These reactions include Friedel-Crafts substitution, Scholl oxidation, alkyne benzannulation, and metal-catalyzed cross-couplings.

Intramolecular Friedel-Crafts electrophilic substitution represents perhaps one of the most common ladderization strategies, broadly used in the construction of ladder-type *p*-phenylenes and subsequently expanded to other frameworks.¹¹⁴⁻¹¹⁷ A pendant group is usually required to serve as the electrophile and is typically activated in acidic conditions. Electron-rich aromatic units which can function as nucleophiles are required to facilitate the reaction. For example, the intramolecular cyclization of acid-activated sulfoxides¹¹⁸⁻¹²⁰ has been used to form various ladder-type sulfur-bridged oligomers including thienothiophenes and thieno-*p*-phenylenes (Scheme 1.12a). In these types of aromatic substitutions, one must strike a balance with steric hindrance. Bulky sidechains sterically insulate molecules from undesirable intermolecular crosslinking, but too much bulkiness may lead to low reactivity of the desired intramolecular annulation, leading to defects and low yields.²



Scheme 1.12. Representative kinetically controlled ladderization reactions through (a) electrophilic aromatic annulation followed by demethylation and removal of TIPS, (b) the Scholl reaction, (c) alkyne benzannulation, and (d) Buchwald coupling followed by removal of TIPS.

Another ubiquitous annulation is the Scholl reaction, in which adjacent aromatic units are coupled through oxidative dehydrogenation. This reaction proceeds from C–H groups and requires no prior functionalization, provided the geometry and electronic density of the coupling partners are aligned for the reaction. As a result, the Scholl reaction has been used extensively as an efficient final step to construct fully fused structures with multiple adjacent aromatic rings, such as in the synthesis of many polycyclic aromatic hydrocarbons after initial coupling steps.¹⁰⁸ In addition, it has recently been used in the annulation of various aromatic units with perylene diimides (PDIs), following an initial metal coupling, simplifying the derivatization of the highly electron-deficient and therefore challenging PDI units, to afford donor-acceptor architectures.^{101, 121-124} The regiochemistry of the oxidation, however, may be difficult to control and the conditions may occasionally give rearrangement products, especially in sterically crowded environments.¹²⁵⁻¹²⁶ Regardless, the synthesis of all-carbon fully fused materials has been heavily dependent on Scholl oxidation. This argument also holds true in smaller oligomers. For example, it found early use in the ladderization of stilbene-like molecules following Wittig olefination in order to create a series of [*n*]phenacene derivatives (Scheme 1.12b),¹²⁷ which are of specific importance as a substructure of graphene and can be used to interpret the properties of smaller graphenic structures. In many cases, Scholl oxidation products can be obtained in high yields, though results may vary widely depending on the substrate and the numerous possible reaction conditions under which the oxidative coupling can proceed.

Another important annulation mechanism involves the transformation of pendant arylethylenes into a conjugated backbone through a variety of electrophile-induced benzannulations, including pi-Lewis or Brønsted acids.¹²⁸⁻¹²⁹ The triple bond is initially activated by the acid, followed by a 6-*endo-dig* cyclization with the aromatic ring, and eventually a proton loss to restore aromaticity. These annulations were used to synthesize a series of pyrene oligomers in two steps promoted by a Brønsted acid (Scheme 1.12c).¹³⁰ The properties of these pyrene oligomers can be modulated by installing different aryl groups on the pendant alkynyls, such as the common electron-donating thiophene unit.¹³¹

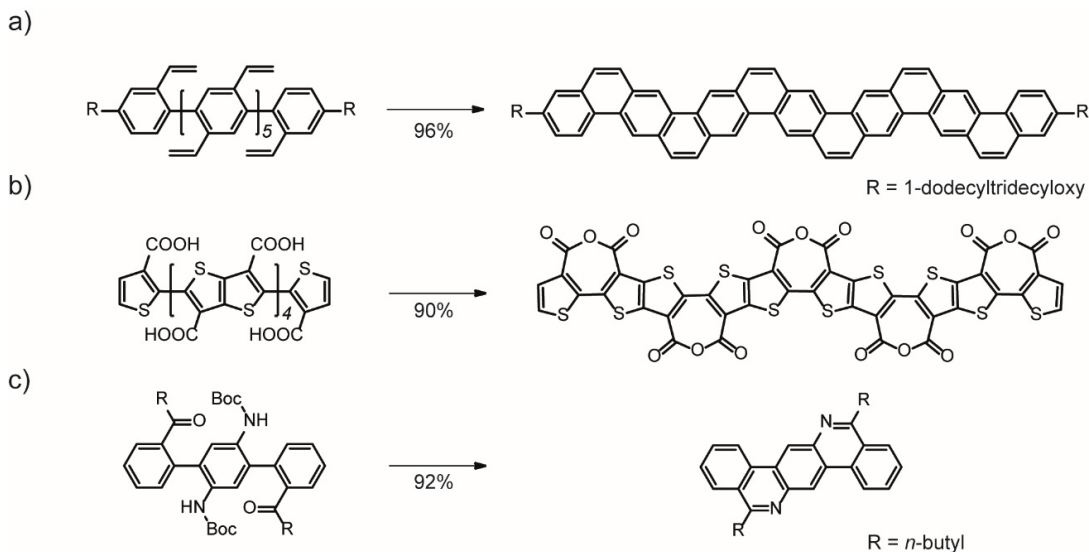
Certain metal-catalyzed cross-couplings can also be employed to ladderize oligomers. These examples involve reactions that couple geometrically preorganized and reactively complementary functional groups on adjacent aromatic units, or the coupling of a bridging reagent with two adjacent aromatic units at specific positions.¹³² For example, Yamamoto coupling was recently used in the ladderization step of a bromide-functionalized macrocyclic oligomer to afford a carbon nanobelt.¹³³ In another report, a primary alkylamine was coupled with two adjacent aryl bromides using Buchwald conditions to afford a fused dithienopyrrole unit (Scheme 1.12d).¹³⁴ It is worthy to highlight a unique requirement for these annulations: as both the oligomerization and ladderization steps proceed via aromatic cross-couplings, the former must possess some degree of orthogonality or selectivity to the latter in order to avoid unwanted side products at different stages of the synthesis.

The potential for regioisomer formation during the annulation reactions presents a common challenge when there are multiple potential reactive sites in the precursors. Careful monomer design is required to activate the desired reaction site or to deactivate or block any undesired reaction sites. This objective can be achieved by substitution on unwanted reaction sites with nonreactive groups, or by electronic modulation of certain positions to preferentially facilitate certain reactions. For example, addition of triisopropylsilyl (TIPS) groups (Scheme 1.2a and d) can serve to prevent intermolecular coupling during annulation before the TIPS groups are removed to afford the final product.

1.2.3. Thermodynamic Annulations

A key requirement for the efficient synthesis of ladder-type materials is that the annulation reaction must be highly efficient and specific to intramolecular reaction; if not, unreacted sites or intermolecular cross-linking reactions will lead to lower yields of the desired products. This requirement becomes more important with increasing oligomer length where even a moderate annulation efficiency would be detrimental to the overall yield of the final product. In this regard, thermodynamically controlled annulation processes with a strong driving force represent a promising approach to the desired high efficiency. The reversible nature of these reactions lends them an “error-checking” ability when intermolecular reactions give undesired side products, which are not kinetically trapped and instead can easily revert back. The thermodynamic driving force is derived from the stability of the final product compared to the starting materials, side products,

and intermediates. In the case of fully conjugated ladder-type oligomers, this driving force is significantly bolstered by the added stabilization of aromaticity.



Scheme 1.13. Examples of thermodynamic ladderization reactions through (a) RCM, (b) dehydration of carboxylic acids, and (c) imine condensation

We recently reported a thermodynamic ladderization approach utilizing ring-closing olefin metathesis (RCM) of adjacent vinyl-functionalized aromatic units.^{7, 135} The backbone aromatization provides the needed thermodynamic driving force and, in combination with the reversibility of RCM, yields nearly quantitative conversion to the polycyclic aromatic product.^{54, 136-137} The addition of a radical scavenger was essential to prevent radical-initiated cross-linking of the vinyl-pendant groups. The efficient nature of these ladderization processes is not affected by increasing backbone length, leading to a series of benzo[*k*]tetrathene (BTp)-derived oligomers of up to 13 fused rings in over 96% yields (Scheme 1.13a). The oligomeric precursors were prepared by sequential Suzuki

couplings of divinyl dibromobenzenes and divinylphenyldiboronic esters followed by endcapping with a terminal branched alkyl group. These side-chains solubilized the highly rigid molecules without direct backbone modification.

In general, RCM is tolerant to a wide substrate scope due to its neutral reaction conditions, provided that the desired monomer can be functionalized with pendant vinyl groups. Like alkyne benzannulations, RCM creates an aromatic fused ring from hydrocarbon precursors, which holds promise in the synthesis of extended linear graphenic materials. The position of the vinyl groups governs the regiochemistry, enabling future construction of ladder-type molecules with specific backbone constitutions for precise structure-property correlations.

Other thermodynamic annulation methods have also demonstrated high efficiency in the ladderization of oligomers. For example, a recent synthesis of heterocyclic imides gave above a 90% yield in the annulation step of a 15-ring fused oligomer.¹³⁸ The thermodynamic condensation of adjacent arylcarboxylic acids afforded ladder-type thienothiophene oligomers through the formation of five nonaromatic anhydride bridging groups (Scheme 1.13b). After ladderization, these anhydrides were converted to alkylated imides, rendering good solubility to the ladder-type oligomers. Imine condensation has also been employed successfully to construct ladder-type structures in both polymers and small molecules, and so may be a useful method for future longer oligomers.^{17, 139-140} In one example (Scheme 1.13c), the annulation is induced by acid cleavage of *t*-butyloxycarbonyl (Boc) groups to give free arylamines, which then undergo condensation with adjacent ketones to give the final ladderized imines, in an excellent yield over 90%.

Overall, though thermodynamic annulations are preferable from an efficiency standpoint, the scope of available reactions is still limited. Finding other suitable thermodynamically controlled annulation reactions, especially those affording C–C or C=C bonds, is desired for widespread adoption of this strategy.

CHAPTER II
EXTENDED FUSED POLYCYCLIC HETEROARENES VIA
THERMODYNAMICALLY CONTROLLED RING-CLOSING OLEFIN
METATHESIS

2.1. Introduction

Fused-ring aromatic materials have attracted tremendous attention due to their versatile properties in various applications, such as organic field effect transistors (OFET)¹⁴¹⁻¹⁴² or organic photovoltaics (OPVs).¹⁴³⁻¹⁴⁷ In addition, introducing heteroatoms to a fused-ring system demonstrates intriguing material properties.^{113, 148} Research into this century-old field is propelled by growing interest in organic electronics. Furthermore, the construction of extended fused-ring aromatic materials such as graphene nanoribbons (GNRs) using a bottom-up synthesis has been the focus of intense research effort during the past decade owing to the scalability.^{68, 111} As the theoretical and practical importance of bottom-up synthesis of fused-ring aromatic materials increases, more versatile and efficient ring annulation methods are required to construct a well-defined fused-ring system. Various synthetic strategies have been employed to synthesize a well-defined fused aromatic compound, such as Scholl oxidation,¹⁰⁸ which successfully converts a pre-organized conjugated material into GNRs. However, Scholl oxidation is highly substrate-dependent and affords rearranged side products in many cases.⁹³ Another important method is cyclocondensation between pyrene tetraketones and di- or tetraamino building blocks. This method afforded a pyrazine-containing hetero aromatic ring, but typically

suffers from a low yield and limited availability of starting materials.^{90, 100, 148} Furthermore, Friedel-Crafts ring annulation,^{118, 124} alkyne benzannulation,^{128, 130, 149} and transition-metal mediated ring annulation¹³⁴ were applied to construct extended fused heteroarenes. Despite these successful examples, it requires an effective synthetic method to expand the scope of fused-ring systems.

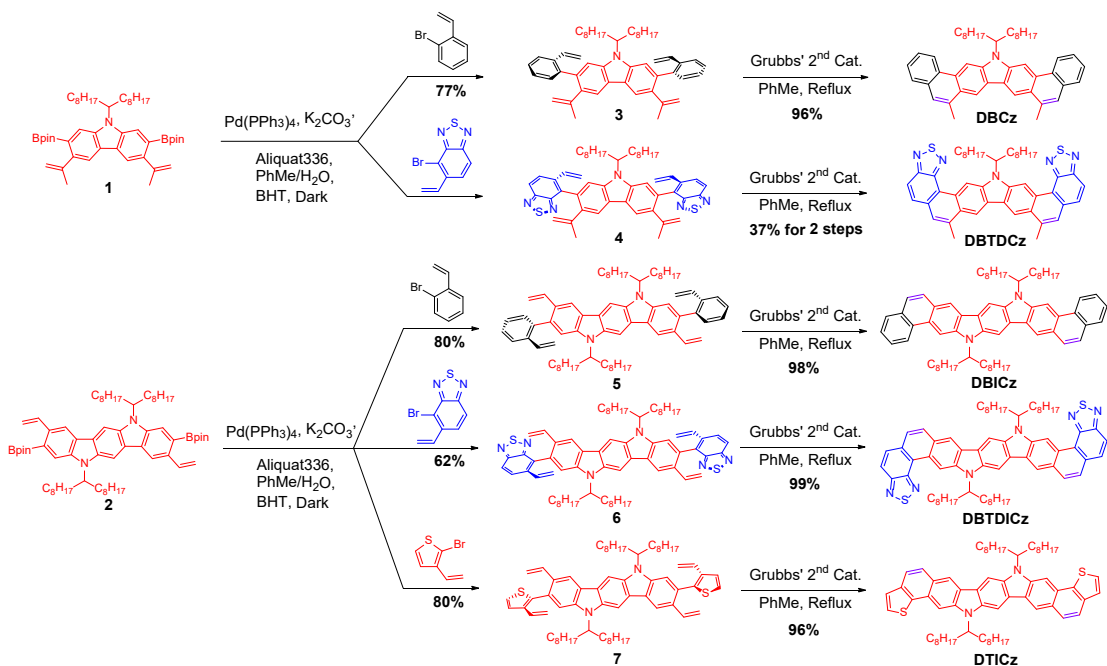
We recently reported the synthesis of extended fused-ring oligomers and ladder polymers by thermodynamically controlled ring-closing olefin metathesis (RCM) affording the resulting fused-ring aromatic materials with excellent yields and minimal structural defects.^{7, 150-151} Furthermore, RCM does not show a decreased reactivity during the ring annulation with an electron deficient unit.¹⁵¹ This efficient and versatile synthetic method provides a powerful tool to construct a fused-ring aromatic material. Herein, we report the synthesis of various fused polycyclic heteroarenes with up to 11 fused rings via RCM. In addition, the analysis of single crystal structures, optical properties, and the formation of charge transfer complexes (CTC) induced by their rigid coplanar nature were investigated.

2.2. Results and Discussion

In order to introduce a RCM compatible functional group for RCM, the carbazole precursor was acetylated using Friedel-Crafts acylation and further converted to the vinyl group through Wittig olefination. It is worthy to note that installation of the aldehyde on carbazole via the Vilsmeier-Haack reaction only afforded 17% of the mono-formylated product. The second formylation was hindered after the first iminium salt was installed

because the electron donating effect of the carbazole nitrogen was significantly diminished, resulting in deactivation of nucleophilic substitution. On the other hand, in the example of indolo[3,2-*b*]carbazole, it afforded the diformylated product in 63% yield through the Vilsmeier-Haack reaction. Since the two nitrogens of indolo[3,2-*b*]carbazole are separated by a central benzene ring, the first installation of an iminium salt minimally affected the further substitution.

For coupling partners of carbazole and indolo[3,2-*b*]carbazole, benzene (relatively neutral), 2,1,3-benzothiadizole (BTD, electron deficient), and thiophene (electron rich) were employed to prepare different fused-ring systems. For functional group addition, BTD required a pre-positioned methyl group, which was transformed into a vinyl group by benzylic bromination and Wittig olefination.



Scheme 2.1. Synthesis of extended fused polycyclic heteroarenes **DBCz**, **DBTDCz**, **DBICz**, **DBTDCz**, and **DTICz**.

With all the coupling partners in hand, precursors **1** and **2** were cross-coupled with vinyl-functionalized benzene, BTD, and thiophene via a Suzuki coupling reaction to afford tetra-vinyl derivatives **3~7** (Scheme 2.1). It is important to note that butylated hydroxytoluene (BHT) was used in the reaction as a radical scavenger to inhibit free-radical cross-linking of the vinyl functional groups. Compound **4** proved difficult to purify and was used for the next step without column purification. The subsequent RCM step for the tetra-vinyl derivatives **3~7** successfully afforded the desired fused polycyclic heteroarenes **DBCz**, **DBTDCz**, **DBICz**, **DBTDICz**, and **DTICz** in excellent yields over 96%. Although post-polymerization annulation of electron deficient units is challenging and can lead to incomplete conversion and low yields, aromatic ring annulation by RCM did not result in any difference between electron-deficient and -rich vinyl groups due to a strong aromatization driving force. In the case of **DBTDCz**, obtained in 37% yield in 2 steps, because the thermodynamically controlled RCM step showed almost quantitative conversion regardless of electron-deficiency, the low yield could be mainly a result of the Suzuki coupling reaction. The 1-octylnonyl side-chain of the fused-ring compounds, containing 7-, 9-, and 11-fused heteroaromatic rings, led to good solubility in common organic solvents, such as chloroform, toluene, and tetrahydrofuran.

¹H NMR spectra of the tetra-vinyl derivatives and the fused-ring compounds clearly showed the disappearance of the vinyl groups after RCM (see Appendix A). It is worthy to note that the indolo[3,2-*b*]carbazole-derived intermediates and fused heteroarenes exhibited atropisomerism caused by hindered rotation of the two sets of α -branched alkyl chains, resulting in distinct two sets of peaks. Furthermore, down-field

shifted aromatic peaks were observed due to the sterically crowded environments in the bay and fjord regions. In addition, the proton resonance peaks of **DBTDCz** and **DBTDICz** in the fjord region adjacent to the thiadiazoles shifted beyond 11.0 ppm due to the unusual intramolecular interaction between the thiadiazole nitrogen and the aromatic hydrogen originating from the rigid and coplanar structures.¹⁵¹⁻¹⁵³

The structures of the fused polycyclic heteroarenes were unambiguously confirmed by single crystal X-ray diffraction (Figure 2.1). The crystal structures demonstrated that the α -branched alkyl side-chains were perpendicular to the extended backbones, interrupting possibly strong intermolecular π - π interactions. Furthermore, all the backbones adopted a rigid coplanar geometry. The crystal structure of **DBCz** demonstrated that one molecule paired with another molecule upside down in a face-centered stacking manner (green and orange) due to C_{2v} symmetry of the carbazole backbone and the steric hindrance of the alkyl side-chains (Figure 2.1a). The π - π stacking distance of this paired molecules was measured to be 3.40 Å. These paired molecules also exhibited π - π interactions between very small π -faces of the end benzene rings in an off-centered parallel stacking manner with the distance of 3.49 Å. Moreover, the paired molecules were sandwiched by two different sets of paired molecules (orange) orthogonally. In addition, these paired molecules were surrounded by single molecules (blue). **DBCz** exhibited two different torsional angles based on the stacking manner. The torsional angles of the molecules in a face-stacking (green and orange) were measured to be 0.39° and 0.88°.

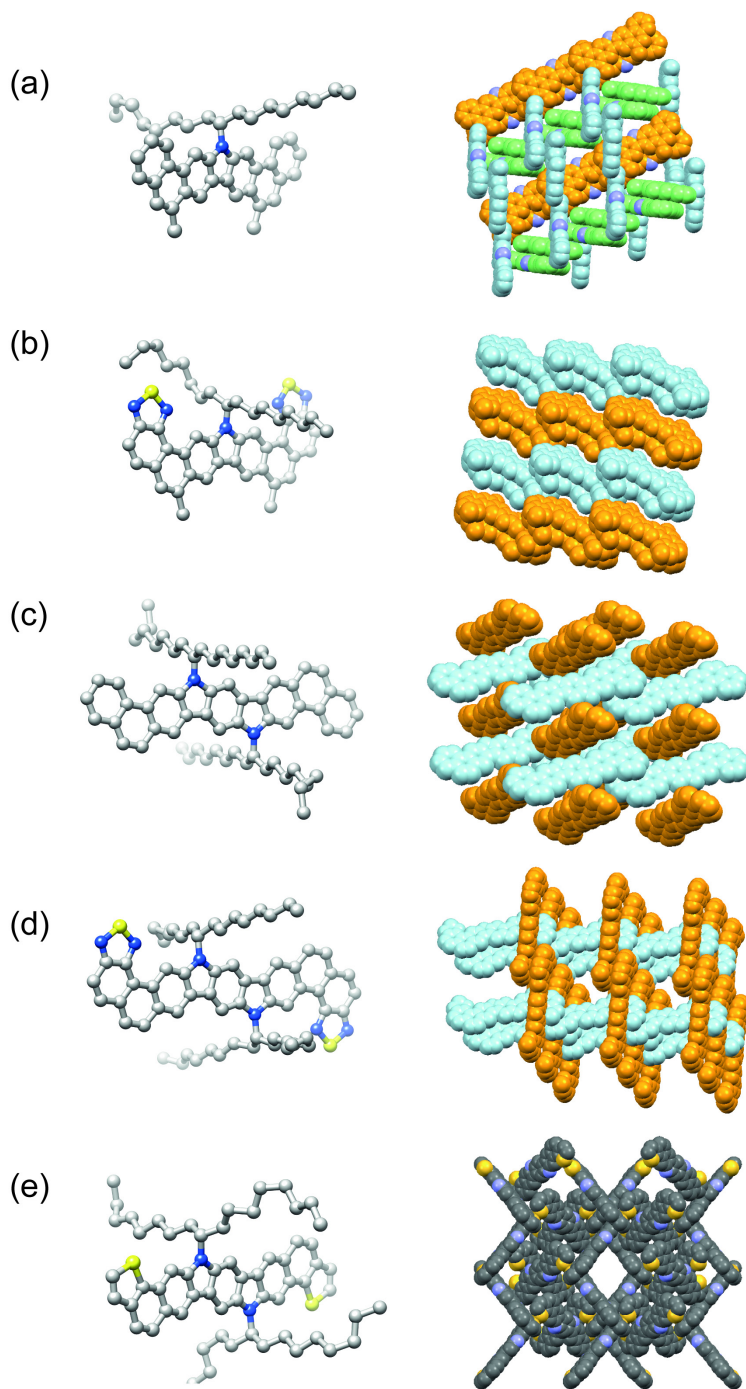


Figure 2.1. X-ray single crystal structures (left) and packing structures (right) of (a) DBCz, (b) DBTDCz, (c) DBICz, (d) DBTDICz, and (e) DTICz. Hydrogen atoms (left) and alkyl side chains (right) have been omitted for clarity. Colors indicate different layers of packing structures.

However, that of peripheral single molecules (blue) were measured to be 1.58° and 4.66° . This result suggests that coplanarization of the rigid backbone was induced by stronger π - π interactions. The crystal structure of **DBTDCz** also exhibited two paired molecules in a face-centered stacking manner (blue and orange) with a π - π stacking distance of 3.56 Å (Figure 2.1b). In addition, these paired molecules displayed much shorter π - π interactions between BTd faces in an off-center parallel stacking manner with a distance of 3.40 Å without orthogonally oriented molecules. The electron-deficient BTd resulted in the shorter π - π stacking distance than that of the paired molecules in a face-centered stacking. The torsional angles of **DBTDCz** (2.82° and 5.21°) were revealed larger than that of **DBCz** due to the more sterically crowded fjord regions. On the other hand, indolo[3,2-*b*]carbazole-based fused-ring molecules did not show a set of paired stacking due to the two sets of α -branched alkyl side-chains on C_{2h} backbones. **DBICz** displayed weak π - π interactions in the similar manner as **DBCz** with a distance of 3.40 Å (Figure 2.1c). In addition, this off-centered stacking layer was sandwiched between single molecules orthogonally. It was also found that **DBICz** in the off-centered stacking layer possessed a smaller torsional angle of 1.02° compared to the single molecules' torsional angle of 2.59° . In the example of **DBTDICz**, it demonstrated alternating crossed off-centered stacking layers with the π - π stacking distance of 3.45 Å (Figure 2.1d). The crossed stacking layers was caused by weak intermolecular S \cdots N interactions of BTd. The distance between sulfur and nitrogen was measured to be 3.53 Å, which is slightly longer than the sum of the van der Waals radii of sulfur and nitrogen atoms (3.35 Å). **DBTDICz** also showed larger torsional angle (3.66°) originating from the fjord regions.

Interestingly, the crystal structure of **DTICz** did not display significant π - π interactions (Figure 2.1e); instead, repulsive interactions originating from electron rich thiophene hindered off-centered and edge-to-face packing modes. However, **DTICz** clearly exhibited intermolecular S \cdots S interactions of thiophene on both sides, which was the main driving force of the crystal growth. The sulfur–sulfur distance was measured to be 3.52 Å, which is slightly shorter than the sum of the van der Waals radii of sulfur (3.60 Å).

Optical properties of fused-ring compounds were also investigated (Figure 2.2). UV-vis absorption spectra of all five compounds exhibited distinctive vibrational progressions as a result of highly rigid backbones (Figure 2.2a). Furthermore, the absorption spectrum of **DBICz** was red-shifted about 40 nm compared to that of **DBCz** due to the extended π -conjugation. Meanwhile, acceptor-donor-acceptor (A-D-A) type **DBTDCz** and **DBTDICz** displayed an approximately 60 nm red-shift compared to **DBCz** and **DBICz**, respectively because of the acceptor-donor-acceptor architecture. As expected, **DBTDICz** showed the most red-shifted absorption spectrum originating from the combined effect of π -extension and alternating donor-acceptor constitution. Interestingly, all fused heteroarenes showed optically weak HOMO-LUMO transitions due to the symmetry forbidden transitions, similar to the analogous ladder polymers. Moreover, they displayed red-shifted emission spectra in chloroform, similar to their UV-vis absorptions (Figure 2.2b). However, the narrow and well-structured emission spectra of **DBCz**, **DBICz**, and **DTICz** as a result of the highly rigid π -system became broad and featureless spectra in **DBTDCz** and **DBTDICz**. Furthermore, Stokes shifts of A-D-A type heteroarenes **DBTDCz** and **DBTDICz** were observed to be much larger (over 22 nm) than

that of **DBCz** (4 nm), **DBICz** (7 nm), and **DTICz** (8 nm). These results can be attributed to the presence of intramolecular charge transfer (ICT) originating from the alternating donor-acceptor constitution.^{36, 151}

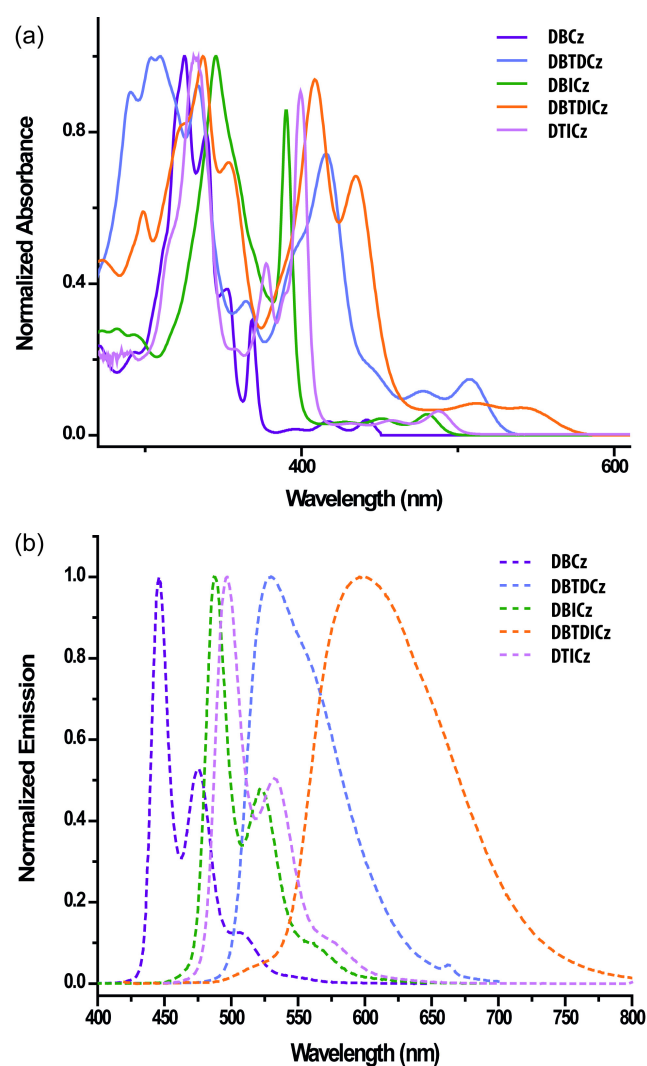


Figure 2.2. (a) UV-vis absorption spectra and (b) Fluorescence emission spectra of fused polycyclic heteroarenes in CHCl_3 .

The rigid coplanar backbones of the fused polycyclic heteroarenes are expected to form a charge transfer complex with an electron-deficient coplanar dopant, 2,3,5,6-tetrafluoro-7,7,8,8-tetracyanoquinodimethane (F_4TCNQ), affording an intermolecular charge transfer complex (CTC).¹⁵¹ The formation of a CTC between fused heteroarenes and F_4TCNQ was investigated (Figure 2.3). The UV-vis-NIR spectra of **DBICz**, **DBTDICz**, and **DTICz** showed a clear absorption of F_4TCNQ anion at 768 nm and 874 nm, and broad polaron absorptions were observed up to 1600 nm. The polaron absorption of **DBTDICz** (1211 nm) was red-shifted than that of **DBICz** (980 nm) and that of **DTICz** (1023 nm) due to the lower energy band gap of **DBTDICz**. Interestingly, the polaron absorption intensity of these three molecules showed a clear trend affected by the end unit of the backbone. It was revealed that electron rich thiophene fused **DTICz** exhibited the highest intensity, while electron-deficient BTD-fused **DBTDICz** displayed the lowest

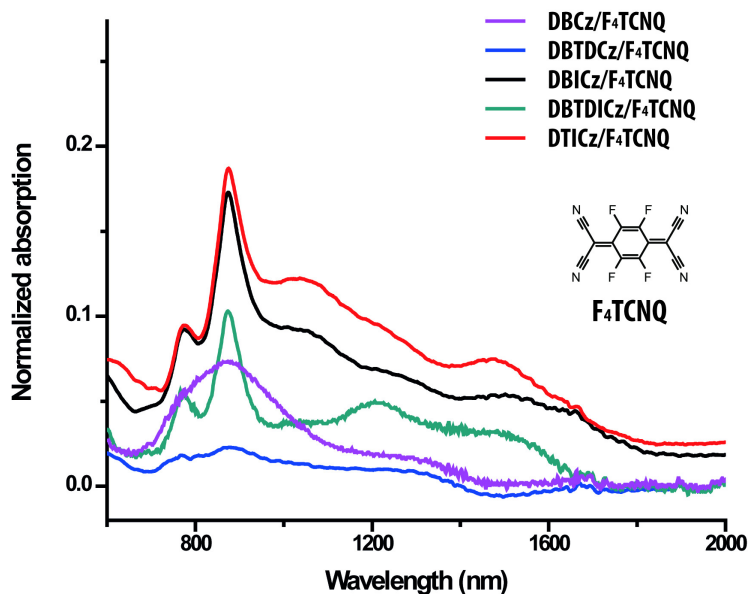


Figure 2.3. UV-vis-NIR spectra of *p*-doped fused polycyclic heteroarenes with F_4TCNQ . The spectra were observed at 2.5×10^{-3} M concentration in 1,2-dichlorobenzene.

intensity. This result suggests that F₄TCNQ preferentially accesses the less hindered end unit faces rather than sterically isolated indolo[3,2-*b*]carbazole face. UV-vis-NIR spectra of **DBCz** and **DBTDCz** with F₄TCNQ also showed similar results as the others. However, **DBCz** and **DBTDCz** showed lower polaron absorption intensity, compared to **DBICz** and **DBTDICz**. In addition, **DBTDCz**-F₄TCNQ displayed very weak charge transfer bands because the more extended stronger donor, indolo[3,2-*b*]carbazole, helped to promote CTC with F₄TCNQ.

2.3. Experimental Section

2.3.1. General Information

Starting materials and reagents were purchased from Alfa-aesar, Combi-blocks, Oakwood, and Suna-tech and used as received without further purification. Toluene and THF were dried using IT pure solvent system (PureSolv-MD-5) and used without further treatment. 2,7-Dibromo-*N*-(heptadecan-9-yl)-carbazole,¹⁵⁴ 3,9-dibromo-5,11-dihydro-5,11-di(1-octylnonyl)indolo[3,2-*b*]carbazole,¹⁵⁵ and 4-bromo-5-methyl-2,1,3-benzothiadiazole¹⁵⁶ were synthesized according to procedure reported in the literature. Analytical thin-layer chromatography (TLC) was performed on glass that is precoated with silica gel 60-F₂₅₄ (Sorbtech). Flash column chromatography was carried out using Biotage® Isolera™ Prime instrument with various size of SiO₂ Biotage ZIP® cartridge. UV/vis absorption spectra were recorded using Shimadzu UV-2600, while the fluorescent emission spectra were measured on Horiba Fluoromax-4. UV-visible-Near IR spectra were measured on a Hitachi U-4100 spectrometer. ¹H and ¹³C NMR spectra were obtained

on a 500 MHz Varian Inova at room temperature and processed by MestReNova 6.1.0. Chemical shifts are reported in ppm relative to the signals corresponding to the residual non-deuterated solvents (CDCl_3 : δ 7.26 for ^1H and 77.16 for ^{13}C at room temperature). High-resolution Matrix-assisted laser desorption/ionization (HR-MALDI) mass spectra were measured on Applied Biosystems 4800 MALDI-TOF. X-ray single crystal diffraction measurement was made on a BRUKER APEX 2 X-ray (three-circle) diffractometer. The X-ray radiation employed was generated from a Mo sealed X-ray tube ($K = 0.70173\text{\AA}$ with a potential of 40 kV and a current of 40 mA) fitted with a graphite monochromator in the parallel mode (175 mm collimator with 0.5 mm pinholes).

2.4. Conclusion

In summary, a highly efficient thermodynamic synthesis employing RCM to achieve ladder-type fused aromatic materials was successfully demonstrated. RCM constructed well-defined fused polycyclic heteroarenes up to 11 fused rings in excellent yields. Moreover, the potential challenge of inefficient ring-closing metathesis with an electron-deficient olefin was overcome by the strong driving force of aromatization. The structures of the fused polycyclic heteroarenes were all confirmed by single crystal X-ray structures and analyzed the packing structures. The optical properties of the fused heteroarenes were also analyzed, demonstrating the highly rigid nature of the backbones. In addition, the fused aromatic materials displayed the formation of charge transfer complexes with F_4TCNQ induced by the rigid coplanar nature of the backbones.

CHAPTER III
THERMODYNAMIC SYNTHESIS OF SOLUTION PROCESSABLE LADDER
POLYMERS*

3.1. Introduction

Fully conjugated ladder polymers with coplanar, sp^2 atom-rich backbones represent a captivating class of macromolecules, on account of their well-defined rigid structures, intriguing syntheses, and promising potential in materials applications.^{21, 34, 157-159} By definition,¹⁶⁰ ladder polymers have a distinctive architecture, whereby the chain consists of an uninterrupted sequence of rings, fused together in a way that adjacent rings share two or more atoms in common, resulting in a constrained chain conformation.^{129, 161-162} Possessing a backbone of fused aromatic rings, a fully conjugated ladder polymer is intrinsically free of possible torsional disorders that are resulted from σ -bond rotations in between the monomeric units. Without the interruption from these conformational disorders, as a result, its coherent π -conjugation length of a coplanar ladder backbone is much more extended.¹⁶³ Such a well-defined conformation would afford a faster intra-chain charge/phonon transport,^{9, 164} and a longer exciton diffusion length compared to conjugated polymers with free rotating torsional motions.¹⁰ This argument is further corroborated by the unparalleled electronic and thermal conductivity of graphene nanoribbons,¹⁶⁵⁻¹⁶⁶ which can be viewed as insoluble ladder polymers composed of only

*Reprinted with permission from “Thermodynamic Synthesis of Solution Processable Ladder Polymers” by Jongbok Lee, Bharath Bangalore Rajeeva, Tianyu Yuan, Zi-Hao Guo, Yen-Hao Lin, Mohammed Al-Hashimi, Yuebing Zheng, and Lei Fang, *Chem. Sci.*, **2016**, 7, 881-889. Copyright 2016 The Royal Society of Chemistry.

sp^2 carbon atoms. Combining the advantages of conventional polymeric materials such as solution processability and structural versatility, ladder polymers emerge as promising candidates for the next-generation synthetic organic materials with breakthrough performances.

The synthesis of a well-defined ladder polymer, however, is a challenging task because of (i) the potential structural defects originated from moderately efficient ring-closing reactions, and (ii) the often poor solubility of structurally rigid intermediates or products. In an effort to overcome these obstacles, a highly efficient synthetic method and a rationally designed structural characteristic that enables solubility need to be achieved and integrated simultaneously. On one hand, kinetically controlled annulation reactions such as Scholl oxidation and electrophilic cyclization have been widely used^{2, 12, 38, 41, 45, 110, 167-169} in the preparation of conjugated ladder polymers from pre-organized polymer precursors, affording a number of materials with fascinating optical and electronic properties. On the other hand, thermodynamically controlled annulation reactions, in principle, can offer unique advantages in the synthesis of well-defined ladder polymers: It enables the opportunities of “error-checking” and “proof-reading”⁵² while pushing the reversible equilibrium to the most stable position. As a result, during the post-polymerization ring-closing step, one could prevent the potential formation of unreacted defects and inter-chain cross-linking, which could be detrimental to the desired materials properties. Despite the early examples and a few subsequent advances involving imine condensation,^{12, 17, 170} this promising strategy has not been extensively explored up to date. Herein, we report the synthesis of a fully conjugated ladder polymer with an extremely

low level of unreacted defects, by taking advantage of thermodynamically controlled ring-closing olefin metathesis (RCM) reaction. The carefully designed structure rendered good solubility of the ladder polymer in common organic solvents, which allowed for excellent solution processability, and extensive solution- and solid-state characterization.

3.2. Results and Discussion

We envisioned that RCM reaction held^{54, 137, 171-174} the promise for the synthesis of conjugated ladder polymers, because (i) it can produce C=C double bond by releasing about 28 kcal/mol of enthalpy in forming a stable aromatic benzene ring,^{54, 174} and (ii) its mild condition enables a wide substrate scope and excellent functional group tolerance.¹⁷⁵ Given a properly designed precursor, RCM reaction should lead to an uncross-linked, stable, and conjugated ladder polymer with minimum unreacted defects.

Guided by these principles, a synthetic route (Figure 3.1a) was designed and executed. This synthesis involved two essential steps: First, step-growth polymerization of two divinyl-functionalized monomers affords a conjugated polymer with pre-organized pendant vinyl groups. In the second step, RCM reaction forms the bridging aromatic rings and hence leads to a coplanar ladder polymer. Carbazole unit was employed as the primary building block in this design (Figure 3.1b), motivated by the following facts: Firstly, it is inexpensive and feasible to prepare functionalized carbazole derivatives with excellent regioselectivity.¹⁷⁶⁻¹⁷⁷ For example, in the designed carbazole precursor **1**, two boronic ester functions were installed on the 2,7-positions for the step-growth polymerization step while the 3,6-positions were functionalized with vinyl groups for RCM annulation.

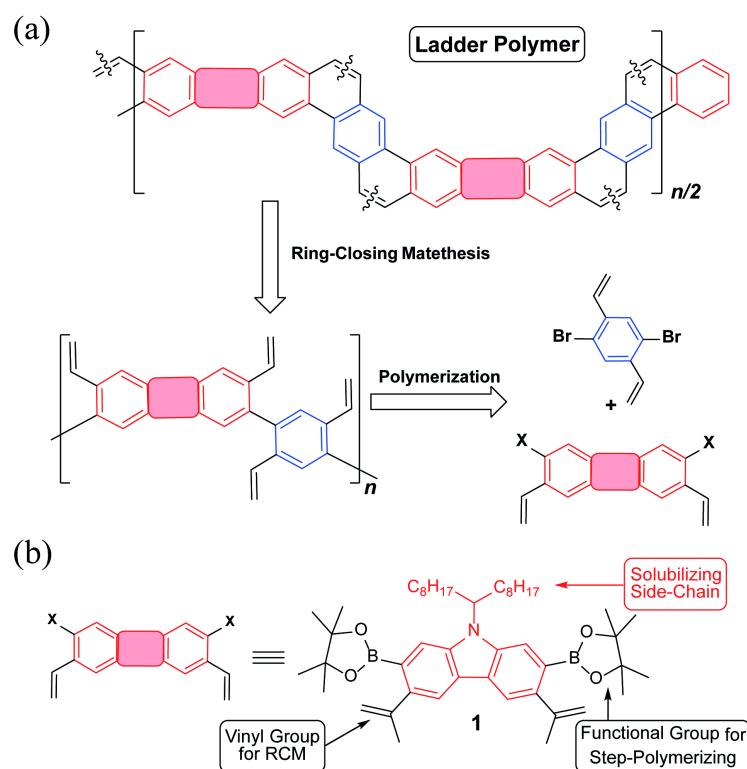
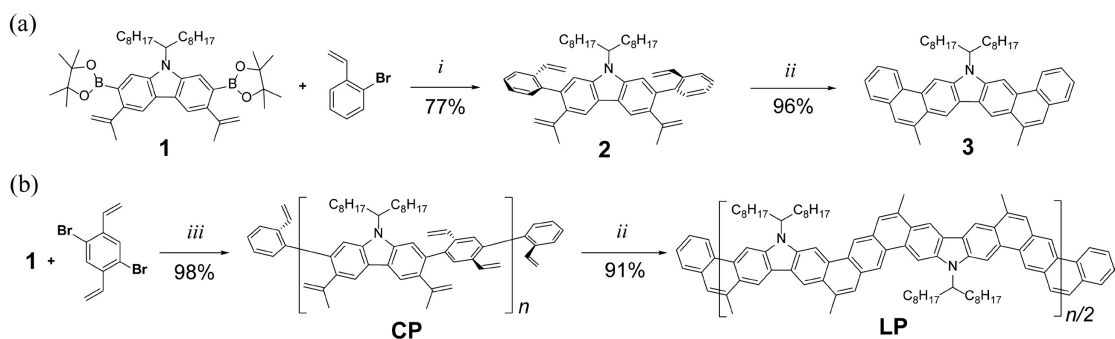


Figure 3.1. (a) A general retrosynthetic analysis for the designed ladder polymer; (b) Structural formula of the carbazole-derived monomer **1**.

Secondly, the presence of an easy-to-alkylate nitrogen position on carbazole unit allows for the installation of an α -branched alkyl group (1-octylnonyl in this case) to enhance the solubility of the rigid ladder polymer product. Such a side-chain would extend in a perpendicular direction with respect to the π -system, so that solubility could be drastically enhanced by breaking the potentially too strong intermolecular π - π stacking interactions.¹⁷⁸⁻¹⁷⁹ Finally, carbazole-containing organic materials have demonstrated high performance in applications associated with photovoltaics¹⁸⁰⁻¹⁸¹ and light emitting diodes.¹⁸²⁻¹⁸³ Thus, successful synthesis of ladder polymers derived from carbazole can be readily translated into applications in these fields.



Scheme 3.1. (a) Synthesis of small molecular model compound **3**; (b) synthesis of ladder polymer **LP**. Reaction conditions: *i*) Pd(PPh₃)₄, K₂CO₃, aliquat 336, BHT, PhMe, H₂O, 100 °C, 24 h. *ii*) Grubbs' 2nd generation catalyst, PhMe, reflux, 6 h. *iii*) Pd(PPh₃)₄, K₂CO₃, aliquat 336, BHT, PhMe, H₂O, 100 °C, 24 h; then 2-bromostyrene and 2-vinylphenylboronic acid.

Precursor **1** was synthesized from 2,7-dibromocarbazole in 60% overall yields on a ~ 3 grams scale (see Appendix A). Before exploring the synthesis of the target polymer, a small molecular model compound **3** was synthesized to validate the strategy and to assist future characterization (Scheme 3.1a). 2-Bromostyrene and compound **1** were cross-coupled by Suzuki reaction to give a tetra-vinyl derivative **2**. Butylated hydroxytoluene (BHT) was used in this reaction as a radical scavenger to inhibit free-radical polymerization of the styrene derivatives. During the subsequent RCM step, it was critical to achieve quantitative conversion of the vinyl groups. This was particularly important for the later-on synthesis of polymer **LP** (Scheme 3.1b). A subset of conditions for the RCM reaction was tested on **2** (Table B.1). In the most efficient method identified, the catalyst was added with a syringe pump over 4 hr at reflux temperature to give product **3** in 96% isolated yield. According to liquid chromatogram, the conversion of the RCM reaction

was close to quantitative. In this transformation, reversible nature of RCM prevented undesired side reactions such as intermolecular cross olefin metathesis of vinyl groups and afforded the thermodynamically most stable product in a nearly quantitative conversion. The structure of **3** was characterized unambiguously by ^1H - ^1H NOESY NMR spectroscopy (Figure B.6) and single crystal X-ray diffraction (Figure 3.2a). The crystal structure clearly demonstrated that the annulated aromatic rings extended in a coplanar geometry. The 1-octylonyl side-chain was perpendicular to the π -backbone in the solid state. As a result, the potential strong intermolecular π - π stacking interactions were suppressed, leading to its good solubility in common organic solvents, such as chloroform, tetrahydrofuran, and toluene. In the ^1H NMR spectra of **2** and **3** (Figure 3.3a), as expected, the vinyl peaks at 5.0 - 7.0 ppm in **2** disappeared in **3** after the RCM reaction, while other peaks shifted downfield. Moreover, after RCM, IR spectrum of **3** revealed the disappearance of the alkenyl C-H and C=C stretching peaks originally present in the spectrum of **2** (Figure B.4).

The comparison of optical properties between **2** and **3** clearly illustrated (Figure 3.2b) the impact of aromatic ring-closure on the electronic structures. UV-vis absorption spectrum of the annulated compound **3** was red-shifted compared to that of **2** because of the more extended conjugation and a covalently enforced coplanar π -electron system. Moreover, both the absorption and emission spectra of **3** showed distinctive vibrational progressions that were indicative of a rigid conjugated system with insignificant conformational fluctuation.¹⁸⁴ Interestingly, the absorption spectrum of **3** showed a weak, symmetrically forbidden HOMO-LUMO transition similar to that of C_{60} .¹⁸⁵ Time-

dependent density functional theory (TDDFT) [B3LYP/6-311G(d,p)] was performed to obtain the calculated electronic transitions of **3**, which were in excellent agreement with the experimental data (Figure 3.2b). Furthermore, the fluorescent emission spectrum of **3** (Figure 3.2c) was also red-shifted and enhanced in terms of intensity relative to that of **2**. This phenomenon corroborated again the extended π -conjugation of **3**. Overall, the successful synthesis and unambiguous characterization of the small molecular model compound provided a firm basis for the preparation and investigation of ladder polymer **LP** using a similar strategy.

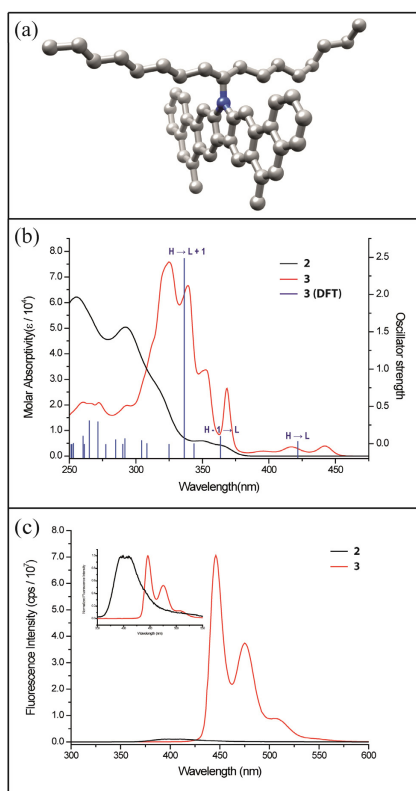


Figure 3.2. (a) Solid-state structure of compound **3** obtained from single-crystal X-ray diffraction; (b) UV-vis absorption spectra of compound **2** (black) and **3** (red) in CHCl_3 , with the TDDFT calculated electronic transitions of **3** shown as blue bar; (c) Fluorescent emission spectra of **2** (black) and **3** (red) with absolute intensity scale. Inset is the same spectra with normalized intensity.

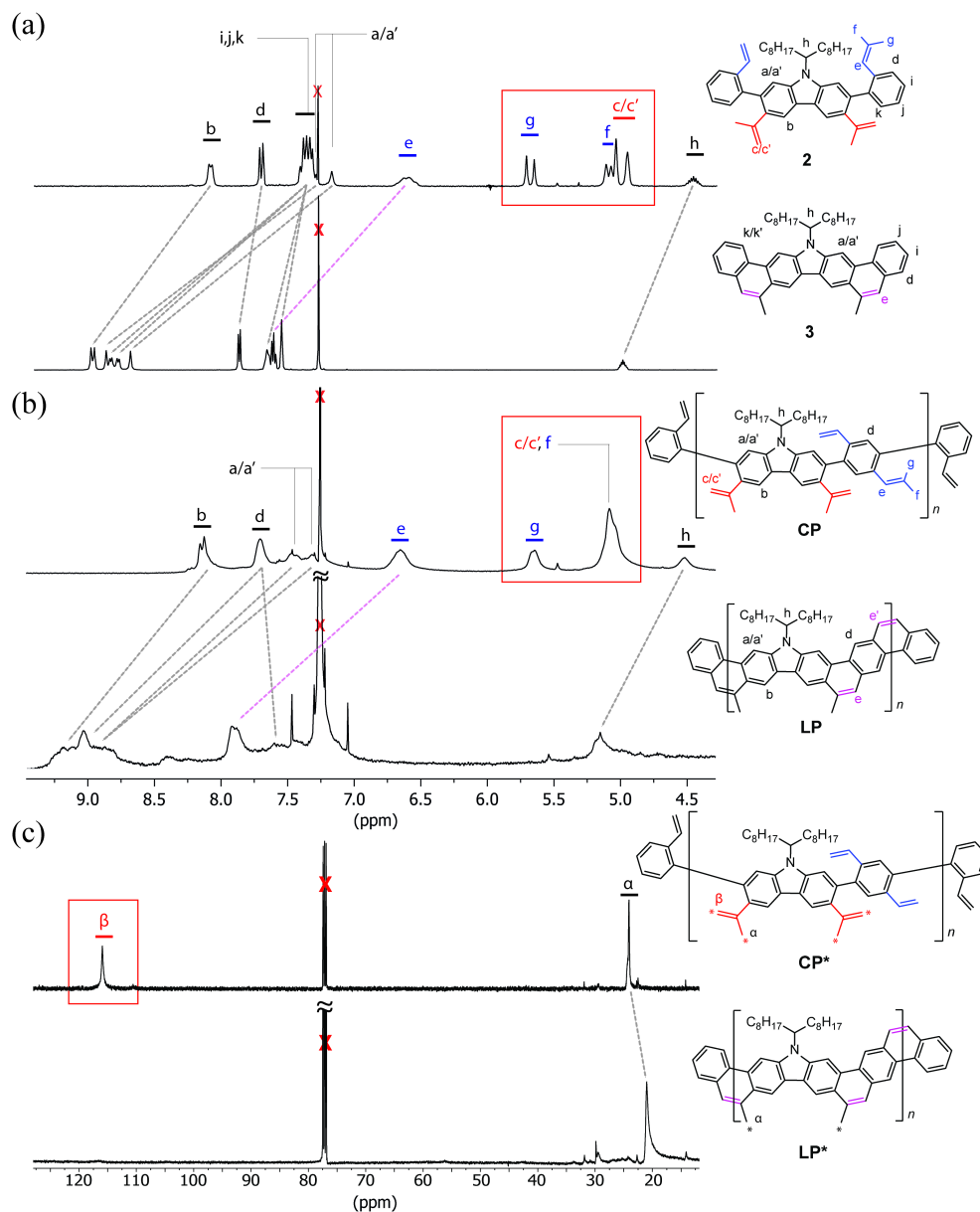


Figure 3.3. (a) Partial ^1H NMR spectra of **2** and **3**. Dotted lines represent the change of chemical shift of each resonance peak after RCM reaction. Proton resonance peaks for *c*, *c'*, *f* and *g* in the box all disappeared after converting **2** into **3**; (b) Partial ^1H NMR spectra of **CP** and **LP** showing the similar change of chemical shift. Proton resonance peaks for the terminal vinyl groups *c*, *c'*, *f*, and *g* in the box all disappeared after the RCM reaction; (c) ^{13}C NMR spectra of **CP*** (S/N = 94 after 413 scans) and **LP*** (S/N = 367 after 17816 scans). The carbons labeled with “*” are 99% ^{13}C isotope enriched. ^{13}C resonance peaks for the terminal vinyl carbon β in the box disappeared after the RCM reaction.

In the subsequent RCM step, the optimized condition screened from the synthesis of **3** was employed to convert **CP** into the ladder-type product **LP** in 91% yield. The resulting product **LP** was purified by precipitation and Soxhlet extraction. The molecular weight of **LP** ($M_n^{\text{SEC}} = 15 \text{ kg/mol}$, PDI = 2.00) was slightly smaller than its precursor **CP** because the higher molecular weight fraction was partially removed during these purification steps due to its lower solubility at high concentration (Figure B.3). Despite the lower solubility of **LP** compared to **CP**, it was still feasible to prepare a solution of purified **LP** in CHCl_3 at a concentration of 5 mg/ml. This good solubility allowed for extensive NMR investigation, SEC analysis, and solution processing into thin films.

The comparison of ^1H NMR spectra of **CP** and **LP** resembled that of model compounds **2** and **3**: The resonance peaks associated with the terminal protons on the vinyl groups disappeared after RCM (Figure 3.3b). In addition, IR spectra of **LP** also showed the disappearance of the alkenyl C–H and C=C stretching after RCM, similar to that of **3** (Figure B.5). Despite these promising results, however, the possibility of unreacted vinyl groups in **LP** could not be ruled out by these characterization methods. ^1H NMR resonance signals were too broad to be useful for a rigorous quantification of defects, especially if the amount of unreacted vinyl groups was less than 5%. Such a structural defect, however, could be critical to the electronic, optical, and mechanical properties of conjugated ladder polymers.^{3, 42, 44} In this context, ^{13}C isotope labeling method¹⁸⁶ was employed to track the terminal vinyl carbons using much sharper ^{13}C NMR resonance peaks. Therefore, a much sensitive analysis of the unreacted defects of **LP** could be performed. The same synthetic procedures afforded ^{13}C labeled **CP***, in which a methyl carbon α and the terminal alkenyl

carbon β are 99% ^{13}C isotope enriched (Figure 3.3c). ^{13}C NMR spectrum of **CP*** showed two expected intense sharp peaks for these ^{13}C isotope enriched carbons at 116.0 ppm and 24.1 ppm with good signal/noise ratio (S/N = 94 after 413 scans). **CP*** was then subjected to the optimized RCM condition to afford **LP***. The resonance signal associated with the terminal vinyl carbon at 116.0 ppm disappeared completely while the peak at 21.0 ppm retained an excellent signal/noise ratio (S/N = 367 after 17816 scans). This result corroborated that the unreacted vinyl defect in **LP*** was less than 1%. Considering that the degree of polymerization of **LP** and **LP*** was around 23 ~ 27, the average possible defect site in a single polymer chain was in fact much less than one. Based on these numbers, we can conclude that most of the polymer chains should be free of defect, but there might still be a small fraction of the polymer chains possessing one or more unreacted defects.

UV-vis absorption and fluorescent emission spectra of **CP** and **LP** were recorded in CHCl_3 solution (Figure 3.4a and b). Similar to that of **3**, both absorption and emission spectra of **LP** were red-shifted compared to that of **CP**, as a result of the much more delocalized and larger conjugated π -system. In addition, HOMO-LUMO transition of **LP** was weak and optically forbidden, similar to that of **3**. Meanwhile, the almost zero wavelength difference (Figure B.20b) between HOMO-LUMO transition of absorption and LUMO-HOMO transition of emission and distinctive vibrational progression were in accordance with the highly rigid nature of **LP** backbone, which prevented any significant conformational change between the excited and the ground states.¹⁸⁴ Unlike the unstructured and low emission of **CP** (quantum yield < 1%), the emission spectrum of **LP**

was composed of well-structured vibrational progressions with much higher quantum yield (15%). Furthermore, it was observed that solid-state UV-vis absorption of **CP** was red-shifted compared to that in the solution phase. Such a red-shift can be attributed to solid-state packing-induced coplanarization of **CP** backbone, similar to that of the well-studied regioregular poly(3-alkylthiophene).¹⁸⁷⁻¹⁸⁸ In contrast, the solution-phase and solid-state absorption spectra of **LP** were almost identical because **LP** in solution was already coplanar and rigid, hence solid-state packing could not change the spectra by alternating its conformation (Figure 3.4c and d). These photophysical observations

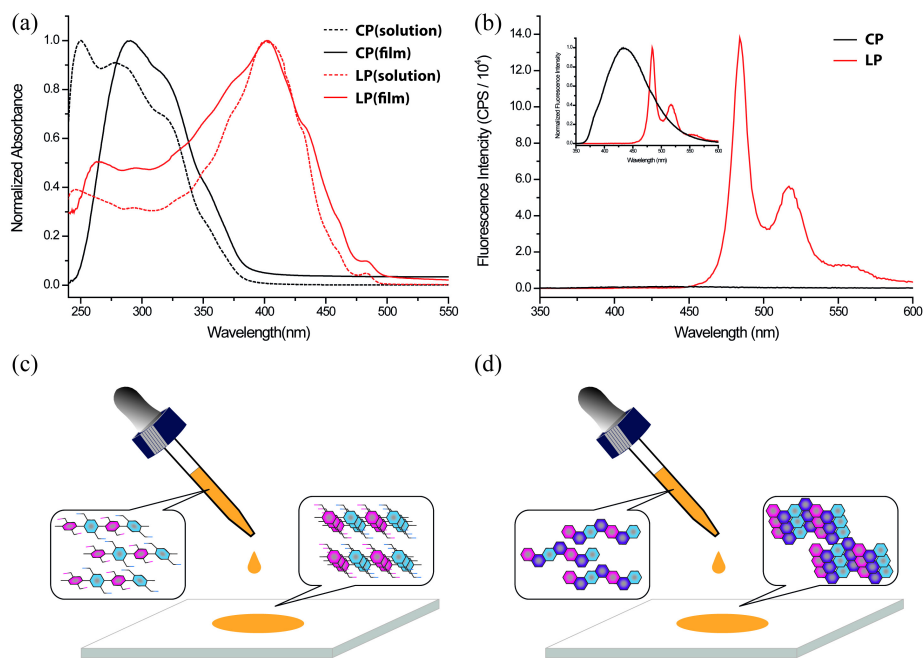


Figure 3.4. (a) UV-vis absorption spectra of **CP** (black) and **LP** (red) in CHCl_3 and as thin films; (b) Fluorescence emission spectra of **CP** (black) and **LP** (red) in CHCl_3 with absolute intensity scale. Inset is the same spectra with normalized intensity. Graphical illustration of the conformational change of (c) **CP** and (d) **LP** between in solution and in the solid state.

suggested that ladder polymer **LP** possessed a highly rigid backbone and well-extended π -conjugation.

It is expected that sp^2 atom rich, aromatic ladder-type polymers have a backbone that is stable at high temperatures, resembling fused ring carbon materials like carbon nanotubes and graphene nanoribbons.¹⁸⁹⁻¹⁹⁰ Thermogravimetric analysis (TGA, Figure B.23) of **CP** showed a clear weight loss in the range of 380 ~ 480 °C, corresponding to the thermal cleavage of the sp^3 1-octylonyl side-chains. Upon further increasing the temperature the non-ladder type backbone of **CP** saw a continuous weight lost, affording only a 34% carbonization yield at 900 °C. In comparison, polymer **LP** also experienced a weight loss due to the alkyl chain cleavage at around 348 ~ 480 °C. The remaining backbone, however, was stable up to 900 °C, giving a carbonization yield of 52%. The result is in good agreement with the weight percentage of the aromatic backbone (57%). The high thermal stability of the **LP** backbone was a result of its ladder-type nature and promised its potential in applications as pre-functionalized precursors for sp^2 carbon materials.¹⁹¹⁻¹⁹² Differential scanning calorimetric (DSC, Figure B.24 and B.25) analysis of **CP** showed an irreversible exothermic transition at 129 °C. This transition was attributed to a thermal triggered cross-linking reaction between the vinyl groups, which indeed converted **CP** into an insoluble material after just one heating cycle. In comparison, **LP** possessed a thermally stable backbone, showing no thermal transition before its side-chain cleavage temperature in the DSC measurement.

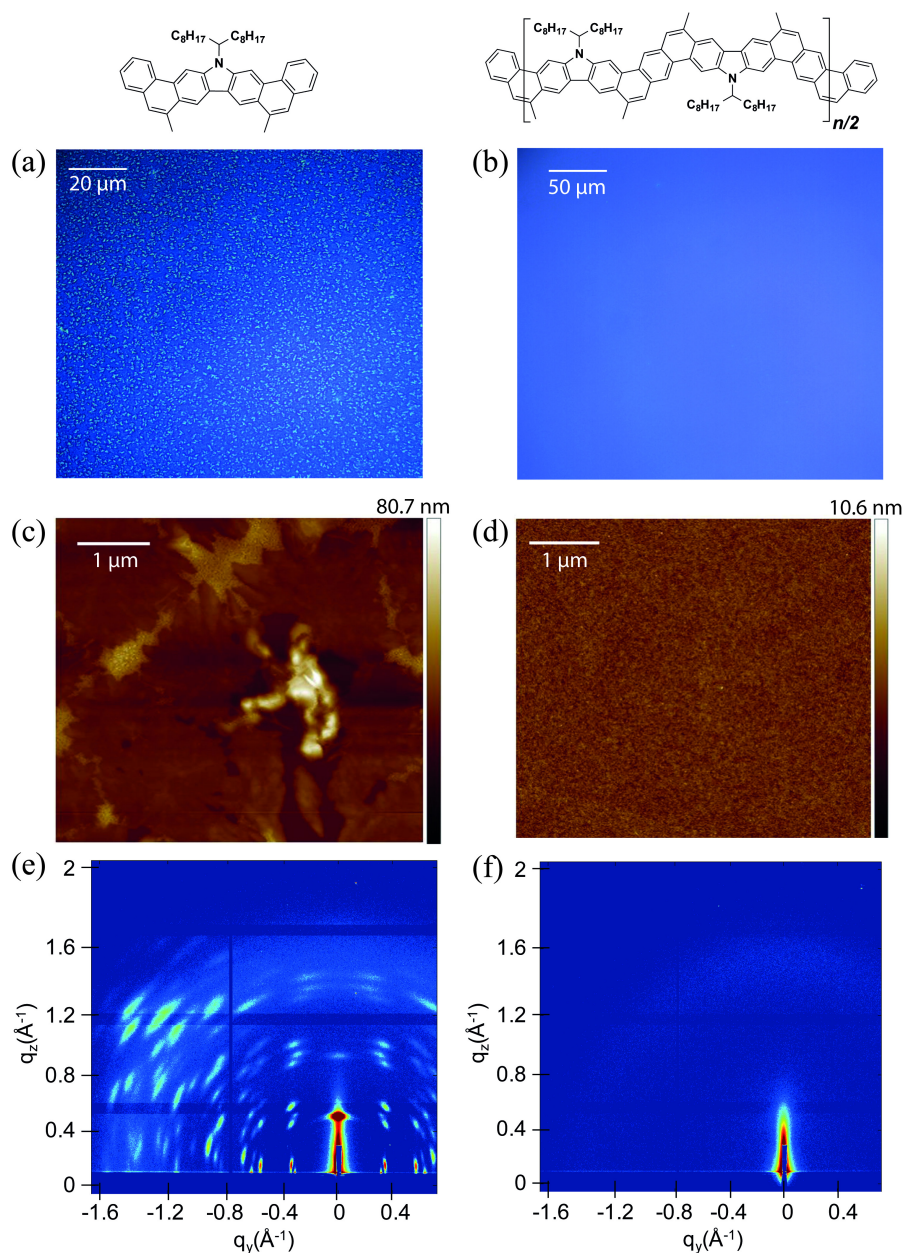


Figure 3.5. Film morphology comparison of **3** and **LP**. The thin films were deposited on UV-Ozone cleaned silicon wafers by spin-casting solutions (2 mg/ml in toluene) at a rate of 2000 rpm. (a) Optical microscope image of **3** with observed microcrystals (1 ~ 3 μm) and (b) that of **LP** with no optical feature; (c) AFM images of microcrystals of **3** (RMS = 5.39 nm) and (d) amorphous morphology of **LP** (RMS = 0.45 nm); (e) GIWAXS patterns of **3** and (f) **LP**. Both samples were measured at an incident angle of 0.2° and 30 second exposure time, and both images have the same color scale.

Solution processing of **LP** into thin films would be a key step for future exploration of its applications. Compared to its small molecular counterpart **3**, polymeric **LP** was expected to possess better processability for uniform thin films. Thin film morphologies of **3** and **LP** on SiO₂ substrates were investigated after spin-casting or solution-shearing casting from solutions in toluene (Figure 3.5). For small molecule **3**, both methods afforded polycrystalline thin films, which were composed of randomly distributed microcrystals with sizes in the range of 1 - 3 μm. Atomic force microscopy (AFM) revealed a very rough surface for this polycrystalline film with root mean square (RMS) roughness of 5.39 nm. In contrast, **LP** can be processed into uniform thin films by either method. No observable feature can be identified under optical microscope. AFM image demonstrated an amorphous morphology with much lower roughness (RMS = 0.45 nm). Grazing incidence wide-angle X-ray scattering (GIWAXS) revealed highly crystalline scattering peaks for the thin film of **3** and no observable diffraction feature for that of **LP** (Figure 3.5e and f). These results suggested that the polymer chains were packed in an amorphous manner on SiO₂ substrates despite its rigid backbone. The excellent film formation ability of **LP** enables future investigation of its material properties.

In order to further characterize the solid-state dimension, conformation, and self-assembly of **LP**, scanning tunneling microscopic (STM) images were recorded on highly ordered pyrolytic graphite (HOPG) (Figure 3.6). A solution of **LP** (0.3 mg/ml) in chloroform was drop-casted onto heated HOPG substrate and analyzed by STM. The image exhibited uniform and fully extended rod-like morphology, indicating self-assembly of the rigid polymer chain of **LP** on HOPG substrate.^{68, 169} The highly ordered

self-assembly was likely a result of the strong π - π interaction between HOPG substrate and the aromatic ladder-type backbone.¹⁹³⁻¹⁹⁴ These rods under STM showed alternating sections of high and low signal with a periodic length at around 1.27 nm. According to the single crystal structure of **3** and DFT calculation of model oligomers resembling **LP**, the feature length of each repeating unit on **LP** was close to 1.26 nm, matching well with the experimental result. The periodic distance between the rods under STM was around 0.7 nm, while the width of calculated polymer backbone without alkyl chain is close to 0.68

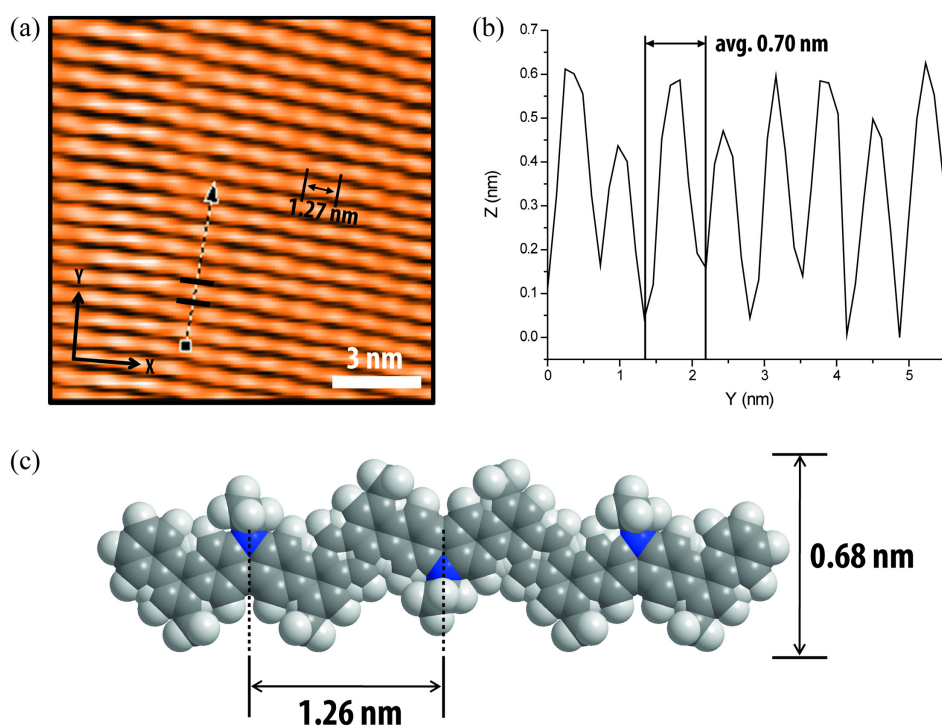


Figure 3.6. (a) STM image of **LP** on highly-ordered pyrolytic graphite; (b) Section profile along the arrow line drawn in (a). The STM image was obtained with a tunneling current set point of 0.9 nA and sample bias of 50 mV. The distance between consecutive convex spots along the X-axis is 1.27 nm, and average distance between peaks along the Y-axis is 0.70 nm. (c) Theoretical dimensions of an oligomeric model **LP** backbone from DFT calculation (B3LYP/6-311G).

nm. Taking consideration of the additional contribution to the width from the side-chains, it is likely that the neighboring **LP** rods were partially stacked, in a manner similar to the literature reported graphene nanoribbons.⁶⁸ In a sharp contrast, STM analysis of **CP** showed no ordered feature, probably a result of low surface interaction between the non-ladder backbone and the HOPG substrate (Figure B.29).

3.3. Experimental Section

3.3.1. General Information

Starting materials and reagents were purchased from Aldrich, Alfa-aesar, and Suna-tech and used as received without further purification. Toluene and THF were dried using IT pure solvent system (PureSolv-MD-5) and used without further treatment. 1,4-dibromo-2,5-divinylbenzene⁵⁴ and methyl-¹³C-triphenylphosphonium iodide (99% ¹³C isotope enriched)¹⁹⁵ were synthesized according to procedure reported in the literature. Analytical thin-layer chromatography (TLC) was performed on glass that is precoated with silica gel 60-F₂₅₄ (Sorbtech). Flash column chromatography was carried out using Biotage[®] Isolera[™] Prime instrument with various size of SiO₂ Biotage ZIP[®] cartridge. UV/vis absorption spectra were recorded using Shimadzu UV-2600, while the fluorescent emission spectra were measured on Horiba Fluoromax-4. FT-IR spectra were recorded with ZnSe ATR using Shimadzu IRAffinity-1S. ¹H and ¹³C NMR spectra were obtained on a 500 MHz Varian Inova at room temperature and processed by MestReNova 6.1.0. Chemical shifts are reported in ppm relative to the signals corresponding to the residual non-deuterated solvents (CDCl₃: δ 7.26 for ¹H and 77.16 for ¹³C at room temperature).

Size exclusion chromatography (SEC) was performed on TOSOH EcoSEC (HLC-8320GPC) in THF solution at 40 °C temperature and the molecular weights calculated using a calibration curve based on polystyrene standards, equipped with TSKgel SuperHM-M and TSKgel SuperH-RC. Preparative SEC was performed in chloroform solution at room temperature using JAI recycling preparative HPLC (LC-92XXII NEXT SERIES). Thermal gravimetric analysis (TGA) was recorded under nitrogen atmosphere with heating rate of 10 °C min⁻¹ from 40 to 900 °C using TA Q500. Differential scanning calorimetry (DSC) was measured on TA Q20 with a heating rate of 10 °C min⁻¹ from 40 to 300 °C. Quantum yields were measured by Edinburgh Instruments FLS920, equipped with integrating sphere system. High-resolution Matrix-assisted laser desorption/ionization (HR-MALDI) mass spectra were measured on Applied Biosystems 4800 MALDI-TOF. Atomic force microscopy (AFM) images were recorded with Bruker Dimension Icon AFM in a tapping mode and processed using NanoScope Analysis. Optical microscope images were obtained using Olympus BX41 microscope. Grazing-incidence wide-angle X-ray scattering (GIWAXS) measurements were carried out on Sector 8-ID-E at the Advanced Photon Source, Argonne National Laboratory.¹⁹⁶ Beamline 8-ID-E operates at an energy of 7.35 keV and images were collected from a Pilatus 1MF camera (Dectris), with two exposures for different vertical position of the detector. After flat field correction for detector nonuniformity, the images are combined to fill in the gaps for rows at the borders between modules, leaving dark only the columns of inactive pixels at the center. Using the GIXSGUI package for Matlab (Mathworks), data are corrected for X-ray polarization, detector sensitivity and geometrical solid-angle. The beam size is 200

μm (h) \times 20 μm (v). Sample detector distance is 204 mm. Sample measurement and thermal annealing were carried out under vacuum which is in the range of $2\sim 3 \times 10^{-6}$ bar, with the sample stage interfaced with a Lakeshore 340 unit. Scanning tunneling microscopy (STM) measurement was performed at room temperature using Easyscan 2 system from Nanosurf Inc. The tips were mechanically cut from Pt/Ir wire (80%/20%, 0.25mm diameter, Nanoscience). Highly ordered pyrolytic graphite (HOPG) substrate purchased from Nanosurf Inc. The STM image was obtained with a tunneling current set point of 0.9 nA and sample bias of 50 mV. X-ray single crystal diffraction measurement was made on a BRUKER APEX 2 X-ray (three-circle) diffractometer. The X-ray radiation employed was generated from a Mo sealed X-ray tube ($\lambda = 0.70173\text{\AA}$ with a potential of 40 kV and a current of 40 mA) fitted with a graphite monochromator in the parallel mode (175 mm collimator with 0.5 mm pinholes).

3.3.2. *Synthesis of CP*

To a 100 mL Schlenk flask was added **1** (1.03 g, 1.40 mmol), 1,4-dibromo-2,5-divinylbenzene (0.40 g, 1.40 mmol), Pd(PPh₃)₄ (0.16 g, 10 mol%), K₂CO₃ (1.16 g, 8.40 mmol), Aliquat 336 (0.65 mL, 0.35 mmol), and several crystals of BHT under N₂. Degassed toluene (40 mL) and water (8 mL) were added and further degassed 3 times by freeze-pump-thaw. The reaction mixture was stirred at 100 °C for 24 h in darkness, before it was cooled down to room temperature. 2-Bromostyrene (0.77 mL, 5.60 mmol) was added into the flask, and the mixture was stirred at 100 °C for 24 h. After 24 h, 2-vinylphenylboronic acid (1.73 g, 11.2 mmol) was added into the flask, and the mixture

was stirred at 100 °C for another 24 h. The resulting product was precipitated from methanol, filtered, and washed with acetone. The solid was dried under vacuum to afford **CP** (0.84 g, 98%, $M_n^{\text{SEC}} = 10$ kg/mol, PDI = 2.78 by SEC). **CP** was further purified by preparative recycling SEC to remove oligomers to afford a purified batch with higher M_n and lower PDI (0.64 g, 75%, $M_n^{\text{SEC}} = 20$ kg/mol, PDI = 1.88 by SEC).

3.3.3. *Synthesis of LP*

To a 100 mL Schlenk flask was added **CP** (120 mg, 0.20 mmol) and Grubbs' 2nd generation catalyst (8 mg, 5 mol%) under N₂. Subsequently, degassed toluene (12 mL) was added, and the reaction mixture was stirred at reflux temperature. Immediately, another portion of Grubbs' 2nd generation catalyst (26 mg, 15 mol%) in degassed toluene (8 mL) was added for 4 h using syringe pump. After that, the reaction mixture was stirred for an additional 2 h at reflux temperature before cooling down to room temperature. The resulting product was then precipitated from methanol and filtered. The product was further washed *via* Soxhlet extraction with acetone and hexane, before extracted with chloroform. The chloroform solution was filtered and condensed under reduced pressure. The desired product was precipitated from methanol. The precipitate was filtered and dried under vacuum to afford **LP** (100 mg, 91%, $M_n^{\text{SEC}} = 15$ kg/mol, PDI = 2.00 by SEC).

3.4. **Conclusion**

In conclusion, a highly efficient synthetic approach to a conjugated ladder-type polymer has been established on the basis of thermodynamically controlled ring-closing

olefin metathesis reaction. The resulting polymer possesses highly rigid backbone with less than one defect per chain on average, meanwhile maintaining good solubility and solution processability. The feasible and versatile nature of this method enables an efficient and impactful way to the synthesis of novel polymer materials with desirable features that will potentially be useful for thin film devices.

CHAPTER IV

DONOR-ACCEPTOR CONJUGATED LADDER POLYMER VIA AROMATIZATION-DRIVEN THERMODYNAMIC ANNULATION*

4.1. Introduction

Conjugated ladder-type polymers⁹⁴ are macromolecules in which the pi-conjugated backbone units are connected and fused with multiple strands of covalent bonds (Figure 3.1a). These polymers possess unique properties as a result of their fused constitution, rigid conformation, and lack of torsional disorders.^{1-2, 94-95, 197} Integration of a ladder-type constitution into functional conjugated macromolecules presents an intriguing strategy for enhancing their materials performance. The construction of multiple strands of bonds along the conjugated polymer main-chain in a precise manner, however, still remains a major synthetic challenge, despite significant advances in the past decade.^{1-2, 94-95} Moreover, the incorporation of structural features that are critical to materials applications imposes additional constraints on the synthesis of functional ladder polymers. It is urgently desirable to overcome these difficulties in order to exploit the promising material properties of conjugated ladder polymers,^{5, 15, 110, 198-200} such as their thermal and chemical stability,^{5, 7, 45, 51} high conductivity,^{9, 20, 165-166, 201} and low energy bandgap.^{110, 149}

*Reprinted with permission from “Donor-acceptor Conjugated Ladder Polymer *via* Aromatization-driven Thermodynamic Annulation” by Jongbok Lee, Alexander J. Kalin, Chenxu Wang, Julia T. Early, Mohammed Al-Hashimi, and Lei Fang, *Polym. Chem.*, **2018**, *9*, 1603-1609. Copyright 2018 The Royal Society of Chemistry.

Conjugated polymers with alternating electron-rich donor units and electron-deficient acceptor units (D-A polymers) predominate as active materials in high performance organic photovoltaic devices.²⁰²⁻²⁰³ Fusing the conjugated main-chain of D-A polymers into a ladder-type constitution can potentially break through the limits of exciton diffusion,¹⁰ inter-chain electronic coupling, and bandgap engineering.⁹⁴ The syntheses of D-A ladder polymers, however, are rarely reported^{17, 35-36, 204} due to the combined challenges originating from the electron-deficient monomer and the ladder-type backbone. The electron deficiency of the acceptor monomer makes it difficult to attach functional groups necessary for backbone annulation. Moreover, the electron-poor units often lead to decreased reaction efficiencies on the subsequent postpolymerization ladderization, such as the widely used Friedel-Crafts intramolecular cyclization^{2, 38, 41, 205} and Scholl oxidation,^{35, 110} resulting in structural defects along the polymer chains.²⁰⁶⁻²⁰⁸ Scherf and coworkers reported the synthesis of a D-A ladder polymer by Friedel-Crafts annulation,³⁶ in which the acceptor was pre-fused with electron-rich units before polymerization, so that the potentially inefficient cyclization was avoided.

Recently, we demonstrated that thermodynamically controlled ring-closing olefin metathesis (RCM) is a powerful tool to ladderize conjugated polymers⁷ and oligomers in high efficiency.¹⁵⁰ The reversible nature of RCM prevents undesired intermolecular cross-metathesis side products, while the formation of stable aromatic rings facilitates quantitative conversion in the ring annulation step.^{7, 54, 137, 150} Furthermore, the mild and neutral reaction conditions allow for a wide substrate scope and excellent functional group tolerance.¹⁷⁵ Although RCM of electron-deficient olefins is still potentially challenging,

we hypothesized that aromatization could provide the thermodynamic driving force to overcome this problem and lead to an efficient ring annulation. Herein, we report the efficient synthesis of a D-A ladder polymer through RCM ladderization. Induced by coplanarity of the ladder polymer backbone, this polymer demonstrated intriguing optical properties and formed a charge transfer complex (CTC) with an electron-deficient dopant.

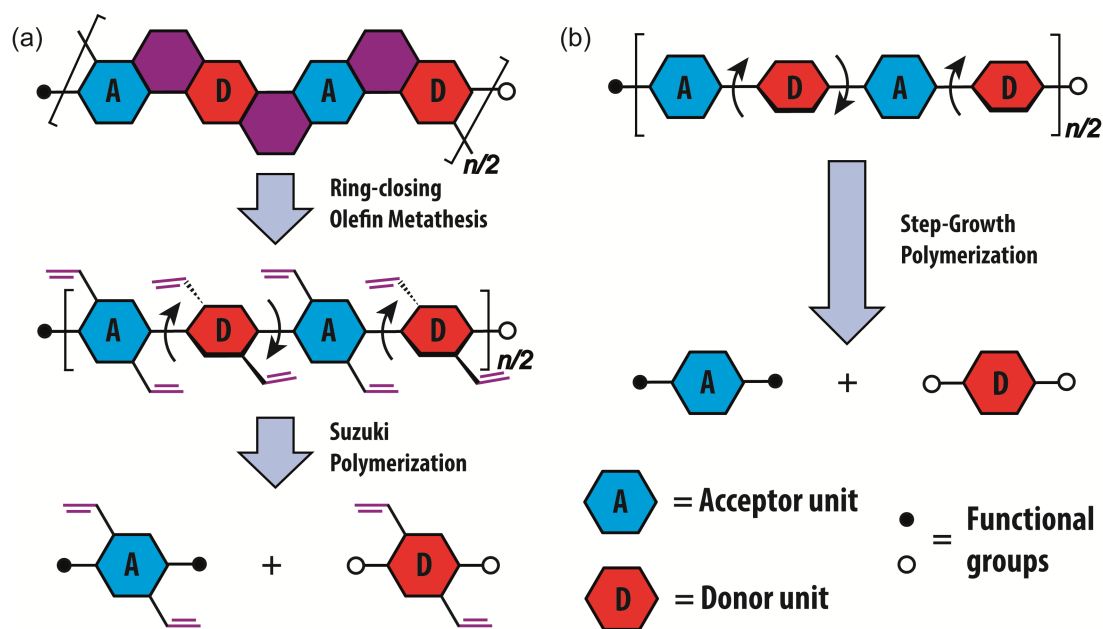


Figure 4.1. General retrosynthesis of (a) a D-A type ladder polymer and (b) a D-A type conjugated polymer. The curved arrows indicate free torsional motions.

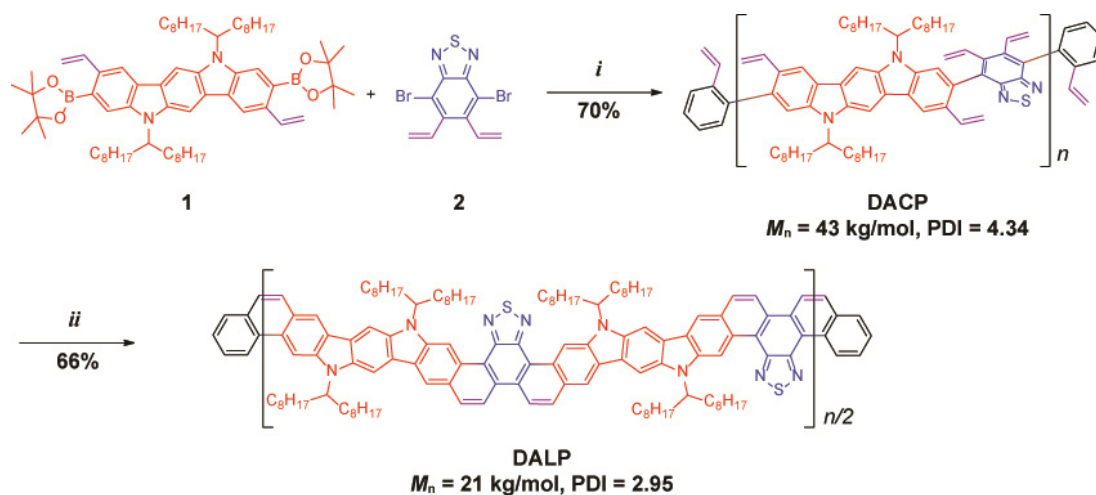
4.2. Results and Discussion

To obtain the desired D-A ladder polymer, a Suzuki coupling polymerization of vinyl-functionalized donor and acceptor monomers can be used to construct a conjugated D-A precursor (**DACP**), similar to the conventional synthesis of non-ladder type D-A

polymers (Figure 4.1b). Subsequently, it can undergo thermodynamically controlled RCM to afford the D-A ladder polymer (**DALP**) (Figure 4.1a). It is noteworthy that at least one of the monomeric units needs to be centrosymmetric in order to afford a linear ladder backbone. In this example, 2,1,3-benzothiadiazole (BTD) was employed as the acceptor unit due to the following factors: (i) its low-lying molecular orbital energy levels render it sufficiently electron-deficient for many D-A conjugated polymers, (ii) its 4,7-positions are easily functionalized to serve as Suzuki coupling sites, and (iii) its 5,6-positions can be easily transformed into vinyl groups for RCM from pre-positioned methyl groups. Due to the non-centrosymmetric nature of BTD, indolo[3,2-*b*]carbazole with C_{2h} symmetry was selected to serve as the donor unit in order to maintain the desired linear constitution of the resulting rigid polymer.

The indolocarbazole-derived monomer **1** was synthesized from a 3,9-dibromoindolo[3,2-*b*]carbazole derivative through Vilsmeier-Haack formylation followed by Wittig olefination and borylation (see Appendix A). The α -branched 1-octylnonyl alkyl chains were installed on the *N*-positions to enhance the solubility of the desired D-A ladder polymer by breaking the potentially strong intermolecular π - π stacking interactions.⁷ The BTD derived monomer **2** was synthesized through Wittig olefination of 4,7-dibromo-5,6-bis(bromomethyl)-2,1,3-benzothiadiazole (Scheme C.1). With monomers **1** and **2** in hand, the conjugated D-A ladder polymer was synthesized in two steps (Scheme 4.1). Step-growth Suzuki polymerization between **1** and **2** afforded a vinyl-pendant non-ladder type D-A conjugated polymer, which was subsequently end-capped *in situ* by 2-bromostyrene and 2-vinyl(phenylboronic acid pinacol ester) to give the polymeric intermediate **DACP**.

In this reaction, butylated hydroxytoluene (BHT) served as an essential radical-scavenging additive to prevent undesired radical-initiated cross-linking of the vinyl groups. **DACP** was purified by recycling preparative size exclusion chromatography (SEC) to remove lower molecular weight oligomers, affording a batch with a high observed molecular weight ($M_n^{\text{SEC}} = 43 \text{ kg mol}^{-1}$, PDI = 4.34) in a 70% yield. This higher molecular weight and wide polydispersity index indicated possible aggregation. Under RCM conditions in refluxing toluene, **DACP** was converted into the desired D-A ladder polymer **DALP** in 98% yield. After Soxhlet extraction with chloroform, the final material was obtained in a 66% isolated yield from the solution fraction. This fraction of **DALP** ($M_n^{\text{SEC}} = 21 \text{ kg mol}^{-1}$, PDI = 2.95) possessed good solubility at room temperature in common organic solvents, such as chloroform, toluene, and THF. The decrease of the isolated yield, compared to our previously reported RCM ladderization steps,^{7, 150} was mainly due to the low solubility of the high molecular weight material left over in the Soxhlet extractor (27%). In order to further confirm the efficiency of the ring annulation, RCM was also performed on a batch of low molecular weight **DACP** ($M_n^{\text{SEC}} = 14 \text{ kg mol}^{-1}$, PDI = 1.43) to produce fully soluble **DALP** ($M_n^{\text{SEC}} = 11 \text{ kg mol}^{-1}$, PDI = 1.52) in 93% yield after Soxhlet extraction. In this article, unless specifically noted, all the following characterization and tests on **DACP** and **DALP** were performed on the fraction with high molecular weights (**DACP**: $M_n^{\text{SEC}} = 43 \text{ kg mol}^{-1}$; **DALP**: $M_n^{\text{SEC}} = 21 \text{ kg mol}^{-1}$).



Scheme 4.1. Synthesis of D-A ladder polymer **DACP** and **DALP**. (i) Pd(PPh₃)₄, K₂CO₃, aliquat 336, BHT, PhMe, H₂O, 100 °C, 24 h; then 2-bromostyrene and 2-vinylphenylboronic acid. (ii) Grubbs' 2nd generation catalyst, PhMe, reflux, 6 h.

¹H NMR spectra showed clear conversion of **DACP** into **DALP**. The resonance peaks associated with the vinyl groups at 5.0 – 7.0 ppm disappeared after RCM, while other peaks shifted further down-field (Figure 4.2). Among them, protons a/a' downfield shifted beyond 11.0 ppm partially due to the sterically crowded environments in the fjord region adjacent to the thiadiazoles after ring annulation.¹⁵² An unusual intramolecular interaction between the thiadiazole nitrogen and the aromatic hydrogen originating from the rigid and coplanar nature of **DALP** also contributed to the down-field shift of proton a/a'.¹⁵³ It is also noteworthy that the monomers and polymers form atropisomers caused by hindered rotation of the two sets of α-branched alkyl chains, resulting in distinct peaks of these alkyl chains in ¹H and ¹³C NMR.

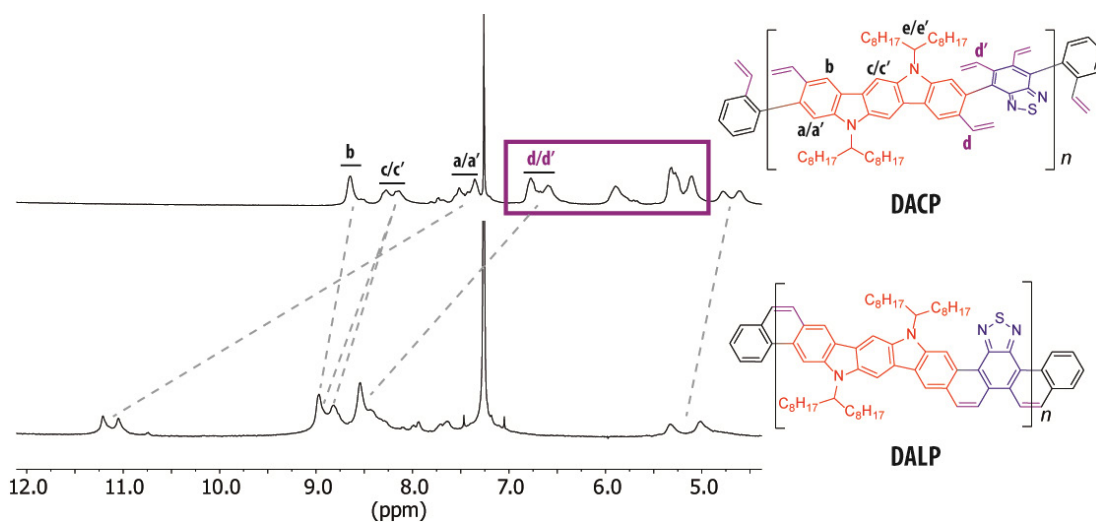


Figure 4.2. Partial ^1H NMR spectra of **DACP** and **DALP**. Dotted lines represent the change of chemical shifts of each resonance peak after RCM. Proton resonance peaks for the vinyl groups in the box all disappeared after RCM.

Optical properties of **DACP** and **DALP** were examined by UV-vis absorption and fluorescence emission spectra in toluene solution (Figure 4.3a). As expected, the absorption edge of **DALP** displayed an approximately 100 nm red-shift compared to that of **DACP**, as well as previously reported ladder polymer **LP** that lacks the D-A architecture⁷. This observation demonstrated that the combined effect of extended π -conjugation in the ladder-type backbone and the alternating donor-acceptor constitution was responsible for the lower bandgap of **DALP**. Furthermore, distinctive vibrational progressions were observed as a result of the highly rigid nature of **DALP**, in contrast to the broad and featureless spectrum of **DACP**. Interestingly, both **DACP** (434 nm) and **DALP** (547 nm) showed optically weak HOMO-LUMO transitions, similar to those observed in previously reported analogous ladder polymers and oligomers.^{7, 150}

Electrochemical analysis revealed HOMO and LUMO of **DALP** to be -4.79 eV and -3.07 eV, respectively by cyclic voltammetry. The fluorescence emission spectrum of **DALP** also showed well-structured vibrational progressions and a narrower spectral width than the broad and featureless emission spectrum of **DACP**.²⁰⁹ Despite its much lower absorption energy, **DALP** emitted at a similar energy ($\lambda_{\text{max}} = 569$ nm) compared to **DACP** ($\lambda_{\text{max}} = 573$ nm), resulting in a much smaller Stokes shift (22 nm) than that of **DACP** (138 nm). This observation can be attributed to the small energy loss of the rigid ladder-type backbone during excitation and emission. The 22 nm Stokes shift, however, was still much larger³⁶ than typical ladder-type molecules,^{2, 94} suggesting the presence of intramolecular charge transfer (ICT).^{36, 210} In order to confirm the ICT process, absorption and emission of **DALP** were recorded in various solvents with different dielectric constants, including toluene, chlorobenzene, chloroform, 1,2-dichlorobenzene, tetrahydrofuran, dichloromethane, and 1,2-dichloroethane (Figure 4.3b and C.3). The absorption spectra in these different solvents displayed no significant change, while the emission spectra maxima red-shifted as the solvent polarity increased from toluene to dichloromethane. Furthermore, the well-structured vibrational progressions of emission observed in toluene became broader in more polar solvents. This characteristic solvatochromic effect was quantified by a linear Lippert-Mataga plot (Table C.1 and Figure C.4).²¹¹ The good coefficient of determination ($R^2 = 0.8821$) indicated a strong dipole moment stabilization effect of the excited state in polar solvents, corroborating the ICT process.

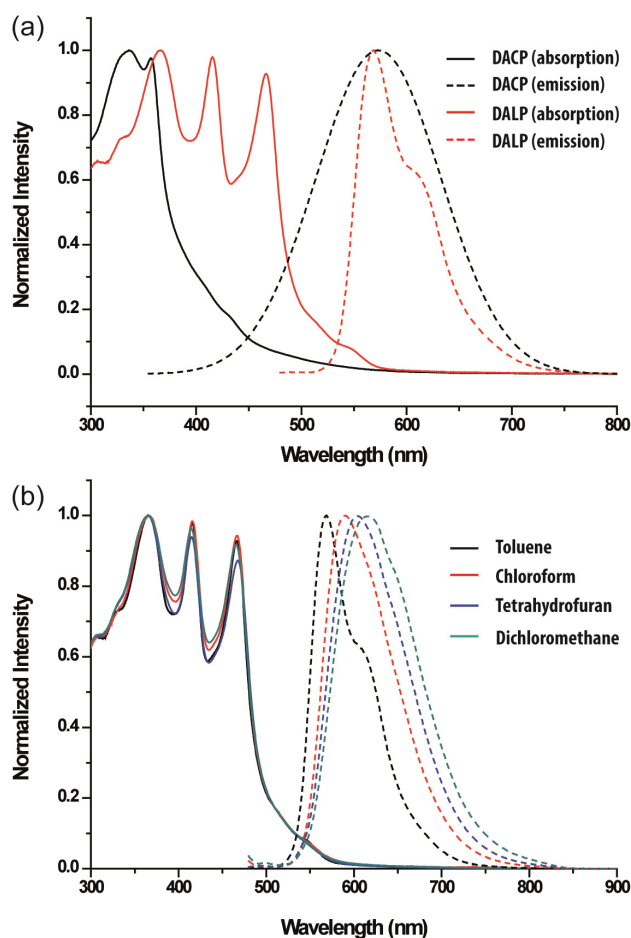


Figure 4.3. (a) UV-vis absorption and fluorescence emission spectra of **DACP** and **DALP** in toluene. (b) UV-vis absorption and fluorescence emission spectra of **DALP** in different solvents.

The rigid coplanar backbone of **DALP** was expected to promote the formation of a charge transfer complex (CTC) with a dopant. Formation of a CTC is a common method to dope and tune the electronic properties of conjugated polymers.²¹²⁻²¹⁵ For example, doping poly(3-hexylthiophene) with 2,3,5,6-tetrafluoro-7,7,8,8-tetracyanoquinodimethane (F₄TCNQ) improved its conductivity up to 22 S cm⁻¹.²¹⁶ Considering the rigid and coplanar constitution of both F₄TCNQ and **DALP**, the formation

of a CTC complex should be highly favorable.^{214, 217} Charge transfer properties of ladder polymers **LP** and **DALP** with F₄TCNQ were investigated. The UV-vis-NIR spectrum of **LP** with F₄TCNQ in 1,2-dichlorobenzene revealed clear absorption of the F₄TCNQ anion at 770 nm and 874 nm^{213, 217} and broad polaron absorptions from 700 – 1200 nm, which overlapped with the F₄TCNQ anion peak (Figure 4.4a). The spectrum of **DALP**-F₄TCNQ also displayed the F₄TCNQ anion absorption (Figure 4.4b). However, the polaron absorption peaks of **DALP**-F₄TCNQ complex were red-shifted to 1215 and 1450 nm as a result of the intrinsically decreased energy band gap of **DALP**. On the other hand, the polaron absorption of **LP** at 1014 nm showed stronger intensity with an absorption cross section of 2.7×10^{-18} cm²/charge compared to that of **DALP** at 1215 nm with an absorption cross section of 1.1×10^{-18} cm²/charge. The charge transfer absorption bands were visible with a doping concentration as low as 3.3 wt% [molar ratio between dopant and polymer repeating units (MR) = 0.05] for **LP** and 1.6 wt% (MR = 0.05) for **DALP**. The doping level reached a maximum intensity at 24.9 wt% (MR = 0.4) for **LP** (Figure C.5) and 11.5 wt% (MR = 0.3) for **DALP** (Figure C.6). These results indicate that F₄TCNQ primarily accesses the less hindered benzene- or BTD-fused π -faces rather than the carbazole and the indolo[3,2-*b*]carbazole faces, sterically isolated by the α -branched alkyl chains. Therefore, the electron-rich fused benzene rings in **LP** form a stronger CTC with F₄TCNQ than the electron-poor BTD in **DALP**. In order to further confirm the effect of the ladder-type constitution on CTC formation, non-ladder type precursors **DACP** and **CP** (Figure B.7), both having large torsional angles due to the steric hindrance of the adjacent vinyl groups, were treated with F₄TCNQ in a control experiment (Figure 4.4a and b). Though

the non-ladder type **DACP** and **CP** polymers contain the same planar aromatic building blocks as **DALP** and **LP**, neither polymer showed any charge transfer bands. This drastic contrast suggests that the extended coplanar pi-faces of the ladder polymers were essential in promoting the interactions with F₄TCNQ to form a CTC.

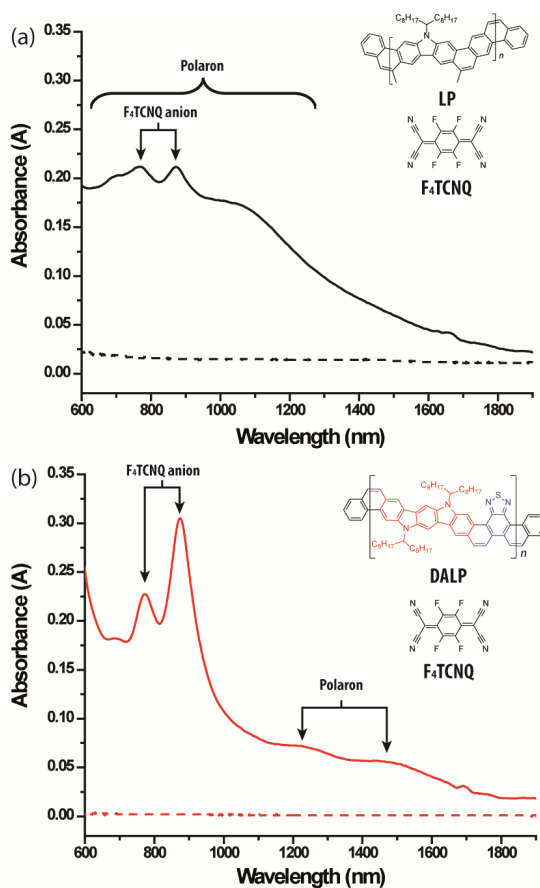


Figure 4.4. UV-vis-NIR spectra of (a) *p*-doped **LP** with F₄TCNQ (24.9 wt%, MR = 0.4, black solid line) and (b) **DALP** with F₄TCNQ (11.5 wt%, MR = 0.3, red solid line) and control spectra of **CP** (black dashed line, MR = 0.4) and **DACP** (red dashed line, MR = 0.3) with F₄TCNQ. The structure of **CP** can be found in Figure C.7. The spectra were observed at 2.5×10^{-3} M concentration in 1,2-dichlorobenzene.

A ladder polymer backbone was also expected to have higher thermal stability than an non-ladder type conjugated polymer backbone due to its double-stranded constitution.⁹⁴ Thermal gravimetric analysis (TGA, Figure 4.5c) of the non-ladder precursor **DACP** showed an alkyl side-chain cleavage at 360-480 °C. It experienced continuous weight loss upon heating resulting in a 34% carbonization yield at 900 °C. A weight loss of **DALP** also occurred at 340-480 °C owing to the alkyl chain cleavage. However, the fused-ring sp^2 backbone of **DALP** demonstrated higher thermal stability after alkyl chain cleavage, affording a carbonization yield of 42% at 900 °C. This result was in good agreement with the theoretical weight percentage of the aromatic backbone (47%).

Solution processability and the resulting solid-state packing are important for practical applications of donor-acceptor polymers. The good solubility of **DALP** allowed for the preparation of uniform thin films on SiO₂ substrates by spin-casting (5 mg mL⁻¹ in chloroform). The thin film morphology of **DALP** was studied by grazing incidence wide-angle X-ray scattering (GIWAXS). The amorphous morphology of **DALP** was observed in the as-cast film (Figure C.8), which did not change after thermal annealing at 250 °C (Figure 4.5a). However, after thermal annealing the thin film at 500 °C for 30 min, which cleaved the alkyl side-chains, a clear diffraction peak at $q \approx 1.68 \text{ \AA}^{-1}$ in the out-of-plane direction (010) was observed (Figure 4.5b).²¹⁸ It suggested that the rigid and coplanar polymer backbone preferentially reorganized into a face-on orientation with a π - π distance of 3.7 Å after alkyl chain cleavage. These data suggested that the reorganization to face-on orientation of **DALP** after thermally induced cleavage of sp^3 carbons may give the resulting thin film interesting properties for future applications.

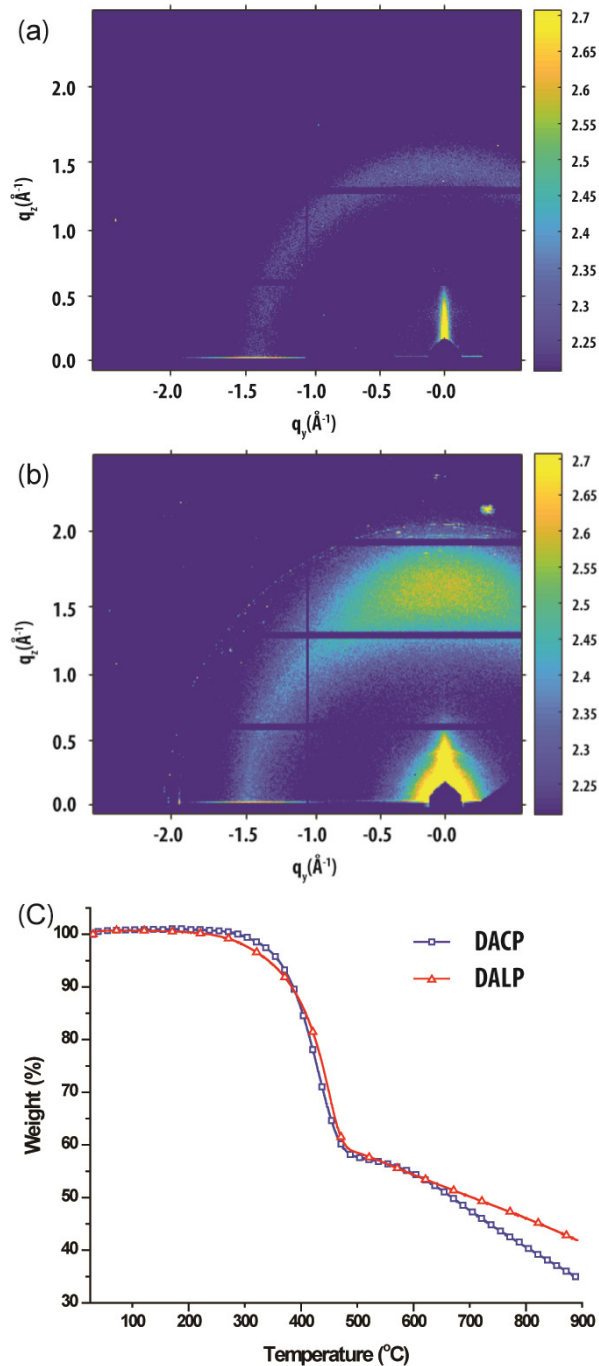


Figure 4.5. GIWAXS image of (a) **DALP** after annealing at 250 $^{\circ}\text{C}$ and (b) after alkyl chain cleavage at 500 $^{\circ}\text{C}$. Both samples were measured at an incident angle of 0.14° and 30 second exposure time, and both images have the same color scale. (c) TGA trace of **DACP** and **DALP**. Decomposition temperature of **DACP** (T_d , 5 % weight loss) was 361 $^{\circ}\text{C}$ with a 34 % carbonization yield at 900 $^{\circ}\text{C}$, and that of **DALP** (T_d , 5 % weight loss) is 342 $^{\circ}\text{C}$ with a 42 % carbonization yield at 900 $^{\circ}\text{C}$.

4.3. Experimental Section

4.3.1. General Information

Starting materials and reagents were purchased from Aldrich, Alfa Aesar, TCI, and Acros, and were used as received without further purification unless specified. Toluene and DMF were dried using Inert Technology pure solvent system (PureSolv-MD-5a) and used without further treatment. Anhydrous THF was distilled with Na/benzophenone before uses. Anhydrous 1,2-dichloroethane and 1,4-Dioxane were purchased from Acros. 4,7-dibromo-5,6-bis(bromomethyl)-2,1,3-benzothiadiazole²¹⁹ was synthesized according to reported procedures in literatures. Analytical thin-layer chromatography (TLC) tests were performed on glass that was precoated with silica gel 60-F₂₅₄ (Sorbtech). Flash column chromatography was carried out using a Biotage[®] Isolera[™] Prime with various sizes of SiO₂ Biotage ZIP[®] cartridges. UV-visible absorption spectra and fluorescence emission spectra were recorded using a Shimadzu UV-2600 and a Horiba Fluoromax-4 spectrometer, respectively. UV-visible-Near IR spectra were measured on a Hitachi U-4100 spectrometer. ¹H and ¹³C NMR spectra were obtained on a 500 MHz Varian Inova at room temperature unless specified. The NMR data were processed in MestReNova 6.1.0. Chemical shifts were reported in ppm relative to the signals corresponding to the residual non-deuterated solvents (CDCl₃: δ 7.26 for ¹H and 77.16 for ¹³C at room temperature. Size exclusion chromatography (SEC) was performed on Tosoh EcoSEC (HLC-8320GPC) in THF solution at 40 °C with a flow rate of 0.4 mL/min through TSKgel SuperHM-M and TSKgel SuperH-RC columns. The molecular weights were calculated based on the retention time, using a calibration curve constructed from polystyrene

standards. Preparative SEC was performed in chloroform solution at room temperature using a JAI recycling preparative HPLC (LC-92XXII NEXT SERIES). High-resolution Thermal gravimetric analysis (TGA) was recorded under nitrogen atmosphere with heating rate of $10\text{ }^{\circ}\text{C min}^{-1}$ from 25 to $900\text{ }^{\circ}\text{C}$ using TA Q500. High-resolution Matrix-assisted laser desorption/ionization (HR-MALDI) mass spectra and low-resolution atmospheric pressure chemical ionization (LR-APCI) mass spectra were measured on Applied Biosystems 4800 MALDI-TOF and a Thermo Scientific LCQ-DECA, respectively. Grazing-incidence wide-angle X-ray scattering (GIWAXS) measurements were carried out in Sector 8-ID-E at the Advanced Photon Source, Argonne National Laboratory.¹⁹⁶ Beamline 8-ID-E operates at an energy of 10.91 keV and the images were collected from a Pilatus 1MF camera (Dectris), with two exposures for different vertical positions of the detector. Using the GIXSGUI package for MATLAB (Mathworks), data are corrected for X-ray polarization, detector sensitivity and geometrical solid-angle. The beam size is $0.8\text{ mm} \times 0.5\text{ mm}$ and the resolution ($\Delta E/E$) is 1×10^{-4} . Sample detector distance is 278 mm. Solid-state samples for GIWAXS were deposited on silicon wafers by spin-casting with the solutions (5 mg/mL in CHCl_3) at a spin rate of 1500 rpm and annealed at $250\text{ }^{\circ}\text{C}$ or $500\text{ }^{\circ}\text{C}$ for 30 min.

4.3.2. *Synthesis of DACP*

Under N_2 , degassed toluene (4 mL) and water (0.8 mL) was added to a mixture of **1** (100 mg, 0.096 mmol), **2** (33 mg, 0.096 mmol), $\text{Pd}(\text{PPh}_3)_4$ (11 mg, 10 mol%), K_2CO_3 (80 mg, 0.58 mmol), a drop of aliquat 336, and several crystals of BHT. The solution was

further degassed for 3 times by freeze–pump–thaw. The reaction mixture was stirred at 100 °C for 24 h in darkness, before it was cooled down to room temperature. 2-Bromostyrene (50 μ L, 0.38 mmol) was added into the flask at room temperature, and the mixture was heated up again and stirred at 100 °C for 24 h. Subsequently, 2-vinylphenylboronic acid (110 mg, 0.77 mmol) was added into the flask, and the mixture was stirred at 100 °C for another 24 h. The resulting product was precipitated from methanol, filtered, and washed with acetone. The solid was dried under vacuum to afford **DACP** (91 mg, 98%, $M_n = 28 \text{ kg mol}^{-1}$, PDI = 5.16 by SEC). **DACP** was further purified by preparative recycling SEC to remove lower molecular weight oligomers to afford a batch with higher M_n and lower PDI (65 mg, 70%, $M_n = 43 \text{ kg mol}^{-1}$, PDI = 4.34 by SEC). $^1\text{H NMR}$ (500 MHz, CDCl_3): δ 8.64 (bs, 2H), 8.27, 8.15 (two m^\dagger , 2H), 7.52, 7.36 (two m^\dagger , 2H), 6.78 (m, 2H), 6.58 (m, 2H), 5.90 (m, 2H), 5.32 (m, 4H), 5.10 (m, 2H), 4.79, 4.62 (two bs^\dagger , 2H), 2.55, 2.33 (two m^\dagger , 4H), 1.98 (m, 4H), 1.18 (m, 46H), 0.82 (m, 12H). † Peak separations were observed due to the atropisomers by hindered rotation of α -branched alkyl chain.

4.3.3. Synthesis of **DALP**

To a 50 mL Schlenk flask was added **DACP** (126 mg, 0.13 mmol) and Grubbs' 2nd generation catalyst (6 mg, 5 mol%) under N_2 . Subsequently, degassed toluene (12 mL) was added, and the reaction mixture was heated up to reflux temperature while stirring. At this point, additional solution of Grubbs' 2nd generation catalyst (16 mg, 15 mol%) in degassed toluene (8 mL) was injected into the reaction mixture slowly using syringe pump

over the course of 4 h. The reaction was kept running for an additional 2 h at reflux temperature before cooling down to room temperature. The resulting product was precipitated from methanol and filtered. The crude solid was washed *via* Soxhlet extraction with acetone and hexane, before being extracted by chloroform. The chloroform solution was filtered and condensed under reduced pressure. The desired **DALP** product was precipitated from methanol and isolated by filtration and drying under vacuum (73 mg, 66%, $M_n = 21 \text{ kg mol}^{-1}$, PDI = 2.95 by SEC). The insoluble high molecular weight fraction left over as a solid in the Soxhlet extractor was also collected and dried under vacuum (30 mg, 27 %). $^1\text{H NMR}$ (500 MHz, CDCl_3): δ 11.21, 11.05 (two bs[†], 2H), 8.97 (m, 3H), 8.82 (m, 1H), 8.54 (m, 4H), 5.33, 5.01 (two bs[†], 2H), 2.94, 2.76 (two m[†], 4H), 2.30 (m, 4H), 1.10 (m, 46H), 0.70 (m, 12H). [†]Peak separations were observed due to the atropisomers by hindered rotation of α -branched alkyl chain.

4.4. Conclusion

In summary, the efficient synthesis of donor-acceptor ladder polymer **DALP** was achieved by ring-closing olefin metathesis. The potential issue of low efficiency in the ladderization step caused by electron-deficient acceptor units was addressed by the strong thermodynamic driving force of aromatization. Consequently, the desired ladder polymer was produced in good yield without detectable structural defects. Spectroscopic investigation revealed that **DALP** exhibits a lower energy band gap compared to that of **DACP** and **LP**. A dipole moment stabilization effect of the excited state in polar solvents confirmed the presence of intramolecular charge transfer. The rigid, coplanar nature of

DALP and **LP** promoted the formation of charge transfer complexes with electron deficient dopant F₄TCNQ, which were not observable on their non-ladder type analogues. The solid-state packing structure of **DALP** was investigated by GIWAXS, demonstrating its amorphous morphology. However, after the thermally induced alkyl chain cleavage, the residual ladder polymer backbone preferentially reorganized into a face-on orientation with a π - π distance of 3.7 Å. These results provide fundamental understanding of D-A ladder polymers for potential future applications in solid-state electronic and optoelectronic devices.

CHAPTER V

EXTENDED LADDER-TYPE BENZO[*K*]TETRAPHENE-DERIVED OLIGOMERS*

5.1. Introduction

Extended benzo[*k*]tetraphene-based fused-ring hydrocarbons (BTp) are an important class of molecular substructures of armchair graphene nanoribbons and carbon nanotubes, analogous to [*n*]acenes²²⁰⁻²²³ and [*n*]phenacenes^{127, 224-226} (Figure 5.1). Preliminary studies demonstrated high charge carrier mobility ($2.5 \text{ cm}^2/\text{Vs}$)²²⁷ among small molecular BTp derivatives and superior stability compared to [*n*]acenes. The investigation and application of precisely defined, longer BTp oligomers, however, are challenging due to the difficulty in precision synthesis²²⁸ and low solubility.²²⁹⁻²³⁰ In general, small molecular BTp derivatives have been prepared through transition metal-catalyzed kinetic ring annulation.²²⁸⁻²³¹ The synthesis of an oligomeric BTp system with up to 9 fused rings was reported using ruthenium-mediated aromatization, but required at least 11 steps.²²⁹ Recently, a remarkable macrocyclic BTp nanobelt composed of 12 fused rings was synthesized through Yamamoto coupling, although the final step yielded only 1% of the product.¹³³ BTp-based polymers were also synthesized through two different methods,^{49, 232} but showed discrepancies in the optical properties, indicating constitutional uncertainty of these polymeric products. In general, reliable and precise synthesis of extended BTp oligomers has not yet been well established.

*Reprinted with permission from “Extended Ladder-Type Benzo[*k*]tetraphene-Derived Oligomers” by Jongbok Lee, Haunbin Li, Alexander J. Kalin, Tianyu Yuan, Chenxu Wang, Troy Olson, Hanying Li, and Lei Fang, *Angew. Chem. Int. Ed.*, **2017**, 56, 13727-13731. Copyright 2017 Wiley-VCH Verlag GmbH & Co. KGaA, Weinheim.

In order to establish fundamental structure-property correlations and to capitalize on the promising potential applications of BTP-derivatives, efficient synthesis of well-defined oligomers^{118, 130, 134, 233-234} is an urgent need for this important class of compounds. Herein, we report a novel approach to BTP oligomers composed of up to 13 fused rings in the conjugated backbone, using thermodynamic ring-closing olefin metathesis (RCM) as the key annulation method.^{7, 54} The challenges associated with undesired side-reactions, low yields, and poor solubility were addressed. Optical properties, effective conjugation lengths, and crystallization dynamics of this series of oligomers depicted a clear picture of the evolving material properties in accordance with the extension of the π -conjugated BTP backbones.

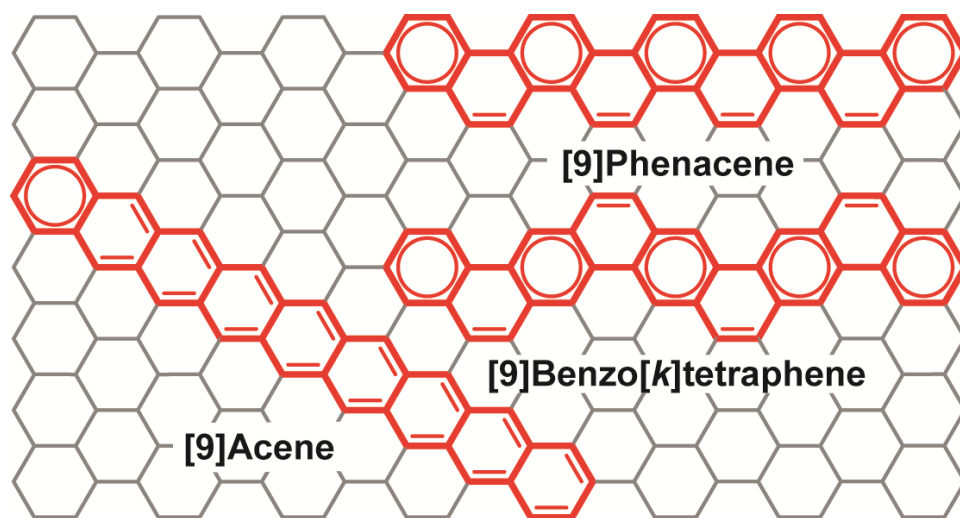
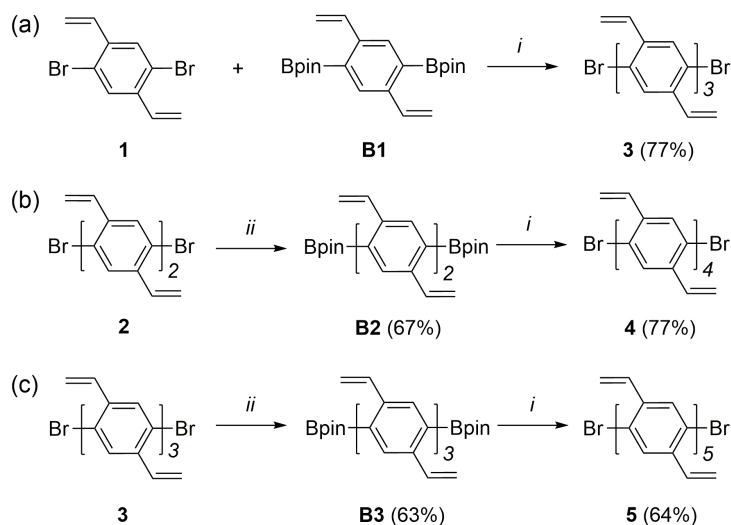


Figure 5.1. Structures of [9]benzo[*k*]tetraphene and its constitutional isomers, [9]acene and [9]phenacene, superimposed on a piece of armchair graphene. Clar's aromatic sextets are shown with circles.

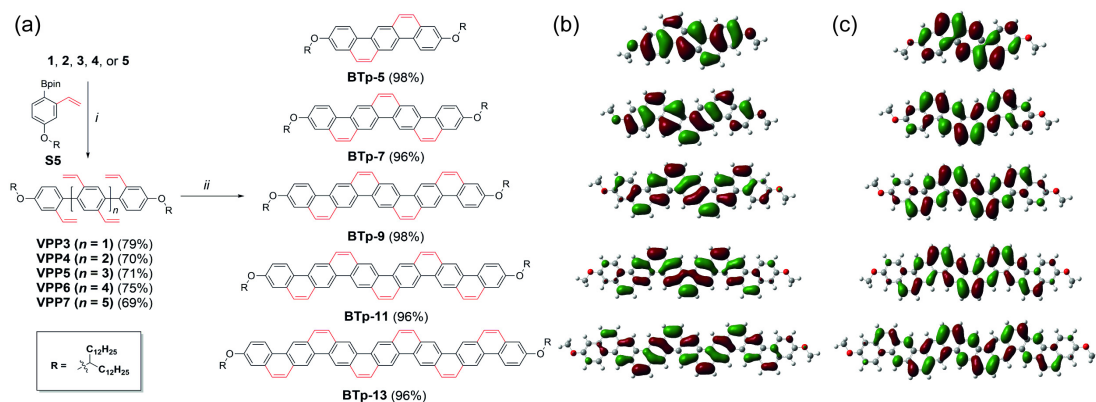
5.2. Results and Discussion



Scheme 5.1. Structural formula and synthesis of vinyl-functionalized *p*-phenylene derivatives **1**~**5**. (i) **1**, Pd(PPh₃)₄, K₂CO₃, aliquat 336, BHT, PhMe, H₂O, 100 °C, 24 h. (ii) B₂pin₂, Pd₂dba₃, SPhos, KOAc, BHT, Dioxane, 70 °C, 18 h.

The target oligomer backbones consist of 5, 7, 9, 11, or 13 fused aromatic rings arranged as linearly repeating benzo[*k*]tetraphenes.¹⁹² In order to render solubility but to minimize interference of solubilizing groups on the molecular packing mode, branched alkoxy chains were installed on the two terminal aromatic rings. In this way, the majority of the backbone remained unsubstituted, allowing for a clearer correlation of the structures with their properties, especially in the solid state. The syntheses began with the construction of a series of vinyl functionalized *p*-phenylene oligomers (**1**~**5**), through iterative Suzuki coupling and modified Miyaura borylation (Scheme 5.1). During the preparation of the boronic ester-functionalized precursors **B1**, **B2**, and **B3**, Miyaura borylation was challenging on account of the undesired Heck coupling and free-radical

side-reactions of the pendant vinyl groups. Reaction screening was performed (Table D.2) on 1,4-dibromo-2,5-divinylbenzene **1** to identify an optimized condition, which involved Pd₂dba₃, SPhos, and dioxane. The iterative Suzuki coupling reactions afforded vinyl-functionalized oligomeric intermediates **1**~**5**. They were subsequently end-capped by boronic ester-functionalized styrene derivative **S10** through another Suzuki coupling reaction to afford oligomers **VPP3**~**7**, which were decorated with branched 1-dodecyl-tridecyloxy solubilizing groups (Scheme 5.2). It is noteworthy that the addition of radical scavenger 2,6-di-*t*-butyl-4-methylphenol (BHT) was essential for both the optimized Miyaura borylation and the Suzuki coupling in order to prevent undesired free-radical addition of the vinyl groups.⁷



Scheme 5.2. (a) Synthesis of ladder-type oligomers **BTp-5**~**13**. (i) Pd(PPh₃)₄, K₂CO₃, aliquat 336, BHT, PhMe, H₂O, 100 °C, 24 h. (ii) Grubbs' 2nd generation catalyst, PhMe, reflux, 6 h (*o*-DCB at 130 °C was used for **BTp-13**). (b) HOMOs and (c) LUMOs of **BTp-5**~**13**, calculated by DFT at B3LYP/6-311G(d,p) level of theory.

In order to explore the feasibility of the subsequent RCM reaction, torsional barriers between adjacent divinyl phenylene units in **3**, **4**, and **5** were measured using variable temperature ^1H NMR spectroscopy (Figure D.1-D.3 and Table D.1). A consistent value of 17.2 kcal/mol demonstrated the possibility of free torsional motion of these units at elevated temperature. Such torsional freedom was essential to the success of the RCM annulation, which requires conformational change of the molecule to bring the neighboring vinyl groups into close proximity. Because of the reversible nature of thermodynamically controlled RCM and the driving force of aromaticity,^{7, 54} the annulation step was expected to afford the fused-ring constitution with excellent efficiency without undesirable side products. In addition, this strategy intrinsically prevents the regioisomer formation often seen on precedent ring annulation methods.²²⁹ Indeed, under optimized conditions, **VPP3~7** were all transformed successfully into the corresponding ladder-type derivatives **BTp-5~13** in almost quantitative conversions. This efficient step did not require any further purification other than precipitation in methanol, affording the products in over 96% isolated yields. Through this route, only 5 steps were needed to synthesize the longest oligomer **BTp-13** from commercially available starting material **5**, with an overall yield of 20.6%.

The oligomers **BTp-5~11** were soluble in common organic solvents at room temperature while **BTp-13** was slightly soluble at room temperature and highly soluble at 90 °C in 1,2-dichlorobenzene, allowing for extensive solution phase elucidation of the molecular structures. ^1H NMR spectra of **BTp-5~13** all demonstrated well-resolved resonance signals (Figure 5.2). Progressing from upfield to downfield in the aromatic

region, the protons *ortho*- to the alkoxy groups (green), the K-region protons (purple and orange), the protons in the “shallow” bay region (yellow and pink), and the protons in the “deep” bay region (blue) were all clearly identified for all oligomers. The structural elucidations were further corroborated by mass spectrometry, elemental analysis, and ^1H - ^1H NOESY NMR on **BTp-5~13** (Figure D.6-D.10). It was worth noting that ubiquitous upfield shifts of aromatic proton signals were observed on **BTp-9** and **BTp-11** in concentrated solutions, as expected for the aggregation of these large, rigid, and coplanar π -systems (Figure D.4 and D.5).²³⁵

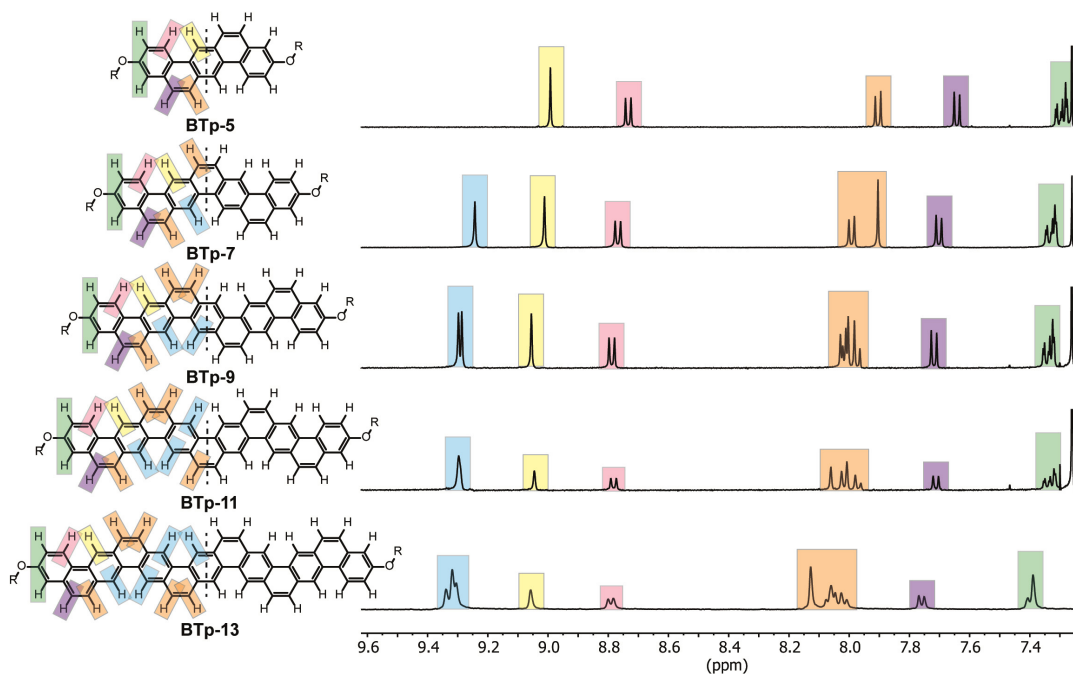


Figure 5.2. The aromatic regions of ^1H NMR spectra (500 MHz) of **BTp-5~13**, color-coded by corresponding groups of protons. **BTp-5~11**: CDCl_3 , 298K; **BTp-13**: $\text{C}_2\text{D}_2\text{Cl}_4$, 373K.

Electronic structures and optical properties of these oligomers were investigated by using a combination of simulations and experiments. For all the BTp oligomers, DFT calculations demonstrated delocalized a highest occupied molecular orbital (HOMO) and lowest unoccupied molecular orbital (LUMO) throughout the rigid and coplanar backbone (Scheme 5.2b and c). The terminal rings showed slightly weaker aromatic character than those in the center (rings **a** and **b**, respectively, Figure D.20).¹³³ In addition, electrochemical properties of BTp derivatives were investigated by cyclic voltammetry, which revealed that the HOMO energy levels of BTp oligomers remain relatively unchanged while the LUMOs gradually decrease as π -conjugation extends, in a good agreement with the calculated HOMOs and LUMOs (Table D.4). UV-vis absorption spectra displayed three characteristic α - (lowest energy), p - (intermediate energy), and β -bands (higher energy), with distinctive vibrational progressions as a result of the backbone rigidity (Figure 5.3a), similar to that of typical polycyclic aromatic hydrocarbons reported in literature.²³⁶⁻²³⁷ The α -bands of **BTp** derivatives were extremely weak in intensity due to the symmetry forbidden nature of the transition (Figure 5.3b).⁷ Comparison of the spectra of **BTp-5~13** demonstrated that as π -conjugation increases, the relative intensity of the p -band increases continuously while that of the β -band decreases.²³⁶ Such a clear and progressive change of the relative intensity of these two bands provided a feasible and practical indicator of π -extension of BTp ladder-type macromolecules. Furthermore, Stokes shifts between the weak α -band and the emission maxima (Figure D.13) were extremely small (0~2.6 nm), as a result of the highly rigid π -system that prevented significant energy loss of the excited state through conformational relaxation.

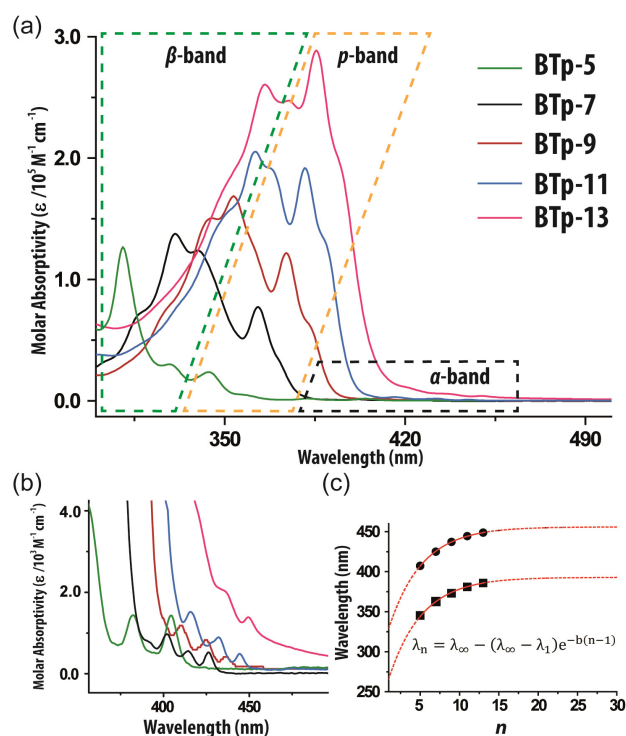


Figure 5.3. (a) UV-vis absorption of **BTp** derivatives in CHCl_3 . Boxes indicate the characteristic α - (black), p - (yellow) and β -bands (green); (b) Expanded view of the α -bands; (c) Correlation plots and exponential fits of **BTp** derivatives between the absorption maxima of the p -band ($\lambda_{a, \text{max}}$, ■) and the fluorescence emission maxima ($\lambda_{e, \text{max}}$, ●) vs number of benzene rings (n).

As expected, extension of the π -conjugation from **BTp-5** to **13** saw bathochromic shifts of both the absorption and emission spectra (Figure 5.3 and D.12). The convergence of these energies upon π -system extension was evaluated by fitting to an exponential function (Figure 5.3c and Table D.3), to elucidate the effective conjugation length (ECL) of **BTp** derivatives.²³⁸ Thanks to the backbone rigidity that prevents significant conformational disorder, both exponential function fits yielded the same rate of convergence, leading to an extrapolated ECL of 21 fused aromatic rings for ladder-type

BTp derivatives. This value was similar to that of ethano-bridged *p*-phenylenes (≈ 21) possessing a torsional angle of 20° ,²³⁹ despite the intuitive hypothesis that structural planarization increases coherent π -conjugation.⁸ According to these data and related literature reports²³⁹, backbone coplanarity is likely not the most important limiting parameter on ECL of linear ladder-type graphene substructures. Other factors, such as the conjugation width and the edge type (BTp vs phenacene vs acene), could play a more important role.⁹³

Because of the charge trapping effect of the branched alkoxy side-chains, **BTp5~11** did not show output current in bottom-gate, top-contact field effect transistor devices. However, access to this series of **BTp** oligomers with extended conjugation up to 13 rings, enabled an unprecedented, precise correlation of the oligomer sizes with solid-state crystallization dynamics. Establishment of such correlation is crucial for solid-state processing and device performances of sp^2 carbon-based materials, and is important to better understand the grand challenge on crystallization of macromolecules.²⁴⁰ For **BTp-5**, the solid-state absorption spectrum of the as-cast film was identical to that in the solution phase, indicating that (i) the molecular conformation remained persistent as a result of the fused-ring rigidity and (ii) there was no significant intermolecular electronic coupling due to the small π -face and relatively bulky solubilizing chains (Figure C.11a). Grazing-incidence wide-angle X-ray scattering (GIWAXS) pattern of **BTp-5** showed only moderately ordered face-on and edge-on packing, and no significant change before and after annealing (Figure 4a), suggesting that the film was already in a thermodynamically stable, weakly crystalline state as cast at room temperature. For **BTp-7** and **9**, the solid-

state spectra were bathochromically shifted while maintaining well-structured vibrational progression (Figure D.11b and c), indicating the presence of intermolecular electronic coupling in an ordered packing mode due to the large π -faces. Indeed, in GIWAXS, the as-cast film of **BTp-7** afforded highly crystalline scattering peaks with out-of-plane lamellar packing and edge-on π - π stacking at room temperature (Figure 5.4b). The thin film of **BTp-9** afforded less crystalline scattering peaks than **BTp-7** at room temperature and remained largely unchanged upon annealing (Figure 5.4c). For larger oligomers such as **BTp-11**, however, solid-state absorption of the as-cast film showed a broad and featureless spectrum, indicative of a kinetically trapped amorphous phase as a result of low molecular mobility and over-strengthened intermolecular interaction originating from the larger π -faces (Figure D.11d).²⁴¹ GIWAXS of the as-cast sample of **BTp-11** demonstrated weak crystallinity and only face-on π - π stacking. After annealing at 250 °C, however, the absorption spectrum of **BTp-11** regained a well-defined vibrational progression, as a result of a thermally induced crystallization process that gave back the highly ordered packing mode. GIWAXS of the annealed sample demonstrated well-resolved and highly crystalline scattering peaks with out-of-plane lamellar packing and edge-on π - π stacking (Figure 4.4d). Such phenomena were also observed in the more extreme case of **BTp-13**, but the annealing process gave less profound molecular reorganization due to the prohibitively large π -systems, hence low reorganization dynamics (Figure D.11e).

These results suggested that the balance between molecular mobility and intermolecular interaction was crucial in obtaining highly crystalline solid-state packing for ladder-type BTP-derived materials.²⁴² As observed above, larger π -systems facilitated stronger intermolecular interaction but also rendered lower molecular mobility for crystallization. These two counteractive factors must be optimally balanced to achieve good crystallinity at a certain temperature. The BTP oligomers with fine-tuned size differences enabled a unique opportunity to strike this balance. The best ordered solid-state packing from room temperature casting was seen on the somewhat smaller **BTP-7**, while after annealing, the highest crystallinity thin film was observed on the larger **BTP-11** (Figure 5.4e).

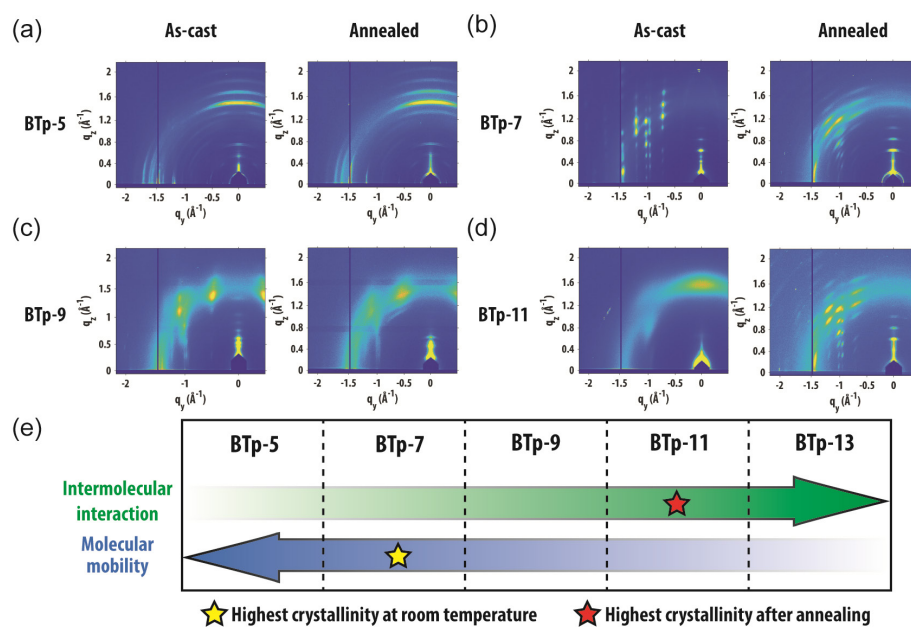


Figure 5.4. GIWAXS images of (a) **BTP-5**, (b) **BTP-7**, (c) **BTP-9**, and (d) **BTP-11** thin films as-cast and after annealing. (e) Correlation chart between intermolecular interaction and molecular mobility based on the relative size of building block to the alkyl chain. Low solubility of **BTP-13** prevented processing of thin films of adequate quality for GIWAXS.

5.3 Experimental Section

5.3.1. General Information

Starting materials and reagents were purchased from Aldrich, Alfa Aesar, TCI, and Acros, and were used as received without further purification. Toluene and DMF were dried using Inert Technology pure solvent system (PureSolv-MD-5a) and used without further treatment. THF was distilled with Na/benzophenone before uses. Anhydrous 1,2-dichloroethane and 1,4-Dioxane were purchased from Acros. 1,4-Dibromo-2,5-divinylbenzene,⁵⁴ 4,4'-dibromo-2,2',5,5'-tetramethyl-1,1'-biphenyl,²⁴³ and 13-(4-methylbenzenesulfonate)-13-pentacosanol²⁴⁴ were synthesized according to reported procedures in literatures. Analytical thin-layer chromatography (TLC) tests were performed on glass that was precoated with silica gel 60-F₂₅₄ (Sorbtech). Flash column chromatography was carried out using a Biotage[®] Isolera[™] Prime with various sizes of SiO₂ Biotage ZIP[®] cartridges. UV/vis absorption spectra and fluorescence spectra were recorded using a Shimadzu UV-2600 and a Horiba Fluoromax-4 spectrometer, while the UV-vis-NIR spectra were measured on a Hitachi U-4100 spectrometer. FT-IR spectra were recorded with ZnSe ATR using a Shimadzu IRAffinity-1S spectrometer. Cyclic voltammograms were recorded with Bio-Logic Science SP200 potentiostat. ¹H and ¹³C NMR spectra were obtained on a 500 MHz Varian Inova at room temperature unless specified. The NMR data were processed in MestReNova 6.1.0. Chemical shifts are reported in ppm relative to the signals corresponding to the residual non-deuterated solvents (CDCl₃: δ 7.26 for ¹H and 77.16 for ¹³C at room temperature, C₂D₂Cl₄: δ 6.00 for ¹H and 73.78 for ¹³C at 100 °C). Some ¹H and ¹³C NMR spectra contain observable 2,6-

di-*t*-butyl-4-methylphenol (BHT) peaks, which was used as a stabilizer. Size exclusion chromatography (SEC) was performed on TOSOH EcoSEC (HLC-8320GPC) in THF solution at 40 °C with a flow rate of 0.4 mL/min and the molecular weights were calculated using a calibration curve based on polystyrene standards, equipped with TSKgel SuperHM-M and TSKgel SuperH-RC. Preparative SEC was performed in chloroform solution at room temperature using a JAI recycling preparative HPLC (LC-92XXII NEXT SERIES). High-resolution Electrospray Ionization (HR-ESI) mass spectra and low-resolution Atmospheric Pressure Chemical Ionization (LR-APCI) mass spectra were measured on a Thermo Scientific Fusion (Orbitrap fusion tribrid) and a Thermo Scientific LCQ-DECA, respectively. Optical microscope images were obtained using an Olympus BX41 microscope. Grazing-incidence wide-angle X-ray scattering (GIWAXS) measurements were carried out in Sector 8-ID-E at the Advanced Photon Source, Argonne National Laboratory.¹⁹⁶ Beamline 8-ID-E operates at an energy of 10.91 keV and the images were collected from a Pilatus 1MF camera (Dectris), with two exposures for different vertical positions of the detector. After flat field correction for detector nonuniformity, the images are combined to fill in the gaps for rows at the borders between modules, leaving dark only the columns of inactive pixels at the center. Using the GIXSGUI package for MATLAB (Mathworks), data are corrected for X-ray polarization, detector sensitivity and geometrical solid-angle. The beam size is 0.8 mm × 0.5 mm and the resolution ($\Delta E/E$) is 1×10^{-4} . Sample detector distance is 228 mm. Solid-state samples for GIWAXS and optical microscope analysis were deposited on UV-Ozone cleaned silicon wafers by spin-casting with the solutions (2 mg/mL in CHCl_3) at a spin rate of

1000 rpm. Solid-state samples for UV-vis analysis were deposited on glasses by drop-casting with the solutions (2 mg/mL in CHCl₃).

5.3.2. Synthesis of **VPP3**, **VPP4**, **VPP5**, **VPP6**, and **VPP7**

To a mixture of the vinyl oligomer (compound **6**, **7**, **8**, **9**, or **10**) (0.1 g scale), compound **S10** (3.0 equiv.), K₂CO₃ (6.0 equiv.), aliquat 336 (0.25 equiv.), several crystals of BHT, and Pd(PPh₃)₄ (10 mol%) were added degassed toluene (5 mL) and water (1 mL) under a N₂ atmosphere. The reaction mixture was stirred at 100 °C for 24 h in darkness. After being cooled to room temperature, the reaction mixture was concentrated under reduced pressure, and the residue was extracted with CH₂Cl₂ (3 × 10 mL). The combined organic layer was dried over MgSO₄, filtered through Celite, and concentrated under reduced pressure. The residue was purified by flash column chromatography to give the products **VPP3**, **VPP4**, **VPP5**, **VPP6**, and **VPP7** as sticky liquids.

VPP3: Yield: 79%, ¹H NMR (500 MHz, CDCl₃): δ 7.45 (m, 2H), 7.22 (m, 2H), 7.13 (m, 2H), 6.86 (dd, *J*₁ = 8.5 Hz, *J*₂ = 2.5 Hz, 2H), 6.49 (m, 4H), 5.68 (d, *J* = 17.5 Hz, 1H), 5.67 (d, *J* = 17.5 Hz, 1H), 5.61 (d, *J* = 17.5 Hz, 2H), 5.16 (d, *J* = 12.0 Hz, 1H), 5.14 (d, *J* = 12.0 Hz, 1H), 5.07 (d, *J* = 12.0 Hz, 2H), 4.30 (quint, *J* = 6.0 Hz, 2H), 1.68 (m, 8H), 1.47 (m, 4H), 1.40 (m, 4H), 1.26 (m, 72H), 0.88 (t, *J* = 7.0 Hz, 12H). ¹³C NMR (125 MHz, CDCl₃): δ 158.30, 138.65, 138.63, 137.84, 137.40, 137.33, 135.76, 135.54, 135.51, 135.39, 135.30, 134.87, 131.72, 131.69, 129.01, 128.20, 127.23, 125.29, 114.94, 114.47, 114.40, 114.29, 114.27, 111.74, 77.98, 34.03, 32.00, 29.84, 29.77, 29.75, 29.73, 29.70,

29.44, 25.51, 22.76, 14.11. LRMS (APCI): calcd for $C_{76}H_{122}O_2$ $[M+H]^+$ $m/z = 1067.95$; found $m/z = 1068.02$.

VPP4: Yield: 70%, 1H NMR (500 MHz, $CDCl_3$): δ 7.54 (m, 2H), 7.50 (m, 2H), 7.21 (m, 2H), 7.16 (m, 2H), 6.88 (dd, $J_1 = 8.5$ Hz, $J_2 = 2.5$ Hz, 2H), 6.53 (m, 6H), 5.68 (m, 6H), 5.14 (m, 6H), 4.31 (quint, $J = 6.0$ Hz, 2H), 1.70 (m, 8H), 1.48 (m, 4H), 1.41 (m, 4H), 1.26 (m, 72H), 0.88 (t, $J = 7.0$ Hz, 12H). ^{13}C NMR (125 MHz, $CDCl_3$): δ 158.39, 139.03, 139.00, 138.67, 138.65, 137.98, 137.54, 137.46, 135.87, 135.81, 135.78, 135.49, 135.38, 135.36, 135.29, 135.22, 134.95, 134.91, 134.83, 134.79, 134.73, 134.70, 131.84, 131.79, 129.17, 128.36, 127.40, 126.99, 125.44, 115.02, 114.91, 114.83, 114.77, 114.70, 111.92, 111.89, 78.14, 34.41, 32.09, 29.94, 29.86, 29.84, 29.82, 29.80, 29.53, 25.63, 22.86, 14.29. LRMS (APCI): calcd for $C_{86}H_{130}O_2$ $[M+H]^+$ $m/z = 1196.01$; found $m/z = 1196.15$.

VPP5: Yield: 71%, 1H NMR (500 MHz, $CDCl_3$): δ 7.58 (m, 4H), 7.52 (m, 2H), 7.22 (m, 2H), 7.16 (m, 2H), 6.89 (dd, $J_1 = 8.5$ Hz, $J_2 = 2.5$ Hz, 2H), 6.52 (m, 8H), 5.69 (m, 8H), 5.20 (m, 8H), 4.31 (quint, $J = 6.0$ Hz, 2H), 1.70 (m, 8H), 1.48 (m, 4H), 1.41 (m, 4H), 1.26 (m, 72H), 0.88 (t, $J = 7.0$ Hz, 12H). ^{13}C NMR (125 MHz, $CDCl_3$): δ 158.42, 139.12, 139.10, 139.02, 138.97, 138.6, 137.56, 137.48, 135.85, 135.51, 135.39, 135.32, 135.26, 134.93, 134.79, 134.72, 131.84, 131.77, 127.46, 127.05, 127.02, 115.02, 114.91, 114.84, 114.76, 114.69, 111.95, 111.93, 78.10, 34.16, 32.10, 29.95, 29.87, 29.85, 29.83, 29.80, 29.54, 25.63, 22.87, 14.30. LRMS (APCI): calcd for $C_{96}H_{138}O_2$ $[M+H]^+$ $m/z = 1325.08$; found $m/z = 1325.28$.

VPP6: Yield: 75%, ^1H NMR (500 MHz, CDCl_3): δ 7.62 (m, 4H), 7.57 (m, 2H), 7.53 (m, 2H), 7.23 (m, 2H), 7.17 (m, 2H), 6.89 (dd, $J_1 = 8.5$ Hz, $J_2 = 2.5$ Hz, 2H), 6.55 (m, 10H), 5.72 (m, 10H), 5.16 (m, 10H), 4.31 (quint, $J = 6.0$ Hz, 2H), 1.71 (m, 8H), 1.50 (m, 4H), 1.41 (m, 4H), 1.26 (m, 72H), 0.88 (t, $J = 7.0$ Hz, 12H). ^{13}C NMR (125 MHz, CDCl_3): δ 158.42, 139.09, 138.93, 138.89, 138.59, 138.55, 137.56, 137.48, 135.89, 135.85, 135.50, 135.38, 135.32, 135.30, 135.24, 134.97, 134.95, 134.92, 134.78, 134.72, 134.70, 131.85, 131.77, 127.47, 127.46, 127.07, 127.02, 115.16, 115.05, 114.96, 114.88, 114.81, 114.71, 111.95, 111.93, 78.18, 34.15, 32.09, 29.94, 29.86, 29.84, 29.82, 29.80, 29.53, 25.64, 22.86, 14.29. LRMS (APCI): calcd for $\text{C}_{106}\text{H}_{146}\text{O}_2$ $[M+\text{H}]^+$ $m/z = 1453.14$; found $m/z = 1453.27$.

VPP7: Yield: 69%, ^1H NMR (500 MHz, CDCl_3): δ 7.65 (m, 6H), 7.60 (m, 2H), 7.55 (m, 2H), 7.25 (m, 2H), 7.19 (m, 2H), 6.91 (dd, $J_1 = 8.5$ Hz, $J_2 = 2.5$ Hz, 2H), 6.59 (m, 12H), 5.74 (m, 12H), 5.13 (m, 6H), 4.34 (quint, $J = 6.0$ Hz, 2H), 1.73 (m, 8H), 1.51 (m, 5H), 1.30 (m, 72H), 0.90 (t, $J = 7.0$ Hz, 12H). ^{13}C NMR (125 MHz, CDCl_3): δ 158.43, 139.11, 139.01, 138.92, 138.86, 138.57, 138.55, 137.56, 137.48, 135.88, 135.51, 135.38, 135.32, 135.30, 135.24, 134.96, 134.92, 134.77, 134.71, 134.67, 131.85, 131.77, 127.47, 127.08, 127.02, 115.16, 115.05, 114.98, 114.89, 114.80, 114.74, 111.93, 78.17, 34.15, 32.09, 29.94, 29.86, 29.84, 29.82, 29.80, 29.53, 25.64, 22.86, 14.29. LRMS (APCI): calcd for $\text{C}_{116}\text{H}_{154}\text{O}_2$ $[M+\text{H}]^+$ $m/z = 1581.21$; found $m/z = 1581.35$.

5.3.3. Synthesis of **BTp-5**, **BTp-7**, **BTp-9**, **BTp-11**, and **BTp-13**

The mixture of **VPP3**, **VPP4**, **VPP5**, **VPP6**, or **VPP7** (0.1 g scale) and Grubbs' 2nd generation catalyst (3 mol%) in degassed toluene (3 mL, *o*-DCB for **VPP7**) was stirred at reflux (at 130 °C for **VPP7**) under a N₂ atmosphere. Immediately, another portion of Grubbs' 2nd generation catalyst (7 mol%) in degassed toluene (5 mL, *o*-DCB for **VPP7**) was added for 4 h using syringe pump. After that, the reaction mixture was stirred for an additional 2 h at reflux temperature (at 130 °C for **VPP7**). After being cooled to room temperature, the reaction mixture was precipitated in methanol, and the precipitate was filtered, washed with methanol, and dried under vacuum to afford the products **BTp-5**, **BTp-7**, **BTp-9**, **BTp-11**, and **BTp-13** as off-white (**BTp-5**) to yellow (**BTp-13**) solids.

BTp-5 (3,10-bis(pentacosan-13-yloxy)benzo[*k*]tetraphene): Yield: 98%, ¹H NMR (500 MHz, CDCl₃): δ 8.99 (s, 2H), 8.73 (d, *J* = 9.0 Hz, 2H), 7.90 (d, *J* = 9.0 Hz, 2H), 7.64 (d, *J* = 9.0 Hz, 2H), 7.30 (m, 4H), 4.44 (quint, *J* = 6.0 Hz, 2H), 1.73 (m, 8H), 1.51 (m, 4H), 1.42 (m, 4H), 1.24 (m, 72H), 0.86 (t, *J* = 7.0 Hz, 12H). ¹³C NMR (125 MHz, CDCl₃): δ 157.80, 133.46, 130.32, 128.68, 128.07, 126.99, 124.49, 124.30, 121.48, 117.96, 111.98, 78.34, 34.12, 32.09, 29.92, 29.85, 29.83, 29.82, 29.78, 29.53, 25.59, 22.86, 14.29. LRMS (APCI): calcd for C₇₂H₁₁₄O₂ [*M*+H]⁺ *m/z* = 1011.89; found *m/z* = 1012.29. Elemental Analysis: calcd for C₇₂H₁₁₄O₂ = C 85.48, H 11.36; found = C 85.03, H 11.36.

BTp-7 (2,11-bis(pentacosan-13-yloxy)benzo[*k*]naphtho[2,1-*b*]tetraphene): Yield: 96%, ¹H NMR (500 MHz, CDCl₃): δ 9.24 (s, 2H), 9.01 (s, 2H), 8.77 (d, *J* = 9.0 Hz, 2H), 7.99 (d, *J* = 9.0 Hz, 2H), 7.90 (s, 2H), 7.70 (d, *J* = 9.0 Hz, 2H), 7.33 (m, 4H), 4.47

(quint, $J = 6.0$ Hz, 2H), 1.76 (m, 8H), 1.52 (m, 4H), 1.44 (m, 4H), 1.25 (m, 72H), 0.87 (t, $J = 7.0$ Hz, 12H). ^{13}C NMR (125 MHz, CDCl_3): δ 157.92, 133.67, 130.98, 130.21, 129.56, 128.43, 128.03, 127.83, 127.05, 124.65, 124.24, 122.39, 121.55, 118.08, 111.86, 78.35, 34.12, 32.09, 29.94, 29.86, 29.84, 29.82, 29.79, 29.53, 25.61, 22.86, 14.29. LRMS (APCI): calcd for $\text{C}_{80}\text{H}_{118}\text{O}_2$ $[M+H]^+$ $m/z = 1111.92$; found $m/z = 1112.31$. Elemental Analysis: calcd for $\text{C}_{80}\text{H}_{118}\text{O}_2 = \text{C } 86.42, \text{H } 10.70$; found = C 86.53, H 10.81.

BTp-9 (3,14-bis(pentacosan-13-yloxy)benzo[1,2- k :4,5- k']ditetraphene): Yield: 98%, ^1H NMR (500 MHz, CDCl_3): δ 9.30 (s, 2H), 9.29 (s, 2H), 9.06 (s, 2H), 8.79 (d, $J = 9.0$ Hz, 2H), 8.03 (d, $J = 9.0$ Hz, 2H), 8.01 (d, $J = 9.0$ Hz, 2H), 7.97 (d, $J = 9.0$ Hz, 2H), 7.72 (d, $J = 9.0$ Hz, 2H), 7.33 (m, 4H), 4.47 (quint, $J = 6.0$ Hz, 2H), 1.76 (m, 8H), 1.51 (m, 4H), 1.46 (m, 4H), 1.25 (m, 72H), 0.87 (t, $J = 7.0$ Hz, 12H). ^{13}C NMR (125 MHz, CDCl_3): δ 157.96, 133.71, 131.06, 130.89, 130.20, 129.65, 129.32, 128.28, 128.05, 127.89, 127.71, 127.10, 124.70, 124.21, 122.53, 122.38, 121.57, 118.08, 111.86, 78.37, 34.12, 32.08, 29.94, 29.86, 29.84, 29.82, 29.79, 29.53, 25.62, 22.85, 14.29. LRMS (APCI): calcd for $\text{C}_{88}\text{H}_{122}\text{O}_2$ $[M+H]^+$ $m/z = 1211.95$; found $m/z = 1212.31$. Elemental Analysis: calcd for $\text{C}_{88}\text{H}_{122}\text{O}_2 = \text{C } 87.21, \text{H } 10.15$; found = C 86.93, H 10.24.

BTp-11 (2,15-bis(pentacosan-13-yloxy)benzo[2,1- b :5,6- b']di(benzo[k]tetraphene)): Yield: 96%, ^1H NMR (500 MHz, CDCl_3): δ 9.16 (s, 2H), 9.14 (s, 2H), 9.13 (s, 2H), 8.72 (d, $J = 9.0$ Hz, 2H), 7.96 (s, 2H), 7.94 (d, $J = 9.0$ Hz, 2H), 7.91 (d, $J = 9.0$ Hz, 2H), 7.87 (d, $J = 9.0$ Hz, 2H), 7.66 (d, $J = 9.0$ Hz, 2H), 7.31 (m, 4H), 4.47 (quint, $J = 6.0$ Hz, 2H), 1.76 (m, 8H), 1.53 (m, 4H), 1.47 (m, 4H), 1.25 (m, 72H), 0.87 (t, $J = 7.0$ Hz, 12H). ^{13}C NMR (125 MHz, CDCl_3): δ 157.98, 133.72, 131.10, 131.03, 130.94, 130.24,

129.73, 129.49, 129.21, 128.28, 128.03, 128.00, 127.85, 127.74, 127.15, 124.70, 124.20, 122.59, 122.54, 122.45, 121.62, 118.11, 111.89, 78.38, 34.12, 32.08, 29.94, 29.86, 29.84, 29.82, 29.79, 29.53, 25.61, 22.85, 14.29. LRMS (APCI): calcd for C₉₆H₁₂₆O₂ [M+H]⁺ *m/z* = 1311.98; found *m/z* = 1312.34. Elemental Analysis: calcd for C₉₆H₁₂₆O₂ = C 87.88, H 9.68; found = C 87.92, H 9.75.

BTp-13 (3,18-bis(pentacosan-13-yloxy)benzo[1,2-*n*:4,5-*n'*]di(naphtho[2,1-*b*]tetraphene)): Yield: 96%, ¹H NMR (500 MHz, C₂D₂Cl₄, 100 °C): δ 9.32 (m, 8H), 9.06 (s, 2H), 8.79 (d, *J* = 9.0 Hz, 2H), 8.13 (s, 4H), 8.05 (m, 6H), 7.76 (d, *J* = 9.0 Hz, 2H), 7.39 (m, 4H), 4.52 (quint, *J* = 6.0 Hz, 2H), 1.85 (m, 8H), 1.58 (m, 8H), 1.34 (m, 72H), 0.95 (t, *J* = 7.0 Hz, 12H). ¹³C NMR (125 MHz, C₂D₂Cl₄, 100 °C): δ 158.11, 135.57, 131.15, 131.13, 130.93, 130.81, 130.12, 129.63, 129.42, 129.20, 129.02, 128.40, 128.32, 128.09, 127.91, 127.71, 127.58, 127.38, 126.94, 124.27, 124.03, 122.27, 121.32, 118.01, 117.79, 112.48, 78.75, 34.01, 31.65, 29.55, 29.41, 29.03, 25.23, 22.37, 13.74. LRMS (APCI): calcd for C₁₀₄H₁₃₀O₂ [M+H]⁺ *m/z* = 1413.02; found *m/z* = 1413.09. Elemental Analysis: calcd for C₁₀₄H₁₃₀O₂ = C 88.45, H 9.28; found = C 88.62, H 9.26.

5.4. Conclusion

In summary, the syntheses of extended linear benzo[*k*]tetraphene ladder-type oligomers were achieved through iterative Suzuki and Miyaura reactions followed by highly efficient ring-closing olefin metathesis. The longest oligomer, **BTp-13**, was synthesized in 5 steps with a 20.6% overall yield. Access to these well-defined oligomers allowed for a clear correlation of the properties and the molecular sizes for fused-ring

ladder-type π -systems. Spectroscopic investigation revealed the rigid nature of the aromatic backbones, while rapid saturation of the effective conjugation length was observed with the extension of the π -system. Investigation of the optimized size for crystallinity demonstrated the importance of the balance between intermolecular interaction and molecular mobility for achieving highly ordered packing in the solid state. These results provide fundamental guidance for the development of functional ladder-type oligomers for applications requiring highly crystalline conjugated materials, such as single crystal field effect transistors²²³ and non-linear optical devices.²⁴⁵

CHAPTER VI

CONCLUSIONS

This thesis introduced important historical syntheses of conjugated ladder polymers and oligomers, as well as significant advances in the past decade. The intriguing properties of conjugated ladder-type functional organic materials promise their future as next generation functional materials. However, in order to maximize the potential of this class of materials, the challenges associated with the synthesis, structural defects, characterization, solubility, and processability need to be addressed.

For the synthesis of a well-defined ladder-type material, the development of synthetic strategies in either single-step ladderization or post-polymerization ladderization has seen significant progress. Although the single-step approach is limited by the availability of starting materials suitable for the formation of multiple strands of bonds, the idea of using spontaneous intramolecular dynamic bonds enables the possibility of constructing a coplanar ladder-like structure through a single-step polymerization. The stepwise strategy, especially thermodynamic ring annulation, could afford a feasible approach to well-defined ladder polymers with fewer structural defects.

We have demonstrated the synthesis of various ladder-type functional organic materials from small molecules to polymers by employing thermodynamically controlled ring-closing olefin metathesis (RCM). The highly efficient and versatile synthetic method afforded a quantitative conversion by releasing 28 kcal mol⁻¹ in forming a stable aromatic ring. Furthermore, the reversible nature between vinyl functionalized starting materials

and cross-linked side products leads to uncross-linked products with minimum levels of structural defects. We also demonstrated the thermodynamically controlled ring annulation with electron deficient olefin to construct acceptor-donor-acceptor alternating fused polycyclic heteroarenes and donor-acceptor alternating ladder-polymer still kept the excellent reactivity. The synthesized ladder-type materials were well-soluble in common organic solvents at room temperature due to the orthogonally adopted α -branched alkyl chain by weakening the potential strong intermolecular interaction.

In Chapter II, RCM successfully constructed carbazole and indolo[3,2-*b*]carbazole-based polycyclic heteroarenes with up to 11 fused rings in excellent yields. These materials were unambiguously analyzed with single crystal structures demonstrating a unique packing structures affected by molecular symmetry, orthogonally adopted solubilizing groups, and intermolecular S \cdots S interactions. Furthermore, the rigid coplanar nature of the heteroarene backbones induced the formation of intermolecular charge transfer complexes with electron acceptor F₄TCNQ.

In Chapter III, we demonstrated highly efficient synthetic strategy to construct a fully conjugated ladder polymer **LP**. The rigorous analysis on the ¹³C isotope-enriched ladder polymer revealed that the ladder polymer contained less than 1% of unreacted vinyl groups along the polymer chain. The ladder polymer with minimum levels of structural defects was comprehensively analyzed in solution and the solid-state. Furthermore, it was visualized by STM on HOPG, displaying a uniform and extended rod-like morphology, well matched with the theoretical dimensions.

In Chapter IV, we expanded the scope of the synthetic method to construct a donor-acceptor type ladder polymer, **DALP**, which represents a class of promising material candidates. Thermodynamically controlled RCM successfully afforded the donor-acceptor ladder polymer without a decreased reactivity in the ring annulation. **LP** and **DALP** also formed a charge transfer complex with F₄TCNQ displaying charge transfer bands in the NIR region as a result of the rigid coplanar nature of the ladder polymers. Furthermore, GIWAXS analysis of **DALP** after alkyl chain cleavage at 500 °C demonstrated that the residual ladder polymer backbone preferentially reorganized into a face-on orientation with a π - π distance of 3.7 Å.

In Chapter V, we synthesized a series of benzo[k]tetraphene-derived oligomers (BTps), an important class of molecular substructures for armchair graphene nanoribbons. Relatively unexplored compared to isomeric [*n*]acenes and [*n*]phenacenes, the BTP derivatives were successfully prepared with up to 13 fused rings in excellent yields over 96 %. The study of effective conjugation length (ECL) on the BTP oligomers elucidated an ECL of 21 benzene rings. Moreover, crystallization dynamics of BTP oligomers were investigated by solid-state UV-vis and GIWAXS. It suggested that the balance between molecular mobility and intermolecular interactions was crucial to achieve a highly ordered packing structures in the solid state.

Overall, the demonstration of efficient, feasible, and versatile synthetic strategy employing thermodynamically controlled RCM proposes a powerful tool to achieve a fully conjugated ladder-type material with minimum levels of structural defects. Furthermore, the comprehensive analysis on the ladder-type materials provides

fundamental guidance for the development of ladder-type functional organic materials for various applications. Last but not least, this efficient and versatile synthetic strategy would access for an intriguing fused-ring material which has not been achieved. Although the synthesis, process, and application of ladder-type materials still needs to overcome many obstacles, in conjunction with the development of crystallization or self-assembly of a ladder-type material and various efficient synthetic methods, the field of ladder-type materials will see a bright future.

REFERENCES

- 1) Yu, L.; Chen, M.; Dalton, L. R., *Chem. Mater.* **1990**, 6, 649-659.
- 2) Scherf, U., *J. Mater. Chem.* **1999**, 9, 1853-1864.
- 3) Grimsdale, A. C.; Müllen, K., *Macromol. Rapid Commun.* **2007**, 17, 1676-1702.
- 4) R. G. Jones, R. S., E. S. Wilks, M. Hess, T. Kitayama and; Metanomski, W. V., *Compendium of polymer terminology and nomenclature IUPAC recommendations 2008*. The Royal Society of Chemistry: Cambridge, UK, **2008**.
- 5) Wu, Y.; Zhang, J.; Fei, Z.; Bo, Z., *J. Am. Chem. Soc.* **2008**, 23, 7192-7193.
- 6) Zeng, S. Z.; Jin, N. Z.; Zhang, H. L.; Hai, B.; Chen, X. H.; Shi, J. L., *Rsc Advances* **2014**, 36, 18676-18682.
- 7) Lee, J.; Rajeeva, B. B.; Yuan, T.; Guo, Z.-H.; Lin, Y.-H.; Al-Hashimi, M.; Zheng, Y.; Fang, L., *Chem. Sci.* **2016**, 2, 881-889.
- 8) Grozema, F. C.; van Duijnen, P. T.; Berlin, Y. A.; Ratner, M. A.; Siebbeles, L. D. A., *J. Phys. Chem. B* **2002**, 32, 7791-7795.
- 9) Prins, P.; Grozema, F. C.; Schins, J. M.; Patil, S.; Scherf, U.; Siebbeles, L. D. A., *Phys. Rev. Lett.* **2006**, 14.
- 10) Samiullah, M.; Moghe, D.; Scherf, U.; Guha, S., *Phys. Rev. B* **2010**, 20, 205211.
- 11) Bjorgaard, J. A.; Köse, M. E., *J. Phys. Chem. A* **2013**, 18, 3869-3876.
- 12) Van Deusen, R. L., *J. Polym. Sci. B Polym. Lett.* **1966**, 3, 211-214.
- 13) Schlüter, A. D., *Adv. Mater.* **1991**, 6, 282-291.
- 14) Grem, G.; Leising, G., *Synth. Met.* **1993**, 1, 4105-4110.

- 15) Leising, G.; Tasch, S.; Meghdadi, F.; Athouel, L.; Froyer, G.; Scherf, U., *Synth. Met.* **1996**, 2, 185-189.
- 16) Piok, T.; Gamerith, S.; Gadermaier, C.; Plank, H.; Wenzl, F. P.; Patil, S.; Montenegro, R.; Kietzke, T.; Neher, D.; Scherf, U.; Landfester, K.; List, E. J. W., *Adv. Mater.* **2003**, 10, 800-804.
- 17) Durban, M. M.; Kazarinoff, P. D.; Segawa, Y.; Luscombe, C. K., *Macromolecules* **2011**, 12, 4721-4728.
- 18) Babel, A.; Jenekhe, S. A., *Adv. Mater.* **2002**, 5, 371-374.
- 19) Chen, X. L.; Bao, Z.; Schön, J. H.; Lovinger, A. J.; Lin, Y.-Y.; Crone, B.; Dodabalapur, A.; Batlogg, B., *Appl. Phys. Lett.* **2001**, 2, 228-230.
- 20) Babel, A.; Jenekhe, S. A., *J. Am. Chem. Soc.* **2003**, 45, 13656-13657.
- 21) Briseno, A. L.; Mannsfeld, S. C. B.; Shamberger, P. J.; Ohuchi, F. S.; Bao, Z.; Jenekhe, S. A.; Xia, Y., *Chem. Mater.* **2008**, 14, 4712-4719.
- 22) Stille, J. K.; Mainen, E. L., *J. Polym. Sci. B Polym. Lett.* **1966**, 1, 39-41.
- 23) Stille, J. K.; Mainen, E. L., *J. Polym. Sci. B Polym. Lett.* **1966**, 9, 665-667.
- 24) Kim, O.-K., *J. Polym. Sci. B Polym. Lett. Ed.* **1985**, 3, 137-139.
- 25) Schlüter, A. D.; Löffler, M.; Enkelmann, V., *Nature* **1994**, 6474, 831-834.
- 26) Schlicke, B.; Schirmer, H.; Schlüter, A. D., *Adv. Mater.* **1995**, 6, 544-546.
- 27) Delnoye, D. A. P.; Sijbesma, R. P.; Vekemans, J. A. J. M.; Meijer, E. W., *J. Am. Chem. Soc.* **1996**, 36, 8717-8718.
- 28) Pieterse, K.; Vekemans, J. A. J. M.; Kooijman, H.; Spek, A. L.; Meijer, E. W., *Chem. Eur. J.* **2000**, 24, 4597-4603.

- 29) Vetrichelvan, M.; Valiyaveetil, S., *Chem. Eur. J.* **2005**, 20, 5889-5898.
- 30) Wakamiya, A.; Taniguchi, T.; Yamaguchi, S., *Angew. Chem. Int. Ed.* **2006**, 19, 3170-3173.
- 31) Tian, Y.-H.; Kertesz, M., *Macromolecules* **2009**, 7, 2309-2312.
- 32) Zhu, C.; Guo, Z.-H.; Mu, A. U.; Liu, Y.; Wheeler, S. E.; Fang, L., *J. Org. Chem.* **2016**, 10, 4347-4352.
- 33) Crossley, D. L.; Cade, I. A.; Clark, E. R.; Escande, A.; Humphries, M. J.; King, S. M.; Vitorica-Yrezabal, I.; Ingleson, M. J.; Turner, M. L., *Chem. Sci.* **2015**, 9, 5144-5151.
- 34) Scherf, U.; Müllen, K., *Makromol. Chem. Rapid. Commun.* **1991**, 8, 489-497.
- 35) Yuan, Z.; Xiao, Y.; Yang, Y.; Xiong, T., *Macromolecules* **2011**, 7, 1788-1791.
- 36) Kass, K. J.; Forster, M.; Scherf, U., *Angew. Chem. Int. Ed.* **2016**, 27, 7816-20.
- 37) Nehls, B. S.; Földner, S.; Preis, E.; Farrell, T.; Scherf, U., *Macromolecules* **2005**, 3, 687-694.
- 38) Patil, S. A.; Scherf, U.; Kadashchuk, A., *Adv. Funct. Mater.* **2003**, 8, 609-614.
- 39) Forster, M.; Annan, K. O.; Scherf, U., *Macromolecules* **1999**, 9, 3159-3162.
- 40) Fiesel, R.; Huber, J.; Scherf, U., *Angew. Chem. Int. Ed.* **1996**, 18, 2111-2113.
- 41) Scherf, U.; Müllen, K., *Polymer* **1992**, 11, 2443-2446.
- 42) Cho, S. Y.; Grimsdale, A. C.; Jones, D. J.; Watkins, S. E.; Holmes, A. B., *J. Am. Chem. Soc.* **2007**, 39, 11910-11911.
- 43) List, E. J. W.; Guentner, R.; Freitas, P. S. d.; Scherf, U., *Adv. Mater.* **2002**, 5, 374-378.

- 44) Scherf, U.; List, E. J. W., *Adv. Mater.* **2002**, 7, 477-487.
- 45) Qiu, S.; Lu, P.; Liu, X.; Shen, F.; Liu, L.; Ma, Y.; Shen, J., *Macromolecules* **2003**, 26, 9823-9829.
- 46) Chen, Y.; Huang, W.; Li, C.; Bo, Z., *Macromolecules* **2010**, 24, 10216-10220.
- 47) Chmil, K.; Scherf, U., *Makromol. Chem. Rapid Commun.* **1993**, 4, 217-222.
- 48) Chmil, K.; Scherf, U., *Acta Polym.* **1997**, 5-6, 208-211.
- 49) Goldfinger, M. B.; Swager, T. M., *J. Am. Chem. Soc.* **1994**, 17, 7895-7896.
- 50) Debad, J. D.; Bard, A. J., *J. Am. Chem. Soc.* **1998**, 10, 2476-2477.
- 51) Zou, Y.; Ji, X.; Cai, J.; Yuan, T.; Stanton, D. J.; Lin, Y.-H.; Naraghi, M.; Fang, L., *Chem* **2017**, 1, 139-152.
- 52) Rowan, S. J.; Cantrill, S. J.; Cousins, G. R. L.; Sanders, J. K. M.; Stoddart, J. F., *Angew. Chem. Int. Ed.* **2002**, 6, 898-952.
- 53) Tour, J. M.; Lamba, J. J. S., *J. Am. Chem. Soc.* **1993**, 11, 4935-4936.
- 54) Bonifacio, M. C.; Robertson, C. R.; Jung, J. Y.; King, B. T., *J. Org. Chem.* **2005**, 21, 8522-8526.
- 55) Tsai, F. C.; Chang, C. C.; Liu, C. L.; Chen, W. C.; Jenekhe, S. A., *Macromolecules* **2005**, 5, 1958-1966.
- 56) Streifel, B. C.; Peart, P. A.; Martínez Hardigree, J. F.; Katz, H. E.; Tovar, J. D., *Macromolecules* **2012**, 18, 7339-7349.
- 57) Wood, S.; Kim, J. H.; Hwang, D. H.; Kim, J. S., *Chem. Mater.* **2015**, 12, 4196-4204.

- 58) Wang, Q.; Zhang, B.; Liu, L.; Chen, Y.; Qu, Y.; Zhang, X.; Yang, J.; Xie, Z.; Geng, Y.; Wang, L.; Wang, F., *J. Phys. Chem. C* **2012**, 41, 21727-21733.
- 59) Asaoka, S.; Takeda, N.; Iyoda, T.; Cook, A. R.; Miller, J. R., *J. Am. Chem. Soc.* **2008**, 36, 11912-11920.
- 60) Koldemir, U.; Puniredd, S. R.; Wagner, M.; Tongay, S.; McCarley, T. D.; Kamenov, G. D.; Müllen, K.; Pisula, W.; Reynolds, J. R., *Macromolecules* **2015**, 18, 6369-6377.
- 61) Grisorio, R.; Piliago, C.; Striccoli, M.; Cosma, P.; Fini, P.; Gigli, G.; Mastroilli, P.; Suranna, G. P.; Nobile, C. F., *J. Phys. Chem. C* **2008**, 50, 20076-20087.
- 62) Lupton, J. M., *Chem. Phys. Lett.* **2002**, 3-4, 366-368.
- 63) Liu, L.; Yang, B.; Zhang, H.; Tang, S.; Xie, Z.; Wang, H.; Wang, Z.; Lu, P.; Ma, Y., *J. Phys. Chem. C* **2008**, 27, 10273-10278.
- 64) Adachi, T.; Vogelsang, J.; Lupton, J. M., *J. Phys. Chem. Lett.* **2014**, 3, 573-577.
- 65) Becker, K.; Lupton, J. M.; Feldmann, J.; Nehls, B. S.; Galbrecht, F.; Gao, D. Q.; Scherf, U., *Adv. Funct. Mater.* **2006**, 3, 364-370.
- 66) Wang, B.; Forster, M.; Preis, E.; Wang, H.; Ma, Y.; Scherf, U., *J. Polym. Sci. A Polym. Chem.* **2009**, 19, 5137-5143.
- 67) Simpson, C. D.; Brand, J. D.; Berresheim, A. J.; Przybilla, L.; Rader, H. J.; Müllen, K., *Chem. Eur. J.* **2002**, 6, 1424-1429.
- 68) Narita, A.; Feng, X.; Hernandez, Y.; Jensen, S. A.; Bonn, M.; Yang, H.; Verzhbitskiy, I. A.; Casiraghi, C.; Hansen, M. R.; Koch, A. H. R.; Fytas, G.;

- Ivasenko, O.; Li, B.; Mali, K. S.; Balandina, T.; Mahesh, S.; De Feyter, S.; Müllen, K., *Nat. Chem.* **2014**, 2, 126-132.
- 69) Kang, I.; Yun, H.-J.; Chung, D. S.; Kwon, S.-K.; Kim, Y.-H., *J. Am. Chem. Soc.* **2013**, 40, 14896-14899.
- 70) Liu, L.; Han, T.; Wu, X.; Qiu, S.; Wang, B.; Hanif, M.; Xie, Z.; Ma, Y., *J. Phys. Chem. C* **2015**, 21, 11833-11838.
- 71) Lee, J.; Han, A. R.; Yu, H.; Shin, T. J.; Yang, C.; Oh, J. H., *J. Am. Chem. Soc.* **2013**, 25, 9540-9547.
- 72) Lei, T.; Dou, J.-H.; Pei, J., *Adv. Mater.* **2012**, 48, 6457-6461.
- 73) Lei, T.; Wang, J. Y.; Pei, J., *Acc. Chem. Res.* **2014**, 4, 1117-1126.
- 74) Mei, J.; Bao, Z., *Chem. Mater.* **2013**, 1, 604-615.
- 75) Guo, Z.-H.; Ai, N.; McBroom, C. R.; Yuan, T.; Lin, Y.-H.; Roders, M.; Zhu, C.; Ayzner, A. L.; Pei, J.; Fang, L., *Polym. Chem.* **2016**, 3, 648-655.
- 76) Smith, Z. C.; Meyer, D. M.; Simon, M. G.; Staii, C.; Shukla, D.; Thomas, S. W., *Macromolecules* **2015**, 4, 959-966.
- 77) Godt, A.; Schlüter, A.-D., *Die Makromolekulare Chemie* **1992**, 2, 501-506.
- 78) Hickl, P.; Ballauff, M.; Scherf, U.; Müllen, K.; Lindner, P., *Macromolecules* **1997**, 2, 273-279.
- 79) Wong, M.; Hollinger, J.; Kozycz, L. M.; McCormick, T. M.; Lu, Y.; Burns, D. C.; Seferos, D. S., *ACS Macro Lett.* **2012**, 11, 1266-1269.
- 80) März, K.; Lindner, P.; Urban, G.; Ballauff, M.; Kugler, J.; Fischer, E. W., *Acta Polym.* **1993**, 3, 139-147.

- 81) Liu, T.; Xiao, Z., *Macromol. Chem. Phys.* **2012**, 16, 1697-1705.
- 82) Trachtenberg, S.; Hammel, I., Determining the persistence length of biopolymers and rod-like macromolecular assemblies from electron microscope images and deriving some of their mechanical properties. In *Microscopy: Science, Technology, Applications and Education*, Méndez-Vilas, A.; Díaz, J., Eds. 2010; Vol. 3, pp 1690-1695.
- 83) Shetty, A. M.; Wilkins, G. M. H.; Nanda, J.; Solomon, M. J., *J. Phys. Chem. C* **2009**, 17, 7129-7133.
- 84) Su, W.-F., Polymer Size and Polymer Solutions. In *Principles of Polymer Design and Synthesis*, Springer Berlin Heidelberg: Berlin, Heidelberg, 2013; pp 9-26.
- 85) Ebdon, J. R., *Polym. Int.* **1992**, 2, 207-208.
- 86) Striegel, A. M., *Chromatographia* **2016**, 15, 945-960.
- 87) Vanhee, S.; Rulkens, R.; Lehmann, U.; Rosenauer, C.; Schulze, M.; Köhler, W.; Wegner, G., *Macromolecules* **1996**, 15, 5136-5142.
- 88) Molina, R.; Gómez-Ruiz, S.; Montilla, F.; Salinas-Castillo, A.; Fernández-Arroyo, S.; Ramos, M. d. M.; Micol, V.; Mallavia, R., *Macromolecules* **2009**, 15, 5471-5477.
- 89) Cotts, P. M.; Swager, T. M.; Zhou, Q., *Macromolecules* **1996**, 23, 7323-7328.
- 90) Gao, B.; Wang, M.; Cheng, Y.; Wang, L.; Jing, X.; Wang, F., *J. Am. Chem. Soc.* **2008**, 26, 8297-8306.

- 91) Collison, C. J.; Rothberg, L. J.; Treemaneeekarn, V.; Li, Y., *Macromolecules* **2001**, 7, 2346-2352.
- 92) Dudenko, D.; Kiersnowski, A.; Shu, J.; Pisula, W.; Sebastiani, D.; Spiess, H. W.; Hansen, M. R., *Angew. Chem. Int. Ed.* **2012**, 44, 11068-11072.
- 93) Chen, L.; Hernandez, Y.; Feng, X.; Müllen, K., *Angew. Chem. Int. Ed.* **2012**, 31, 7640-7654.
- 94) Lee, J.; Kalin, A. J.; Yuan, T.; Al-Hashimi, M.; Fang, L., *Chem. Sci.* **2017**, 4, 2503-2521.
- 95) Teo, Y. C.; Lai, H. W. H.; Xia, Y., *Chem. Eur. J.* **2017**, 57, 14101-14112.
- 96) Guo, Y.; Li, Y.; Awartani, O.; Han, H.; Zhao, J.; Ade, H.; Yan, H.; Zhao, D., *Adv. Mater.* **2017**, 26, 1700309-n/a.
- 97) Wang, Y.; Yan, Z.; Guo, H.; Uddin, M. A.; Ling, S.; Zhou, X.; Su, H.; Dai, J.; Woo, H. Y.; Guo, X., *Angew. Chem. Int. Ed.* **2017**, 48, 15304-15308.
- 98) Wang, L.; Cai, D.; Yin, Z.; Tang, C.; Chen, S.-C.; Zheng, Q., *Polym. Chem.* **2014**, 23, 6847-6856.
- 99) Yang, M.; Lau, T.-K.; Xiao, S.; Gao, J.; Wang, W.; Lu, X.; Zhang, S.; Wu, J.; Zhan, C.; You, W., *ACS Appl. Mater. Interfaces* **2017**, 40, 35159-35168.
- 100) Bunz, U. H. F., *Acc. Chem. Res.* **2015**, 6, 1676-1686.
- 101) Endres, A. H.; Schaffroth, M.; Paulus, F.; Reiss, H.; Wadepohl, H.; Rominger, F.; Krämer, R.; Bunz, U. H. F., *J. Am. Chem. Soc.* **2016**, 6, 1792-1795.

- 102) Krüger, J.; García, F.; Eisenhut, F.; Skidin, D.; Alonso, J. M.; Guitián, E.; Pérez, D.; Cuniberti, G.; Moresco, F.; Peña, D., *Angew. Chem. Int. Ed.* **2017**, 39, 11945-11948.
- 103) Xie, J.; Rui, X.; Gu, P.; Wu, J.; Xu, Z. J.; Yan, Q.; Zhang, Q., *ACS Appl. Mater. Interfaces* **2016**, 26, 16932-16938.
- 104) Gu, P.-Y.; Zhou, F.; Gao, J.; Li, G.; Wang, C.; Xu, Q.-F.; Zhang, Q.; Lu, J.-M., *J. Am. Chem. Soc.* **2013**, 38, 14086-14089.
- 105) Grimme, J.; Kreyenschmidt, M.; Uckert, F.; Müllen, K.; Scherf, U., *Adv. Mater.* **1995**, 3, 292-295.
- 106) Müllen, K.; Wegner, G., *Electronic Materials: The Oligomer Approach*. Weinheim; New York: Wiley-VCH: **1998**.
- 107) Lawrence, J.; Goto, E.; Ren, J. M.; McDearmon, B.; Kim, D. S.; Ochiai, Y.; Clark, P. G.; Laitar, D.; Higashihara, T.; Hawker, C. J., *J. Am. Chem. Soc.* **2017**, 39, 13735-13739.
- 108) Narita, A.; Wang, X.-Y.; Feng, X.; Mullen, K., *Chem. Soc. Rev.* **2015**, 18, 6616-6643.
- 109) Jacobse, P. H.; Moret, M.-E.; Klein Gebbink, R. J. M.; Swart, I., *Synlett* **2017**, 19, 2509-2516.
- 110) Tsuda, A.; Osuka, A., *Science* **2001**, 5527, 79-82.
- 111) Wu, J.; Pisula, W.; Müllen, K., *Chem. Rev.* **2007**, 3, 718-747.
- 112) Roznyatovskiy, V. V.; Lee, C.-H.; Sessler, J. L., *Chem. Soc. Rev.* **2013**, 5, 1921-1933.

- 113) Stępień, M.; Gońka, E.; Żyła, M.; Sprutta, N., *Chem. Rev.* **2017**, 4, 3479-3716.
- 114) Grimme, J.; Scherf, U., *Macromol. Chem. Phys.* **1996**, 7, 2297-2304.
- 115) Xu, C.; Wakamiya, A.; Yamaguchi, S., *J. Am. Chem. Soc.* **2005**, 6, 1638-1639.
- 116) Vaid, T. P.; Easton, M. E.; Rogers, R. D., *Synth. Met.* **2017**, Supplement C, 44-50.
- 117) Bouchard, J.; Wakim, S.; Leclerc, M., *J. Org. Chem.* **2004**, 17, 5705-5711.
- 118) Zheng, T.; Cai, Z.; Ho-Wu, R.; Yau, S. H.; Shaparov, V.; Goodson, T.; Yu, L., *J. Am. Chem. Soc.* **2016**, 3, 868-875.
- 119) Sirringhaus, H.; Friend, R.; Wang, C.; Leuninger, J.; Mullen, K., *J. Mater. Chem.* **1999**, 9, 2095-2101.
- 120) Gao, P.; Feng, X.; Yang, X.; Enkelmann, V.; Baumgarten, M.; Müllen, K., *J. Org. Chem.* **2008**, 23, 9207-9213.
- 121) Zhong, Y.; Kumar, B.; Oh, S.; Trinh, M. T.; Wu, Y.; Elbert, K.; Li, P.; Zhu, X.; Xiao, S.; Ng, F.; Steigerwald, M. L.; Nuckolls, C., *J. Am. Chem. Soc.* **2014**, 22, 8122-8130.
- 122) Sisto, T. J.; Zhong, Y.; Zhang, B.; Trinh, M. T.; Miyata, K.; Zhong, X.; Zhu, X. Y.; Steigerwald, M. L.; Ng, F.; Nuckolls, C., *J. Am. Chem. Soc.* **2017**, 16, 5648-5651.
- 123) Zhong, Y.; Sisto, T. J.; Zhang, B.; Miyata, K.; Zhu, X. Y.; Steigerwald, M. L.; Ng, F.; Nuckolls, C., *J. Am. Chem. Soc.* **2017**, 16, 5644-5647.

- 124) Cai, Z.; Vázquez, R. J.; Zhao, D.; Li, L.; Lo, W.-y.; Zhang, N.; Wu, Q.; Keller, B.; Eshun, A.; Abeyasinghe, N.; Banaszak-Holl, H.; Goodson, T.; Yu, L., *Chem. Mater.* **2017**, 16, 6726-6732.
- 125) Grzybowski, M.; Skonieczny, K.; Butenschön, H.; Gryko, D. T., *Angew. Chem. Int. Ed.* **2013**, 38, 9900-9930.
- 126) Mallory, F. B.; Regan, C. K.; Bohlen, J. M.; Mallory, C. W.; Bohlen, A. A.; Carroll, P. J., *J. Org. Chem.* **2015**, 1, 8-17.
- 127) Mallory, F. B.; Butler, K. E.; Evans, A. C.; Brondyke, E. J.; Mallory, C. W.; Yang, C.; Ellenstein, A., *J. Am. Chem. Soc.* **1997**, 9, 2119-2124.
- 128) Yang, W.; Chalifoux, W. A., *Synlett* **2017**, 06, 625-632.
- 129) Goldfinger, M. B.; Crawford, K. B.; Swager, T. M., *J. Am. Chem. Soc.* **1997**, 20, 4578-4593.
- 130) Yang, W.; Monteiro, J. H. S. K.; de Bettencourt-Dias, A.; Catalano, V. J.; Chalifoux, W. A., *Angew. Chem. Int. Ed.* **2016**, 35, 10427-10430.
- 131) Yang, W.; Monteiro, J. H. S. K.; de Bettencourt-Dias, A.; Chalifoux, W. A., *Can. J. Chem.* **2016**, 4, 341-345.
- 132) Wakim, S.; Bouchard, J.; Blouin, N.; Michaud, A.; Leclerc, M., *Org. Lett.* **2004**, 19, 3413-3416.
- 133) Povie, G.; Segawa, Y.; Nishihara, T.; Miyauchi, Y.; Itami, K., *Science* **2017**, 6334, 172-175.
- 134) Wetzal, C.; Brier, E.; Vogt, A.; Mishra, A.; Mena-Osteritz, E.; Bäuerle, P., *Angew. Chem. Int. Ed.* **2015**, 42, 12334-12338.

- 135) Murayama, K.; Shibata, Y.; Sugiyama, H.; Uekusa, H.; Tanaka, K., *J. Org. Chem.* **2017**, 2, 1136-1144.
- 136) Katz, T. J.; Rothchild, R., *J. Am. Chem. Soc.* **1976**, 9, 2519-2526.
- 137) Iuliano, A.; Piccioli, P.; Fabbri, D., *Org. Lett.* **2004**, 21, 3711-3714.
- 138) Wang, Y.; Guo, H.; Ling, S.; Arrechea-Marcos, I.; Wang, Y.; López Navarrete, J. T.; Ortiz, R. P.; Guo, X., *Angew. Chem. Int. Ed.* **2017**, 33, 9924-9929.
- 139) Yao, Y.; Tour, J. M., *Macromolecules* **1999**, 8, 2455-2461.
- 140) Lamba, J. J. S.; Tour, J. M., *J. Am. Chem. Soc.* **1994**, 26, 11723-11736.
- 141) Yuan, Y.; Giri, G.; Ayzner, A. L.; Zoombelt, A. P.; Mannsfeld, S. C. B.; Chen, J.; Nordlund, D.; Toney, M. F.; Huang, J.; Bao, Z., *Nat. Commun.* **2014**, 3005.
- 142) Mas-Torrent, M.; Rovira, C., *Chem. Soc. Rev.* **2008**, 4, 827-838.
- 143) Zhao, W.; Qian, D.; Zhang, S.; Li, S.; Inganäs, O.; Gao, F.; Hou, J., *Adv. Mater.* **2016**, 23, 4734-4739.
- 144) Lloyd, M. T.; Anthony, J. E.; Malliaras, G. G., *Mater. Today* **2007**, 11, 34-41.
- 145) Chen, W.; Zhang, Q., *J. Mater. Chem. C* **2017**, 6, 1275-1302.
- 146) Nielsen, C. B.; Holliday, S.; Chen, H.-Y.; Cryer, S. J.; McCulloch, I., *Acc. Chem. Res.* **2015**, 11, 2803-2812.
- 147) Zhang, G.; Zhao, J.; Chow, P. C. Y.; Jiang, K.; Zhang, J.; Zhu, Z.; Zhang, J.; Huang, F.; Yan, H., *Chem. Rev.* **2018**, 7, 3447-3507.
- 148) Mateo-Alonso, A., *Chem. Soc. Rev.* **2014**, 17, 6311-6324.
- 149) Yang, W.; Lucotti, A.; Tommasini, M.; Chalifoux, W. A., *J. Am. Chem. Soc.* **2016**, 29, 9137-9144.

- 150) Lee, J.; Li, H.; Kalin, A. J.; Yuan, T.; Wang, C.; Olson, T.; Li, H.; Fang, L., *Angew. Chem. Int. Ed.* **2017**, 44, 13727-13731.
- 151) Lee, J.; Kalin, A. J.; Wang, C.; Early, J. T.; Al-Hashimi, M.; Fang, L., *Polym. Chem.* **2018**, 13, 1603-1609.
- 152) Kumar, S.; Saravanan, S.; Reuben, P.; Kumar, A., *J. Heterocycl. Chem.* **2005**, 7, 1345-1355.
- 153) Biet, T.; Martin, K.; Hankache, J.; Hellou, N.; Hauser, A.; Bürgi, T.; Vanthuyne, N.; Aharon, T.; Caricato, M.; Crassous, J.; Avarvari, N., *Chem. Eur. J.* **2017**, 2, 437-446.
- 154) Zhang, Z.-G.; Liu, Y.-L.; Yang, Y.; Hou, K.; Peng, B.; Zhao, G.; Zhang, M.; Guo, X.; Kang, E.-T.; Li, Y., *Macromolecules* **2010**, 22, 9376-9383.
- 155) Li, Y.; Wu, Y.; Gardner, S.; Ong, B. S., *Adv. Mater.* **2005**, 7, 849-853.
- 156) Pilgram, K.; Zupan, M.; Skiles, R., *J. Heterocycl. Chem.* **1970**, 3, 629-633.
- 157) Arnold, F. E.; Van Deusen, R. L., *Macromolecules* **1969**, 5, 497-502.
- 158) Schluter, A.-D., *Adv. Mater.* **1991**, 282-291.
- 159) Plumhof, J. D.; Stoferle, T.; Mai, L.; Scherf, U.; Mahrt, R. F., *Nat. Mater.* **2014**, 3, 247-52.
- 160) Richard G. Jones, J. K., Robert Stepto, Edward S. Wilks Michael Hess, Tatsuki Kitayama, W. Val Metanomski, *Compendium of polymer terminology and nomenclature IUPAC recommendations 2008*. The Royal Society of Chemistry: Cambridge, UK, **2008**.
- 161) Liu, S.; Jin, Z.; Teo, Y. C.; Xia, Y., *J. Am. Chem. Soc.* **2014**, 50, 17434-7.

- 162) Carta, M.; Malpass-Evans, R.; Croad, M.; Rogan, Y.; Jansen, J. C.; Bernardo, P.; Bazzarelli, F.; McKeown, N. B., *Science* **2013**, 6117, 303-307.
- 163) Grozema, F. C.; van Duijnen, P. T.; Berlin, Y. A.; Ratner, M. A.; Siebbeles, L. D. A., *J. Phys. Chem. B* **2002**, 32, 7791-7795.
- 164) Dell, E. J.; Capozzi, B.; DuBay, K. H.; Berkelbach, T. C.; Moreno, J. R.; Reichman, D. R.; Venkataraman, L.; Campos, L. M., *J. Am. Chem. Soc.* **2013**, 32, 11724-7.
- 165) Son, Y.-W.; Cohen, M. L.; Louie, S. G., *Nature* **2006**, 7117, 347-349.
- 166) Li, X.; Wang, X.; Zhang, L.; Lee, S.; Dai, H., *Science* **2008**, 5867, 1229-1232.
- 167) Chen, Z. H.; Amara, J. P.; Thomas, S. W.; Swager, T. M., *Macromolecules* **2006**, 9, 3202-3209.
- 168) Schluter, A. D.; Loffler, M.; Enkelmann, V., *Nature* **1994**, 6474, 831-834.
- 169) Yang, X.; Dou, X.; Rouhanipour, A.; Zhi, L.; Räder, H. J.; Müllen, K., *J. Am. Chem. Soc.* **2008**, 13, 4216-4217.
- 170) Yao, Y. X.; Tour, J. M., *Macromolecules* **1999**, 8, 2455-2461.
- 171) Grubbs, R. H.; Miller, S. J.; Fu, G. C., *Acc. Chem. Res.* **1995**, 11, 446-452.
- 172) Donohoe, T. J.; Orr, A. J.; Bingham, M., *Angew. Chem. Int. Ed.* **2006**, 17, 2664-2670.
- 173) Collins, S. K.; Grandbois, A.; Vachon, M. P.; Côté, J., *Angew. Chem. Int. Ed.* **2006**, 18, 2923-2926.
- 174) Vermeulen, N. A.; Karagiari, O.; Sarjeant, A. A.; Stearn, C. L.; Hupp, J. T.; Fahra, O. K.; Stoddart, J. F., *J. Am. Chem. Soc.* **2013**, 14916-14919.

- 175) Trnka, T. M.; Grubbs, R. H., *Acc. Chem. Res.* **2001**, 1, 18-29.
- 176) Morin, J. F.; Leclerc, M., *Macromolecules* **2001**, 14, 4680-4682.
- 177) Blouin, N.; Leclerc, M., *Acc. Chem. Res.* **2008**, 9, 1110-1119.
- 178) Zhou, Y.; Kurosawa, T.; Ma, W.; Guo, Y.; Fang, L.; Vandewal, K.; Diao, Y.; Wang, C.; Yan, Q.; Reinspach, J.; Mei, J.; Appleton, A. L.; Koleilat, G. I.; Gao, Y.; Mannsfeld, S. C. B.; Salleo, A.; Ade, H.; Zhao, D.; Bao, Z., *Adv. Mater.* **2014**, 22, 3767-3772.
- 179) Langhals, H., *Helv. Chim. Acta* **2005**, 6, 1309-1343.
- 180) Li, J.; Grimsdale, A. C., *Chem. Soc. Rev.* **2010**, 7, 2399-410.
- 181) Park, S. H.; Roy, A.; Beaupré, S.; Cho, S.; Coates, N.; Moon, J. S.; Moses, D.; Leclerc, M.; Lee, K.; Heeger, A. J., *Nat. Photonics* **2009**, 297.
- 182) Zou, Y.; Ye, T.; Ma, D.; Qin, J.; Yang, C., *J. Mater. Chem.* **2012**, 44, 23485-23491.
- 183) Hudson, Z. M.; Wang, Z.; Helander, M. G.; Lu, Z. H.; Wang, S., *Adv. Mater.* **2012**, 21, 2922-8.
- 184) Gierschner, J.; Cornil, J.; Egelhaaf, H. J., *Adv. Mater.* **2007**, 2, 173-191.
- 185) Wei-ya, Z.; Si-shen, X.; Sheng-fa, Q.; Gang, W.; Lu-xi, Q., *J. Phys.: Condens. Matter* **1996**, 31, 5793.
- 186) Roex, H.; Adriaensens, P.; Vanderzande, D.; Gelan, J., *Macromolecules* **2003**, 15, 5613-5622.
- 187) Chen, T.-A.; Wu, X.; Rieke, R. D., *J. Am. Chem. Soc.* **1995**, 1, 233-244.

- 188) Aiyar, A. R.; Hong, J.-I.; Nambiar, R.; Collard, D. M.; Reichmanis, E., *Adv. Funct. Mater.* **2011**, 14, 2652-2659.
- 189) Kim, K.; Regan, W.; Geng, B.; Alemán, B.; Kessler, B. M.; Wang, F.; Crommie, M. F.; Zettl, A., *Phys. Status Solidi Rapid Res. Lett.* **2010**, 11, 302-304.
- 190) Yamamoto, T.; Watanabe, K.; Hernández, E., Mechanical Properties, Thermal Stability and Heat Transport in Carbon Nanotubes. In *Carbon Nanotubes*, Jorio, A.; Dresselhaus, G.; Dresselhaus, M., Eds. Springer Berlin Heidelberg: 2008; Vol. 111, pp 165-195.
- 191) McGann, J. P.; Zhong, M.; Kim, E. K.; Natesakhawat, S.; Jaroniec, M.; Whitacre, J. F.; Matyjaszewski, K.; Kowalewski, T., *Macromol. Chem. Phys.* **2012**, 10-11, 1078-1090.
- 192) Bajaj, P.; Roopanwal, A. K., *J. Macromol. Sci., Polym. Rev.* **1997**, 1, 97-147.
- 193) Zheng, Y. B.; Pathem, B. K.; Hohman, J. N.; Thomas, J. C.; Kim, M.; Weiss, P. S., *Adv. Mater.* **2013**, 3, 302-312.
- 194) den Boer, D.; Li, M.; Habets, T.; Iavicoli, P.; Rowan, A. E.; Nolte, R. J. M.; Speller, S.; Amabilino, D. B.; De Feyter, S.; Elemans, J. A. A. W., *Nat. Chem.* **2013**, 7, 621-627.
- 195) Chen, C.; Dugan, T. R.; Brennessel, W. W.; Weix, D. J.; Holland, P. L., *J. Am. Chem. Soc.* **2014**, 3, 945-955.
- 196) Jiang, Z.; Li, X.; Strzalka, J.; Sprung, M.; Sun, T.; Sandy, A. R.; Narayanan, S.; Lee, D. R.; Wang, J., *J. Synchrotron Radiat.* **2012**, 4, 627-636.
- 197) Zhu, C.; Fang, L., *Macromol. Rapid. Commun.* **2018**, 2, 1700241.

- 198) Kallinger, C.; Hilmer, M.; Haugeneder, A.; Perner, M.; Spirkl, W.; Lemmer, U.; Feldmann, J.; Scherf, U.; Müllen, K.; Gombert, A.; Wittwer, V., *Adv. Mater.* **1998**, 12, 920-923.
- 199) Wu, J.; Rui, X.; Long, G.; Chen, W.; Yan, Q.; Zhang, Q., *Angew. Chem. Int. Ed.* **2015**, 25, 7354-7358.
- 200) Wu, J.; Rui, X.; Wang, C.; Pei, W.-B.; Lau, R.; Yan, Q.; Zhang, Q., *Adv. Energy Mater.* **2015**, 9, 1402189.
- 201) Wang, S.; Sun, H.; Ail, U.; Vagin, M.; Persson, P. O.; Andreasen, J. W.; Thiel, W.; Berggren, M.; Crispin, X.; Fazzi, D.; Fabiano, S., *Adv. Mater.* **2016**, 48, 10764-10771.
- 202) Cheng, Y.-J.; Yang, S.-H.; Hsu, C.-S., *Chem. Rev.* **2009**, 11, 5868-5923.
- 203) Lu, L.; Zheng, T.; Wu, Q.; Schneider, A. M.; Zhao, D.; Yu, L., *Chem. Rev.* **2015**, 23, 12666-12731.
- 204) Bheemireddy, S. R.; Hautzinger, M. P.; Li, T.; Lee, B.; Plunkett, K. N., *J. Am. Chem. Soc.* **2017**, 16, 5801-5807.
- 205) Dierschke, F.; Grimsdale, A. C.; Müllen, K., *Macromol. Chem. Phys.* **2004**, 9, 1147-1154.
- 206) Zhai, L.; Shukla, R.; Wadumethrige, S. H.; Rathore, R., *J. Org. Chem.* **2010**, 14, 4748-4760.
- 207) Hayashi, R.; Cook, G. R., *Org. Lett.* **2007**, 7, 1311-1314.
- 208) Bandini, M.; Tragni, M.; Umani-Ronchi, A., *Adv. Synth. Cat.* **2009**, 14-15, 2521-2524.

- 209) Hollingsworth, W. R.; Lee, J.; Fang, L.; Ayzner, A. L., *ACS Energy Lett.* **2017**, 9, 2096-2102.
- 210) Dutta, T.; Woody, K. B.; Parkin, S. R.; Watson, M. D.; Gierschner, J., *J. Am. Chem. Soc.* **2009**, 47, 17321-17327.
- 211) Li, W.; Yang, L.; Tumbleston, J. R.; Yan, L.; Ade, H.; You, W., *Adv. Mater.* **2014**, 26, 4456-4462.
- 212) Walzer, K.; Maennig, B.; Pfeiffer, M.; Leo, K., *Chem. Rev.* **2007**, 4, 1233-1271.
- 213) Pingel, P.; Neher, D., *Phys. Rev. B* **2013**, 11, 115209.
- 214) Goetz, K. P.; Vermeulen, D.; Payne, M. E.; Kloc, C.; McNeil, L. E.; Jurchescu, O. D., *J. Mater. Chem. C* **2014**, 17, 3065-3076.
- 215) Sosorev, A. Y.; Paraschuk, D. Y., *Isr. J. Chem.* **2014**, 5-6, 650-673.
- 216) Hamidi-Sakr, A.; Biniek, L.; Bantignies, J. L.; Maurin, D.; Herrmann, L.; Leclerc, N.; Lévêque, P.; Vijayakumar, V.; Zimmermann, N.; Brinkmann, M., *Adv. Funct. Mater.* **2017**, 25.
- 217) Müller, L.; Nanova, D.; Glaser, T.; Beck, S.; Pucci, A.; Kast, A. K.; Schröder, R. R.; Mankel, E.; Pingel, P.; Neher, D.; Kowalsky, W.; Lovrincic, R., *Chem. Mater.* **2016**, 12, 4432-4439.
- 218) Oh, J. H.; Lee, W.-Y.; Noe, T.; Chen, W.-C.; Könemann, M.; Bao, Z., *J. Am. Chem. Soc.* **2011**, 12, 4204-4207.
- 219) Yoon, K.-J.; Park, J. S.; Lee, S.-J.; Song, M.; Shin, I. A.; Lee, J. W.; Gal, Y.-S.; Jin, S.-H., *J. Polym. Sci. A Polym. Chem.* **2008**, 20, 6762-6769.

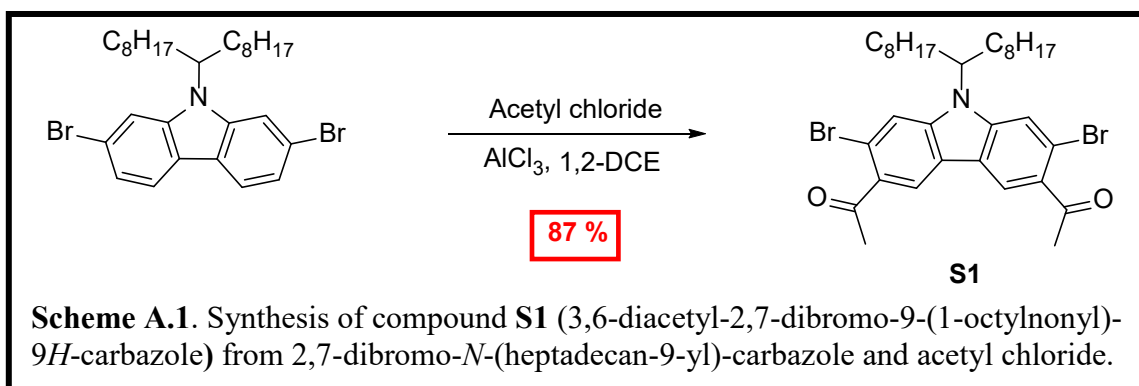
- 220) Klauk, H.; Halik, M.; Zschieschang, U.; Schmid, G.; Radlik, W.; Weber, W., *J. Appl. Phys.* **2002**, 9, 5259-5263.
- 221) Geerts, Y.; Klärner, G.; Müllen, K., Hydrocarbon Oligomers. In *Electronic Materials: The Oligomer Approach*, Wiley-VCH Verlag GmbH: 2007; pp 48-52.
- 222) Anthony, J. E., *Angew. Chem. Int. Ed.* **2008**, 3, 452-483.
- 223) Xue, G.; Fan, C.; Wu, J.; Liu, S.; Liu, Y.; Chen, H.; Xin, H. L.; Li, H., *Mater. Horiz.* **2015**, 3, 344-349.
- 224) Okamoto, H.; Kawasaki, N.; Kaji, Y.; Kubozono, Y.; Fujiwara, A.; Yamaji, M., *J. Am. Chem. Soc.* **2008**, 32, 10470-10471.
- 225) Kaji, Y.; Kawasaki, N.; Lee, X.; Okamoto, H.; Sugawara, Y.; Oikawa, S.; Ito, A.; Okazaki, H.; Yokoya, T.; Fujiwara, A.; Kubozono, Y., *Appl. Phys. Lett.* **2009**, 18, 183302.
- 226) Mallory, F. B.; Mallory, C. W.; Regan, C. K.; Aspden, R. J.; Ricks, A. B.; Racowski, J. M.; Nash, A. I.; Gibbons, A. V.; Carroll, P. J.; Bohen, J. M., *J. Org. Chem.* **2013**, 5, 2040-2045.
- 227) Saito, M.; Nakano, Y.; Nakamura, H.; Kondo, H. U.S. Patent 0,220,884, **2011**.
- 228) Rui, U.; Satoshi, M.; Yutaka, N., *Chem. Lett.* **2012**, 3, 215-217.
- 229) Chen, T. A.; Lee, T. J.; Lin, M. Y.; Sohel, S. M. A.; Diau, E. W. G.; Lush, S. F.; Liu, R. S., *Chem. Eur. J.* **2010**, 6, 1826-1833.
- 230) Haire, B. T.; Heard, K. W. J.; Little, M. S.; Parry, A. V. S.; Raftery, J.; Quayle, P.; Yeates, S. G., *Chem. Eur. J.* **2015**, 28, 9970-9974.

- 231) Kentaroh, K.; Takuya, K.; Masashi, N.; Yutaka, I.; Yoshio, A.; Fumitoshi, K., *Chem. Lett.* **2011**, 3, 300-302.
- 232) Chmil, K.; Scherf, U., *Acta Polym.* **1997**, 5-6, 208-211.
- 233) Guo, L.; Li, K. F.; Zhang, X.; Cheah, K. W.; Wong, M. S., *Angew. Chem. Int. Ed.* **2016**, 36, 10639-10644.
- 234) Wang, Y.; Guo, H.; Ling, S.; Arrechea-Marcos, I.; Wang, Y.; Lopez Navarrete, J. T.; Ortiz, R. P.; Guo, X., *Angew. Chem. Int. Ed.* **2017**, 33, 9924-9929.
- 235) Zhu, C.; Mu, A. U.; Lin, Y.-H.; Guo, Z.-H.; Yuan, T.; Wheeler, S. E.; Fang, L., *Org. Lett.* **2016**, 24, 6332-6335.
- 236) Rieger, R.; Müllen, K., *J. Phys. Org. Chem.* **2010**, 4, 315-325.
- 237) Clar, E., The Annellation Principle. In *Polycyclic Hydrocarbons: Volume 1*, Springer Berlin Heidelberg: Berlin, Heidelberg, 1964; pp 40-69.
- 238) Meier, H.; Stalmach, U.; Kolshorn, H., *Acta Polym.* **1997**, 9, 379-384.
- 239) Grimme, J.; Kreyenschmidt, M.; Uckert, F.; Müllen, K.; Scherf, U., *Adv. Mater.* **1995**, 3, 292-295.
- 240) Ober, C. K.; Cheng, S. Z. D.; Hammond, P. T.; Muthukumar, M.; Reichmanis, E.; Wooley, K. L.; Lodge, T. P., *Macromolecules* **2009**, 2, 465-471.
- 241) Krotzky, S.; Morchutt, C.; Vyas, V. S.; Lotsch, B. V.; Gutzler, R.; Kern, K., *J. Phys. Chem. C* **2016**, 8, 4403-4409.
- 242) Zhou, C.; Cui, Q.; McDowell, C.; Seifrid, M.; Chen, X.; Brédas, J.-L.; Wang, M.; Huang, F.; Bazan, G. C., *Angew. Chem. Int. Ed.* **2017**, 32, 9318-9321.
- 243) Kuss-Petermann, M.; Wenger, O. S., *J. Am. Chem. Soc.* **2016**, 4, 1349-1358.

- 244) Wang, L.; Pan, X.; Zhao, Y.; Chen, Y.; Zhang, W.; Tu, Y.; Zhang, Z.; Zhu, J.; Zhou, N.; Zhu, X., *Macromolecules* **2015**, 5, 1289-1295.
- 245) Dini, D.; Calvete, M. J. F.; Hanack, M., *Chem. Rev.* **2016**, 22, 13043-13233.

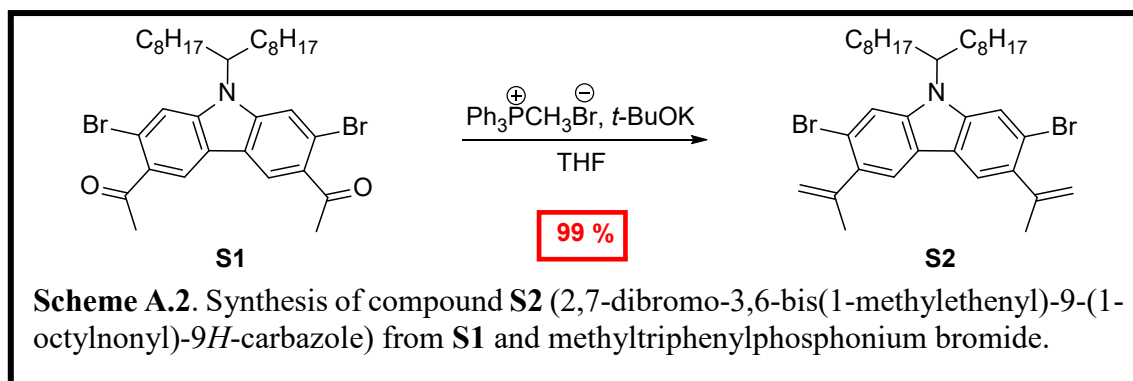
APPENDIX A

A. 1. Synthesis



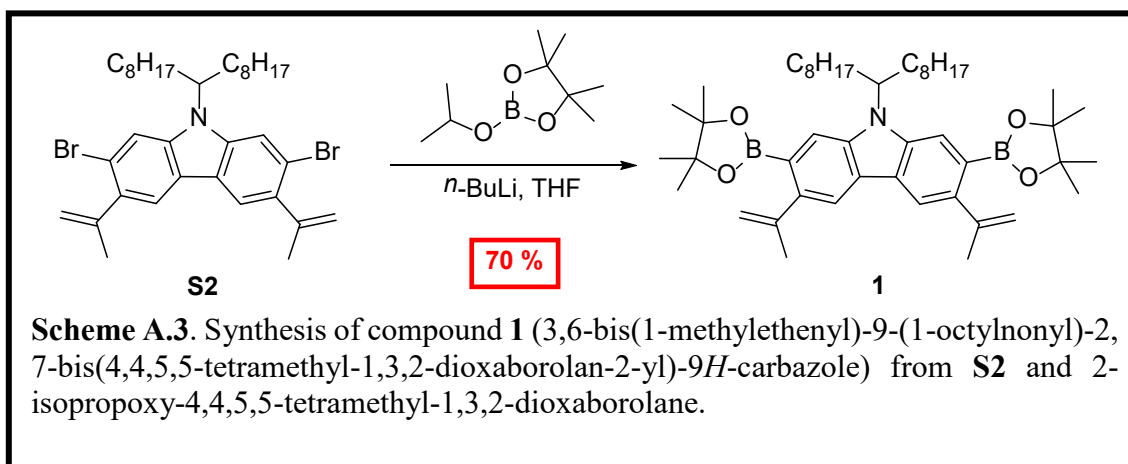
S1 (3,6-diacetyl-2,7-dibromo-9-(1-octylonyl)-9*H*-carbazole): To a mixture of 2,7-dibromo-9-(1-octylonyl)-9*H*-carbazole (4.0 g, 7.1 mmol), AlCl₃ (2.3 g, 17.0 mmol) in 75 mL of anhydrous 1,2-dichloroethane was added acetyl chloride (2.5 mL, 35.5 mmol) slowly under nitrogen atmosphere at room temperature. The reaction mixture was heated to 50 °C with a reflux condenser and stirred for 6 h. The mixture was cooled to 0°C, quenched with ice water, 2*N* HCl, and diluted with DCM. The solution was extracted with CH₂Cl₂ (3 × 30 mL), and the combined organic layer was dried over MgSO₄, filtered through Celite, and concentrated under reduced pressure. The residue was purified by flash column chromatography (SiO₂, hexane/EtOAc 98:2 to 82:18) to give product **S1** (4.0 g, 87%) as a light yellow solid. ¹H NMR (500 MHz, CDCl₃): δ 8.34 (s, 1H), 8.34 (s, 1H), 7.82 (s, 1H), 7.65 (s, 1H), 4.45 (septet, *J* = 5.0 Hz, 1H), 2.77 (s, 6H), 2.19 (m, 2H), 1.93 (m, 2H), 1.18 (m, 22H), 0.95 (m, 2H), 0.82 (t, *J* = 7.0 Hz, 6H). ¹³C NMR (125 MHz, CDCl₃): δ 200.1, 144.5, 141.1, 132.6, 132.5, 122.5, 121.0, 118.2, 117.5, 117.3, 115.1,

57.8, 33.6, 31.8, 30.5, 29.4, 29.2, 26.8, 22.7, 14.2. HR-MALDI: calcd for C₃₃H₄₆Br₂NO₂ [M+H]⁺ *m/z* = 648.1876; found *m/z* = 648.1907.



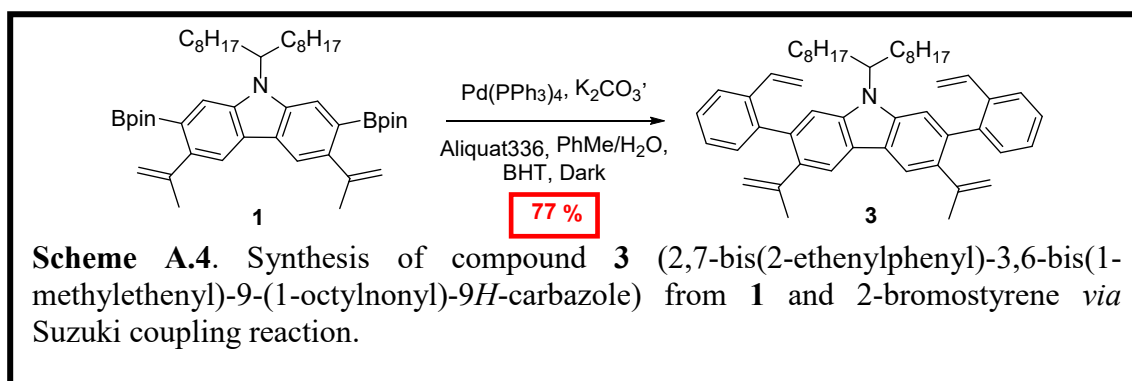
S2 (2,7-dibromo-3,6-bis(1-methylethenyl)-9-(1-octylnonyl)-9*H*-carbazole): To a mixture of methyltriphenylphosphonium bromide (9.4 g, 26.2 mmol) and 100 mL of anhydrous THF was added *t*-BuOK (2.8 g, 24.8 mmol) slowly under nitrogen atmosphere at room temperature. The solution turned light yellow. Compound **S1** (4.0 g, 6.2 mmol) was added into the solution. The mixture was stirred at reflux for 6 h. The reaction mixture was cooled to room temperature and poured into 20 mL of water. THF was removed under reduced pressure, and the residue was extracted with CH₂Cl₂ (3 × 30 mL). The combined organic layer was dried over MgSO₄, filtered through Celite, and concentrated under reduced pressure. The residue was purified by flash column chromatography (SiO₂, hexane) to give product **S2** (3.95 g, 99%) as a clear oil. ¹H NMR (500 MHz, CDCl₃): δ 7.88 (s, 1H), 7.85 (s, 1H), 7.74 (s, 1H), 7.57 (s, 1H), 5.29 (s, 2H), 5.03 (s, 2H), 4.40 (septet, *J* = 5.0 Hz, 1H), 2.20 (s & m, 8H), 1.91 (m, 2H), 1.16 (m, 22H), 1.03 (m, 2H), 0.84 (t, *J* = 7.0 Hz, 6H). ¹³C NMR (125 MHz, CDCl₃): δ 146.7, 142.2, 138.7, 135.7, 122.8, 121.3, 120.9, 120.7, 119.4, 118.9, 116.3, 115.4, 113.1, 57.1, 33.7, 31.9, 29.5, 29.4, 29.3, 26.9,

24.5, 22.8, 14.3. HR-MALDI: calcd for C₃₅H₅₀Br₂N [M+H]⁺ *m/z* = 644.2290; found *m/z* = 644.2261.



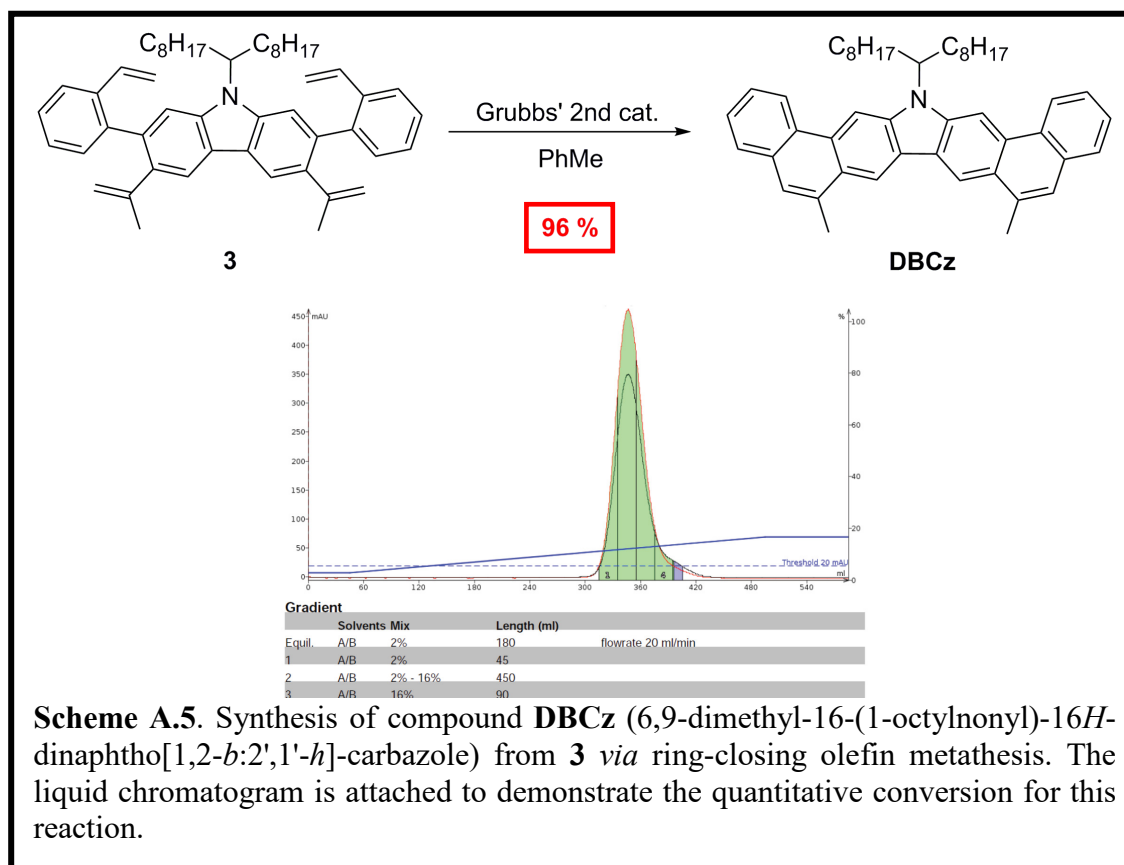
1 (3,6-bis(1-methylethenyl)-9-(1-octylnonyl)-2,7-bis(4,4,5,5-tetramethyl-1,3,2-dioxaborolan-2-yl)-9*H*-carbazole): Compound **S2** (3.0 g, 4.7 mmol) was dissolved in THF (60 mL) under a nitrogen atmosphere and cooled to -78 °C in acetone/dry ice bath. To the mixture was added *n*-BuLi (6.1 mL, 9.8 mmol, 1.6M in hexane) slowly. After 30 min stirring at -78 °C, 2-isopropoxy-4,4,5,5-tetramethyl-1,3,2-dioxaborolane (2.3 mL, 11.3 mmol) was added into the mixture. The mixture was warmed to room temperature and stirred at room temperature for 24 h. The reaction mixture was poured into 20 mL of water. THF was removed under reduced pressure, and the residue was extracted with CH₂Cl₂ (3 × 30 mL). The combined organic layer was dried over MgSO₄, filtered through Celite, and concentrated under reduced pressure. The residue was purified by flash column chromatography (SiO₂, hexane/CH₂Cl₂ 100:0 to 50:50) to give product **1** (2.4 g, 70%) as a white solid. ¹H NMR (500 MHz, CDCl₃): δ 7.96 (s, 1H), 7.94 (s, 1H), 7.81 (s, 1H), 7.65 (s, 1H), 5.11 (s, 2H), 4.95 (s, 2H), 4.59 (septet, *J* = 5.0 Hz, 1H), 2.25 (s & m, 8H), 1.91

(m, 2H), 1.37 (s, 24H), 1.14 (m, 22H) 0.83 (t, $J = 7.0$ Hz, 1H). ^{13}C NMR (125 MHz, CDCl_3): δ 148.3, 141.3, 139.9, 138.0, 126.1, 125.1, 123.7, 119.2, 119.0, 117.6, 115.0, 113.9, 83.7, 56.5, 34.1, 31.9, 29.7, 29.5, 29.4, 26.9, 25.3, 24.9, 22.8, 14.2. HR-MALDI: calcd for $\text{C}_{47}\text{H}_{74}\text{B}_2\text{NO}_4$ $[M+H]^+$ $m/z = 738.5804$; found $m/z = 738.5804$.



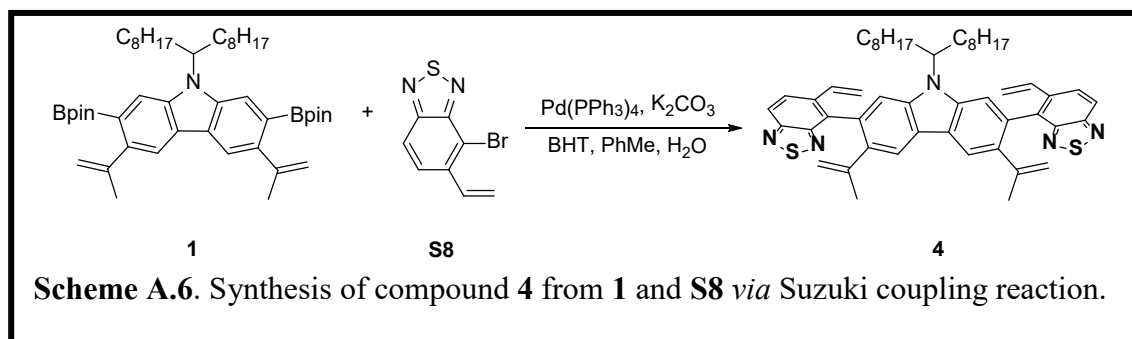
3 (2,7-bis(2-ethenylphenyl)-3,6-bis(1-methylethenyl)-9-(1-octylonyl)-9*H*-carbazole): To a mixture of compound **1** (0.30 g, 0.40 mmol), K_2CO_3 (0.33g, 2.40 mmol), aliquat 336 (0.05 mL, 0.10 mmol), several crystals of 2,6-di-*t*-butyl-4-methylphenol (BHT), and 2-bromostyrene (0.13 mL, 0.96 mmol) in degassed toluene (4 mL) and water (0.8 mL) was added $\text{Pd}(\text{PPh}_3)_4$ (46 mg, 10 mol%) under nitrogen atmosphere. The reaction mixture was stirred at 100 °C for 24 h. After being cooled to room temperature, the reaction mixture was concentrated under reduced pressure, and the residue was extracted with DCM (3×10 mL). The combined organic layer was dried over MgSO_4 , filtered through Celite, and concentrated under reduced pressure. The residue was purified by flash column chromatography (SiO_2 , hexane). The product was further purified by preparative GPC to give product **3** (0.21 g, 77 %) as a light yellow sticky oil. ^1H NMR (500 MHz, CDCl_3): δ 8.08 (s, 1H), 8.05(s, 1H), 7.68 (d, $J = 7.5$ Hz, 2H), 7.37 (m, 4H), 7.30 (m, 3H),

7.15 (s, 1H), 6.59 (m, 2H), 5.66 (d, $J = 17.5$ Hz, 2H), 5.08 (s, 2H), 5.02 (s, 2H), 4.93 (s, 2H), 4.44 (septet, $J = 5.0$ Hz, 1H), 2.18 (m, 2H), 1.79 (m, 2H), 1.75 (s, 6H), 1.18 (m, 22H), 1.03 (m, 2H), 0.82 (t, $J = 7.0$ Hz, 1H). ^{13}C NMR (125 MHz, CDCl_3): δ 146.7, 142.1, 141.9, 141.5, 138.0, 136.4, 136.3, 136.1, 136.0, 135.8, 134.8, 131.0, 127.3, 127.1, 125.2, 125.0, 122.9, 121.5, 120.2, 119.9, 115.7, 114.2, 111.6, 55.7, 33.8, 31.9, 29.6, 29.5, 29.3, 27.1, 26.9, 24.1, 22.8, 14.2. HR-MALDI: calcd for $\text{C}_{51}\text{H}_{64}\text{N}$ [$M+\text{H}$] $^+$ $m/z = 690.5039$; found $m/z = 690.5065$.



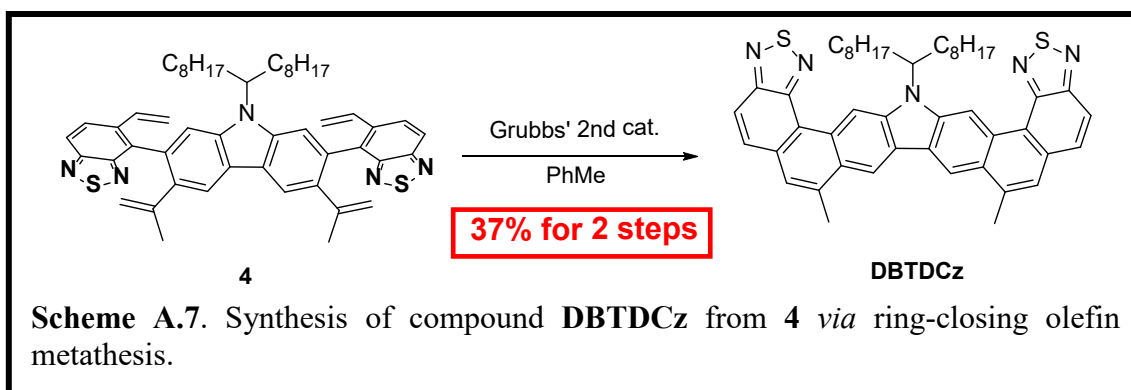
DBCz (6,9-dimethyl-16-(1-octylonyl)-16*H*-dinaphtho[1,2-*b*:2',1'-*h*]-carbazole): The mixture of compound **3** (100 mg, 0.14 mmol) and Grubbs' 2nd generation catalyst (3 mg, 3 mol%) in degassed toluene (5 mL) was stirred at reflux under N_2 . Immediately, another portion of Grubbs' 2nd generation catalyst (9 mg, 7 mol%) in degassed toluene (3 mL) was

added for 4 h using syringe pump. After that, the reaction mixture was stirred for an additional 2 h at reflux temperature. After being cooled to room temperature, the reaction mixture was concentrated under reduced pressure, and the residue was purified by flash column chromatography (SiO₂, hexane:CH₂Cl₂ 98:2 to 84:16) to give product **DBCz** (85 mg, 96 %) as a yellow solid. ¹H NMR (500 MHz, CDCl₃): δ 8.97 (s, 1H), 8.94 (s, 1H), 8.86 (s, 1H), 8.82 (d, *J* = 8.0 Hz, 1H), 8.77 (d, *J* = 8.0 Hz, 1H), 8.67 (s, 1H), 7.86 (d, *J* = 7.5 Hz, 2H), 7.65 (m, 2H), 7.60 (t, *J* = 7.5 Hz, 2H), 7.54 (s, 2H), 4.98 (septet, *J* = 5.0 Hz, 1H), 2.98 (s, 6H), 2.65 (m, 2H), 2.16 (m, 2H), 1.33 (m, 4H), 1.26 (m, 2H), 1.07 (m, 18H), 0.72 (t, *J* = 7.0 Hz, 6H). ¹³C NMR (125 MHz, CDCl₃): δ 143.7, 140.1, 133.2, 132.5, 130.4, 129.9, 128.1, 126.6, 126.0, 125.5, 124.9, 124.2, 124.1, 123.8, 122.7, 116.4, 116.3, 103.4, 100.7, 56.8, 33.8, 30.2, 29.9, 29.7, 29.5, 29.3, 27.1, 22.7, 20.8, 14.1. HR-MALDI: calcd for C₄₇H₅₆N [M+H]⁺ *m/z* = 634.4413; found *m/z* = 634.4427.

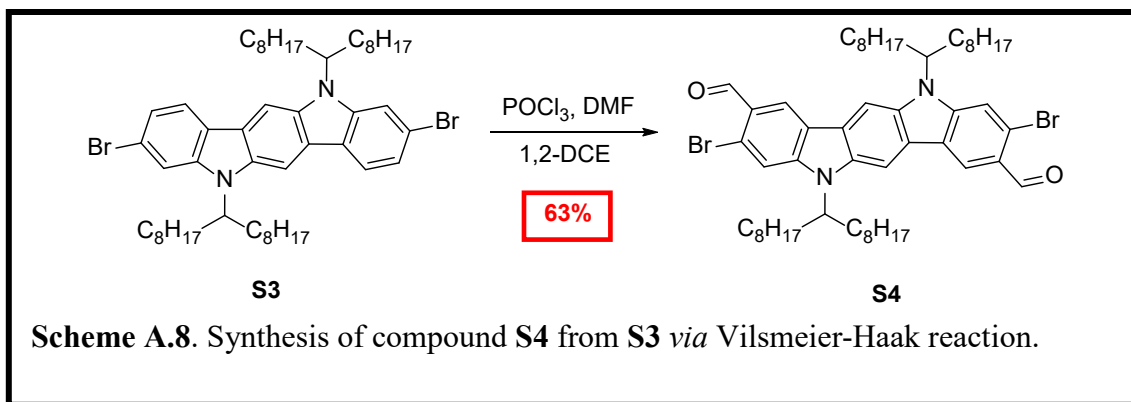


4: To a mixture of compound **1** (200 mg, 0.27 mmol), K₂CO₃ (220 mg, 1.62 mmol), aliquat 336 (30 μL, 0.06 mmol), several crystals of 2,6-di-*t*-butyl-4-methylphenol (BHT), and **S8** (200 mg, 0.81 mmol) in degassed toluene (5 mL) and water (0.8 mL) was added Pd(PPh₃)₄ (31 mg, 10 mol%) under nitrogen atmosphere. The reaction mixture was stirred at 100 °C for 24 h. After being cooled to room temperature, the reaction mixture was concentrated

under reduced pressure, and the residue was extracted with DCM (3×10 mL). The combined organic layer was dried over MgSO_4 , filtered through Celite, and concentrated under reduced pressure. The residue was purified by flash column chromatography (SiO_2 , hexane: $\text{CH}_2\text{Cl}_2 = 94:6$ to $30:70$) to give the crude product of **4**. The crude product was used for the next step.

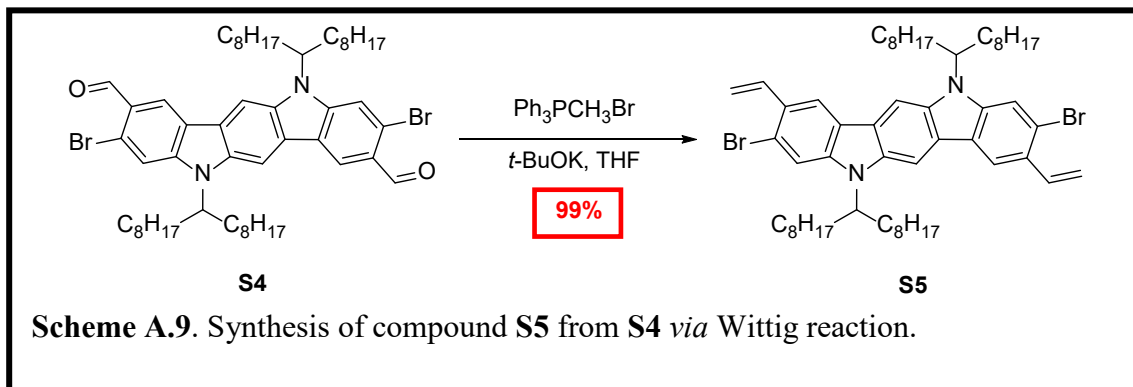


DBTDCz: The mixture of crude product of **4** (150 mg) and Grubbs' 2nd generation catalyst (4 mg, 0.005 mmol) in degassed toluene (7 mL) was stirred at reflux under N_2 . Immediately, another portion of Grubbs' 2nd generation catalyst (12 mg, 0.014 mmol) in degassed toluene (5 mL) was added for 4 h using syringe pump. After that, the reaction mixture was stirred for an additional 2 h at reflux temperature. After being cooled to room temperature, the reaction mixture was concentrated under reduced pressure, and the residue was filtered through silica pad with 10% CH_2Cl_2 in hexane. The product was further purified by preparative GPC to give the product **DBTDCz** (75 mg, 37% for 2 steps) as a red solid. ^1H NMR (500 MHz, CDCl_3): δ 11.05 (s, 1H), 10.86 (s, 1H), 9.14 (m, 2H), 8.05 (dd, $J_1 = 18.0$ Hz, $J_2 = 9.0$ Hz, 4H), 7.70 (s, 2H), 5.28 (m, 1H), 3.12 (s, 6H), 2.95 (m, 2H), 2.31 (m, 2H), 1.25 (m, 24H), 0.62 (m, 6H).



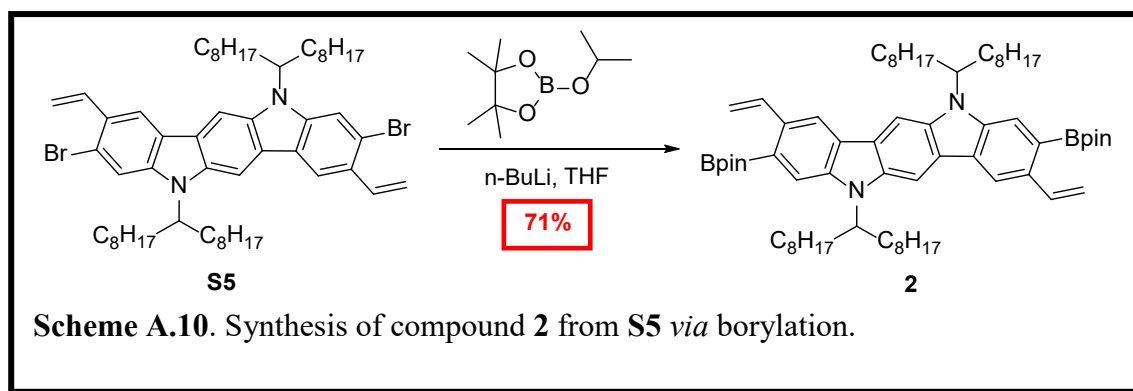
S4 (3,9-dibromo-5,11-dihydro-5,11-di(1-octylonyl)indolo[3,2-*b*]carbazole-2,8-dicarb aldehyde): In a 150 mL sealed tube, DMF (8.7 mL, 112.5 mmol) was added in anhydrous 1,2-DCE (30 mL) and cooled down to 0 °C under N₂. To the mixture was added phosphorus oxychloride (10.5 mL, 112.5 mmol) dropwise at 0 °C. After the reaction mixture was warmed to room temperature, compound **S3** (4.0 g, 4.5 mmol) was added into the flask, and the mixture was stirred at 95 °C for 48 h. The reaction was cooled down to room temperature and quenched with water. The aqueous mixture was basified to pH = 7 by 2M KOH solution. The mixture was extracted with CH₂Cl₂ (3 × 50 mL), and the combined organic layer was dried over MgSO₄, filtered through Celite, and concentrated under reduced pressure. The residue was purified by flash column chromatography (SiO₂, hexane:CH₂Cl₂ = 100:0 to 50:50) to give the product **S4** (2.7 g, 62%) as a yellow solid. ¹H NMR (500MHz, CDCl₃): δ 10.46 (s, 2H), 8.83, 8.81 (two s[†], 2H), 8.27, 8.24, 8.13, 8.10 (four s[†], 2H), 7.86, 7.77 (two s[†], 2H), 4.68, 4.55 (two quint[†], 2H), 2.40, 2.26 (two m[†], 4H), 2.05 (m, 4H), 1.13 (m, 46H), 0.78 (t, *J* = 7.0 Hz, 12H). [†]Peak separations were observed due to the atropisomers by hindered rotation of α-branched alkyl chain. ¹³C NMR (125 MHz, CDCl₃): δ 191.98, 147.06, 143.82, 139.06, 138.93, 135.15, 125.15, 124.68, 124.36, 124.32, 123.72, 123.30, 123.11, 122.97, 122.76, 122.41, 122.04, 121.69, 104.08, 13.68,

103.39, 103.00, 100.96, 100.59, 57.94, 57.59, 33.77, 33.44, 31.84, 29.44, 29.23, 27.36, 26.99, 26.66, 22.70, 14.48, 14.19, 13.84. ^{13}C NMR showed multiple separated peaks due to the atropisomers. HR-MALDI: calcd for $\text{C}_{54}\text{H}_{78}\text{Br}_2\text{N}_2\text{O}_2$ $[\text{M}+\text{H}]^+$ $m/z = 947.4488$; found $m/z = 947.4431$.



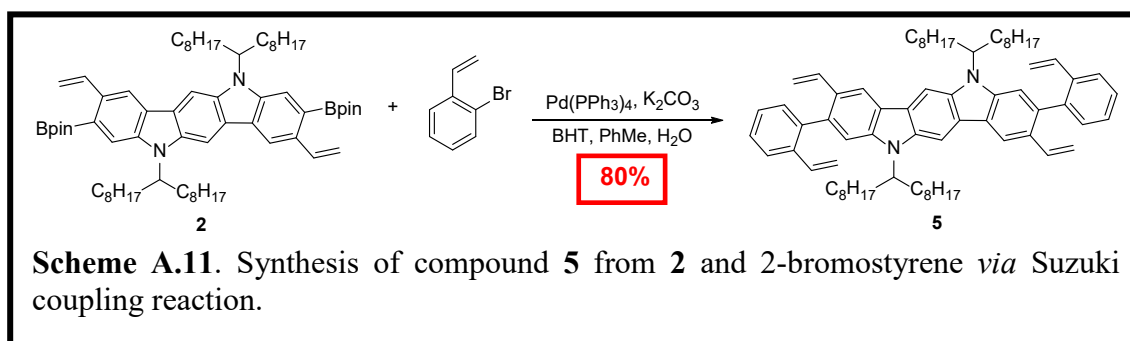
S5 (3,9-dibromo-2,8-diethenyl-5,11-dihydro-5,11-di(1-octylonyl)indolo[3,2-*b*]carbazole): To the mixture of methyltriphenylphosphonium bromide (4.0 g, 11.2 mmol) in THF (80 mL) was added *t*-BuOK (1.18 g, 10.5 mmol) in small portions over 10 min at room temperature. Compound **S4** (2.5 g, 2.63 mmol) was added into the flask (covered with aluminum foil) with several crystals of 2,6-di-*t*-butyl-4-methylphenol (BHT). The mixture was stirred at reflux for 6 h. The reaction was quenched with water and diluted with CH_2Cl_2 . The mixture was extracted with CH_2Cl_2 (3×30 mL) and the combined organic layer was dried over MgSO_4 , filtered through Celite, and concentrated under reduced pressure. The residue was purified by flash column chromatography (SiO_2 , hexane) to give the product **S5** (2.5 g, 99%) as a yellow solid. ^1H NMR (500MHz, CDCl_3): δ 8.38, 8.35 (two s^\dagger , 2H), 8.14, 8.10, 8.00, 7.97 (four s^\dagger , 2H), 7.75, 7.59 (two s^\dagger , 1H), 7.26 (dd, $J_1 = 17.5$ Hz, $J_2 = 11.0$ Hz, 2H), 5.82 (dd, $J_1 = 17.5$ Hz, $J_2 = 11.0$ Hz, 2H), 5.34 (d, J

= 11.0 Hz, 2H), 4.67, 4.48 (two br[†], 2H), 2.42, 2.26 (two m[†], 4H), 2.00 (m, 4H), 1.13 (m, 46H), 0.79 (t, $J = 7.0$ Hz, 12H). [†] Peak separations were observed due to the atropisomers by hindered rotation of α -branched alkyl chain. ¹³C NMR (125 MHz, CDCl₃): δ 143.69, 142.79, 140.14, 138.25, 137.34, 137.12, 136.60, 136.36, 134.40, 127.47, 123.83, 123.55, 122.41, 122.17, 121.51, 120.92, 117.96, 117.78, 117.60, 114.77, 114.55, 113.85, 113.22, 112.49, 112.31, 105.12, 102.25, 101.95, 99.47, 99.26, 57.38, 57.02, 56.43, 33.88, 33.64, 31.88, 29.58, 29.46, 29.31, 27.04, 22.72, 14.21, 14.16. ¹³C NMR showed multiple separated peaks due to the atropisomers. HR-MALDI: calcd for C₅₆H₈₂Br₂N₂ [M+H]⁺ m/z = 944.4923; found m/z = 944.4905.



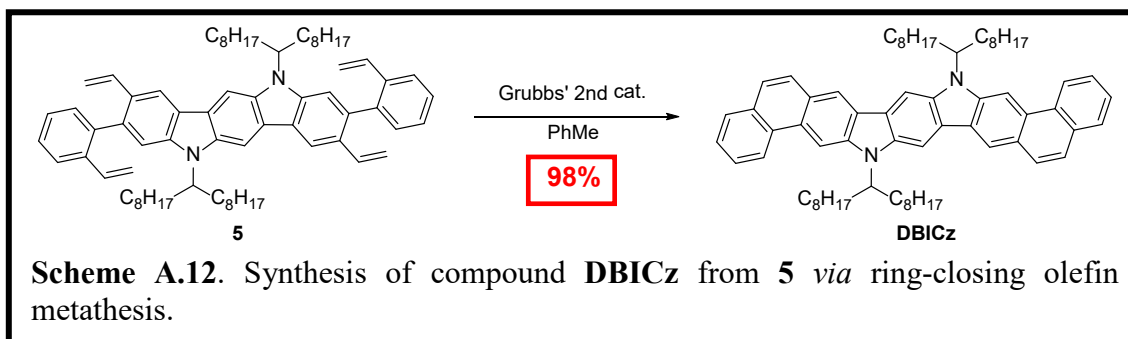
2 (2,8-diethenyl-3,9-bis(4,4,5,5-tetramethyl-1,3,2-dioxaborolan-2-yl)-5,11-dihydro-5,11-di(1-octynonyl)indolo[3,2-*b*]carbazole): To the mixture of compound **S5** (1.07 g, 1.1 mmol) in anhydrous THF (20 mL) at -78 °C was added *n*-BuLi (1.4 mL, 2.31 mmol, 1.6 M in hexane) dropwise over 1 h and stirred for another 1 h at -78 °C. 2-isopropoxy-4,4,5,5-tetramethyl-1,3,2-dioxaborolane (0.53 mL, 2.64 mmol) was added into the mixture, and the mixture was allowed to room temperature and stirred for 24 h. The reaction was quenched with water and diluted with CH₂Cl₂. The mixture was extracted

with CH₂Cl₂ (3 × 30 mL) and the combined organic layer was dried over MgSO₄, filtered through Celite, and concentrated under reduced pressure. The residue was purified by flash column chromatography (SiO₂, hexane:CH₂Cl₂ = 100:0 to 50:50) to give the product **2** (0.81g, 71%) as a yellow solid. ¹H NMR (500MHz, CDCl₃): δ 8.46 (m, 2H), 8.20 (m, 2H), 8.17, 8.05 (two s[†], 1H), 8.01 (s, 1H), 7.85 (s, 1H), 7.76 (dd, *J*₁ = 17.0 Hz, *J*₂ = 11.0 Hz, 2H), 5.85 (d, *J* = 17.0 Hz, 2H), 5.25 (d, *J* = 11.0 Hz, 2H), 4.71 (bs, 2H), 2.44, 2.37 (two m[†], 4H), 2.02 (m, 4H), 1.43 (s, 24H), 1.14 (m, 46H), 0.80 (t, *J* = 7.0 Hz, 12H). [†]Peak separations were observed due to the atropisomers by hindered rotation of α-branched alkyl chain. ¹³C NMR (125 MHz, CDCl₃): 151.67, 142.52, 138.76, 134.70, 133.83, 126.38, 125.67, 125.02, 124.16, 118.46, 116.21, 116.06, 115.88, 111.45, 102.36, 101.98, 99.55, 99.19, 83.73, 56.88, 56.39, 34.09, 33.77, 31.91, 29.69, 29.51, 29.38, 27.12, 26.98, 25.10, 22.73, 14.18. ¹³C NMR showed multiple separated peaks due to the atropisomers. HR-MALDI: calcd for C₆₈H₁₀₆B₂N₂O₄ [M+H]⁺ *m/z* = 1037.8417; found *m/z* = 1037.8499.



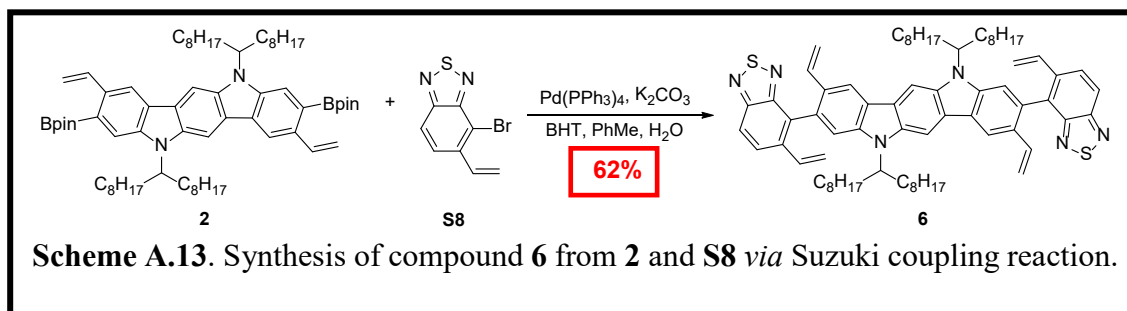
5: To a mixture of compound **2** (150 mg, 0.14 mmol), K₂CO₃ (110 mg, 0.84 mmol), aliquat 336 (20 μL, 0.04 mmol), several crystals of 2,6-di-*t*-butyl-4-methylphenol (BHT), and 2-bromostyrene (40 μL, 0.42 mmol) in degassed toluene (4 mL) and water (0.8 mL) was added Pd(PPh₃)₄ (16 mg, 10 mol%) under nitrogen atmosphere. The reaction mixture was

stirred at 100 °C for 24 h. After being cooled to room temperature, the reaction mixture was concentrated under reduced pressure, and the residue was extracted with DCM (3 × 10 mL). The combined organic layer was dried over MgSO₄, filtered through Celite, and concentrated under reduced pressure. The residue was purified by flash column chromatography (SiO₂, hexane). The product was further purified by preparative GPC to give the product **5** (0.11 g, 80%) as a yellow solid. ¹H NMR (500MHz, CDCl₃): δ 8.50 (m, 2H), 8.16 (m, 2H), 7.73 (d, *J* = 7.5 H, 2H), 7.42 (d, *J* = 7.5 H, 2H), 7.18 (s, 1H), 6.55 (m, 4H), 5.79 (m, 2H), 5.68 (d, *J* = 17.5 Hz, 2H), 5.07 (d, *J* = 10.0 Hz, 2H), 4.64 (m, 2H), 2.39 (m, 4H), 1.95 (m, 4H), 1.13 (m, 46H), 0.79 (m, 12H).

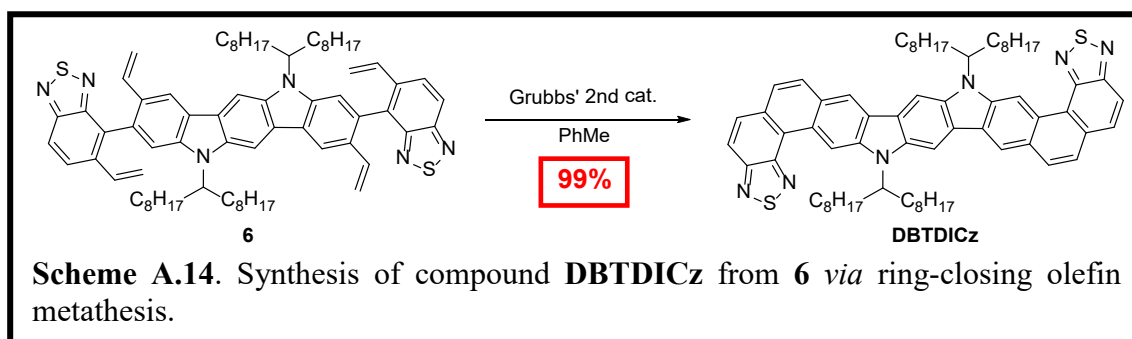


DBICz: The mixture of compound **5** (60 mg, 0.061 mmol) and Grubbs' 2nd generation catalyst (2 mg, 4 mol%) in degassed toluene (5 mL) was stirred at reflux under N₂. Immediately, another portion of Grubbs' 2nd generation catalyst (3 mg, 6 mol%) in degassed toluene (3 mL) was added for 4 h using syringe pump. After that, the reaction mixture was stirred for an additional 2 h at reflux temperature. After being cooled to room temperature, the reaction mixture was concentrated under reduced pressure, and the residue was filtered through silica pad with 10% CH₂Cl₂ in hexane to give the product **DBICz** (56 mg, 98%) as a yellow solid. ¹H NMR (500 MHz, CDCl₃): δ 8.84 (m, 2H), 8.78

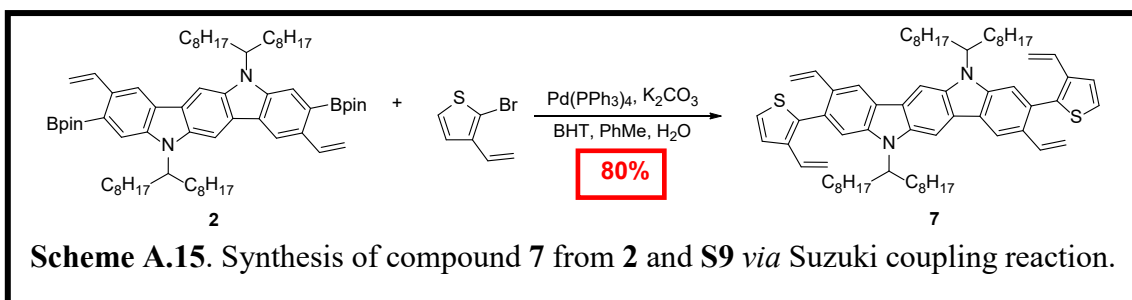
(m, 2H), 8.67 (m, 2H), 8.34 (m, 2H), 7.97 (m, 2H), 7.93 (d, $J = 7.5$ Hz, 2H), 7.70 (m, 2H), 7.63 (m, 4H), 4.92 (m, 2H), 2.61 (m, 4H), 2.16 (m, 4H), 1.12 (m, 46H), 0.73 (t, $J = 7.0$ Hz, 12H).



6: To a mixture of compound **2** (100 mg, 0.096 mmol), K_2CO_3 (80 mg, 0.58 mmol), aliquat 336 (10 μ L, 0.02 mmol), several crystals of 2,6-di-*t*-butyl-4-methylphenol (BHT), and **S8** (70 mg, 0.29 mmol) in degassed toluene (3 mL) and water (0.6 mL) was added $Pd(PPh_3)_4$ (12 mg, 10 mol%) under nitrogen atmosphere. The reaction mixture was stirred at 100 $^{\circ}C$ for 24 h. After being cooled to room temperature, the reaction mixture was concentrated under reduced pressure, and the residue was extracted with DCM (3×10 mL). The combined organic layer was dried over $MgSO_4$, filtered through Celite, and concentrated under reduced pressure. The residue was purified by flash column chromatography (SiO_2 , hexane: $CH_2Cl_2 = 88:12$ to 0:100). The product was further purified by preparative GPC to give the product **6** (66 mg, 62%) as a brown solid. 1H NMR (500MHz, $CDCl_3$): δ 8.61 (m, 2H), 8.20 (m, 2H), 8.05 (s, 4H), 7.40 (s, 1H), 7.24 (s, 1H), 6.72 (m, 2H), 6.39 (dd, $J_1 = 17.0$ Hz, $J_2 = 11.0$ Hz, 2H), 5.95 (d, $J = 18.5$ Hz, 2H), 5.80 (d, $J = 17.0$ Hz, 2H), 5.32 (d, $J = 11.0$ Hz, 2H), 4.98 (d, $J = 11.0$ Hz, 2H), 4.65 (m, 2H), 2.38 (m, 4H), 1.94 (m, 4H), 1.13 (m, 46H), 0.80 (m, 12H).

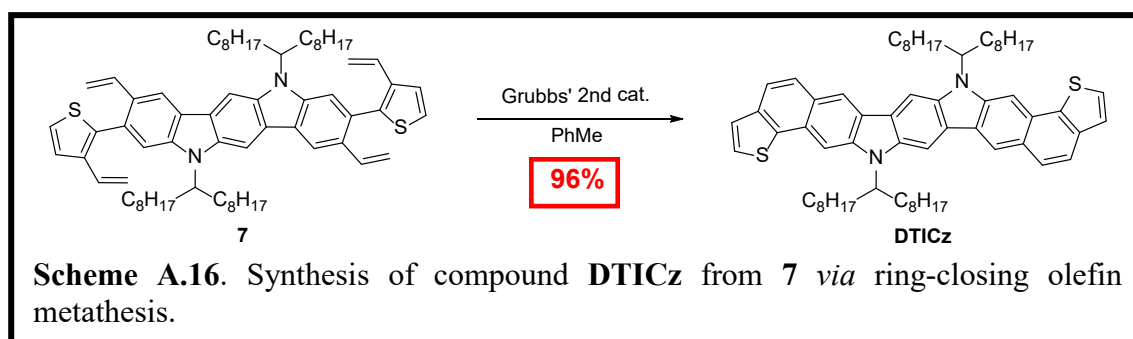


DBTDICz: The mixture of compound **6** (50 mg, 0.04 mmol) and Grubbs' 2nd generation catalyst (2 mg, 5 mol%) in degassed toluene (5 mL) was stirred at reflux under N₂. Immediately, another portion of Grubbs' 2nd generation catalyst (3 mg, 8 mol%) in degassed toluene (3 mL) was added for 4 h using syringe pump. After that, the reaction mixture was stirred for an additional 2 h at reflux temperature. After being cooled to room temperature, the reaction mixture was concentrated under reduced pressure, and the residue was filtered through silica pad with 10% CH₂Cl₂ in hexane to give the product **DBTDICz** (48 mg, 99%) as a red solid. ¹H NMR (500 MHz, CDCl₃): δ 10.84 (m, 2H), 8.91 (s, 2H), 8.52 (m, 1H), 8.37 (m, 3H), 8.09 (dd, *J*₁ = 15.5 Hz, *J*₂ = 9.0 Hz, 4H), 7.83 (s, 2H), 5.10 (m, 2H), 2.77 (m, 4H), 2.23 (m, 4H), 1.05 (m, 44H), 0.85 (m, 2H), 0.68 (m, 12H).



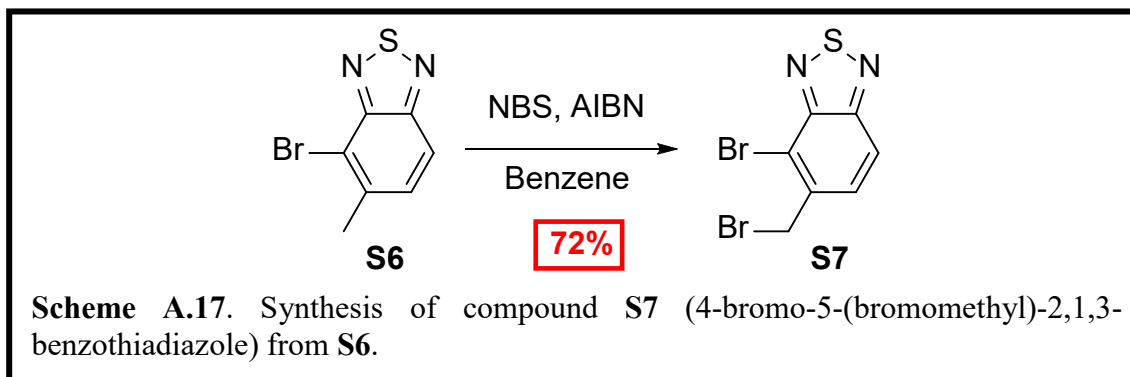
7: To a mixture of compound **2** (0.92 g, 0.88 mmol), K₂CO₃ (0.73 g, 5.32 mmol), aliquat 336 (100 mg, 0.22 mmol), several crystals of BHT, and 2-bromo-3-vinylthiophene (0.5 g,

2.66 mmol) in degassed toluene (20 mL) and water (4 mL) was added Pd(PPh₃)₄ (0.11 g, 0.09 mmol) under nitrogen atmosphere. Then the reaction mixture was stirred for 24 h at 100 °C. After being cooled to room temperature, the reaction was quenched with water and diluted with CH₂Cl₂. The mixture was extracted with CH₂Cl₂ (3 × 30 mL) and the combined organic layer was dried over MgSO₄, filtered through Celite, and concentrated under reduced pressure. The residue was purified by flash column chromatography (SiO₂, hexane/CH₂Cl₂ 98:2). The product was further purified by preparative GPC to give product **7** (0.70g, 80%) as a yellow solid. ¹H NMR (500MHz, CDCl₃): δ8.51(d, J = 12.0 Hz, 2H), 8.17(m, 2H), 7.40(m, 5H), 6.82(m, 2H), 6.45(dd, J₁ = 10.5 Hz, J₂ = 17.5 Hz, 2H), 5.87(m, 2H), 5.60(d, J = 17.5 Hz, 2H), 5.17(dd, J₁ = 10.5 Hz, J₂ = 17.5 Hz, 4H), 4.74(s, 1H), 4.60(s, 1H), 2.51(s, 2H), 2.33(s, 2H), 2.00(s, 2H), 1.56(s, 3H), 1.21(m, 48H), 0.81(t, J = 11.0 Hz, 12H).

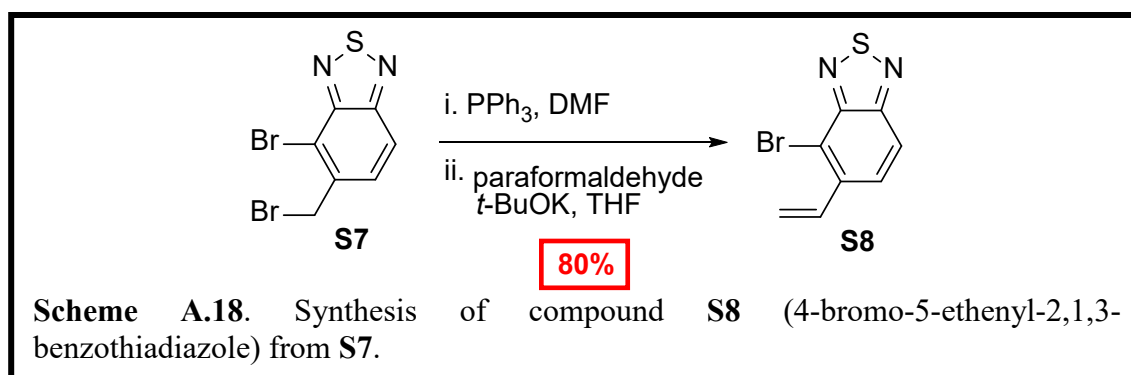


DTICz: The mixture of compound **7** (0.27 g, 0.27 mmol) and Grubbs' 2nd generation catalyst (8 mg, 0.009 mmol) in degassed toluene (3 mL) was stirred at reflux under N₂. Immediately, another portion of Grubbs' 2nd generation catalyst (15 mg, 0.018 mmol) in degassed toluene (3 mL) was added for 4 h using syringe pump. After that, the reaction mixture was stirred for an additional 1 h at reflux temperature. The mixture was diluted with CH₂Cl₂ and concentrated under reduced pressure. The residue was purified by flash

column chromatography (SiO₂, hexane). The product was further purified by preparative GPC to give product **DTICz** (0.25 g, 96%) as a yellow solid. ¹H NMR (500 MHz, CDCl₃): δ 8.80(d, *J* = 14.0 Hz, 2H), 8.28(m, 2H), 8.05(m, 4H), 7.77(d, *J* = 9.0 Hz, 2H), 7.54(m, 4H), 4.86(s, 2H), 2.59(s, 2H), 2.14(m, 4H), 1.25(m, 48H), 0.78(m, 12H).



S7 (4-bromo-5-(bromomethyl)-2,1,3-benzothiadiazole): Compound **S6** (3.6 g, 15.7 mmol) was dissolved in anhydrous benzene (120 mL) under a nitrogen atmosphere at room temperature. To the mixture were added NBS (3.1 g, 17.2 mmol) and AIBN (0.3 g, 0.17 mmol). The mixture was stirred and refluxed for 16 h. After being cooled to room temperature, the precipitate was filtered and washed with hexane. The filtrate was concentrated under reduced pressure and recrystallized using CHCl₃/EtOH to give the product **S7** (3.5 g, 72%) as a white solid. ¹H NMR (500 MHz, CDCl₃): δ 7.95 (d, *J* = 9.0 Hz, 1H), 7.68 (d, *J* = 9.0 Hz, 1H), 4.80 (s, 2H).



S8 (4-bromo-5-ethenyl-2,1,3-benzothiadiazole): The reaction mixture of compound **S7** (3.4 g, 9.2 mmol) and PPh_3 (6.0 g, 23.0 mmol) in DMF (50 mL) was stirred at 80 °C for 18 h. After being cooled to room temperature, the reaction mixture was concentrated under reduced pressure. The reaction mixture and paraformaldehyde (6.3 g) were suspended in THF (90 mL) under N_2 . While stirring, *t*-BuOK (3.1 g, 27.6 mmol) was added in small portions over 10 min. After 30 min, the reaction was quenched with water and extracted with CH_2Cl_2 (3 × 30 mL). The combined organic layer was dried over MgSO_4 , filtered through Celite, and concentrated under reduced pressure. The residue was purified by flash column chromatography (SiO_2 , hexane) to give the product **S8** (2.1 g, 80%) as a white solid. ^1H NMR (500 MHz, CDCl_3): δ 7.90 (d, $J = 9.0$ Hz, 1H), 7.84 (d, $J = 9.0$ Hz, 1H), 7.30 (dd, $J_1 = 17.5$ Hz, $J_2 = 11.0$ Hz, 1H), 5.97 (d, $J = 17.5$ Hz, 1H), 5.64 (d, $J = 11.0$ Hz, 1H).

A. 2. X-ray Crystallography

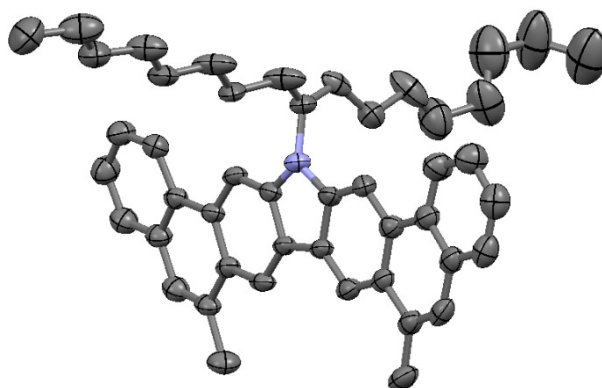


Figure A.1. Single-crystal X-ray structure of **DBCz** with probability ellipsoids set at 50% level. Hydrogen atoms have been omitted for clarity.

DBCz: CCDC-1040797 contains the supplementary crystallographic data for this paper. These data can be obtained free of charge from The Cambridge Crystallographic Data Centre via www.ccdc.cam.ac.uk/data_request/cif. A yellow plate crystal of **DBCz** having approximate dimensions of 0.435 mm x 0.195 mm x 0.056 mm was mounted on a nylon loop. Cell constants and an orientation matrix for data collection corresponded to a Triclinic cell with dimensions:

$$a = 14.501(4) \text{ \AA} \quad \alpha = 62.892(4)^\circ$$

$$b = 20.180(6) \text{ \AA} \quad \beta = 84.149(4)^\circ$$

$$c = 22.027(7) \text{ \AA} \quad \gamma = 77.270(4)^\circ$$

$$V = 5597(3) \text{ \AA}^3$$

For $Z = 6$ and F.W. = 633.92, the calculated density is 1.129 mg/m³. Systematic reflection conditions and statistical tests of the data suggested the space group $P-1$. The data were

collected at a temperature of 110.15 K with a theta range for the data collection of 1.039 to 20.870°.

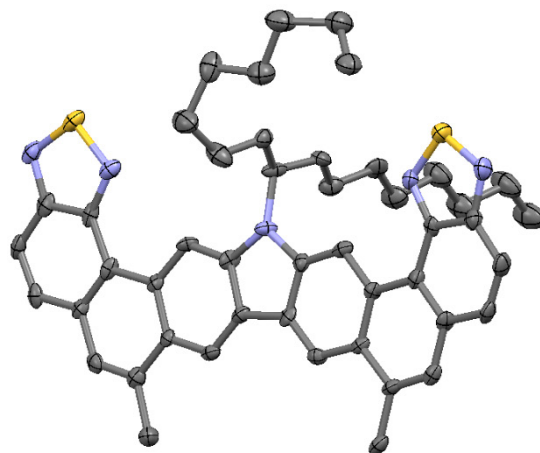


Figure A.2. Single-crystal X-ray structure of **DBTDCz** with probability ellipsoids set at 50% level. Hydrogen atoms have been omitted for clarity.

DBTDCz: CCDC-1840335 contains the supplementary crystallographic data for this paper. These data can be obtained free of charge from The Cambridge Crystallographic Data Centre via www.ccdc.cam.ac.uk/data_request/cif. A red block crystal of **DBTDCz** having approximate dimensions of 0.388 mm x 0.077 mm x 0.038 mm was mounted on a nylon loop. Cell constants and an orientation matrix for data collection corresponded to a Triclinic cell with dimensions:

$$a = 8.7337(2) \text{ \AA} \quad \alpha = 106.335(2)^\circ$$

$$b = 14.0615(4) \text{ \AA} \quad \beta = 90.631(2)^\circ$$

$$c = 17.5080(5) \text{ \AA} \quad \gamma = 92.772(2)^\circ$$

$$V = 2060.25(10) \text{ \AA}^3$$

For $Z = 2$ and $F.W. = 750.04$, the calculated density is 1.209 mg/m^3 . Systematic reflection conditions and statistical tests of the data suggested the space group $P-1$. The data were collected at a temperature of 100 K with a theta range for the data collection of 2.631 to 62.495°.

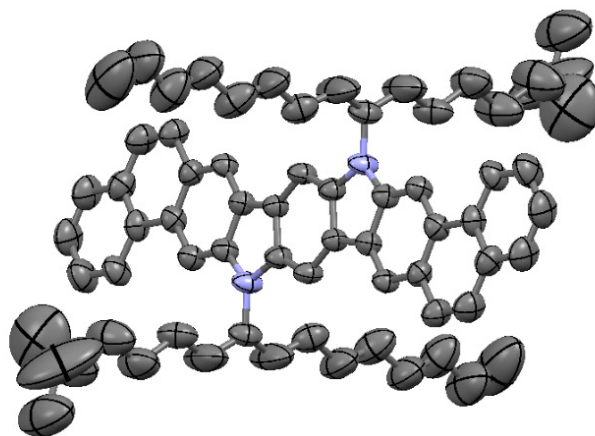


Figure A.3. Single-crystal X-ray structure of **DBICz** with probability ellipsoids set at 50% level. Hydrogen atoms have been omitted for clarity.

DBICz: CCDC-1840336 contains the supplementary crystallographic data for this paper. These data can be obtained free of charge from The Cambridge Crystallographic Data Centre via www.ccdc.cam.ac.uk/data_request/cif. A yellow plate of **DBICz** having approximate dimensions of 0.15 mm x 0.08 mm x 0.06 mm was mounted on a nylon loop. Cell constants and an orientation matrix for data collection corresponded to a Triclinic cell with dimensions:

$$a = 12.531(2) \text{ \AA} \quad \alpha = 63.164(9)^\circ$$

$$b = 15.989(2) \text{ \AA} \quad \beta = 86.767(16)^\circ$$

$$c = 16.278(4) \text{ \AA} \quad \gamma = 79.355(11)^\circ$$

$$V = 2858.8(9) \text{ \AA}^3$$

For $Z = 2$ and $F.W. = 933.40$, the calculated density is 1.084 mg/m^3 . Systematic reflection conditions and statistical tests of the data suggested the space group $P-1$. The data were collected at a temperature of 110 K with a theta range for the data collection of 3.044 to 62.110° .

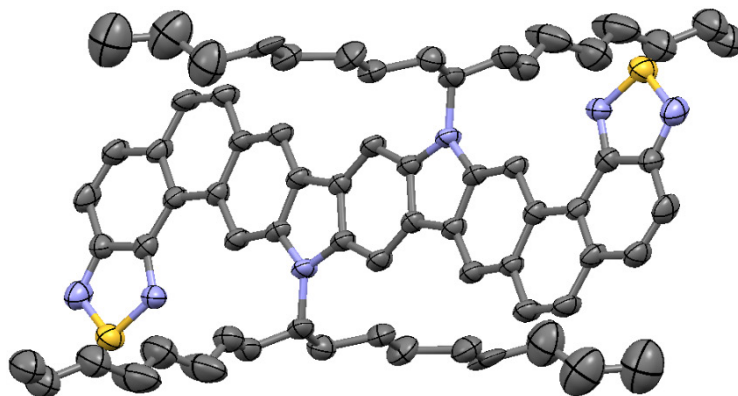


Figure A.4. Single-crystal X-ray structure of **DBTDICz** with probability ellipsoids set at 50% level. Hydrogen atoms have been omitted for clarity.

DBTDICz: CCDC-1840338 contains the supplementary crystallographic data for this paper. These data can be obtained free of charge from The Cambridge Crystallographic Data Centre via www.ccdc.cam.ac.uk/data_request/cif. A red block crystal of **DBTDICz** having approximate dimensions of $0.07 \text{ mm} \times 0.04 \text{ mm} \times 0.02 \text{ mm}$ was mounted on a nylon loop. Cell constants and an orientation matrix for data collection corresponded to a Triclinic cell with dimensions:

$$a = 14.6049(10) \text{ \AA} \quad \alpha = 80.531(5)^\circ$$

$$b = 14.8027(10) \text{ \AA} \quad \beta = 68.917(4)^\circ$$

$$c = 15.7342(10) \text{ \AA} \quad \gamma = 77.225(5)^\circ$$

$$V = 3081.8(4) \text{ \AA}^3$$

For $Z = 2$ and F.W. = 1088.58, the calculated density is 1.173 mg/m^3 . Systematic reflection conditions and statistical tests of the data suggested the space group $P-1$. The data were collected at a temperature of 110.15 K with a theta range for the data collection of 3.023 to 60.931° .

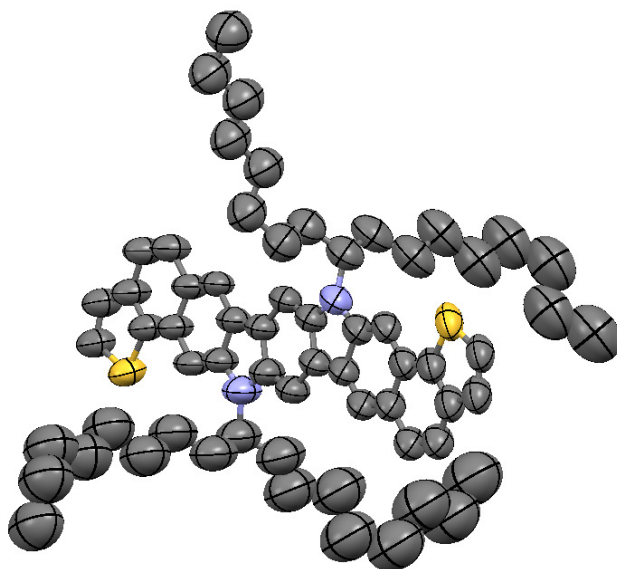


Figure A.5. Single-crystal X-ray structure of **DTICz** with probability ellipsoids set at 50% level. Hydrogen atoms have been omitted for clarity.

DTICz: CCDC-1840339 contains the supplementary crystallographic data for this paper. These data can be obtained free of charge from The Cambridge Crystallographic Data Centre via www.ccdc.cam.ac.uk/data_request/cif. A brown block crystal of **DTICz** having approximate dimensions of $0.247 \text{ mm} \times 0.139 \text{ mm} \times 0.105 \text{ mm}$ was mounted on a nylon loop. Cell constants and an orientation matrix for data collection corresponded to a Triclinic cell with dimensions:

$$a = 22.293(5) \text{ \AA} \quad \alpha = 90^\circ$$

$$b = 22.293(5) \text{ \AA} \quad \beta = 90^\circ$$

$$c = 47.638(12) \text{ \AA} \quad \gamma = 90^\circ$$

$$V = 23674(13) \text{ \AA}^3$$

For $Z = 16$ and F.W. = 945.45, the calculated density is 1.061 mg/m^3 . Systematic reflection conditions and statistical tests of the data suggested the space group $I41/a$. The data were collected at a temperature of 110 K with a theta range for the data collection of 1.008 to 16.735°.

A. 3. ^1H and ^{13}C NMR

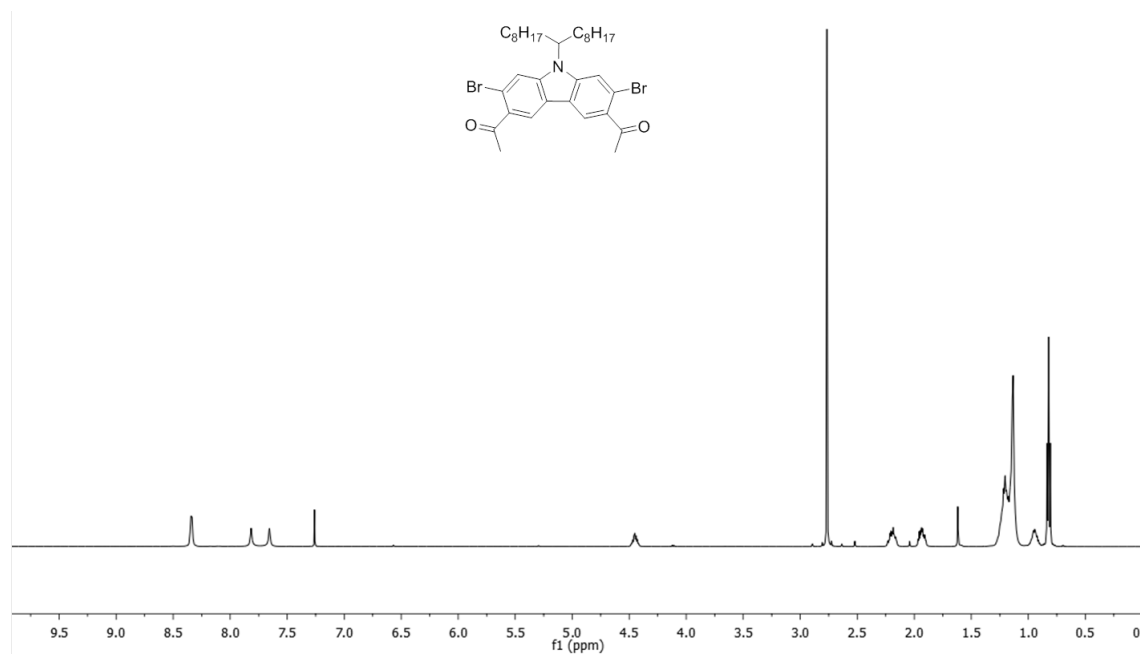


Figure A.6. ^1H NMR of S1 (500 MHz, CDCl_3 , RT).

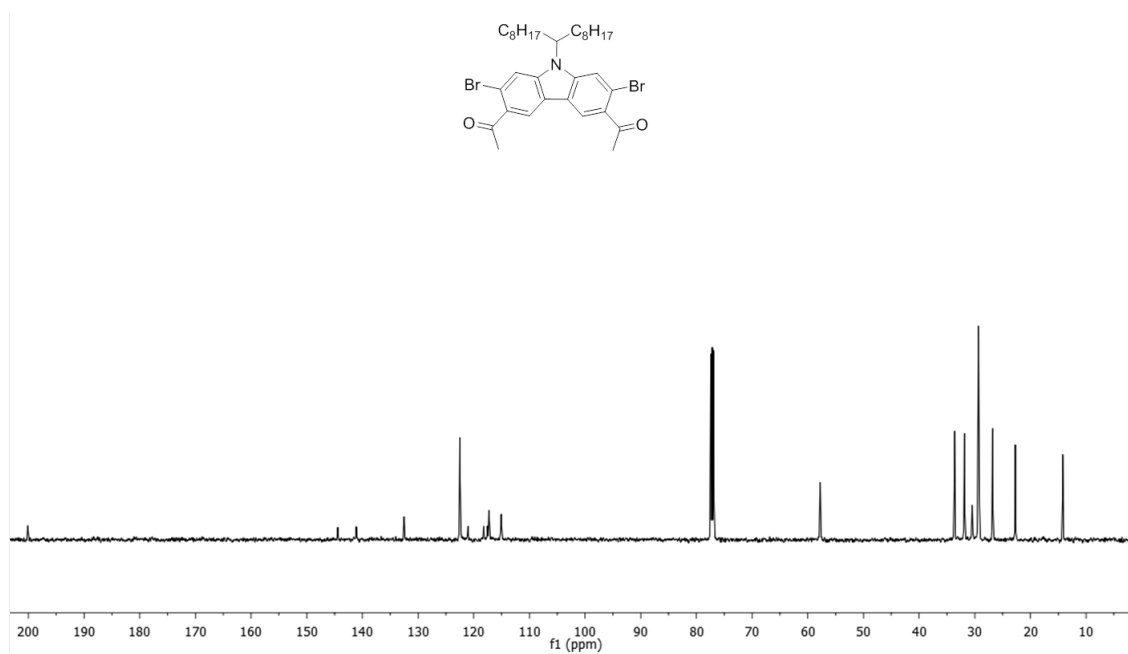


Figure A.7. ^{13}C NMR of S1 (125 MHz, CDCl_3 , RT).

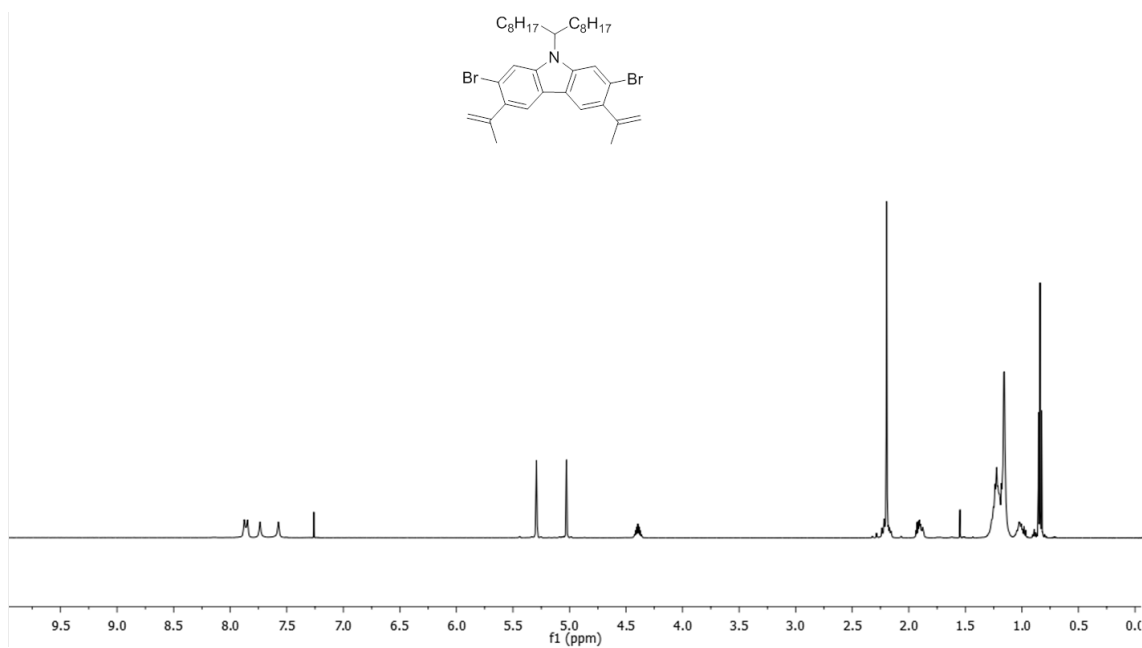


Figure A.8. ^1H NMR of S2 (500 MHz, CDCl_3 , RT).

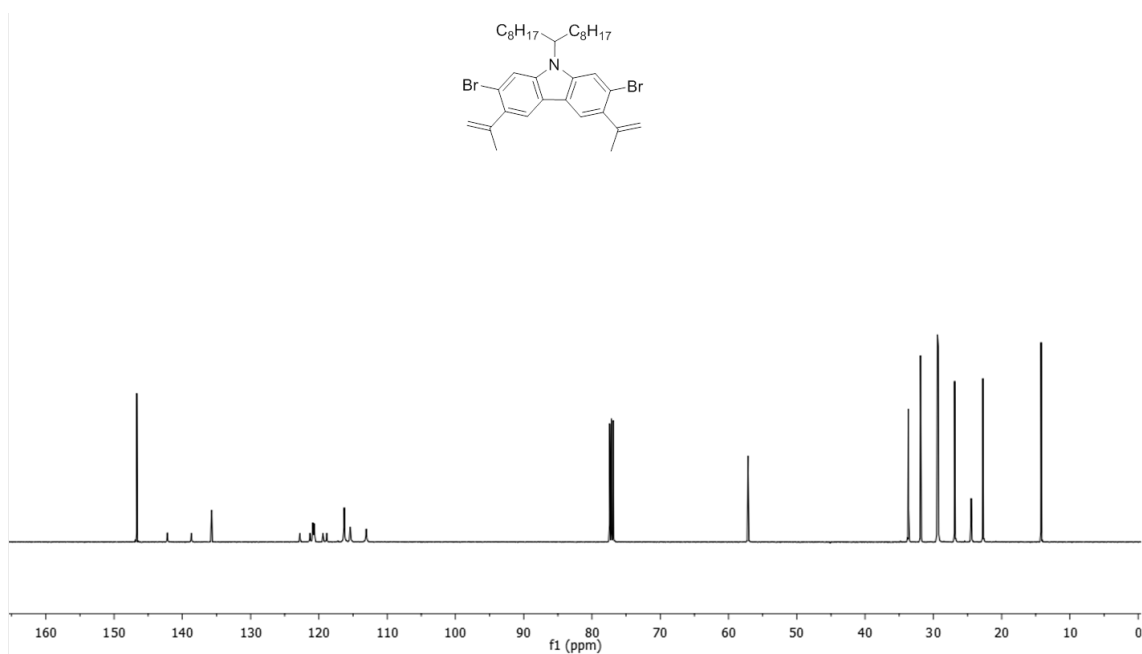


Figure A.9. ¹³C NMR of **S2** (125 MHz, CDCl₃, RT).

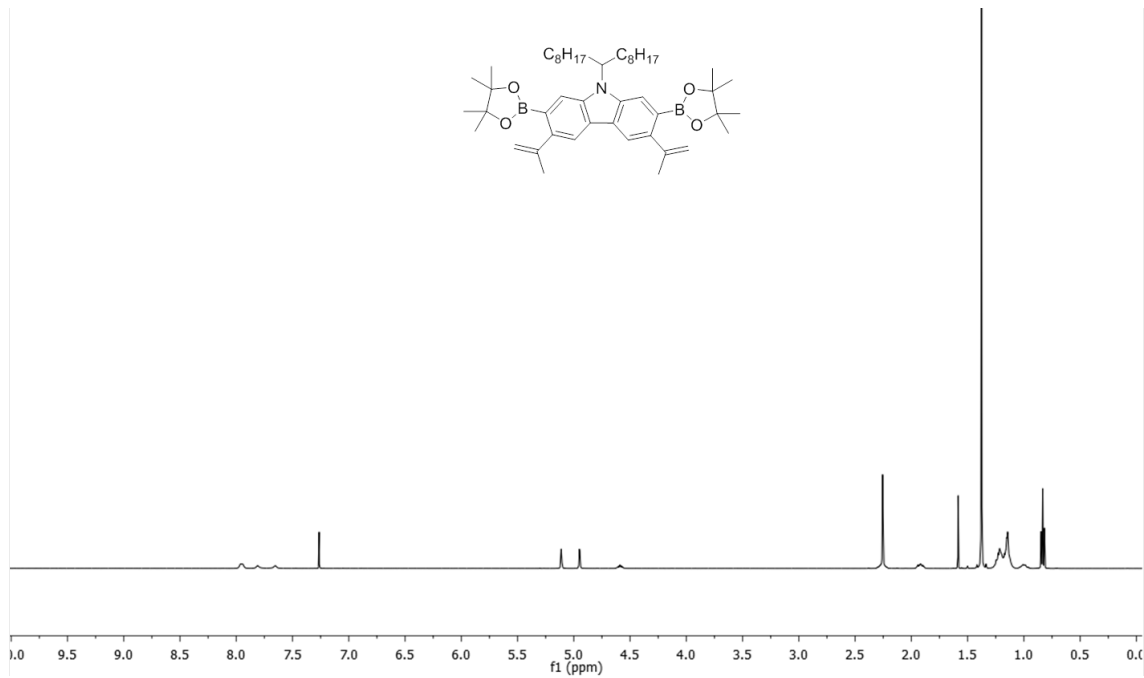


Figure A.10. ¹H NMR of **1** (500 MHz, CDCl₃, RT).

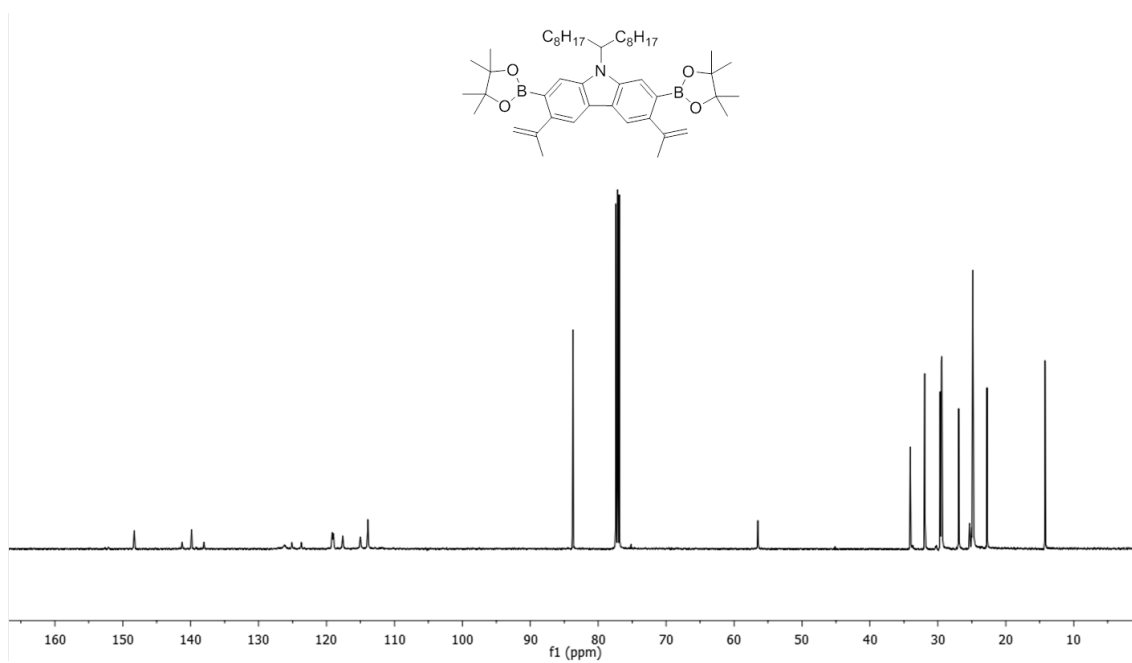


Figure A.11. ¹³C NMR of **1** (125 MHz, CDCl₃, RT).

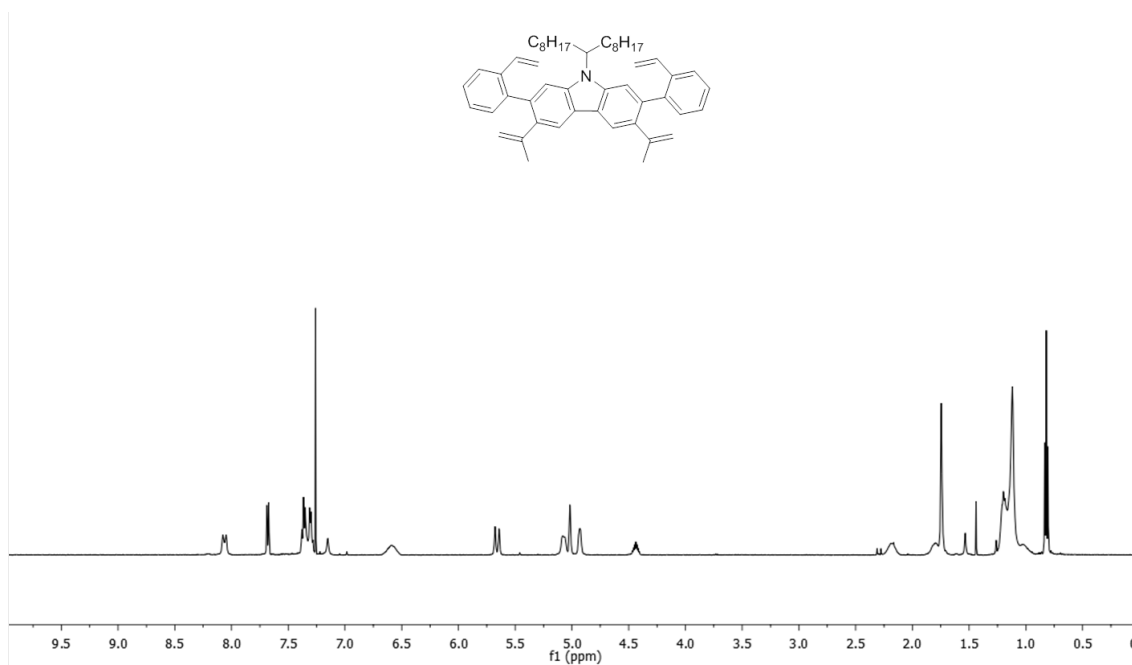


Figure A.12. ¹H NMR of **3** (500 MHz, CDCl₃, RT).

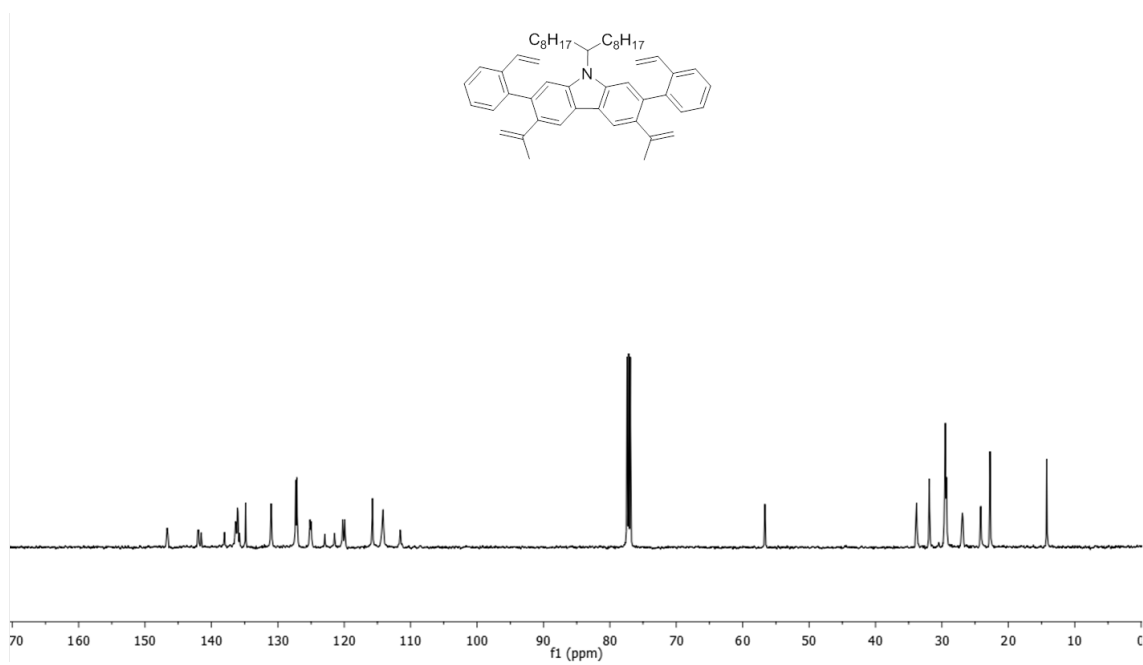


Figure A.13. ¹³C NMR of **3** (125 MHz, CDCl₃, RT).

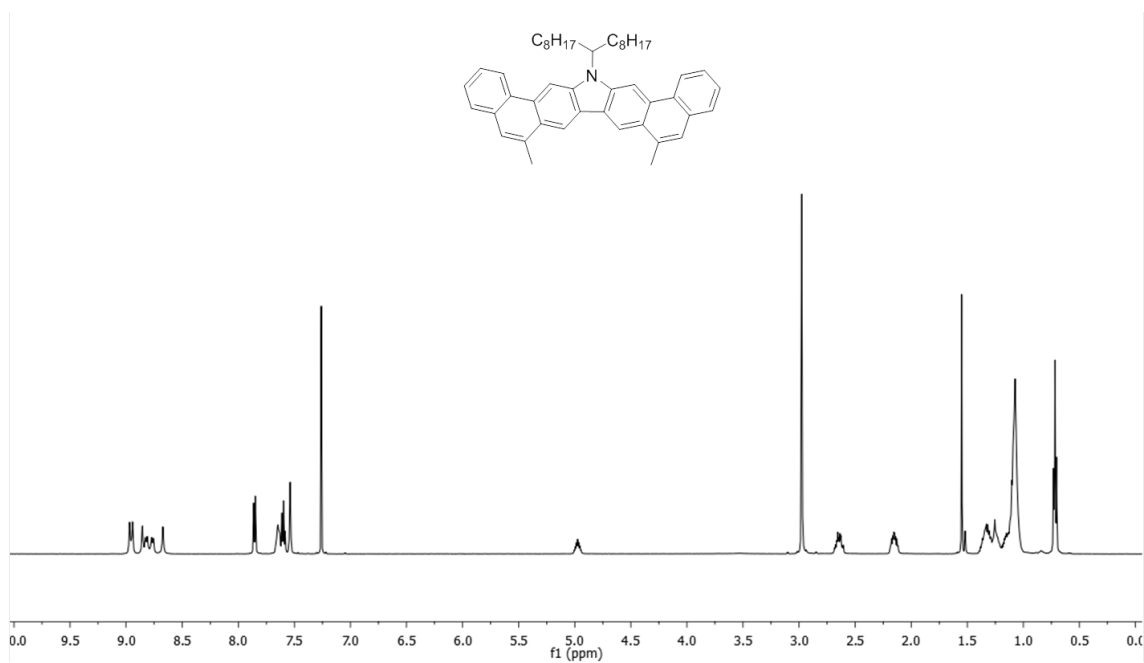


Figure A.14. ¹H NMR of DBCz (500 MHz, CDCl₃, RT).

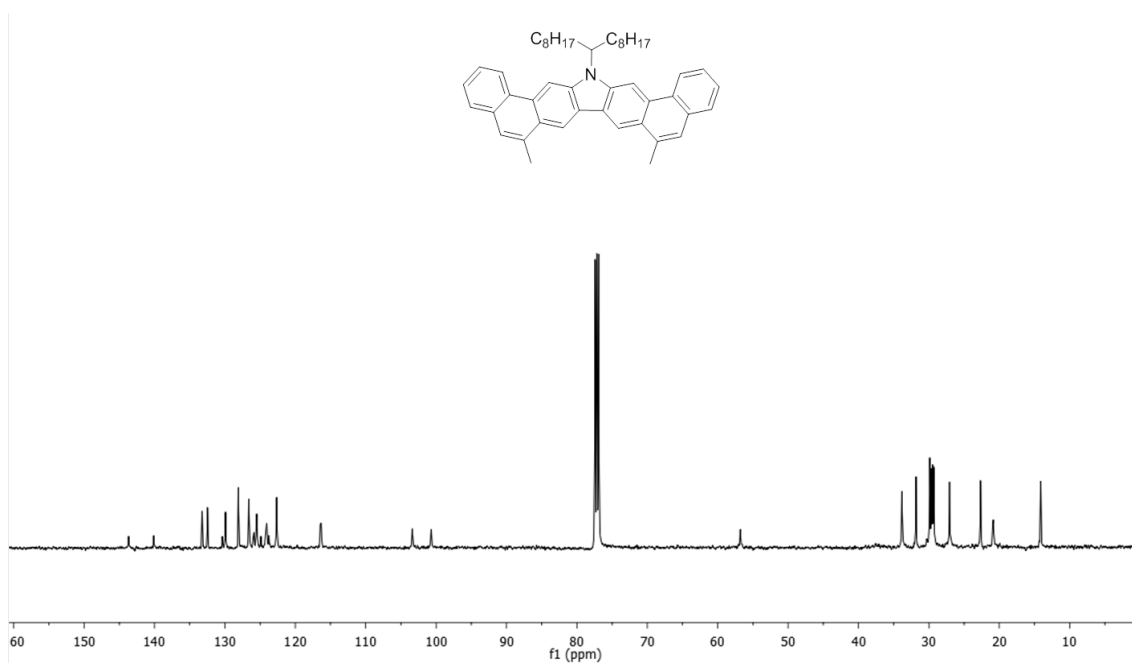


Figure A.15. ^{13}C NMR of **DBCz** (125 MHz, CDCl_3 , RT).

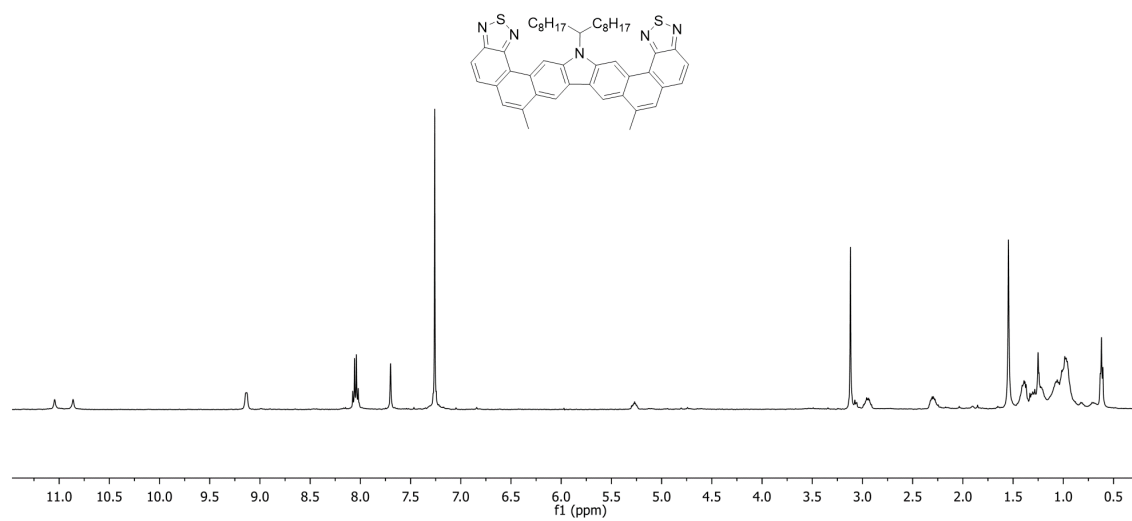


Figure A.16. ^1H NMR of **DBTDCz** (500 MHz, CDCl_3 , RT).

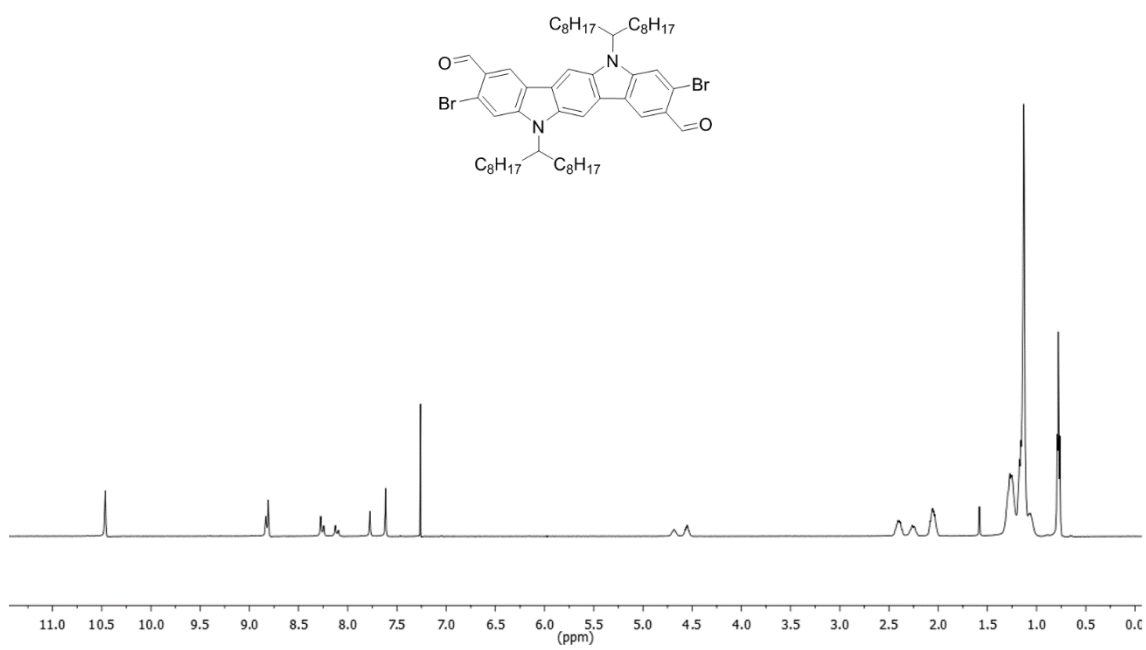


Figure A.17. ^1H NMR of S4 (500 MHz, CDCl_3 , RT).

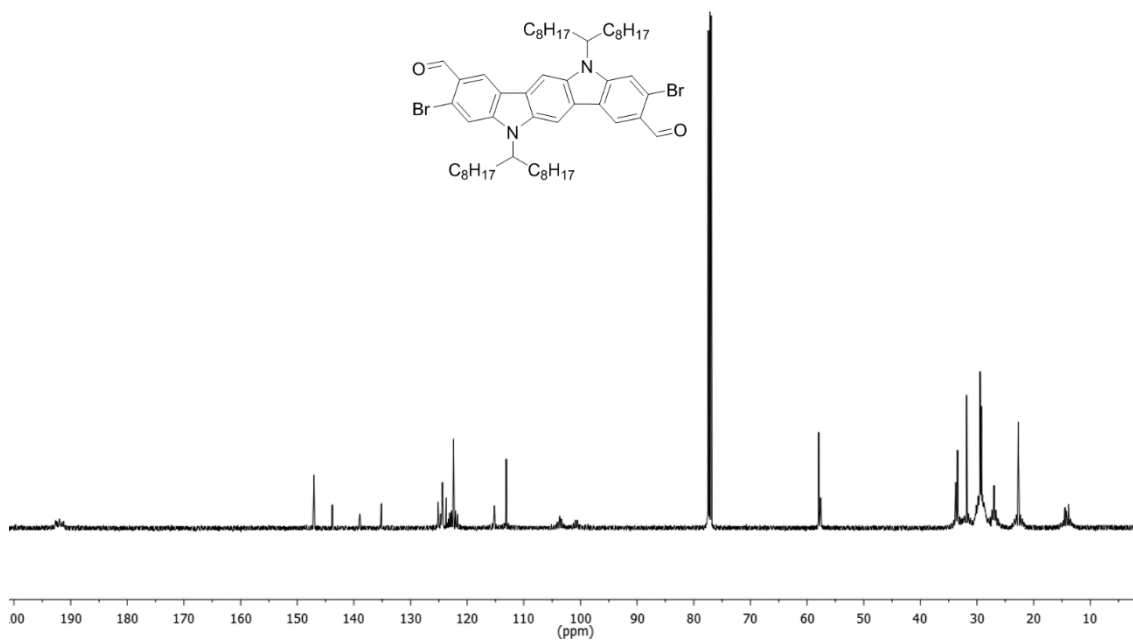


Figure A.18. ^{13}C NMR of S4 (125 MHz, CDCl_3 , RT).

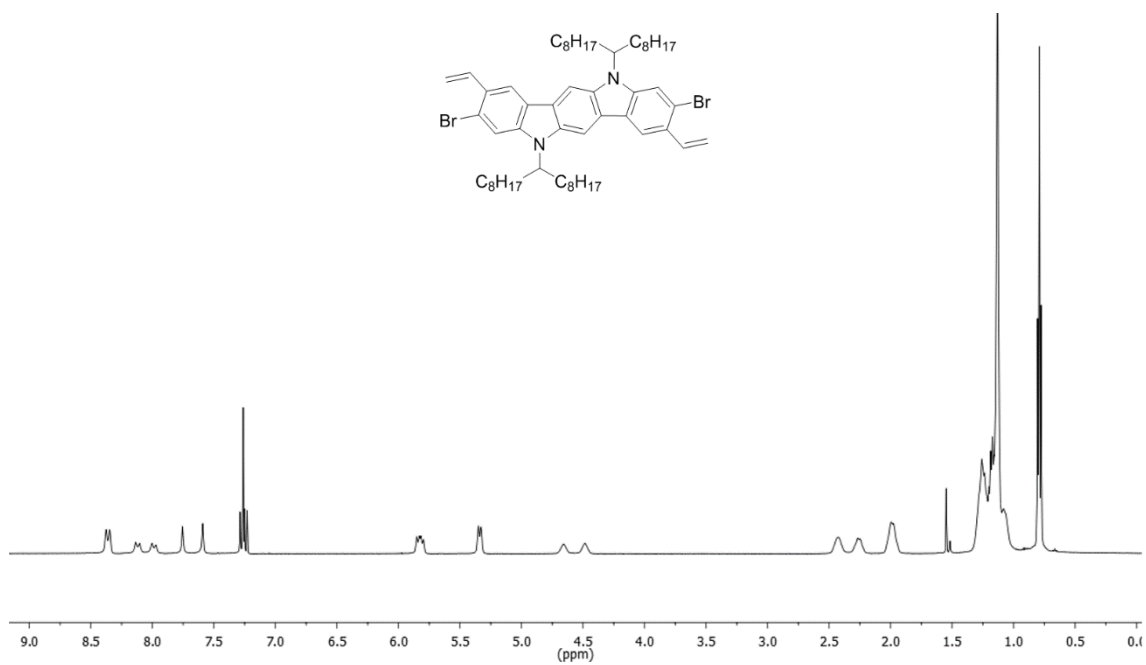


Figure A.19. ^1H NMR of S5 (500 MHz, CDCl_3 , RT).

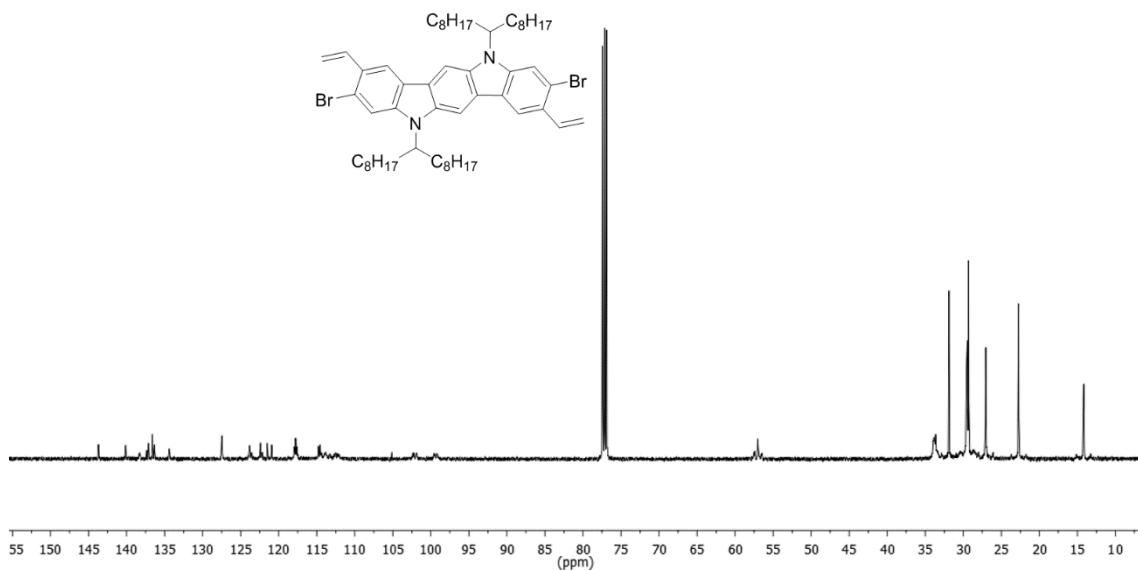


Figure A.20. ^{13}C NMR of S5 (125 MHz, CDCl_3 , RT).

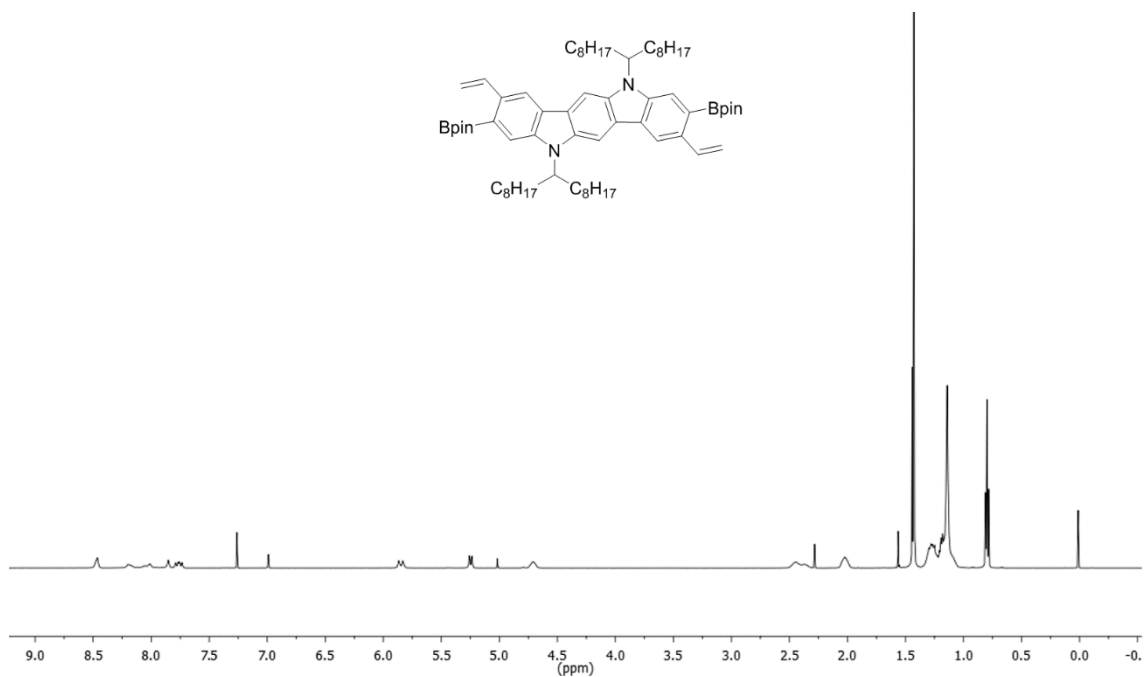


Figure A.21. ^1H NMR of **2** (500 MHz, CDCl_3 , RT).

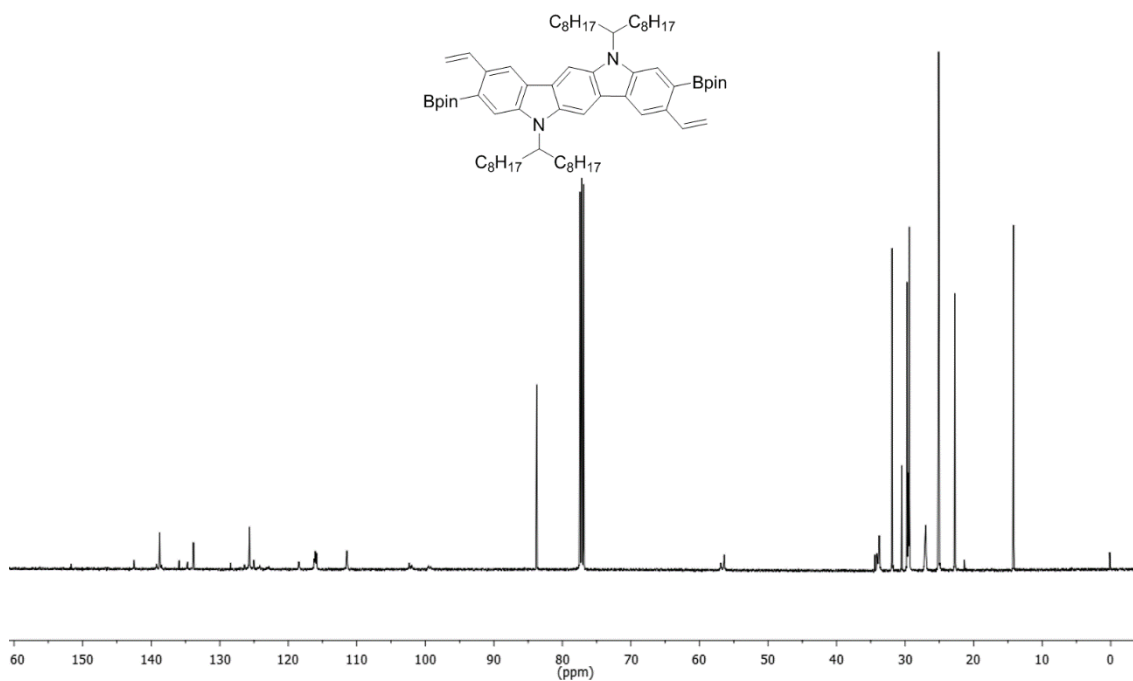


Figure A.22. ^{13}C NMR of **2** (125 MHz, CDCl_3 , RT).

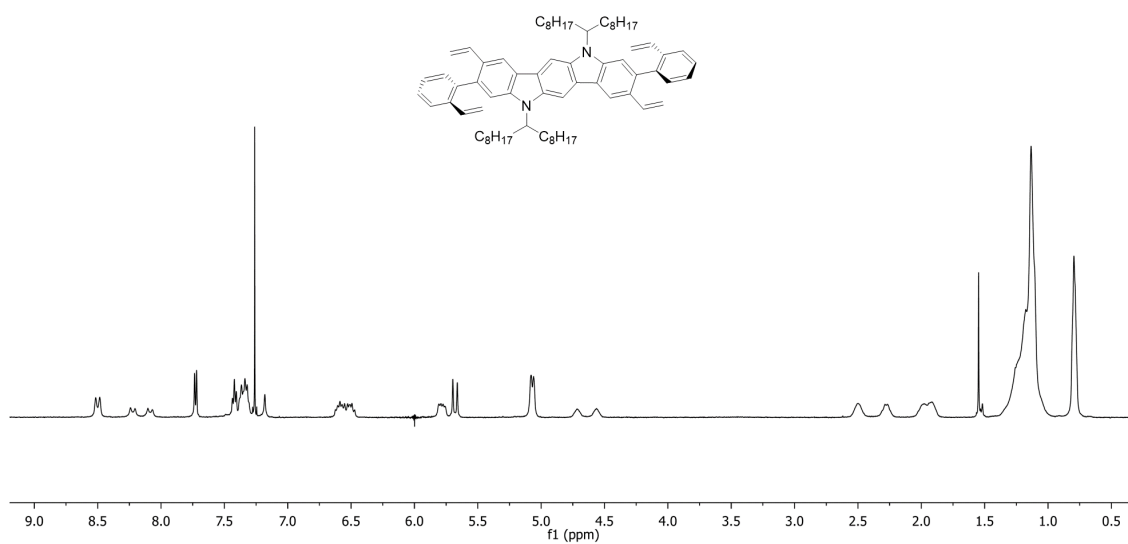


Figure A.23. ¹H NMR of **5** (500 MHz, CDCl₃, RT).

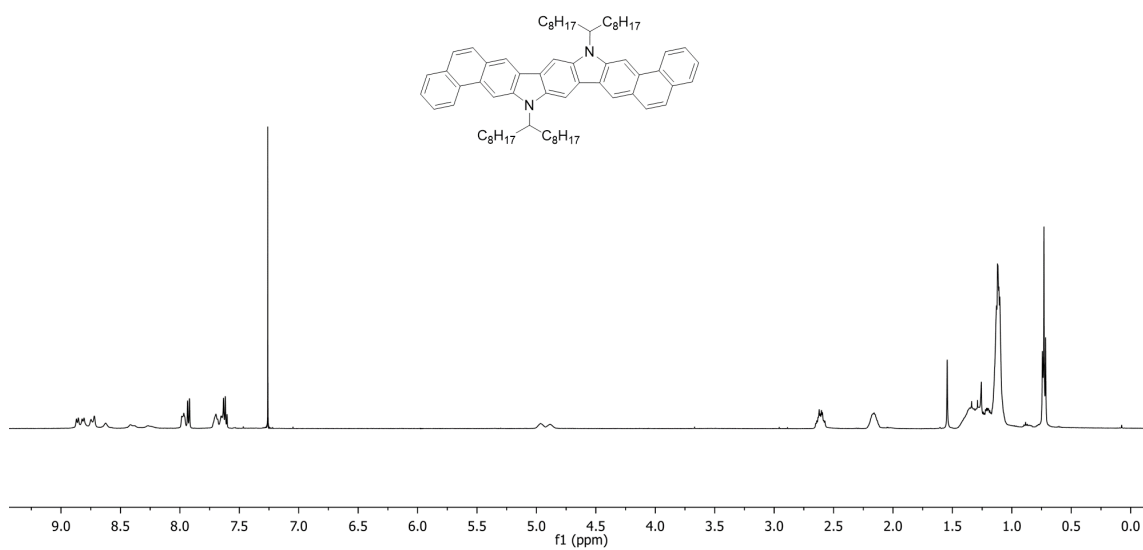


Figure A.24. ¹H NMR of **DBICz** (500 MHz, CDCl₃, RT).

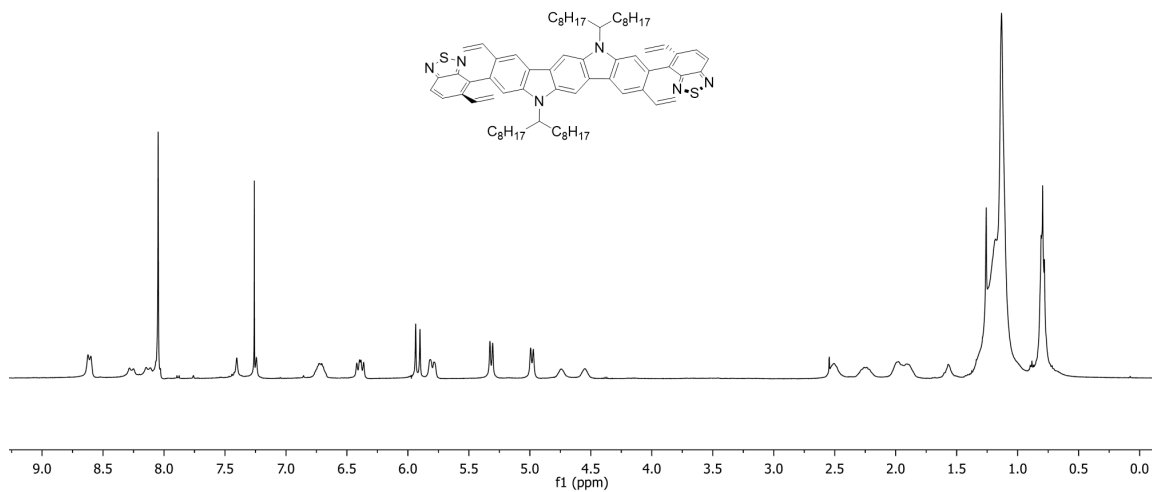


Figure A.25. ^1H NMR of **6** (500 MHz, CDCl_3 , RT).

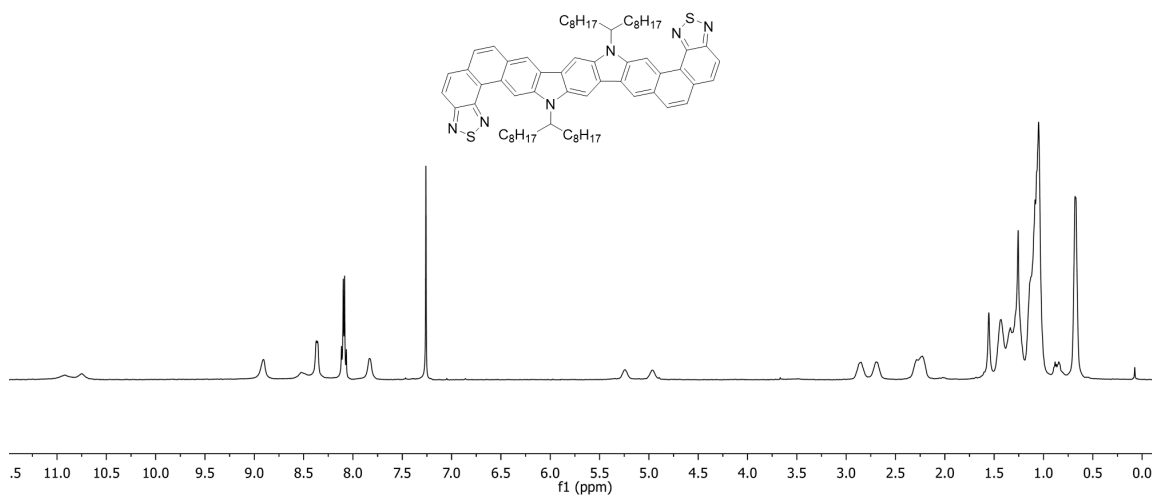


Figure A.26. ^1H NMR of **DBTDICz** (500 MHz, CDCl_3 , RT).

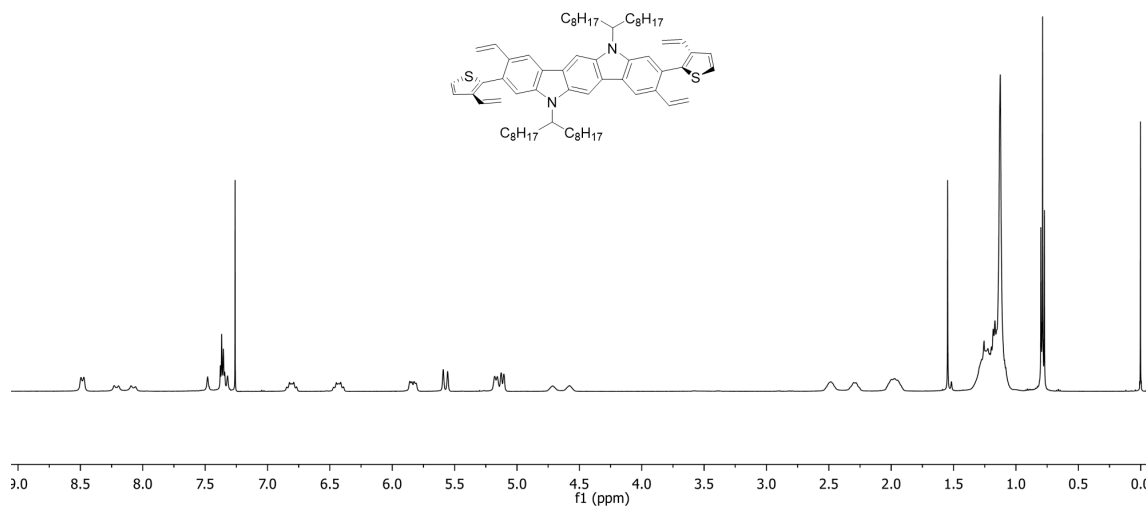


Figure A.27. ^1H NMR of 7 (500 MHz, CDCl_3 , RT).

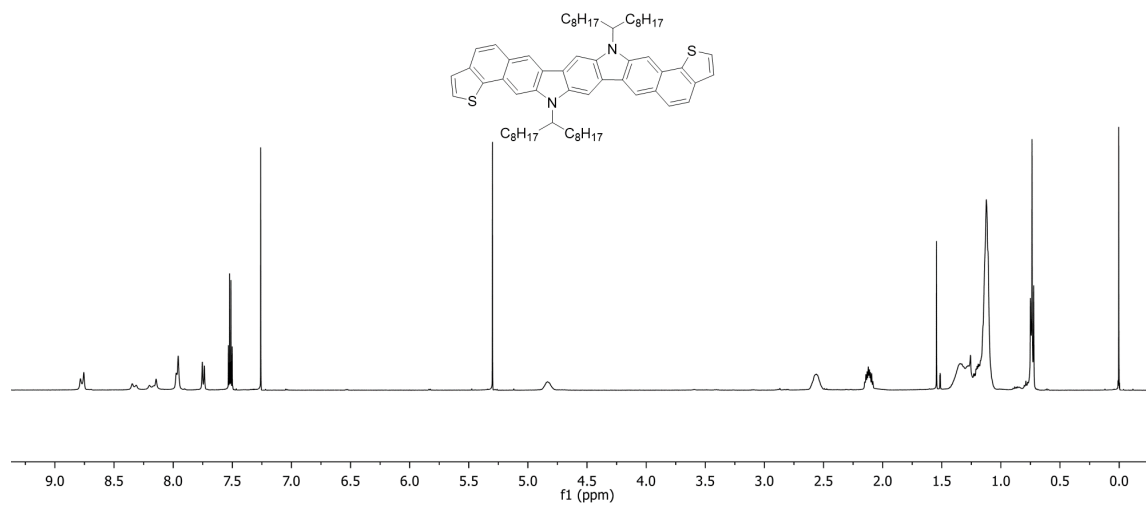


Figure A.28. ^1H NMR of DTICz (500 MHz, CDCl_3 , RT).

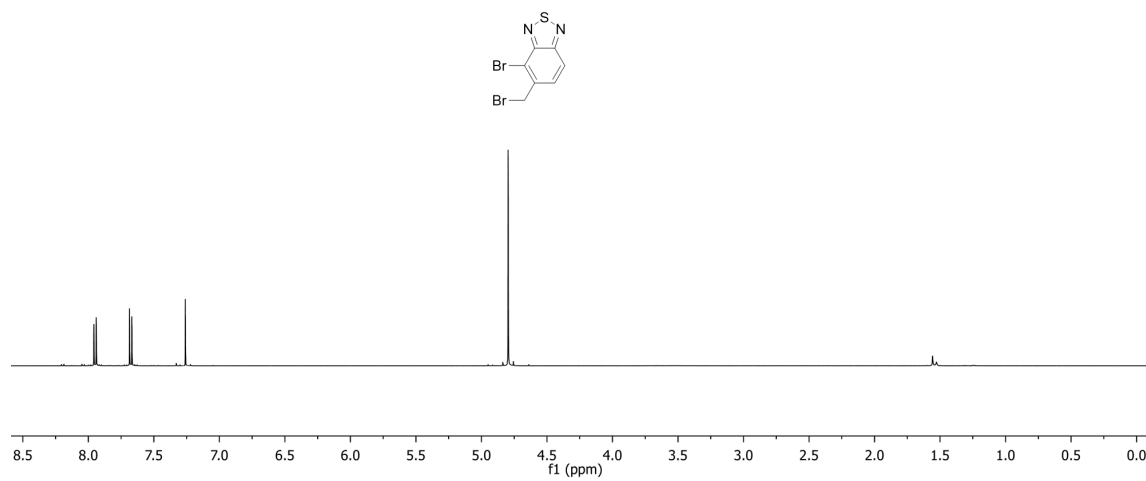


Figure A.29. ^1H NMR of S7 (500 MHz, CDCl_3 , RT).

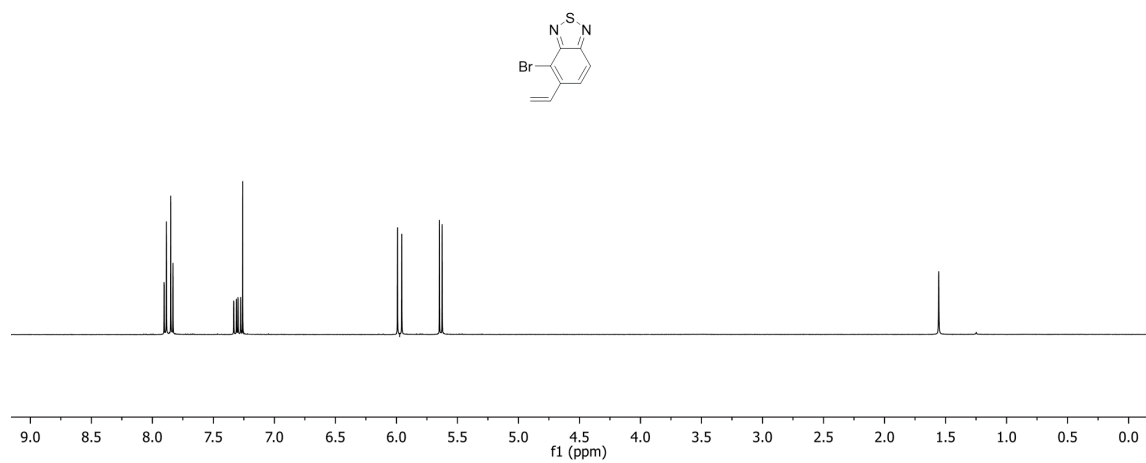
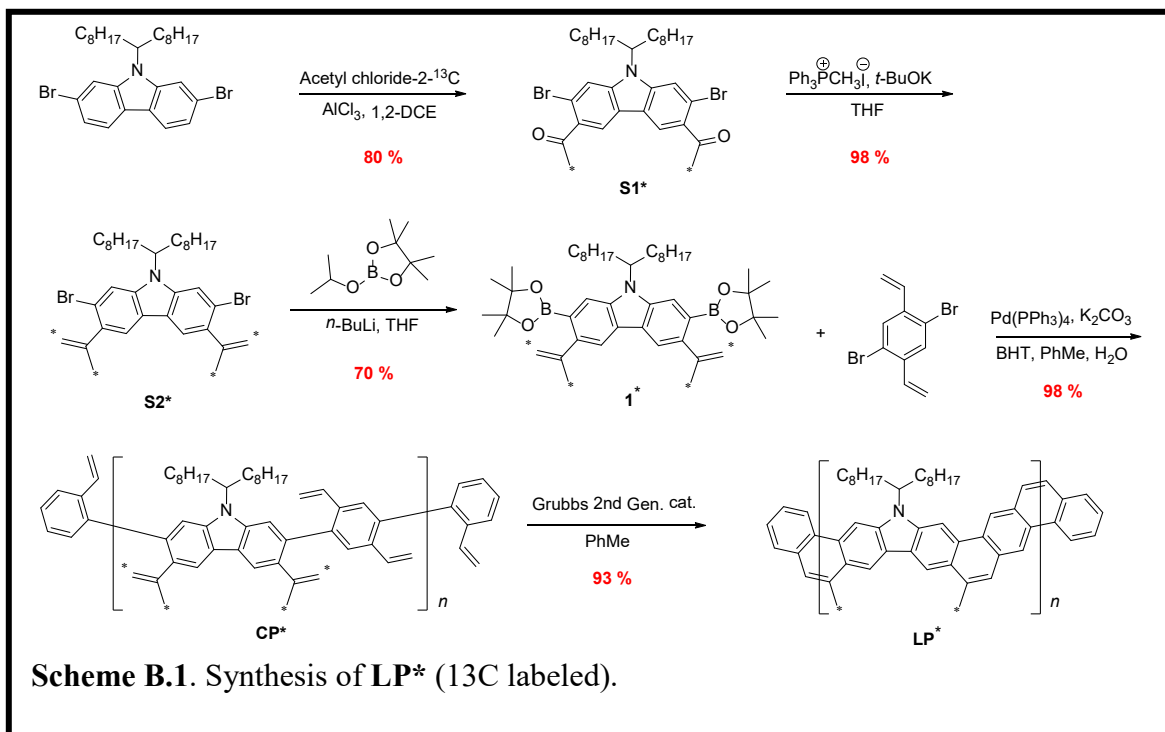


Figure A.30. ^1H NMR of S8 (500 MHz, CDCl_3 , RT).

APPENDIX B

B. 1. Synthesis of ^{13}C Labeled Compounds



S1^* : The same reaction and purification procedure for the synthesis of S1 was followed using acetyl chloride-2- ^{13}C as a carbon-13 source (99% ^{13}C isotope enriched). Yield: 1.3 g (80 %). ^1H NMR (500 MHz, CDCl_3): δ 8.34 (s, 1H), 8.34 (s, 1H), 7.82 (s, 1H), 7.65 (s, 1H), 4.45 (septet, $J = 5.0$ Hz, 1H), 2.77 (d, $^1J_{\text{C-H}} = 128.5$ Hz, 6H), 2.19 (m, 2H), 1.93 (m, 2H), 1.18 (m, 22H), 0.95 (m, 2H), 0.82 (t, $J = 7.0$ Hz, 6H). ^{13}C NMR (125 MHz, CDCl_3): δ 200.1, 144.5, 141.1, 132.6, 132.5, 122.5, 121.0, 118.2, 117.5, 117.3, 115.1, 57.8, 33.6, 31.8, 30.5 (^{13}C enriched), 29.4, 29.2, 26.8, 22.7, 14.2. HR-MALDI: calcd for $\text{C}_{33}\text{H}_{45}\text{Br}_2\text{NO}_2$ [$M+\text{H}$] $^+$ $m/z = 650.1943$; found $m/z = 650.1907$.

S2*: The same reaction and purification procedure for the synthesis of **S2** was followed using methyl-¹³C-triphenylphosphonium iodide as a carbon-13 source (99% ¹³C isotope enriched). Yield: 0.60 g (98 %). ¹H NMR (500 MHz, CDCl₃): δ 7.88 (s, 1H), 7.85 (s, 1H), 7.74 (s, 1H), 7.57 (s, 1H), 5.29 (dd, ¹J_{C-H} = 156.0 Hz, ³J_{C-H} = 6.0 Hz, 2H), 5.03 (dd, ¹J_{C-H} = 157.0 Hz, ³J_{C-H} = 11.0 Hz, 2H), 4.40 (septet, *J* = 5.0 Hz, 1H), 2.20 (dd, ¹J_{C-H} = 127.0 Hz, ³J_{C-H} = 5.5 Hz, 6H), 2.20 (m, 2H), 1.91 (m, 2H), 1.16 (m, 22H), 1.03 (m, 2H), 0.84 (t, *J* = 7.0 Hz, 6H). ¹³C NMR (125 MHz, CDCl₃): δ 146.7, 142.2, 138.7, 135.7, 122.8, 121.3, 120.9, 120.7, 119.4, 118.9, 116.3 (¹³C enriched), 115.4, 113.1, 57.1, 33.7, 31.9, 29.5, 29.4, 29.3, 26.9, 24.5 (¹³C enriched), 22.8, 14.3. HR-MALDI: calcd for C₃₃H₄₅Br₂NO₂ [*M*+H]⁺ *m/z* = 648.2425; found *m/z* = 648.1810.

1*: The same reaction and purification procedure for the synthesis of **1** was followed. Yield: 0.28 g (70 %). ¹H NMR (500 MHz, CDCl₃): δ 7.96 (s, 1H), 7.94 (s, 1H), 7.81 (s, 1H), 7.65 (s, 1H), 5.11 (dd, ¹J_{C-H} = 155.0 Hz, ³J_{C-H} = 6.0 Hz, 2H), 4.95 (dd, ¹J_{C-H} = 155.0 Hz, ³J_{C-H} = 11.0 Hz, 2H), 4.59 (septet, *J* = 5.0 Hz, 1H), 2.25 (dd, ¹J_{C-H} = 126.5 Hz, ³J_{C-H} = 5.5 Hz, 6H), 2.25 (m, 2H), 1.91 (m, 2H), 1.37 (s, 24H), 1.14 (m, 22H) 0.83 (t, *J* = 7.0 Hz, 1H). ¹³C NMR (125 MHz, CDCl₃): δ 148.3, 141.3, 139.9, 138.0, 126.1, 125.1, 123.7, 119.2, 119.0, 117.6, 115.0, 113.9 (¹³C enriched), 83.7, 56.5, 34.1, 31.9, 29.7, 29.5, 29.4, 26.9, 25.3 (¹³C enriched), 24.9, 22.8, 14.2. HR-MALDI: calcd for C₄₇H₇₃B₂NO₄ [*M*+H]⁺ *m/z* = 742.5940; found *m/z* = 742.5876.

CP*: The same reaction and purification procedure for the synthesis of **CP** was followed. Yield: 98 %. (*M_n* = 6 kg/mol, PDI = 2.4). **CP*** was further subjected to

preparative recycling SEC to remove oligomers (0.45 g, 74 %, $M_n = 17$ kg/mol, PDI = 1.37 by SEC).

LP*: The same reaction and purification procedure for the synthesis of **LP** was followed. Yield: 93% (M_n : 13 kg/mol, PDI: 1.71 by SEC).

B. 2. Ring-closing Olefin Metathesis Optimization.

Screened conditions for ring-closing olefin metathesis are summarized in **Table B.1**. In preliminary screening for the synthesis of **3**, higher temperature afforded better yield (**Entry 1–4**). The condition at high temperature for **3**, however, was not enough to convert vinyl groups into aromatic rings quantitatively (**Entry 3–4**), probably due to the thermal decomposition of Grubbs' 2nd generation catalyst.⁶ Therefore, several different ways for the addition of the catalyst were tried (**Entry 5–11**). The optimized condition requires the addition of the catalyst in toluene solution over 4 hr at reflux temperature slowly using syringe pump, followed by stirring the reaction mixture at reflux temperature for an additional 2 hours (**Entry 5**). Using the optimized condition, **CP** was converted to **LP** in 91% yield (**Entry 10**).

Table B.1. The optimization of ring-closing olefin metathesis.

Entry	Product	Catalyst (mol %) ^a	Addition of catalyst	Solvent	Temp. (°C)	Time (h)	Yield (%)
1	3	10 ^b	1 portion	CH ₂ Cl ₂	35	24	39 ^c
2	3	10	1 portion	CH ₂ Cl ₂	35	24	54 ^c
3	3	10	1 portion	PhMe	100	24	69 ^c
4	3	10	1 portion	PhMe	Reflux	24	77 ^c
5	3	10	Syringe pump for 4 h	PhMe	Reflux	6	96 ^c
6	LP	10	1 portion	PhMe	Reflux	24	44 ^d
7	LP	20	1 portion	PhMe	Reflux	24	71 ^d
8	LP	20	2 portions in 12 h	PhMe	reflux	24	89 ^d
9	LP	20	4 portions in 6 h	PhMe	reflux	24	quant. ^d e 91 ^c
10	LP	20	Syringe pump for 4 h	PhMe	reflux	6	quant. ^d e
11	LP	20	Syringe pump For 6 h	PhMe	reflux	8	quant. ^d e

^a Grubbs' 2nd generation catalyst was used. ^b Grubbs' 1st generation catalyst was used ^c Isolated yield. ^d

Conversion yield calculated by ¹H NMR based on the integration ratio between vinyl peaks on 6.75 (2H) and 5.69 ppm (2H) and newly appeared aromatic peaks on 9.03 ppm (5H). ^e Too small amount of unreacted defect which was difficult to integrate was observed.

B. 3. Size Exclusion Chromatography (SEC)

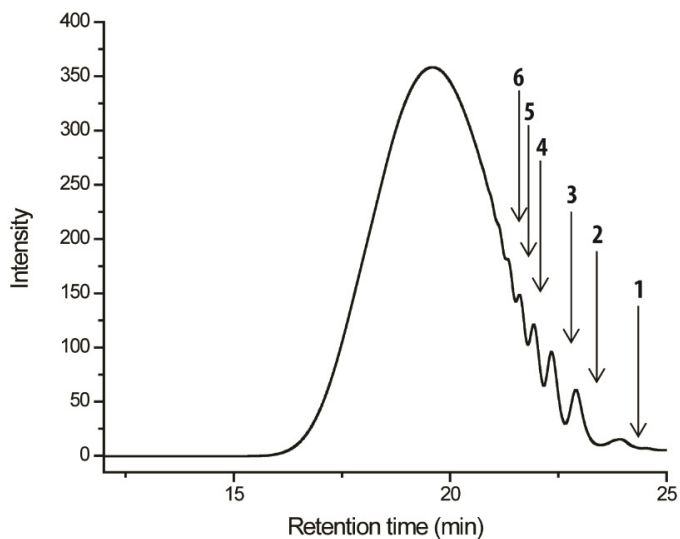


Figure B.1. Size exclusion chromatogram of **CP** before purified by preparative recycling SEC. The oligomers generated in this step-growth polymerization can be clearly identified (the numbered arrows).

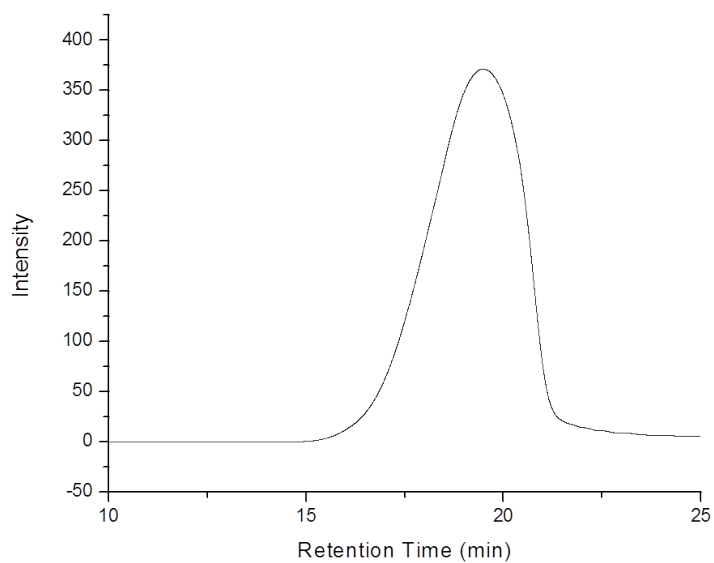


Figure B.2. Size exclusion chromatogram of **CP** after purified by preparative recycling SEC.

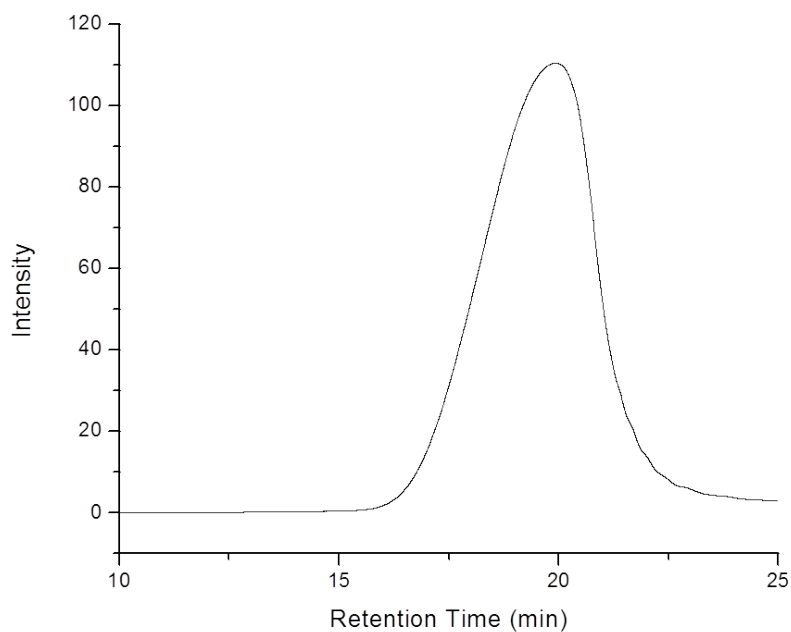
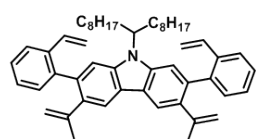


Figure B.3. Size exclusion chromatogram of **LP**.

B. 4. IR spectra

FT-IR spectra of **2**, **3**, **CP**, and **LP** were recorded neat on an ZnSe Attenuated Total Reflection (ATR) apparatus. Alkenyl stretching peaks are indicated as a red arrow. The disappearance of C=C stretching peak (3080 cm^{-1}) and =C-H stretching peak (1626 cm^{-1}) of **2** is indicated as a dashed circle (red) in the spectrum of **3**. The same trend was also observed between **CP** and **LP**. The disappearance of C=C stretching peak (3080 cm^{-1}) and =C-H stretching peak (1624 cm^{-1}) of **CP** is indicated as a dashed circle (red) in the spectrum of **LP**.



Ring Closing
Metathesis

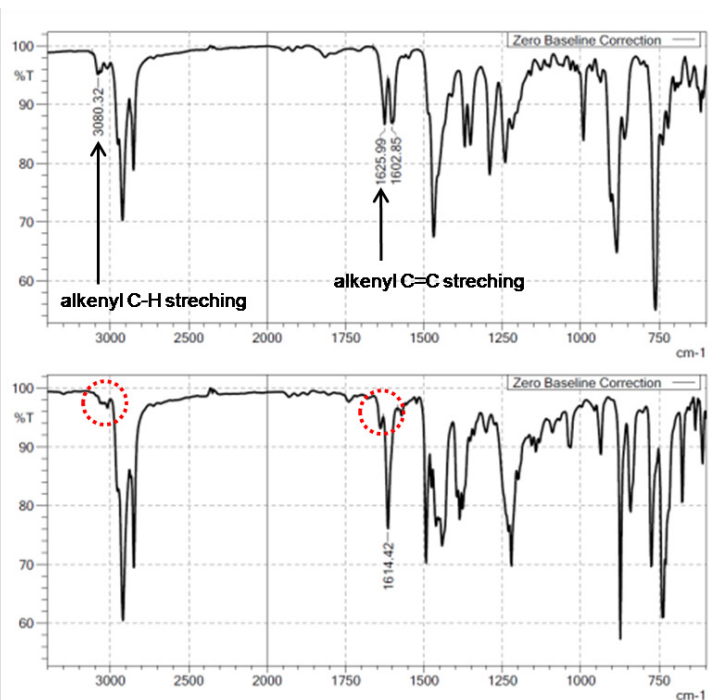
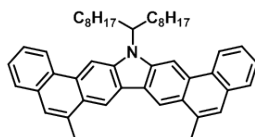
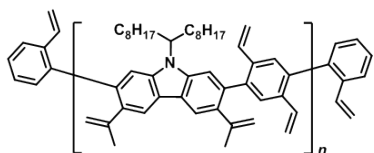


Figure B.4. IR spectra comparison of 2 and 3.



Ring Closing
Metathesis

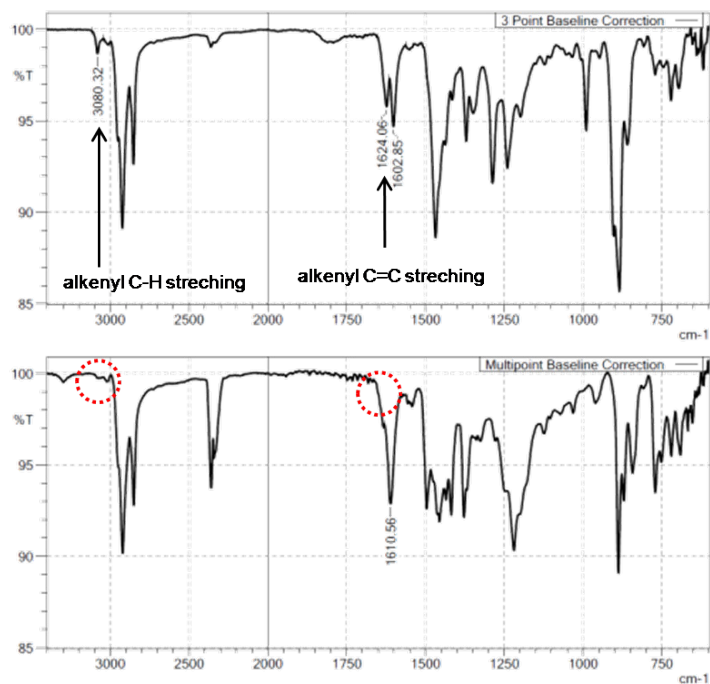
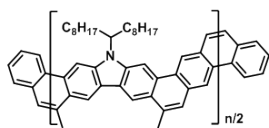


Figure B.5. IR spectra comparison of CP and LP.

B. 5. ^1H - ^1H NOESY NMR Spectrum of **3**

In order to fully assign the proton peaks of **3**, ^1H - ^1H NOESY was recorded at room temperature in CDCl_3 . The sample solution was degassed by freeze-pump-thaw 3 times before the experiment. The experiment was performed after 90° pulse width calibration. Each proton peaks were assigned based on the observed correlation signals (marked as double head arrows).

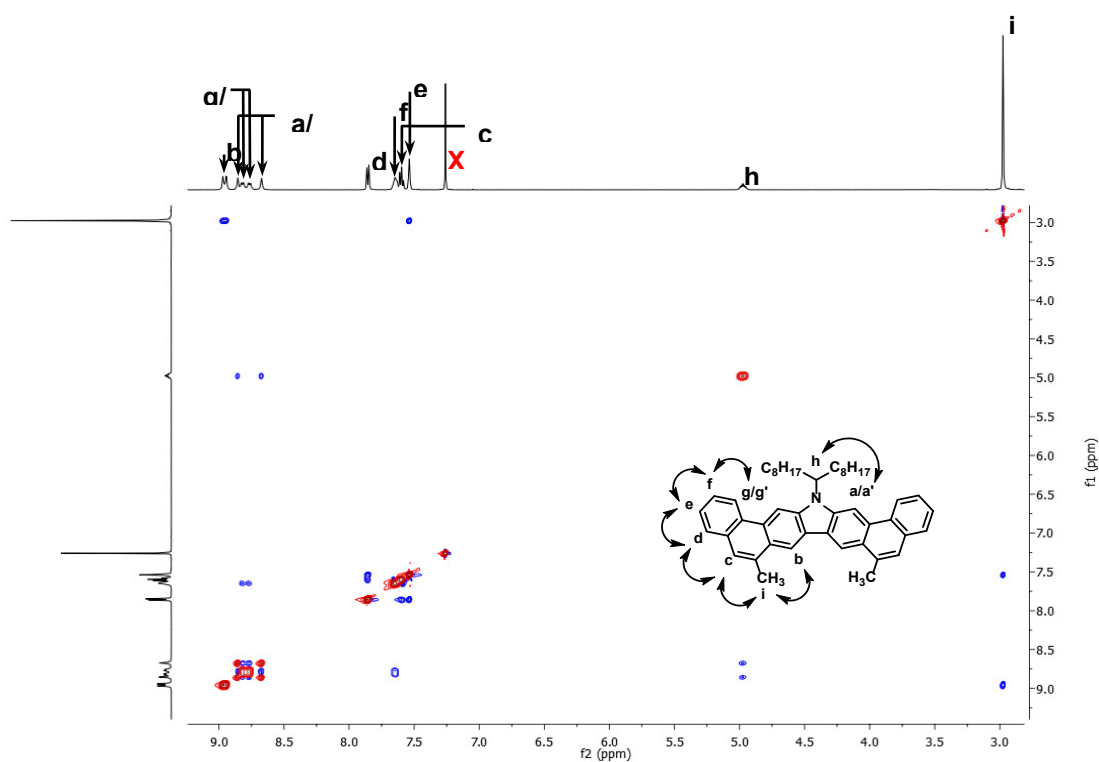


Figure B.6. Partial ^1H - ^1H NOESY spectrum of **3** (500 MHz, CDCl_3 , RT). Double head arrows in the figure indicate the observed through space nuclear overhauser effect in the experiment.

B. 6. ^1H and ^{13}C NMR Spectra

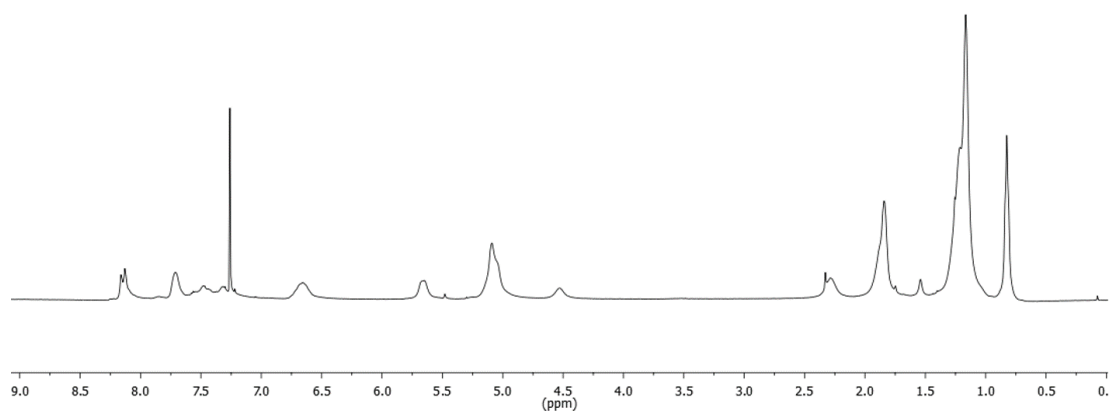
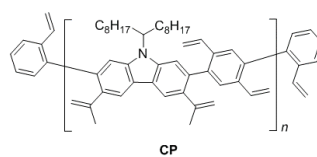


Figure B.7. ^1H NMR of CP (500 MHz, CDCl_3 , RT).

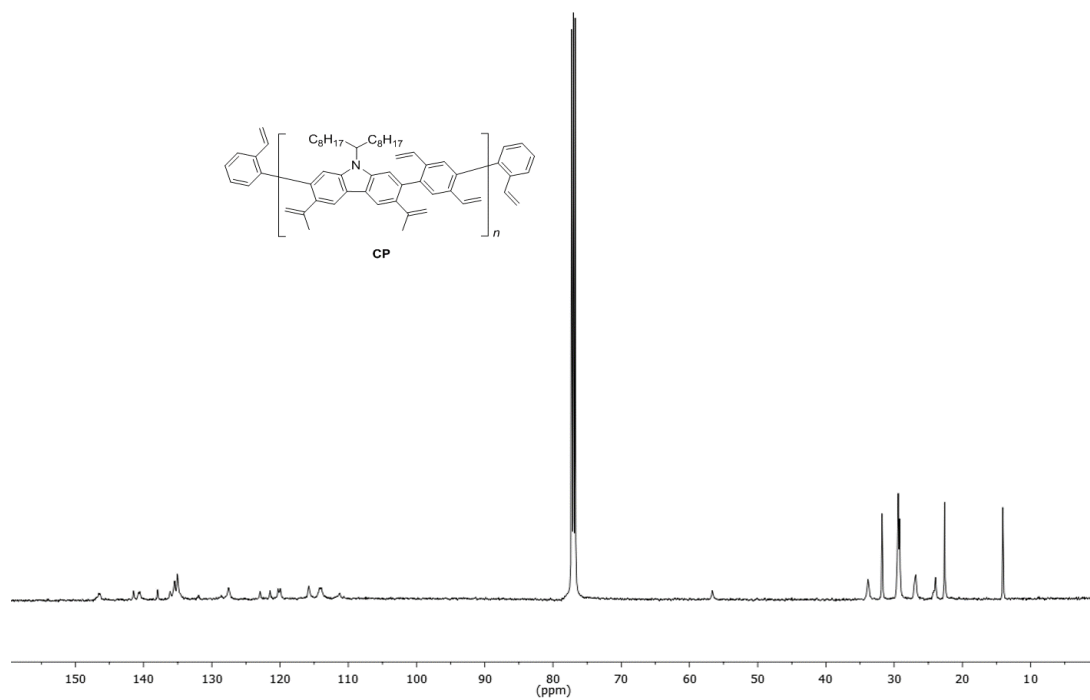


Figure B.8. ^{13}C NMR of CP (125 MHz, CDCl_3 , RT).

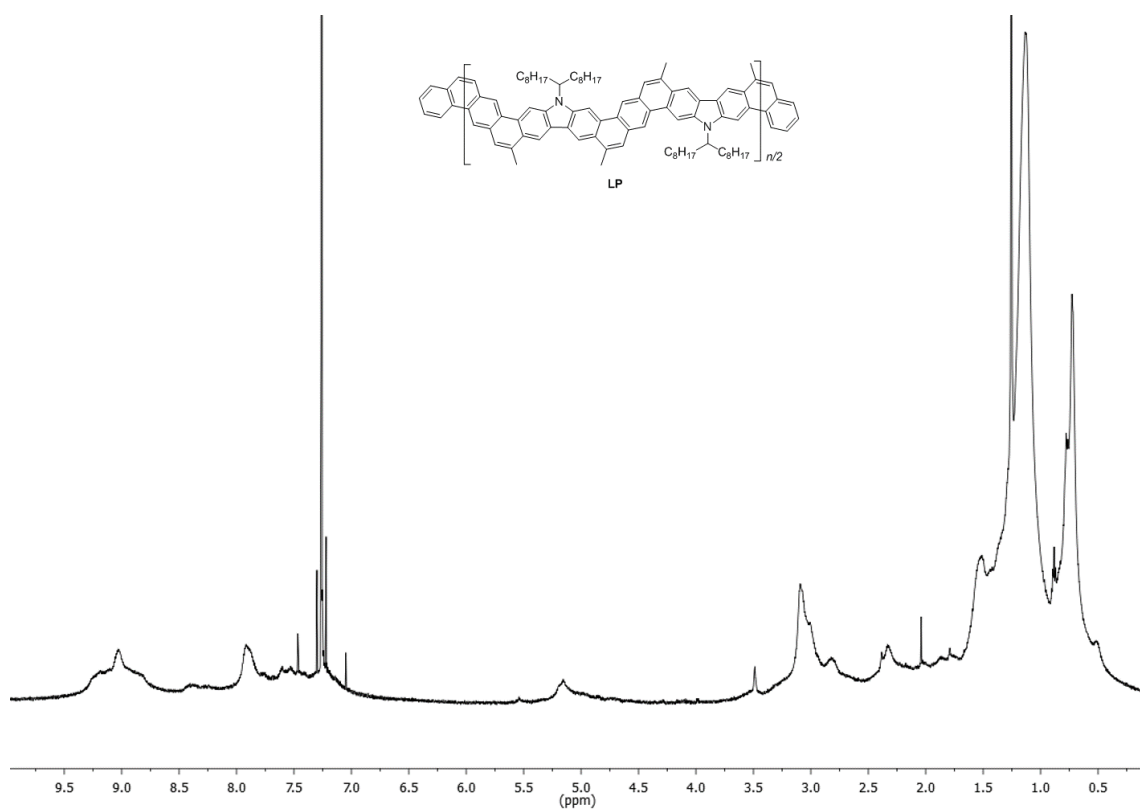


Figure B.9. ^1H NMR of LP (500 MHz, CDCl_3 , RT).

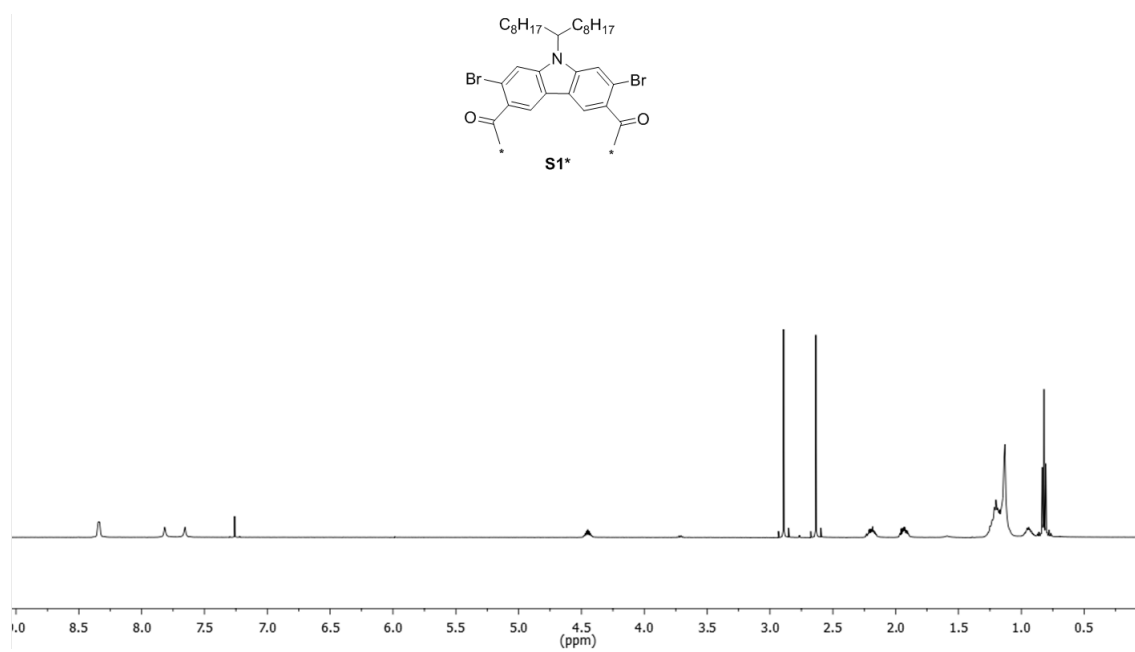


Figure B.10. ^1H NMR of S1* (500 MHz, CDCl_3 , RT).

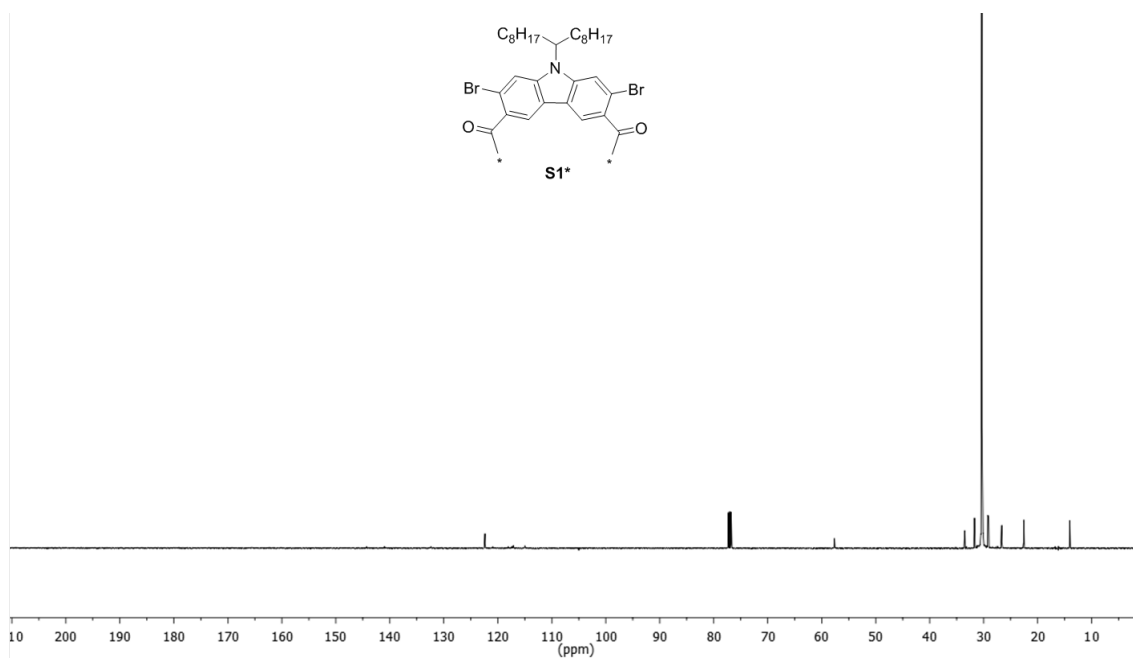


Figure B.11. ¹³C NMR of S1* (125 MHz, CDCl₃, RT).

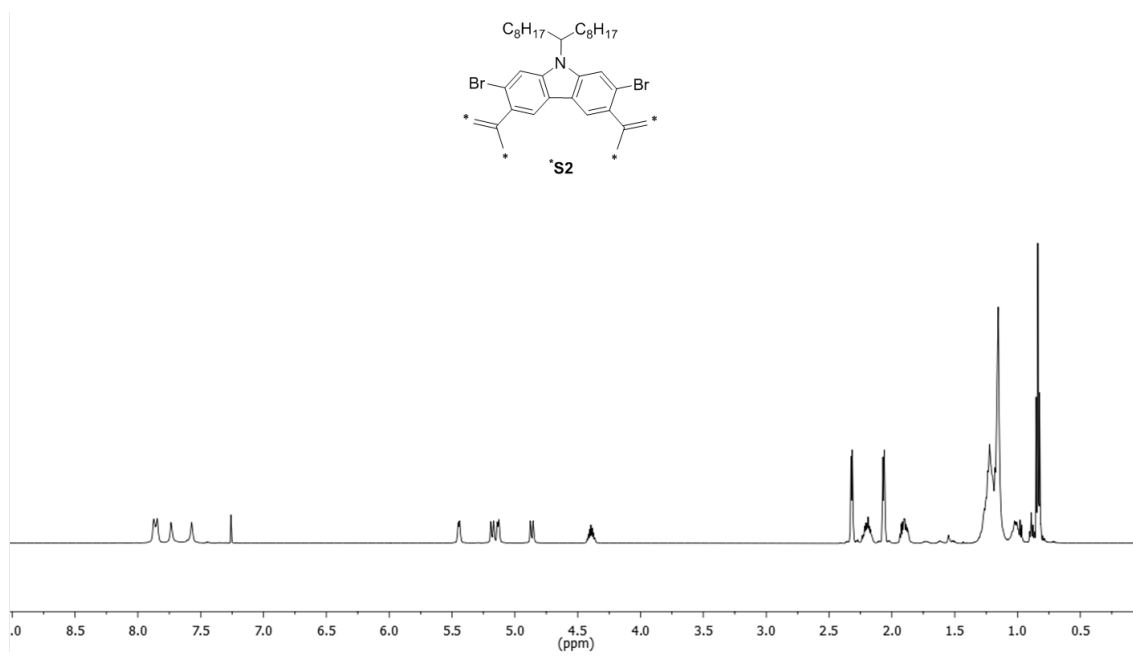


Figure B.12. ¹H NMR of S2* (500 MHz, CDCl₃, RT).

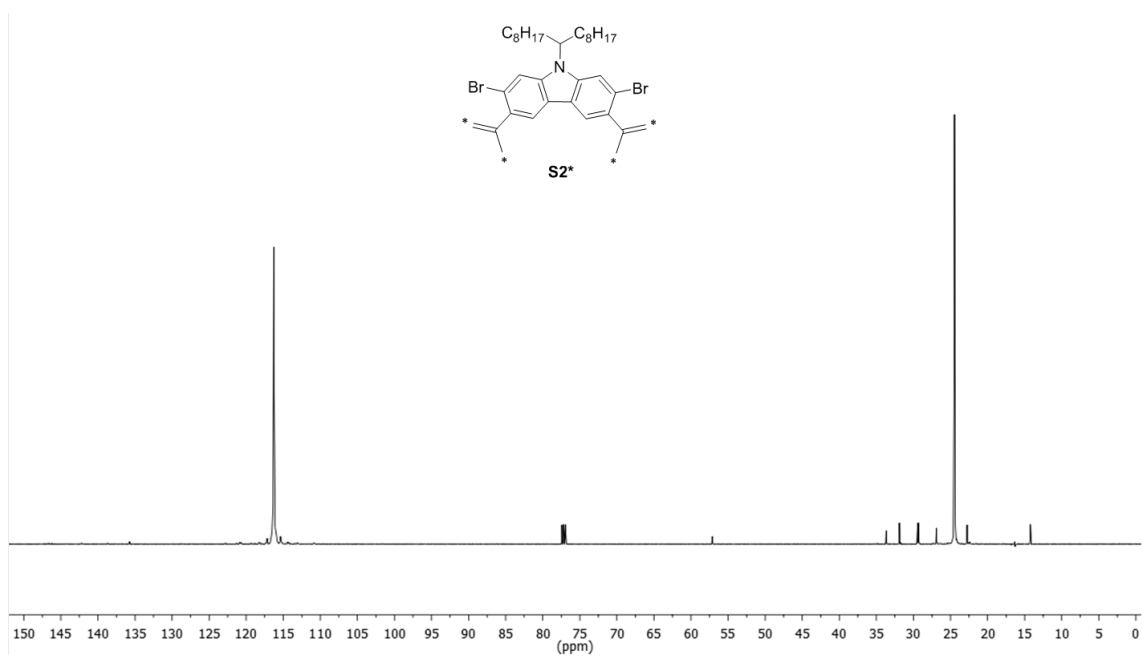


Figure B.13. ¹³C NMR of **S2*** (125 MHz, CDCl₃, RT).

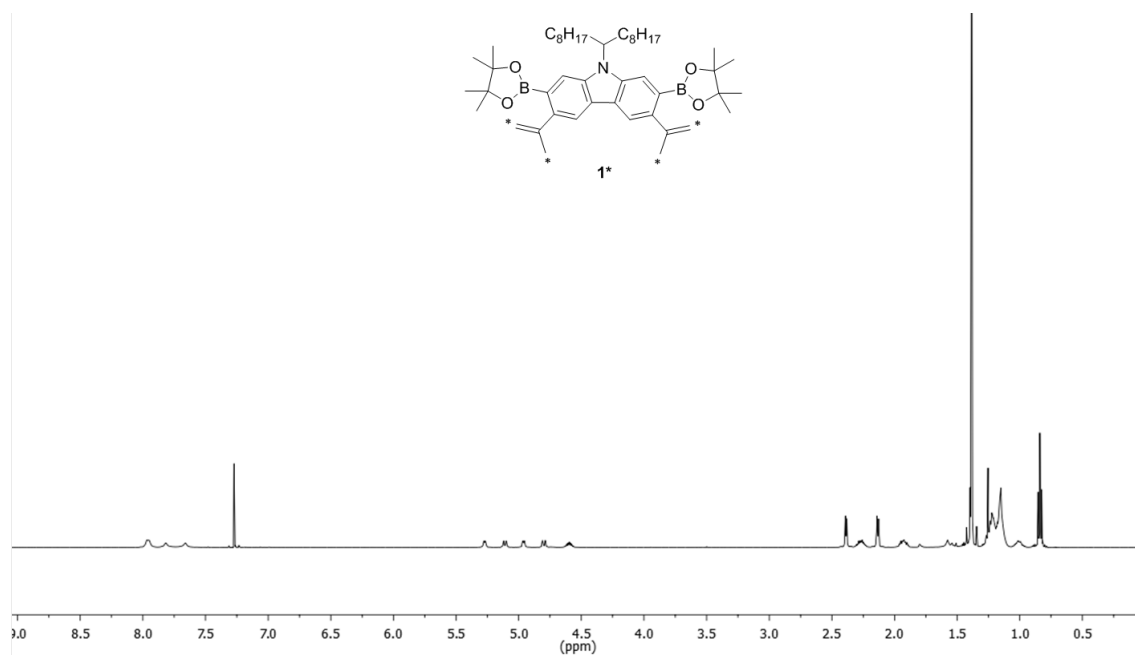


Figure B.14. ¹H NMR of **1*** (500 MHz, CDCl₃, RT).

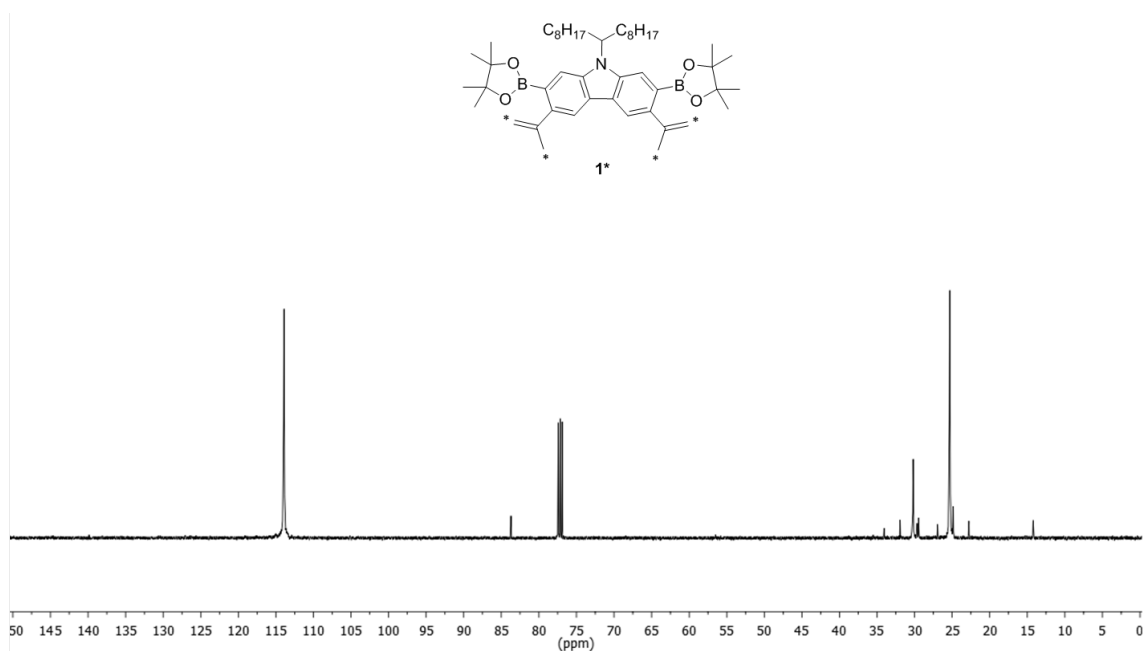


Figure B.15. ^{13}C NMR of **1*** (125 MHz, CDCl_3 , RT).

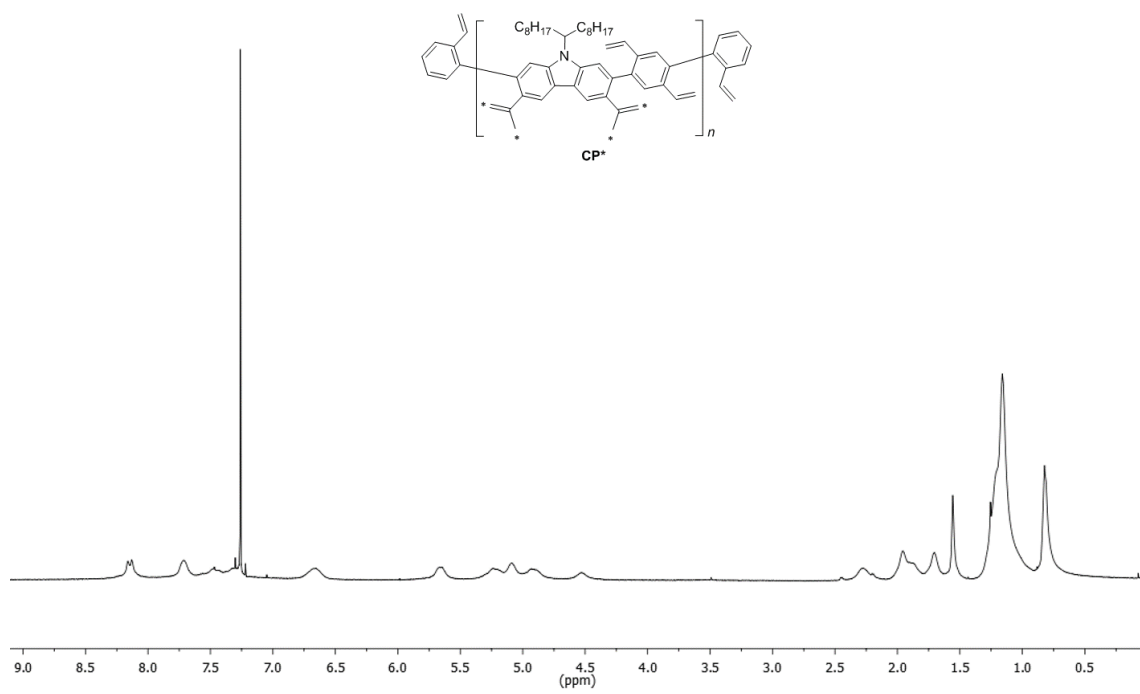


Figure B.16. ^1H NMR of **CP*** (500 MHz, CDCl_3 , RT).

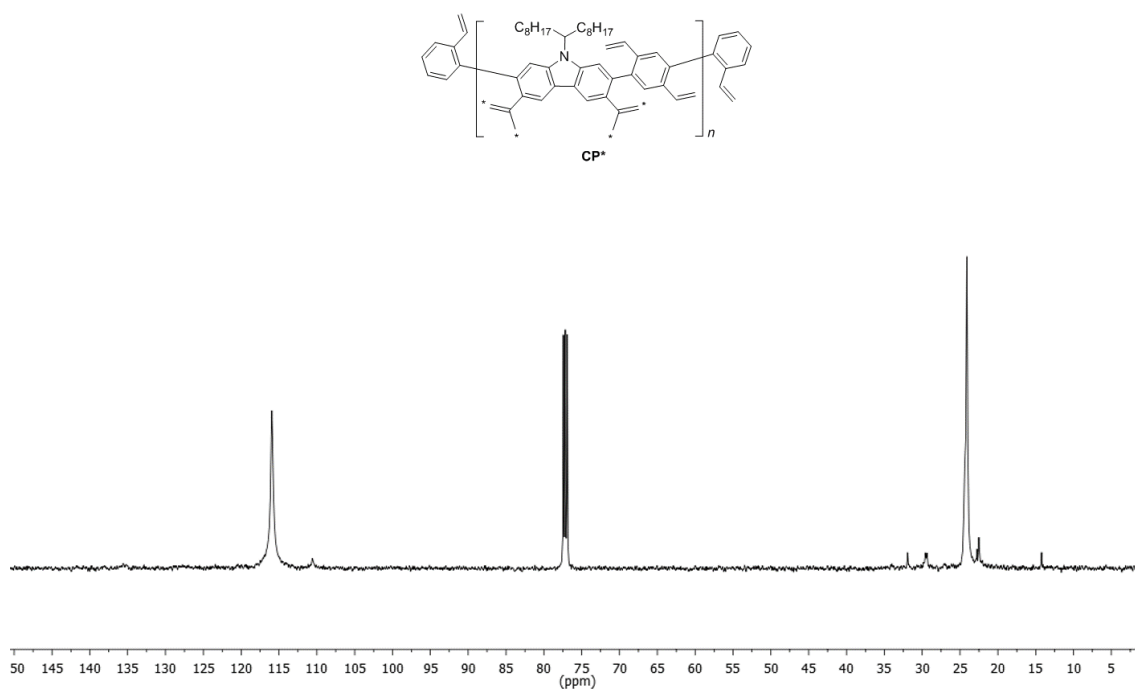


Figure B.17. ¹³C NMR of CP* (125 MHz, CDCl₃, RT). S/N ratio of the spectrum is 94.

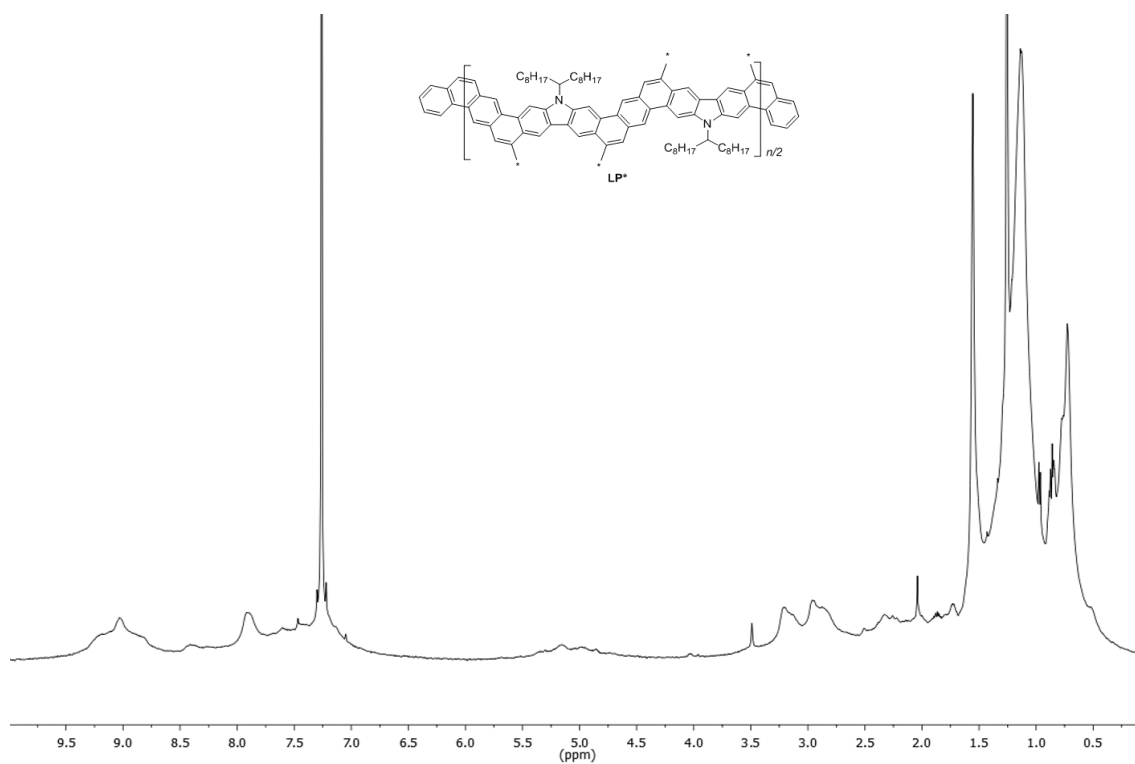


Figure B.18. ¹H NMR of LP* (500 MHz, CDCl₃, RT).

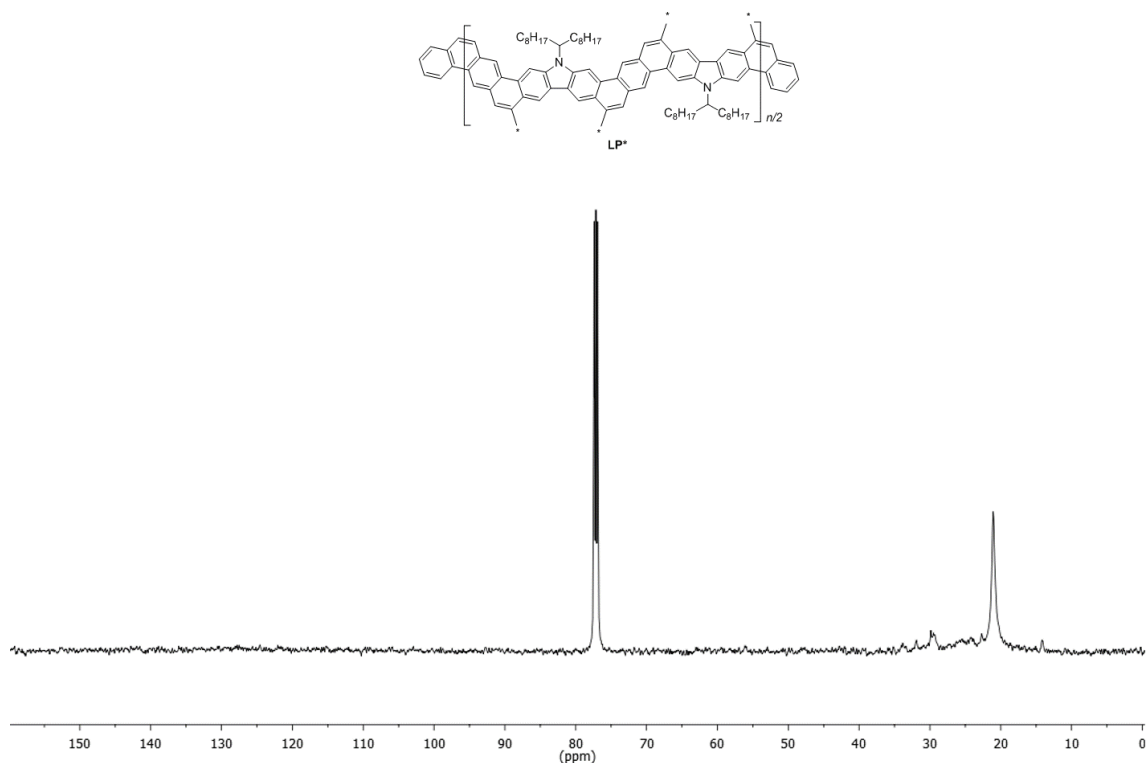


Figure B.19. ^{13}C NMR of **LP*** (125 MHz, CDCl_3 , RT). S/N ratio of the spectrum is 376.

B. 7. Quantum Yield

Quantum yield of **CP** and **LP** was measured by Edinburgh Instruments FLS920. 10^{-6} M solution of **CP** and **LP** in CHCl_3 was used to measure quantum yields by integrating sphere system using the excited wavelength 285 nm and 400 nm, respectively. Quantum yield of **CP** was too low to quantify. Quantum yield of **LP** was measured to be 15 %.

B. 8. UV-vis and Fluorescence Spectra

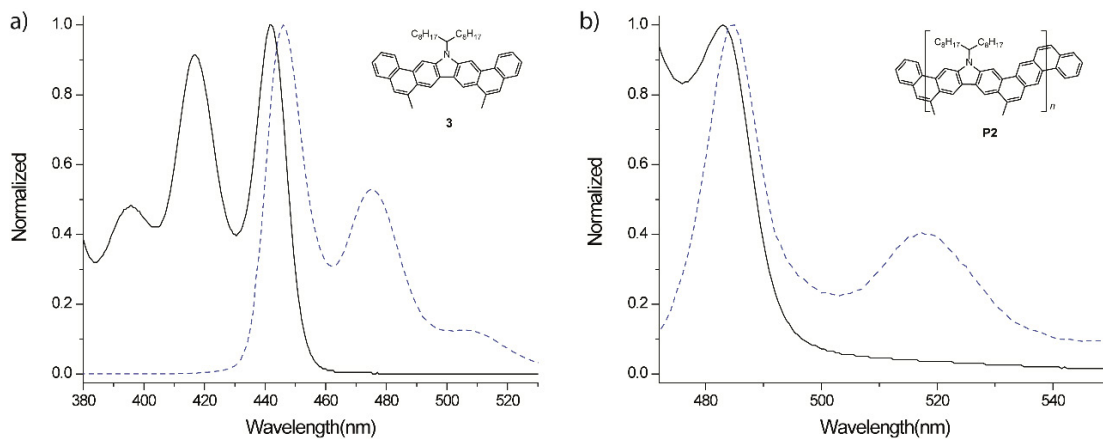


Figure B.20. a) Normalized UV/vis (black solid) and fluorescence (blue dash) spectra of **3** in the range of 380-530 nm. The difference between HOMO-LUMO transition of absorption and LUMO-HOMO transition of emission of **3** was measured to be ~ 4 nm. b) Normalized UV/vis (black solid) and fluorescence (blue dash) spectra of **LP** in the range of 380-530 nm. The difference between HOMO-LUMO transition of absorption and LUMO-HOMO transition of emission of **LP** was measured to be ~ 1 nm.

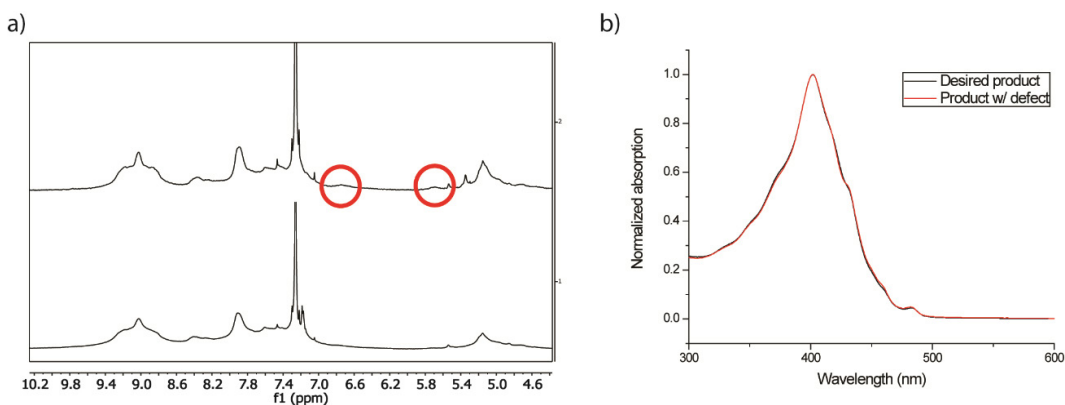


Figure B.21. a) ¹H NMR of **LP** with small amount of defect (red circles, top) and the desired product (bottom). b) Normalized UV-vis spectrum of the product with small amount of defect (red) and the desired product (black).

B. 9. Thermal Gravimetric Analysis (TGA)

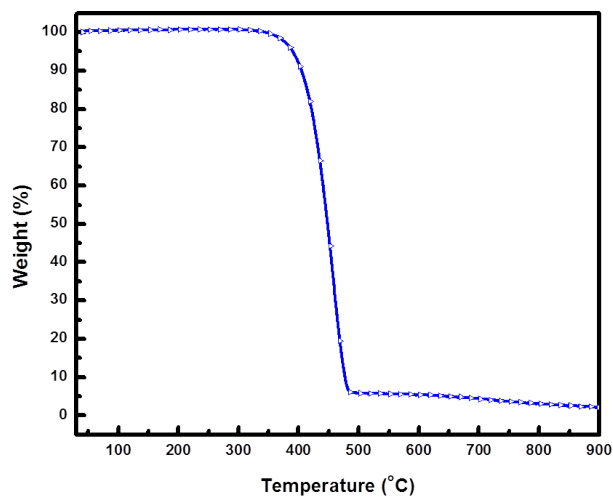


Figure B.22. TGA trace of **3**. The sample lost 5 % weight at 390 °C as a result of sublimation. The full sublimation range was 450 - 485 °C.

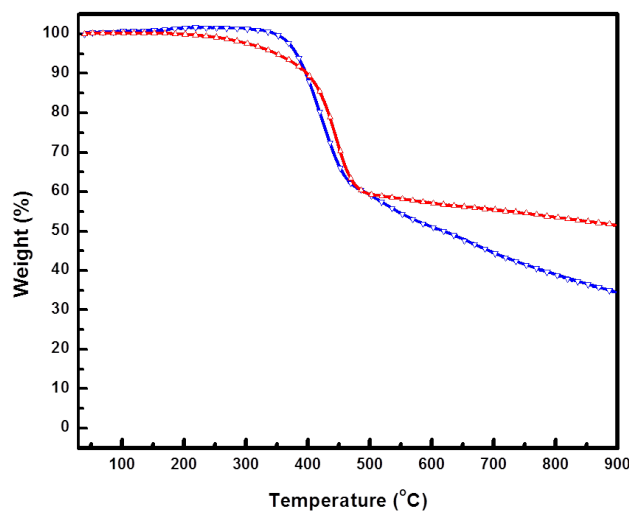


Figure B.23. TGA trace of **CP** (blue) and **LP** (red). Decomposition temperature of **CP** (T_d , 5 % weight loss) was 380 °C with a 34 % carbonization yield at 900 °C. Decomposition temperature of **LP** (T_d , 5 % weight loss) is 348 °C with a 52 % carbonization yield at 900 °C.

B. 10. Differential Scanning Calorimetry (DSC)

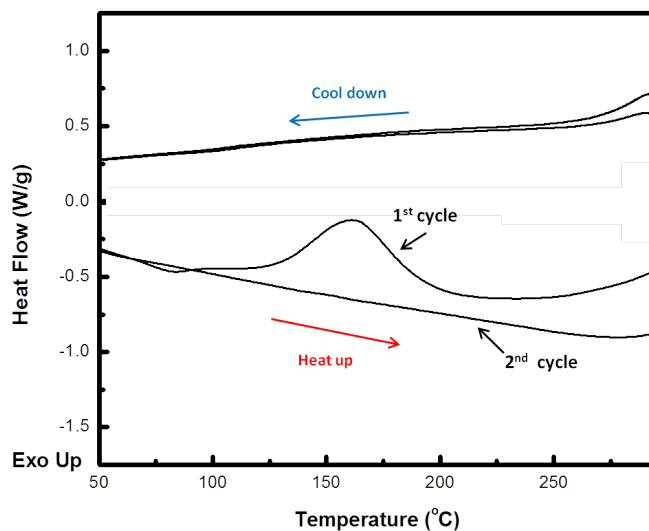


Figure B.24. DSC trace of CP. Onset of the exothermic transition (129 °C) in the 1st cycle indicates an irreversible reaction because no transition was observed in the 2nd cycle. The sample after 2nd cycle was not soluble at all in CHCl₃. The reaction takes place at 129 °C was probably the free radical cross-linking of the vinyl groups.

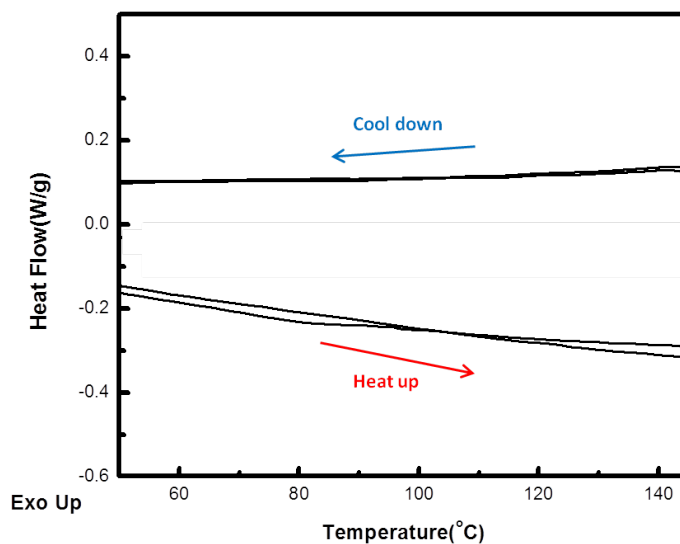


Figure B.25. DSC trace of LP. No thermal transition or reaction was observed.

B. 11. DFT Calculation

Atomic structures of model oligomers were optimized with density functional theory (DFT) calculations using the B3LYP/6-311G. Molecular orbital shapes and energies were calculated at the optimized geometries. The alkyl chains are replaced with isopropyl groups for computational simplicity. Orbital pictures were generated with Gaussview 5.08. For compound **3** computed electronic spectra, B3LYP/6-311G(d,p) was applied to optimize the atomic structure with DFT calculation, and UV/vis spectra was calculated with time-dependent density functional theory (TDDFT) at optimized geometries with same level. All quantum-chemical calculations were performed with the Gaussian09 package.

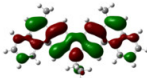
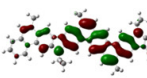
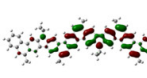
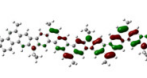
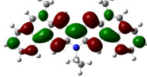
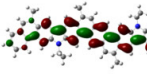
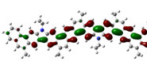
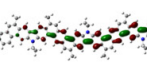
	N=1	N=2	N=3	N=4
LUMO	 -1.63eV	 -1.81eV	 -1.87eV	 -1.90eV
HOMO	 -5.20eV	 -5.03eV	 -4.99eV	 -4.97eV

Figure B.26. HOMO and LUMO energy levels of model oligomer ($N=1, 2, 3$ or 4 at B3LYP/6-311G level).

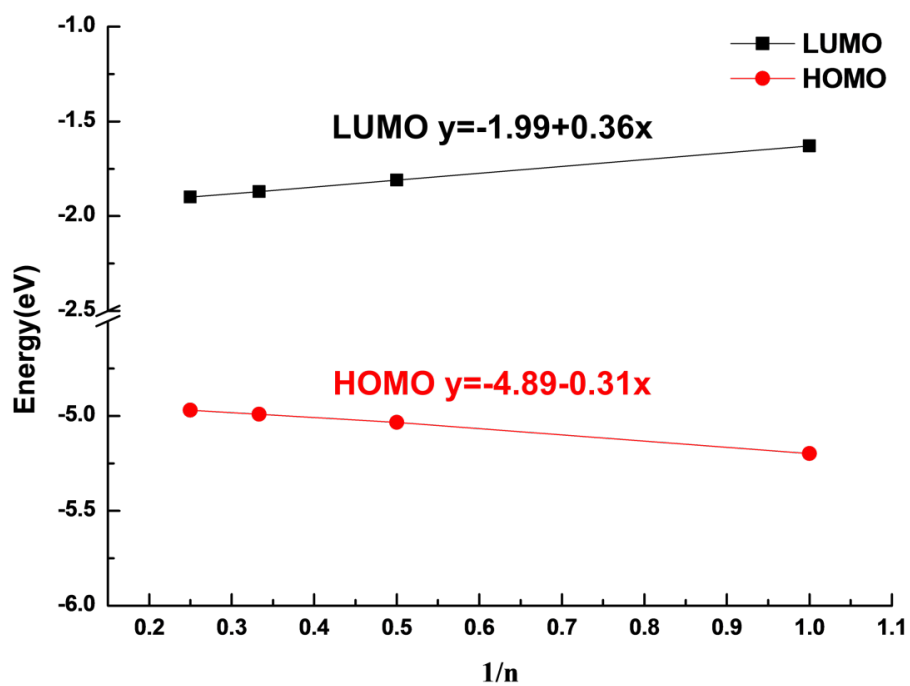


Figure B.27. HOMO and LUMO energy levels for fully conjugated polymer were extrapolated from the values computed for model oligomers ($N = 1, 2, 3$ or 4 at B3LYP/6-311G level). $E_{\text{HOMO}} = -4.89$ eV, $E_{\text{LUMO}} = -1.99$ eV and $E_g = 2.90$ eV.

B. 12. Scanning Tunneling Microscopy (STM)

Scanning tunneling microscopy (STM) measurement was performed at room temperature using Easyscan 2 system from Nanosurf Inc. A 0.5 mM solution of **CP** and **LP** (0.3 mg/ml) in chloroform was prepared with alternative sonication and waiting steps of 3 mins each for ~15 mins to completely dissolve **CP** and **LP**. Highly ordered pyrolytic graphite (HOPG) substrate was heated on a hot plate to 90°C, and a drop of **CP** and **LP** solution was added. The substrate was allowed to cool under ambient conditions before performing the imaging under constant current mode.

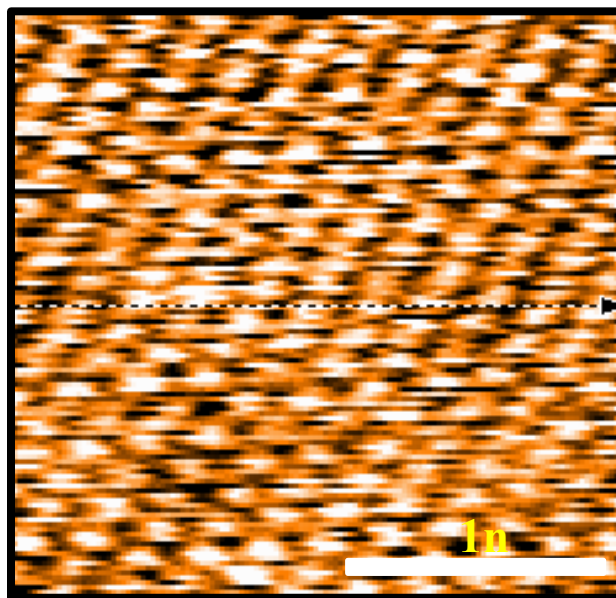


Figure B.28. STM image of the bare HOPG substrate. Note that the scale bar is 1 nm, much smaller than that of the image of **LP** in the main text.

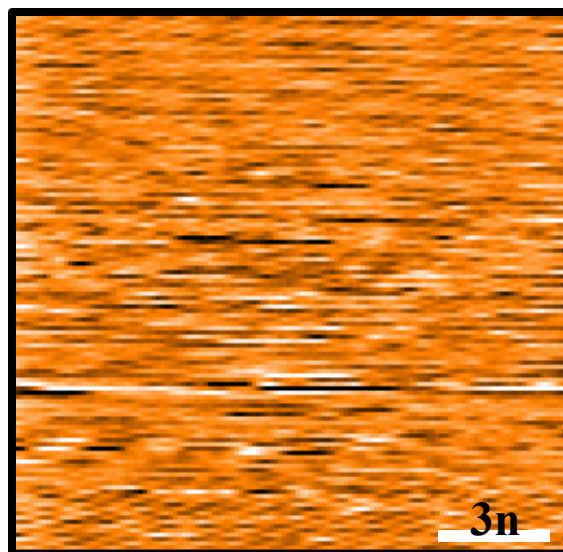
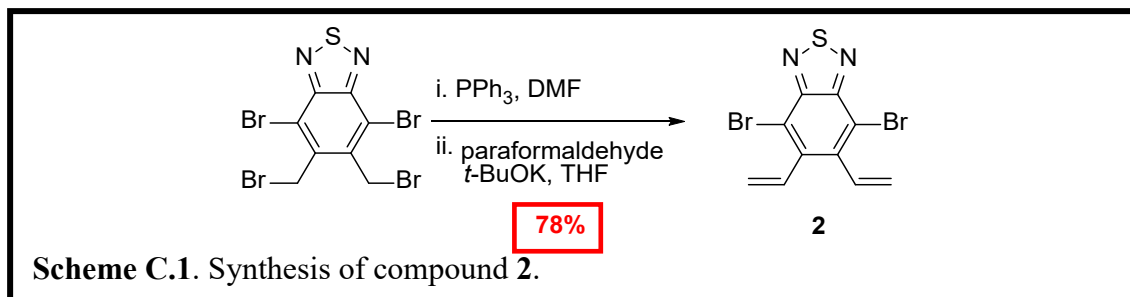


Figure B.29. A representative STM image of the CP sample on HOPG processed under the similar condition, showing poor contact and no ordered feature. Multiple attempts have been made to identify ordered region.

APPENDIX C

C. 1. Synthesis



2 (4,7-dibromo-5,6-diethenyl-2,1,3-benzothiadiazole): The mixture of compound 4,7-dibromo-5,6-bis(bromomethyl)-2,1,3-benzothiadiazole (3.0 g, 6.3 mmol) and PPh₃ (4.1 g, 15.8 mmol) in DMF (40 mL) was stirred at 80 °C for 18 h. After being cooled to room temperature, the reaction mixture was concentrated under reduced pressure. The residue and paraformaldehyde (4.3 g) were suspended in THF (70 mL) under N₂. While stirring, *t*-BuOK (2.1 g, 18.9 mmol) was added in small portions over 10 min. After 30 min, the reaction was quenched with water and extracted with CH₂Cl₂ (3 × 30 mL). The combined organic layer was dried over MgSO₄, filtered through Celite, and concentrated under reduced pressure. The residue was purified by flash column chromatography (SiO₂, hexane) to give the product **2** (1.7 g, 78%) as a white solid. ¹H NMR (500 MHz, CDCl₃): δ 6.70 (dd, *J*₁ = 17.5 Hz, *J*₂ = 12.0 Hz, 2H), 5.76 (d, *J*₁ = 12.0 Hz, *J*₂ = 1.5 Hz, 2H), 5.61 (dd, *J*₁ = 17.5 Hz, *J*₂ = 1.5 Hz, 2H). ¹³C NMR (125 MHz, CDCl₃): δ 152.31, 140.56, 134.42, 124.49, 113.72. LR-APCI: calcd for C₁₀H₆Br₂N₂S [M+H]⁺ *m/z* = 346.87; found *m/z* = 346.93.

C. 2. Size Exclusion Chromatography (SEC).

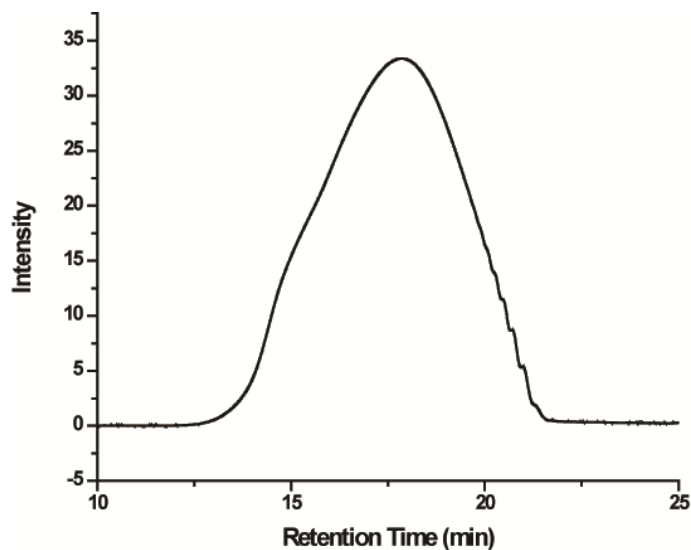


Figure C.1. Size exclusion chromatogram of **DACP** after purification by preparative recycling SEC. $M_n^{\text{SEC}} = 43 \text{ kg/mol}$, PDI = 4.34. It is worthy to note that aggregation feature was observed as a shoulder peak in the high molecular weight region.

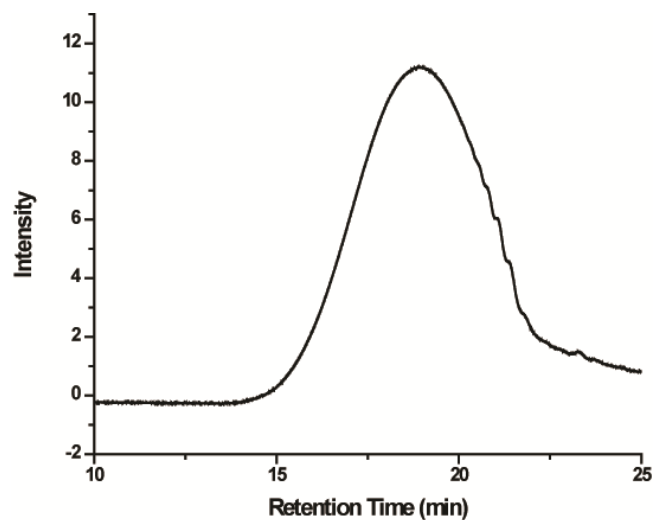


Figure C.2. Size exclusion chromatogram of **DALP** after Soxhlet extraction from CHCl_3 .

$M_n^{\text{SEC}} = 21 \text{ kg/mol}$, PDI = 2.95.

C. 3. Lippert-Martaga Solvatochromism Plot

The positive solvatochromism of **DALP** was demonstrated by a Lippert-Martaga plot using the Lippert-Martaga equation (1).

$$\bar{\nu}_A - \bar{\nu}_E = \frac{2(\mu_G - \mu_E)^2}{hca^3} \Delta f + c \quad (1)$$

Herein, ν_A and ν_E are the absorption maximum and emission maximum in wavenumbers, μ_g and μ_E are, respectively, the ground and excited state dipole moments, h is Planck's constant, c is the speed of light in vacuum, a is the Onsager cavity radius, and Δf is the orientation polarizability. Stokes shift is generally described by the difference of absorption maximum and emission maximum. However, since **DALP** exhibits optically weak HOMO-LUMO transitions in the absorption spectrum, the Stokes shift of **DALP** represents the difference of the weak HOMO-LUMO absorption and the emission maximum. Unfortunately, it was difficult to obtain an accurate wavelength of the weak HOMO-LUMO absorptions in various solvents because the weak absorption shoulder (468 nm) observed in toluene became less characteristic in more polar solvents. Although the difference between absorption maxima and emission maxima does not depicts Stokes shift of **DALP**, the difference, which is more apparent, was plotted as a function of Δf , which is defined as the equation (2).

$$\Delta f = \left(\frac{\varepsilon - 1}{2\varepsilon + 1} \right) - \left(\frac{n^2 - 1}{2n^2 + 1} \right) \quad (2)$$

where, ε is dielectric constant, and n is refractive index of a solvent.

Table C.1. Summary of dielectric constants (ϵ), refractive indices (n), orientation polarizabilities (Δf), absorptions, emissions, and the difference between the absorptions and emissions in various solvents.

	ϵ	n	Δf	λ_{abs} (nm)	λ_{em} (nm)	$\Delta\nu$ (cm ⁻¹)
Toluene	2.38	1.4969	0.013	468	569	3792
Chlorobenzene	5.62	1.5248	0.143	469	591	4401
Chloroform	4.81	1.4459	0.148	467	590	4464
1,2-Dichlorobenzene	9.93	1.5514	0.186	470	608	4829
Tetrahydrofuran	7.58	1.4072	0.210	468	604	4811
Dichloromethane	8.93	1.4242	0.217	466	616	5225
1,2-Dichloroethane	10.37	1.4448	0.221	466	618	5278

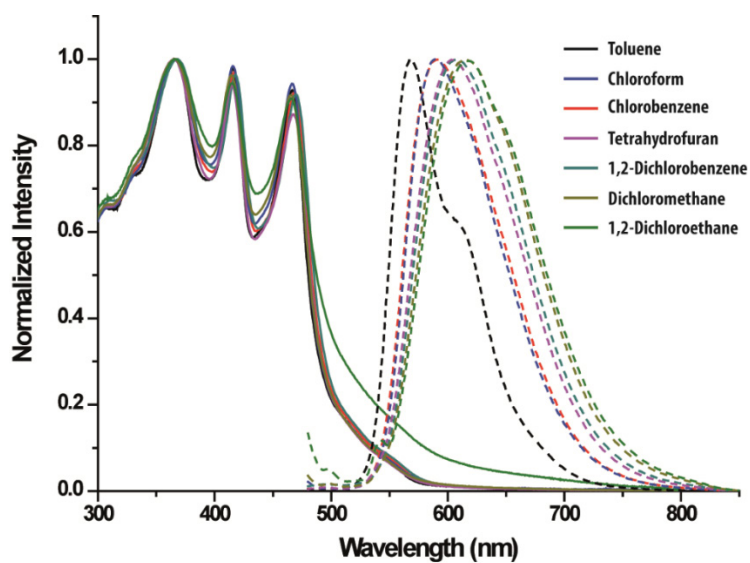


Figure C.3. UV-vis absorption and fluorescence emission spectra of **DALP** in different solvents.

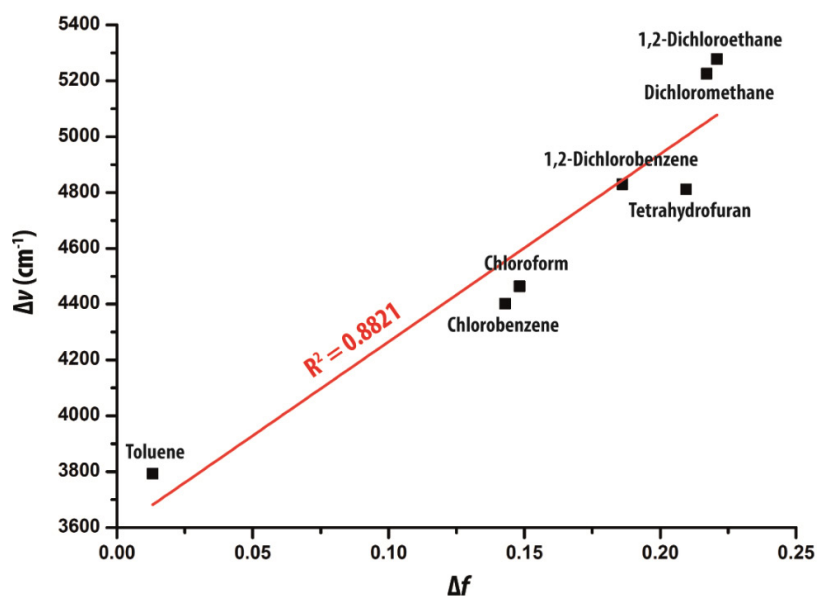


Figure C.4. Lippert-Mataga plot of **DALP**. The red line represents the linear fit ($R^2 = 0.8821$).

C. 4. Charge Transfer Complex

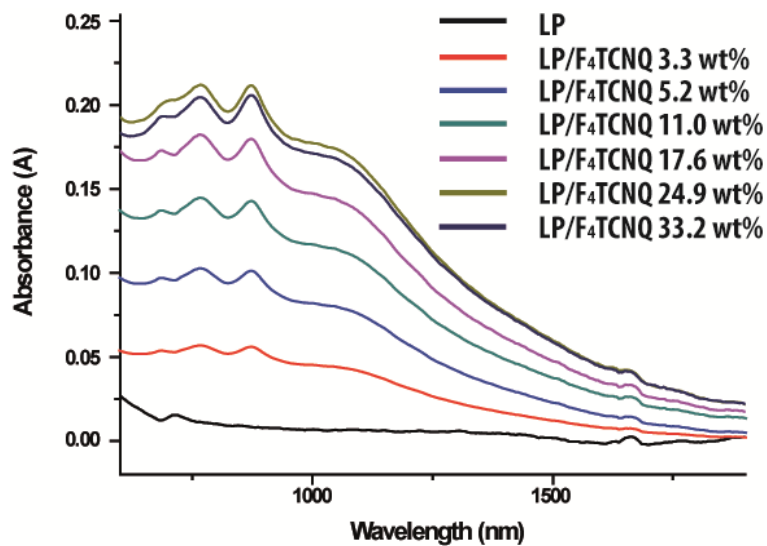


Figure C.5. UV-vis-NIR spectra of **LP** doped with various amounts of **F₄TCNQ** (from 0 wt% to 33.2 wt%).

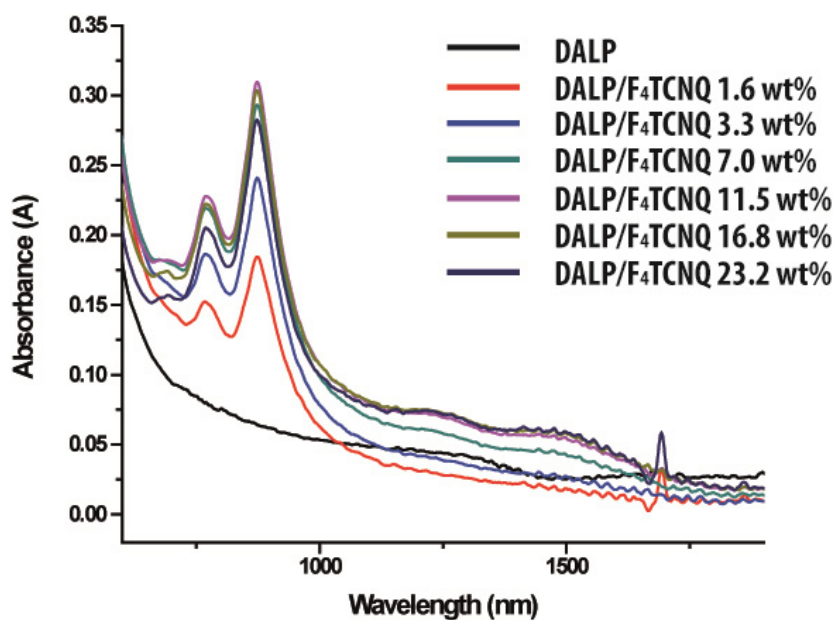


Figure C.6. UV-vis-NIR spectra of **DALP** doped with various amounts of **F₄TCNQ** (from 0 wt% to 23.2 wt%).

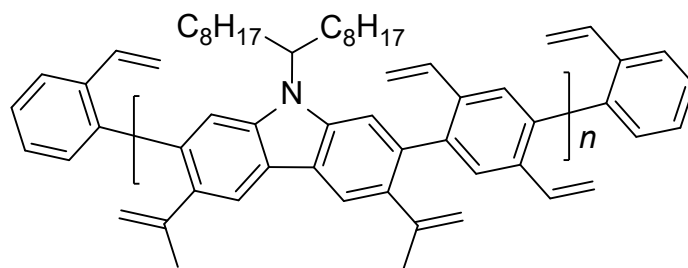


Figure C.7. Structural formula of **CP**, which is the polymeric precursor of **LP**.

C. 5. Grazing Incidence Wide-Angle X-ray Scattering (GIWAXS)

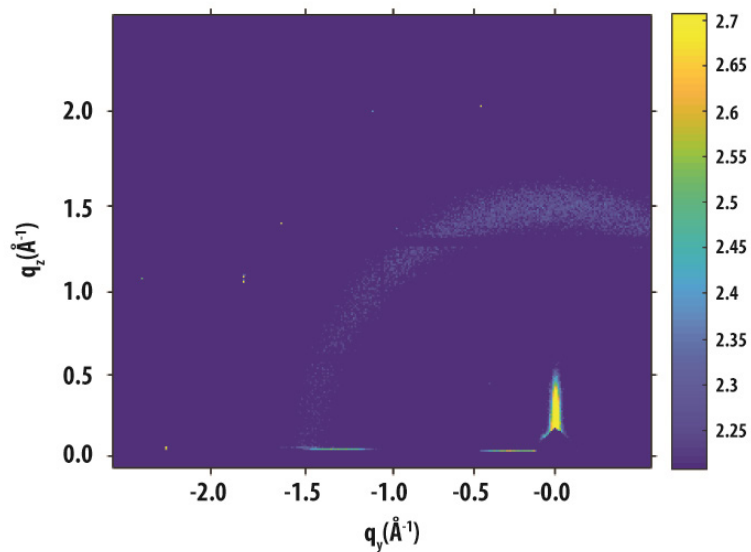


Figure C.8. GIWAXS image of as-cast film of DALP.

C. 6. Cyclic Voltammetry (CV)

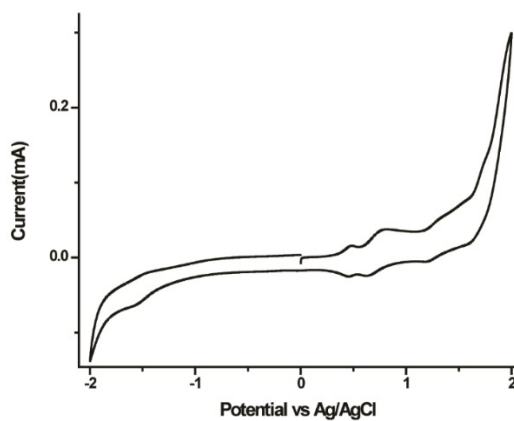


Figure C.9. Cyclic Voltammograms of DALP in DCM (0.1M [*n*-Bu₄N]PF₆) at scan rate of 20 mV/s.

C. 7. ^1H and ^{13}C NMR Spectra

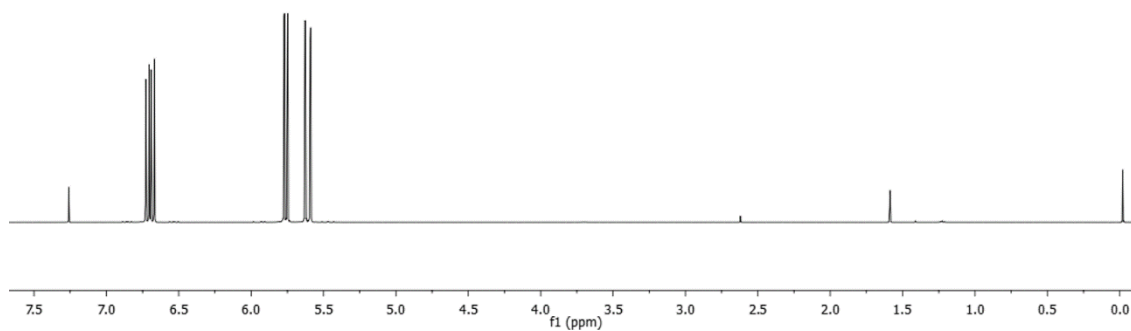
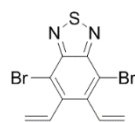


Figure C.10. ^1H NMR of **5** (500 MHz, CDCl_3 , RT).

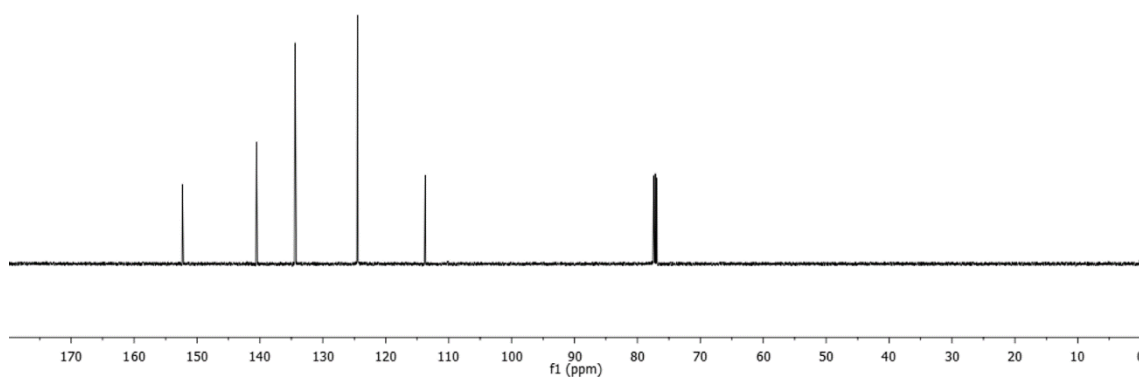
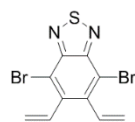


Figure C.11. ^{13}C NMR of **5** (125 MHz, CDCl_3 , RT).

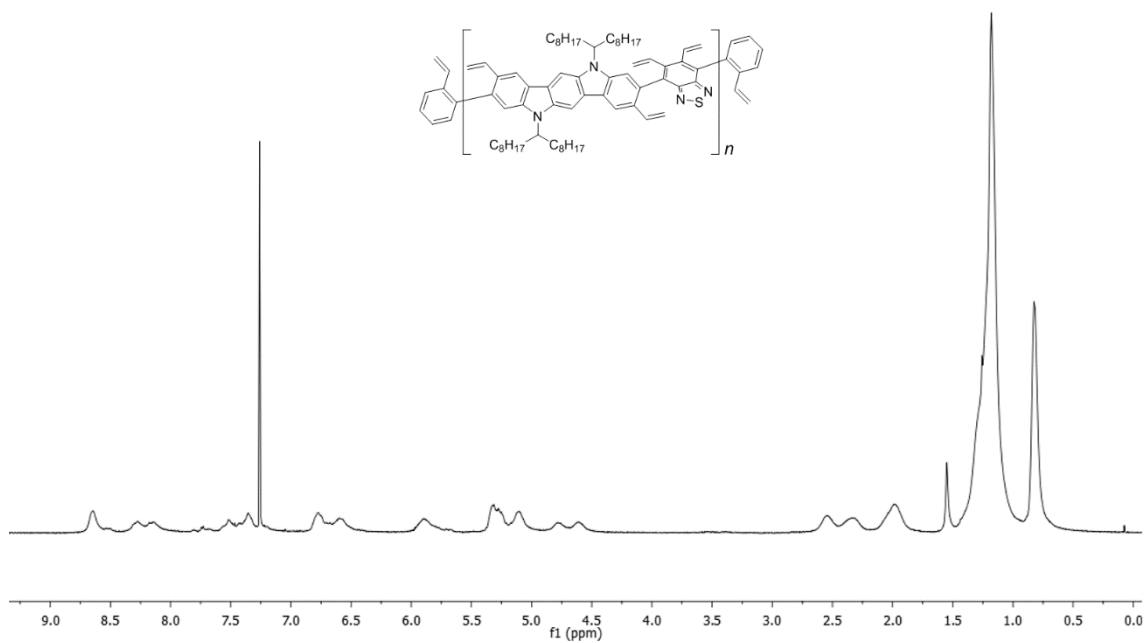


Figure C.12. ^1H NMR of DACP (500 MHz, CDCl_3 , RT).

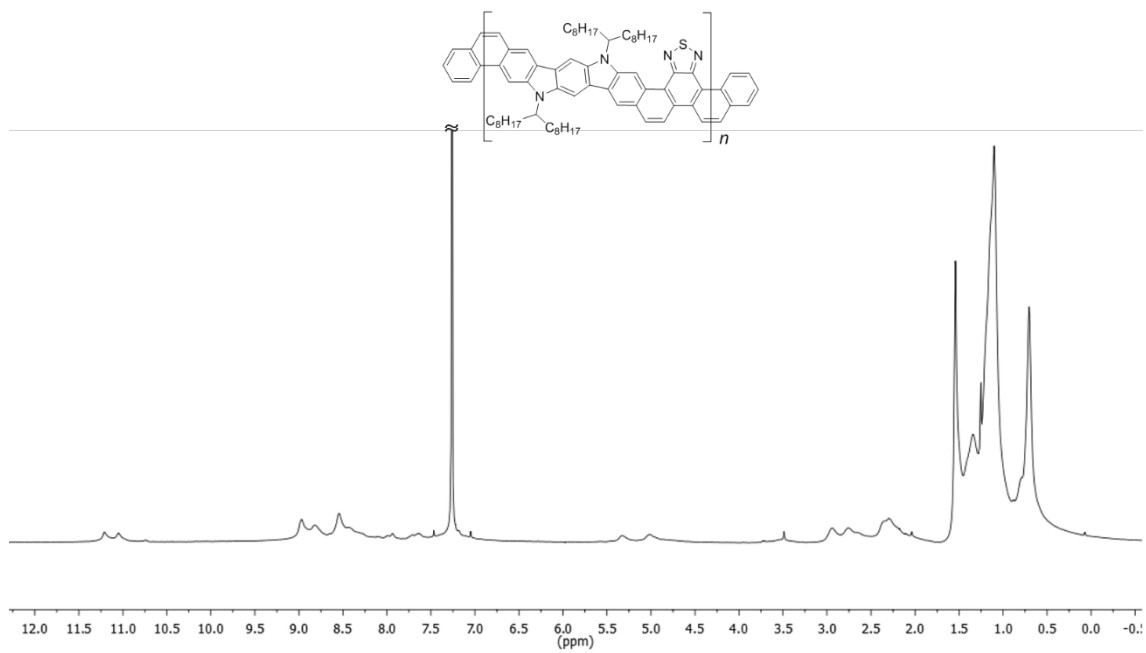
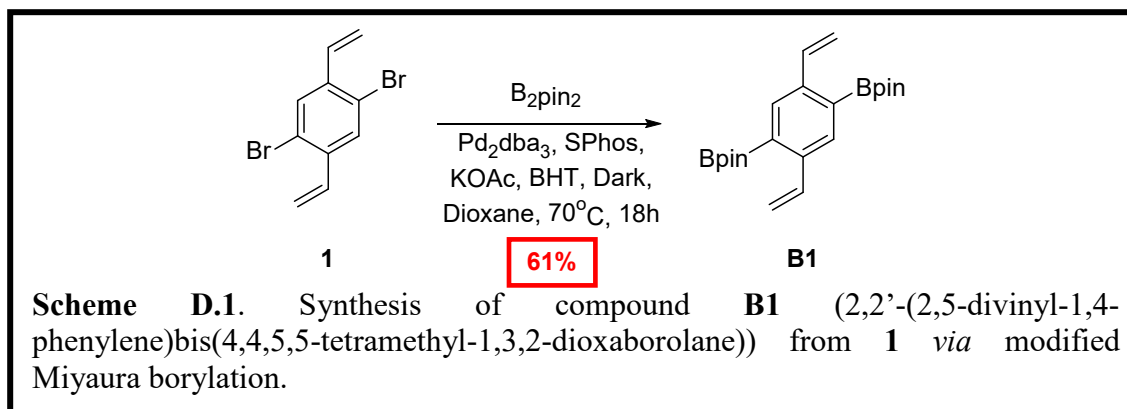


Figure C.13. ^1H NMR of DALP (500 MHz, CDCl_3 , RT).

APPENDIX D

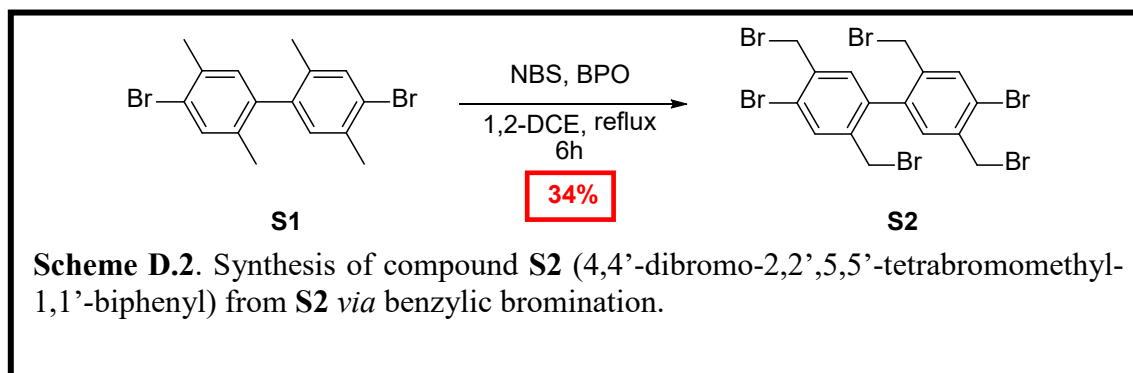
D. 1. Synthesis



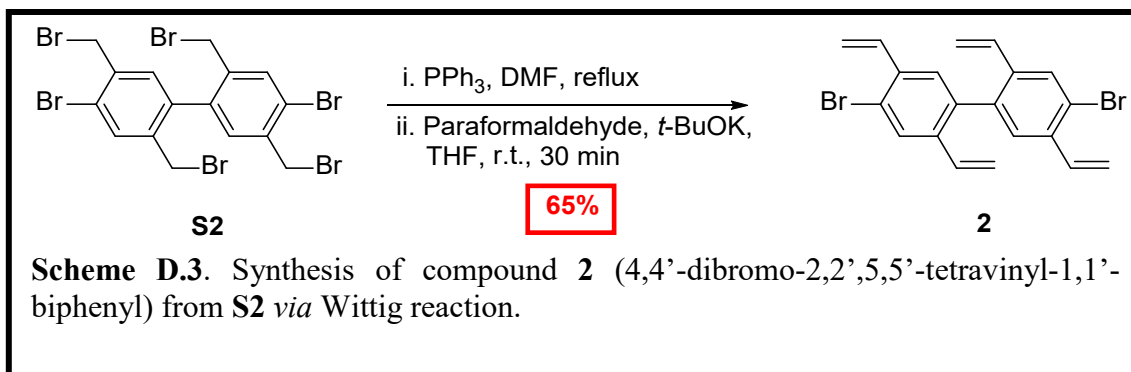
B1 (2,2'-(2,5-divinyl-1,4-phenylene)bis(4,4,5,5-tetramethyl-1,3,2-dioxaborolane)):

Compound **1** (1.5 g, 5.2 mmol), bis(pinacolato)diboron (4.0 g, 15.7 mmol), Pd₂dba₃ (0.24 g, 5.0 mol%), SPhos (0.27 g, 12.5 mol%), KOAc (3.1 g, 31.3 mmol), and several crystals of 2,6-di-*t*-butyl-4-methylphenol (BHT) were dissolved in degassed dioxane (15 mL) under a N₂ atmosphere at room temperature. The reaction mixture was stirred at 70 °C for 18 h in darkness. The reaction was cooled down to room temperature and extracted with CH₂Cl₂ (3 × 20 mL). The combined organic layer was dried over MgSO₄, filtered through Celite, and concentrated under reduced pressure. The residue was purified by flash column chromatography (SiO₂, hexane:CH₂Cl₂ = 88:12 to 0:100) to give **B1** (1.2 g, 61%) as a white solid. ¹H NMR (500 MHz, CDCl₃): δ 8.02 (s, 2H), 7.46 (dd, *J*₁ = 17.5 Hz, *J*₂ = 11.0 Hz, 2H), 5.78 (d, *J* = 17.5 Hz, 2H), 5.25 (d, *J* = 11.0 Hz, 2H), 1.36 (s, 24H). ¹³C NMR

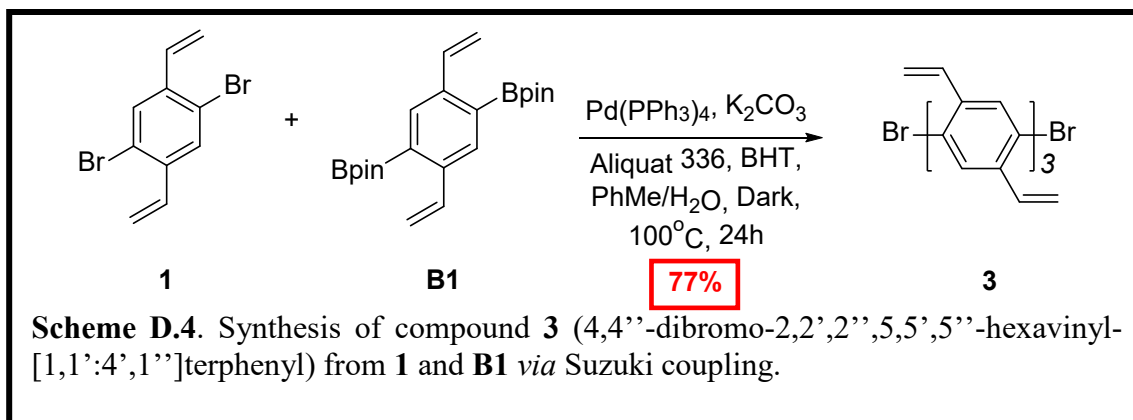
(125 MHz, CDCl₃): δ 141.75, 137.16, 132.02, 114.70, 83.93, 25.02. HRMS (ESI): calcd for C₂₂H₃₂B₂O₄ [M+Na]⁺ m/z = 405.2385; found m/z = 405.2370.



S2 (4,4'-dibromo-2,2',5,5'-tetrabromomethyl-1,1'-biphenyl): Compound **S1** (3.3 g, 9.0 mmol) was dissolved in anhydrous 1,2-dichloroethane (200 mL) under a N₂ atmosphere at room temperature. To the mixture were added NBS (7.0 g, 39.4 mmol) and BPO (50 mg). The mixture was stirred and refluxed for 6 h. Additional BPO (4 × 50 mg) was added every 30 min after reflux. After being cooled to room temperature, the precipitate was filtered and washed with hexane. The filtrate was concentrated under reduced pressure and purified by flash column chromatography (SiO₂, hexane:CH₂Cl₂ = 97:3 to 76:24) to give **S2** (2.1 g, 34%) as a white solid. ¹H NMR (500 MHz, CDCl₃): δ 7.76 (s, 2H), 7.37 (s, 2H), 4.61 (d, J = 10.5 Hz, 2H), 4.58 (d, J = 10.5 Hz, 2H), 4.23 (d, J = 10.5 Hz, 2H), 4.08 (d, J = 10.5 Hz, 2H). ¹³C NMR (125 MHz, CDCl₃): δ 138.08, 137.54, 137.44, 135.43, 132.66, 124.80, 32.35, 29.72. LRMS (APCI): calcd for C₁₆H₁₂Br₆ [M+H]⁺ m/z = 684.61; found m/z = 684.52.

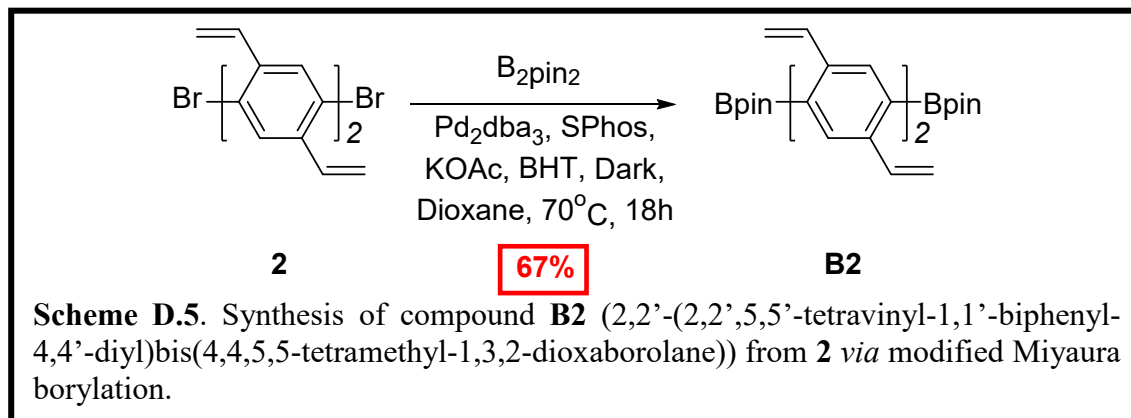


2 (4,4'-dibromo-2,2',5,5'-tetravinyl-1,1'-biphenyl): The reaction mixture of compound **S2** (2.2 g, 3.2 mmol) and PPh_3 (4.2 g, 16.0 mmol) in DMF (70 mL) was stirred at reflux temperature for 18 h. After being cooled to room temperature, the reaction mixture was precipitated by adding acetone and filtered. The precipitate was dried under vacuum and suspended in anhydrous THF (80 mL) with paraformaldehyde (6.5 g) under N_2 . While stirring, $t\text{-BuOK}$ (2.0 g, 17.5 mmol) was added in small portions over 10 min. After 30 min, the reaction was quenched with water and extracted with CH_2Cl_2 (3×30 mL). The combined organic layer was dried over MgSO_4 , filtered through Celite, and concentrated under reduced pressure. The residue was purified by flash column chromatography (SiO_2 , hexane) to give **2** (0.86 g, 65%) as a white solid. ^1H NMR (500 MHz, CDCl_3): δ 7.84 (s, 2H), 7.34 (s, 2H), 7.07 (dd, $J_1 = 17.5$ Hz, $J_2 = 11.0$ Hz, 2H), 6.30 (dd, $J_1 = 17.5$ Hz, $J_2 = 11.0$ Hz, 2H), 5.68 (d, $J = 17.5$ Hz, 2H), 5.67 (d, $J = 17.5$ Hz, 2H) 5.36 (d, $J = 11.0$ Hz, 2H), 5.17 (d, $J = 11.0$ Hz, 2H). ^{13}C NMR (125 MHz, CDCl_3): δ 137.75, 137.36, 136.37, 135.09, 133.34, 129.33, 128.30, 123.48, 117.12, 116.43. LRMS (APCI): calcd for $\text{C}_{20}\text{H}_{16}\text{Br}_2$ [$M+\text{H}$] $^+$ $m/z = 416.97$; found $m/z = 416.95$.

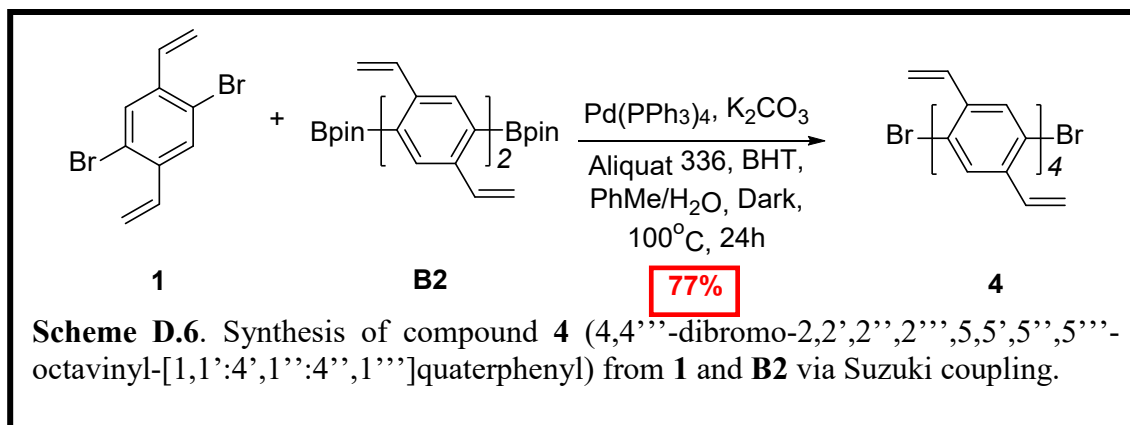


3 (4,4''-dibromo-2,2',2'',5,5',5''-hexavinyl-[1,1':4',1'']terphenyl): To a mixture of compound **1** (3.6 g, 12.6 mmol), compound **B1** (0.79 g, 2.1 mmol), K_2CO_3 (1.73 g, 12.5 mmol), Aliquat 336 (0.24 mL, 0.52 mmol), several crystals of BHT, and $Pd(PPh_3)_4$ (0.24 g, 10 mol%) were added toluene (16 mL) and water (3.2 mL) under a N_2 atmosphere. The reaction mixture was stirred at 100 °C for 24 h in darkness. After being cooled to room temperature, the reaction mixture was concentrated under reduced pressure, and the residue was extracted with CH_2Cl_2 (3 × 20 mL). The combined organic layer was dried over $MgSO_4$, filtered through Celite, and concentrated under reduced pressure. The residue was purified by flash column chromatography (SiO_2 , hexane) to give **3** (0.87 g, 77 %) as a white solid while **1** was partially recovered (2.0 g, 55 %). 1H NMR (500MHz, $CDCl_3$): δ 7.88 (s, 2H), 7.45 (m, 3H), 7.43 (s, 1H), 7.16 (dd, $J_1 = 17.5$ Hz, $J_2 = 11.0$ Hz, 2H), 6.42 (dd, $J_1 = 17.5$ Hz, $J_2 = 11.0$ Hz, 2H), 6.41 (dd, $J_1 = 17.5$ Hz, $J_2 = 11.0$ Hz, 2H), 5.73 (m, 4H), 5.64 (d, $J = 17.5$ Hz, 2H), 5.38 (d, $J = 11.0$ Hz, 1H), 5.37 (d, $J = 11.0$ Hz, 1H), 5.23 (d, $J = 11.0$ Hz, 1H), 5.20 (d, $J = 11.0$ Hz, 1H), 5.13 (d, $J = 11.0$ Hz, 2H). ^{13}C NMR (125 MHz, $CDCl_3$): δ 138.65, 138.22, 138.19, 137.56, 137.45, 136.41, 135.51, 135.45, 135.27, 134.20, 134.16, 133.67, 133.57, 129.26, 128.63, 126.86, 123.32, 117.13,

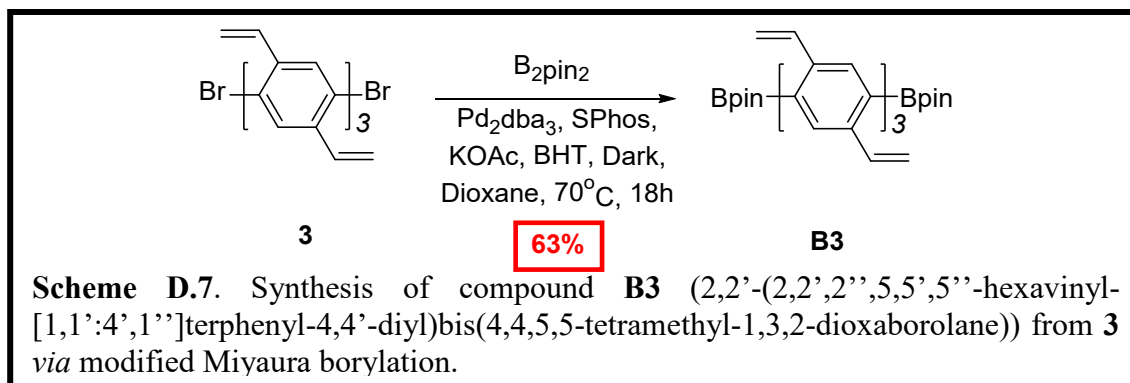
117.08, 116.29, 116.20, 115.70, 115.61. LRMS (APCI): calcd for C₃₀H₂₄Br₂ [M+H]⁺ *m/z* = 545.03; found *m/z* = 545.06.



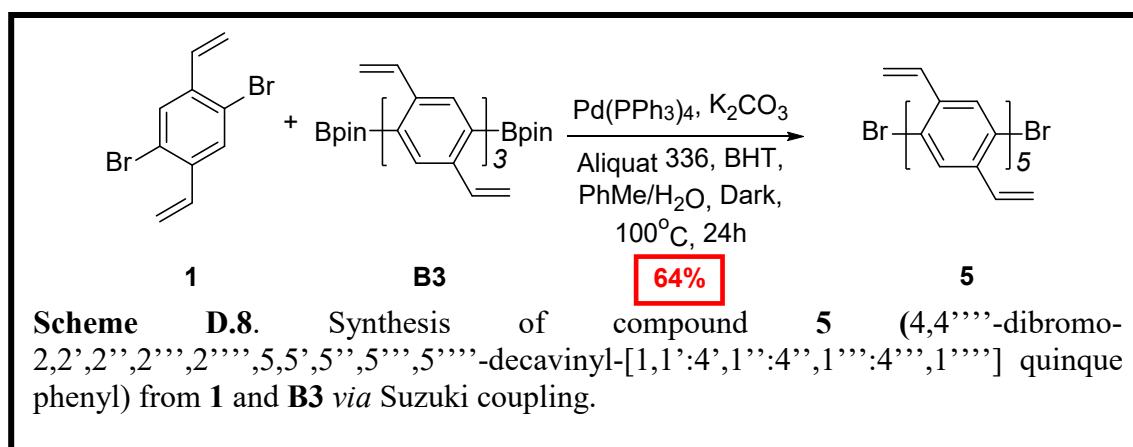
B2 (2,2'-(2,2',5,5'-tetravinyl-1,1'-biphenyl-4,4'-diyl)bis(4,4,5,5-tetramethyl-1,3,2-dioxaborolane)): **B2** was synthesized by the same procedure as the synthesis of **B1** using compound **2** (0.5 g, 1.2 mmol), bis(pinacolato)diboron (0.9 g, 3.6 mmol), Pd₂dba₃ (55 mg, 5.0 mol%), SPhos (62 mg, 12.5 mol%), KOAc (0.7 g, 7.2 mmol), and several crystals of BHT in degassed dioxane (5 mL). After purification by flash column chromatography (SiO₂, hexane:CH₂Cl₂ = 94:6 to 50:50), the product **B2** (0.41 g, 67 %) was isolated as a white solid. ¹H NMR (500 MHz, CDCl₃): δ 8.09 (s, 2H), 7.55 (dd, *J*₁ = 17.5 Hz, *J*₂ = 11.0 Hz, 2H), 7.43 (s, 2H), 6.37 (dd, *J*₁ = 17.5 Hz, *J*₂ = 11.0 Hz, 2H), 5.71 (d, *J* = 17.5 Hz, 2H), 5.67 (d, *J* = 17.5 Hz, 2H), 5.25 (d, *J* = 11.0 Hz, 2H), 5.07 (d, *J* = 11.0 Hz, 2H), 1.38 (s, 24H). ¹³C NMR (125 MHz, CDCl₃): δ 142.66, 142.19, 136.97, 134.78, 134.55, 132.82, 126.28, 115.05, 114.98, 83.97, 25.05. HRMS (ESI): calcd for C₃₂H₄₀B₂O₄ [M+Na]⁺ *m/z* = 533.3011; found *m/z* = 533.3008.



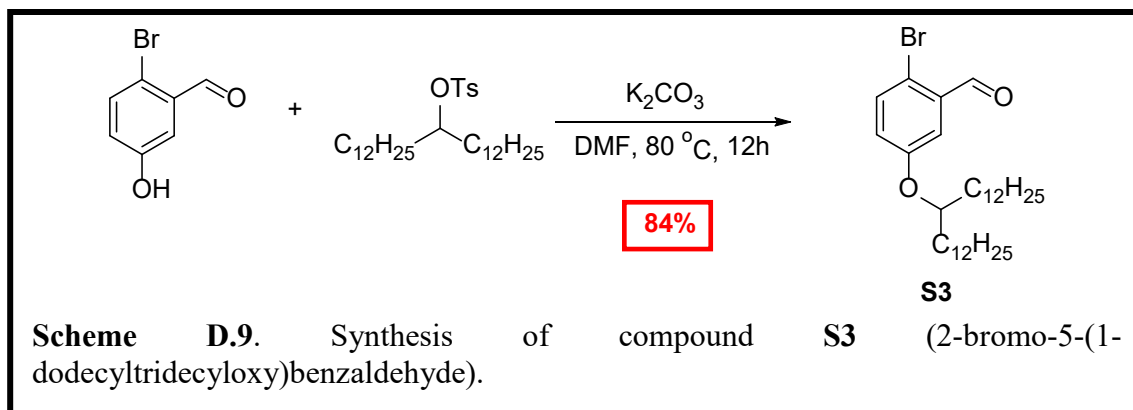
4 (4,4''-dibromo-2,2',2'',2''',5,5',5'',5'''-octavinyl-[1,1':4',1'':4'',1''']quaterphenyl): **4** was synthesized by the same procedure as the synthesis of **3** using compound **1** (0.67 g, 2.34 mmol), compound **B2** (0.2 g, 0.39 mmol), K₂CO₃ (0.32 g, 2.34 mmol), Aliquat 336 (1 drop), several crystals of BHT, and Pd(PPh₃)₄ (46 mg, 10 mol%) in degassed toluene (5 mL) and water (1 mL). After purification by flash column chromatography (SiO₂, hexane:CH₂Cl₂ = 98:2 to 88:12), the product **4** (0.20 g, 77 %) was isolated as a white solid. ¹H NMR (500MHz, CDCl₃): δ 7.90 (s, 1H), 7.89 (s, 1H), 7.55 (m, 2H), 7.49 (m, 2H), 7.48 (s, 1H), 7.46 (s, 1H), 7.10 (dd, *J*₁ = 17.5 Hz, *J*₂ = 11.0 Hz, 2H), 6.53 (dd, *J*₁ = 17.5 Hz, *J*₂ = 11.0 Hz, 2H), 6.44 (m, 4H), 5.72 (m, 8H), 5.39 (d, *J* = 11.0 Hz, 1H), 5.38 (d, *J* = 11.0 Hz, 1H), 5.24 (d, *J* = 11.0 Hz, 1H), 5.22 (d, *J* = 11.0 Hz, 1H), 5.15 (m, 4H). ¹³C NMR (125 MHz, CDCl₃): δ 139.05, 139.01, 138.99, 138.97, 138.79, 138.76, 138.06, 138.05, 138.04, 138.02, 138.00, 137.60, 137.49, 136.40, 135.55, 135.51, 135.48, 135.45, 135.29, 134.50, 134.44, 134.39, 134.33, 134.30, 133.74, 133.63, 129.26, 129.23, 128.7, 127.13, 127.10, 126.77, 126.76, 123.30, 117.12, 117.08, 116.25, 116.16, 115.63, 115.58, 115.55, 115.49, 115.40, 115.39, 115.32, 115.31. LRMS (APCI): calcd for C₄₀H₃₂Br₂ [*M*+H]⁺ *m/z* = 673.09; found *m/z* = 673.17.



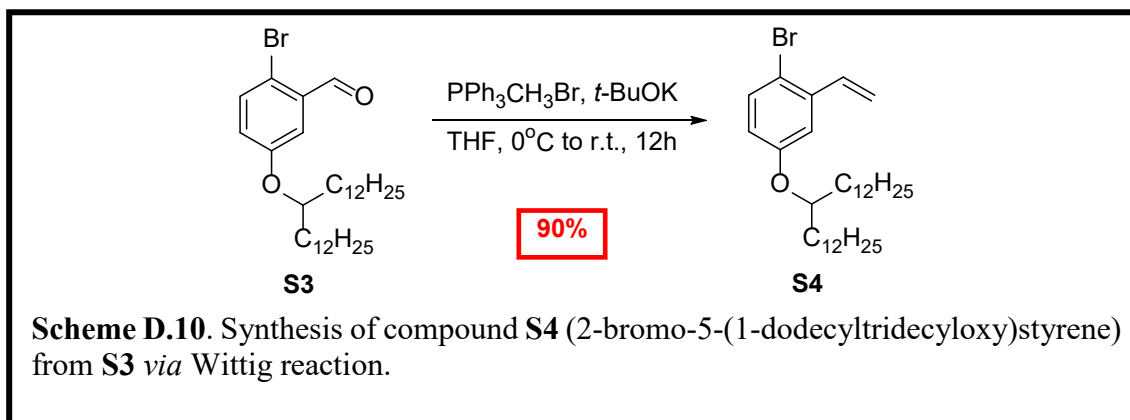
B3 (2,2'-(2,2',2'',5,5',5''-hexavinyl-[1,1':4',1'']terphenyl-4,4'-diyl)bis(4,4,5,5-tetramethyl-1,3,2-dioxaborolane): **B3** was synthesized by the same procedure as the synthesis of **B1** using compound **3** (0.5 g, 0.9 mmol), bis(pinacolato)diboron (0.7 g, 2.8 mmol), Pd₂dba₃ (42 mg, 5.0 mol%), SPhos (49 mg, 12.5 mol%), KOAc (0.5 g, 5.5 mmol), and several crystals of BHT in degassed dioxane (7 mL). After purification by flash column chromatography (SiO₂, hexane:CH₂Cl₂ = 95:5 to 55:45), the product **B3** (0.37 g, 63 %) was isolated as a white solid. ¹H NMR (500 MHz, CDCl₃): δ 8.14 (s, 1H), 8.13 (s, 1H), 7.57 (dd, *J*₁ = 17.5 Hz, *J*₂ = 11.0 Hz, 2H), 7.54 (s, 1H), 7.53 (s, 1H), 7.48 (s, 1H), 7.47 (s, 1H), 6.505 (dd, *J*₁ = 17.5 Hz, *J*₂ = 11.0 Hz, 1H), 6.501 (dd, *J*₁ = 17.5 Hz, *J*₂ = 11.0 Hz, 1H), 6.41 (dd, *J*₁ = 17.5 Hz, *J*₂ = 11.0 Hz, 2H), 5.79 (d, *J* = 17.5 Hz, 2H), 5.75 (d, *J* = 17.0 Hz, 1H), 5.72 (d, *J* = 17.0 Hz, 1H), 5.62 (d, *J* = 17.0 Hz, 2H), 5.29 (d, *J* = 11.0 Hz, 1H), 5.28 (d, *J* = 11.0 Hz, 1H), 5.18 (d, *J* = 11.0 Hz, 1H), 5.16 (d, *J* = 11.0 Hz, 1H), 5.07 (d, *J* = 11.0 Hz, 2H), 1.40 (s, 24H). ¹³C NMR (125 MHz, CDCl₃): δ 142.76, 142.75, 141.98, 141.95, 139.15, 139.11, 137.03, 135.29, 135.21, 135.01, 134.90, 134.67, 134.67, 134.55, 134.50, 132.88, 132.84, 126.72, 126.69, 126.58, 115.16, 115.12, 115.09, 115.06, 115.05, 115.02, 83.99, 25.06. HRMS (ESI): calcd for C₄₂H₄₈B₂O₄ [M+Na]⁺ *m/z* = 661.3637; found *m/z* = 661.3617.



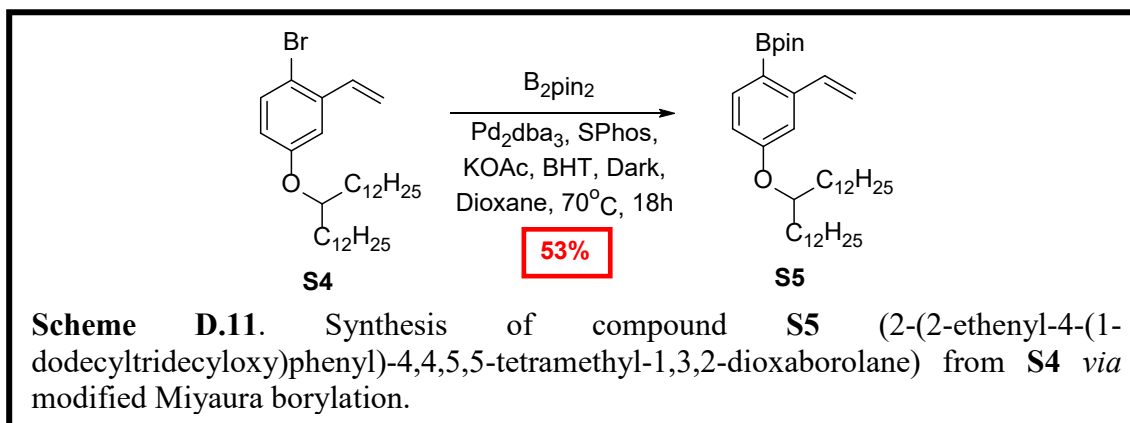
5 (4,4''''-dibromo-2,2',2'',2''',2''''-decavinyl-[1,1':4',1'':4'',1''':4''',1''''] quinquephenyl): **5** was synthesized by the same procedure as the synthesis of **3** using compound **1** (0.28 g, 0.96 mmol), compound **B3** (0.10 g, 0.16 mmol), K₂CO₃ (0.13 g, 0.96 mmol), aliquat 336 (1 drop), several crystals of BHT, and Pd(PPh₃)₄ (23 mg, 10 mol%) in degassed toluene (5 mL) and water (1 mL). After purification by flash column chromatography (SiO₂, hexane:CH₂Cl₂ = 98:2 to 80:20) the product **5** (82 mg, 64 %) was isolated as a white solid. ¹H NMR (500MHz, CDCl₃): δ 7.90 (m, 2H), 7.58 (m, 4H), 7.50 (m, 2H), 7.49 (s, 1H), 7.47 (s, 1H), 7.11 (dd, *J*₁ = 17.5 Hz, *J*₂ = 11.0 Hz, 2H), 6.56 (m, 4H), 6.46 (m, 4H), 5.72 (m, 10H), 5.40 (d, *J* = 11.0 Hz, 1H), 5.39 (d, *J* = 11.0 Hz, 1H), 5.20 (m, 8H). ¹³C NMR (125 MHz, CDCl₃, 50 °C): δ 139.30, 138.98, 138.14, 137.79, 137.76, 137.75, 136.65, 135.82, 135.81, 135.78, 135.75, 135.73, 135.68, 135.52, 134.81, 134.78, 134.74, 134.59, 133.99, 133.95, 133.91, 129.52, 128.91, 127.48, 127.33, 127.06, 123.32, 117.03, 117.00, 116.18, 116.16, 115.59, 115.58, 115.57, 115.54, 115.37, 115.35, 115.33, 115.31, 115.28. LRMS (APCI): calcd for C₅₀H₄₀Br₂ [*M*+H]⁺ *m/z* = 801.16; found *m/z* = 801.24.



S3 (2-bromo-5-(1-dodecyltridecyloxy)benzaldehyde): To a mixture of 2-bromo-5-hydroxybenzaldehyde (3.0 g, 14.7 mmol), 13-(4-methylbenzenesulfonate)-13-pentacosanol (10.0 g, 19.1 mmol) in anhydrous DMF (150 mL) was added K_2CO_3 (10.1 g, 73.5 mmol) under a N_2 atmosphere. The reaction mixture was stirred at 80 °C for 12 h. The reaction mixture was allowed to cool down to room temperature and quenched with water (50 mL) and diluted with Et_2O (50 mL). It was washed with water (3×30 mL) and brine (30 mL). The combined organic layer was dried over $MgSO_4$, filtered through Celite, and concentrated under reduced pressure. The residue was purified by flash column chromatography (SiO_2 , hexane: CH_2Cl_2 = 96:4 to 66:34) to give **S3** (6.8 g, 84 %) as a white solid. 1H NMR (500MHz, $CDCl_3$): δ 10.30 (s, 1H), 7.50 (d, J = 9.0 Hz, 1H), 7.40 (d, J = 3.0 Hz, 1H), 6.99 (dd, J_1 = 9.0 Hz, J_2 = 3.0 Hz, 1H), 4.27 (quint, J = 5.5 Hz, 1H), 1.60 (m, 4H), 1.24 (m, 40H), 0.88 (t, J = 7.0 Hz, 6H). ^{13}C NMR (125 MHz, $CDCl_3$): δ 191.86, 158.55, 134.69, 134.04, 124.43, 117.36, 114.87, 78.74, 34.19, 33.77, 32.07, 29.81, 29.79, 29.78, 29.71, 29.68, 29.61, 29.51, 25.38, 25.35, 22.84, 14.27. HRMS (ESI): calcd for $C_{32}H_{55}BrO_2 [M+Na]^+$ m/z = 573.3283; found m/z = 573.3238.



S4 (2-bromo-5-(1-dodecyltridecyloxy)styrene): To a solution of methyltriphenylphosphonium bromide (1.78 g, 4.98 mmol) in anhydrous THF (50 mL) was slowly added *t*-BuOK (0.66 g, 5.89 mmol) at room temperature. The mixture was cooled down to 0 °C and the compound **S3** in anhydrous THF (50 mL) was added dropwise for 30 min. After the addition of **S3**, the reaction mixture was warmed to room temperature and stirred for 12 h. The reaction was then quenched with water (30 mL) and extracted with Et₂O (3 × 30 mL). The combined organic layer was dried over MgSO₄, filtered through Celite, and concentrated under reduced pressure. The residue was purified by flash column chromatography (SiO₂, hexane) to give **S4** (2.1 g, 90 %) as a white solid. ¹H NMR (500 MHz, CDCl₃): δ 7.40 (d, *J* = 8.5 Hz, 1H), 7.07 (d, *J* = 3.0 Hz, 1H), 7.01 (dd, *J*₁ = 17.5 Hz, *J*₂ = 11.0 Hz, 1H), 6.68 (dd, *J*₁ = 8.5 Hz, *J*₂ = 3.0 Hz, 1H), 5.67 (d, *J* = 17.5 Hz, 1H), 5.34 (d, *J* = 11.0 Hz, 1H), 4.19 (quint, *J* = 6.0 Hz, 1H), 1.62 (m, 4H), 1.36 (m, 40H), 0.88 (t, *J* = 7.0 Hz, 6H). ¹³C NMR (125 MHz, CDCl₃): δ 158.25, 138.28, 136.06, 133.50, 116.97, 116.61, 114.28, 113.98, 78.52, 33.99, 32.09, 29.85, 29.84, 29.81, 29.75, 29.73, 29.53, 25.50, 22.86, 14.29. LRMS (APCI): calcd for C₃₃H₅₇BrO [*M*+H]⁺ *m/z* = 549.37; found *m/z* = 549.40.



S5 (2-(2-ethenyl-4-(1-dodecyltridecyloxy)phenyl)-4,4,5,5-tetramethyl-1,3,2-dioxaborolane): Compound **S4** (4.9 g, 8.9 mmol), bis(pinacolato)diboron (3.4 g, 13.4 mmol), Pd₂dba₃ (0.41 g, 5.0 mol%), SPhos (0.46 g, 12.5 mol%), KOAc (2.6 g, 26.7 mmol), and several crystals of BHT were dissolved in degassed Dioxane (30 mL) under a N₂ atmosphere at room temperature. The reaction mixture was stirred at 70 °C for 18 h in darkness. The reaction was cooled down to room temperature and extracted with CH₂Cl₂ (3 × 30 mL). The combined organic layer was dried over MgSO₄, filtered through Celite, and concentrated under reduced pressure. The residue was first purified by flash column chromatography (SiO₂, hexane:CH₂Cl₂ = 95:5 to 60:40) and subsequently by preparative SEC to give the product **S5** (2.8 g, 53 %) as a colorless liquid. ¹H NMR (500 MHz, CDCl₃): δ 7.74 (d, *J* = 8.5 Hz, 1H), 7.55 (dd, *J*₁ = 17.5 Hz, *J*₂ = 11.0 Hz, 1H), 7.13 (d, *J* = 2.5 Hz, 1H), 6.77 (dd, *J*₁ = 8.5 Hz, *J*₂ = 2.5 Hz, 1H), 5.68 (d, *J* = 17.5 Hz, 1H), 5.26 (d, *J* = 11.0 Hz, 1H), 4.29 (quint, *J* = 6.0 Hz, 1H), 1.62 (m, 4H), 1.33 (s, 12H), 1.24 (m, 40H), 0.88 (t, *J* = 7.0 Hz, 6H). ¹³C NMR (125 MHz, CDCl₃): δ 161.25, 145.92, 138.16, 137.73, 114.47, 114.27, 111.76, 83.46, 77.66, 34.10, 32.08, 29.86, 29.82, 29.80, 29.75, 29.51,

25.52, 25.00, 22.85, 14.28. HRMS (ESI): calcd for C₃₉H₆₉BO₃ [M+Na]⁺ *m/z* = 619.5238; found *m/z* = 619.5197.

D. 2. Determination of Rotational Barriers

Rotational barrier of vinyl-functionalized *p*-phenylene intermediates (**3**, **4**, and **5**) were calculated from the coalescence temperature by variable temperature ¹H NMR.

$$\Delta G^\ddagger = 4.58T_c(10.32 + \log T_c/K_c)$$

Where ΔG^\ddagger = activation energy at coalescence (cal/mol), T_c = coalescence temp. (K), K_c = rate constants at coalescence temp. ($\Delta\nu \times 2.22$), $\Delta\nu$ = the limiting chemical shift between the exchanging proton resonances (Hz). The results were summarized in **Table D.1** and the red boxes in **Figure D.1-3** indicate the peaks associated with the calculation.

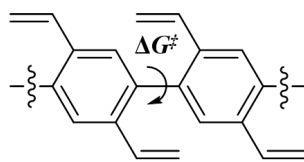


Table D.1. Summary of rotational barriers.

Compound	Peak 1 (ppm)	Peak 2 (ppm)	$\Delta\nu$ (Hz)	T_c (K)	ΔG^\ddagger
3	5.237	5.215	11.0	328	17.2 Kcal/mol
4	5.251	5.230	10.5	328	17.2 Kcal/mol
5	5.256	5.235	10.5	328	17.2 Kcal/mol

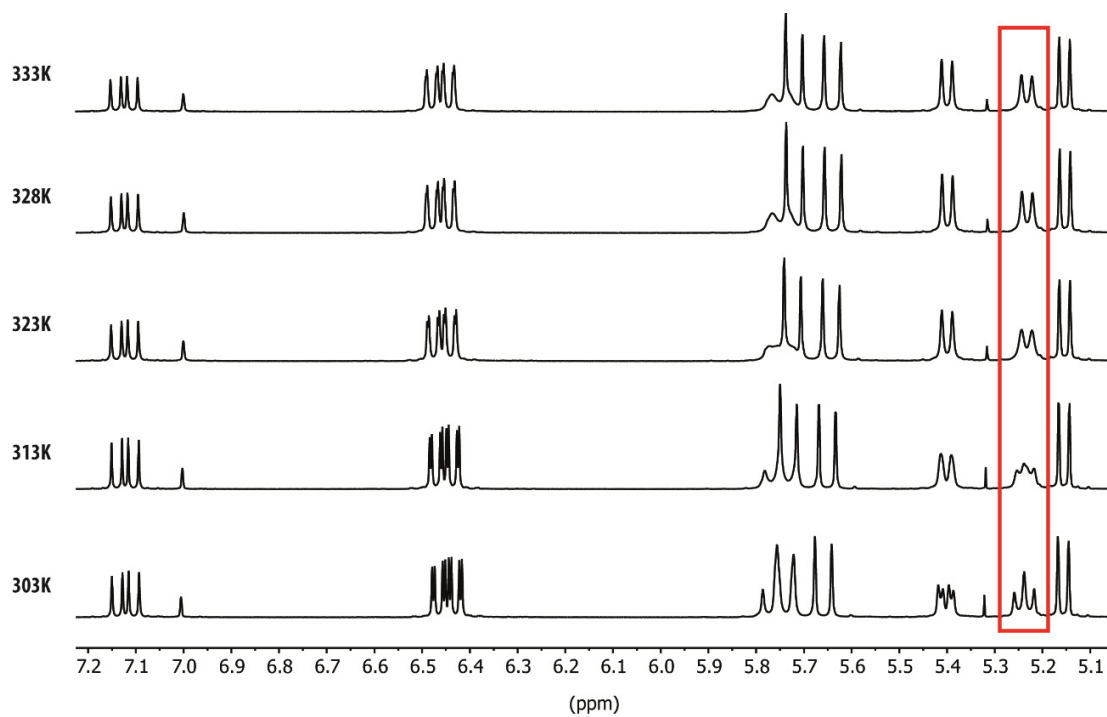


Figure D.1. Partial variable temperature ^1H NMR of **3**.

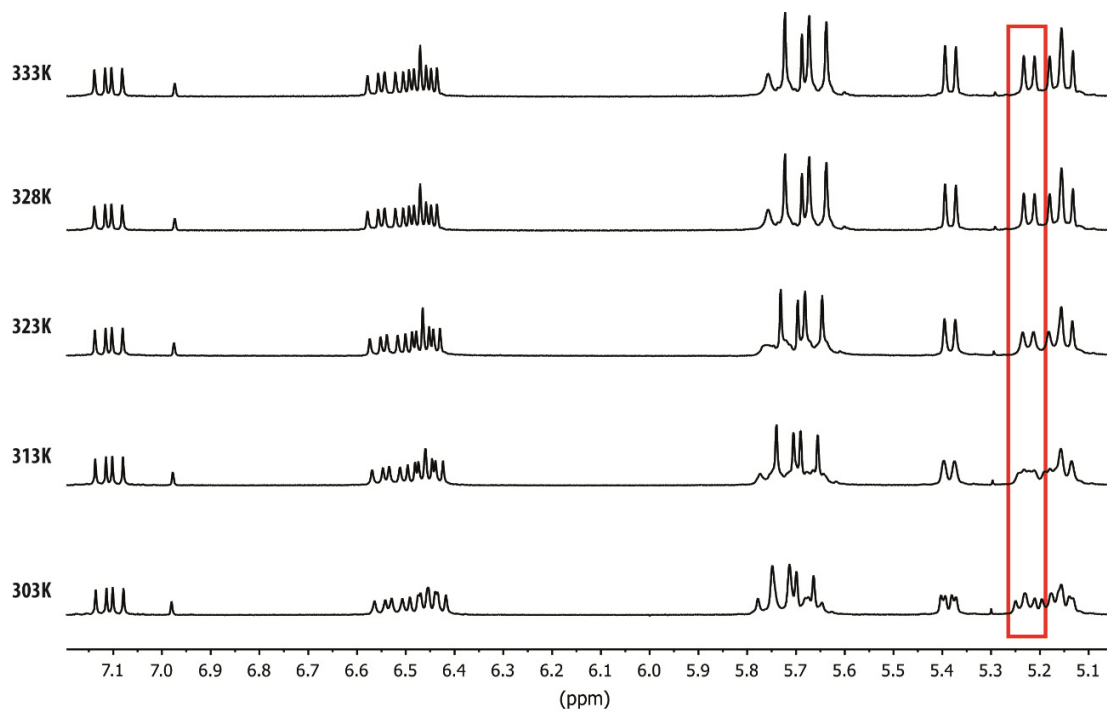


Figure D.2. Partial variable temperature ^1H NMR of **4**.

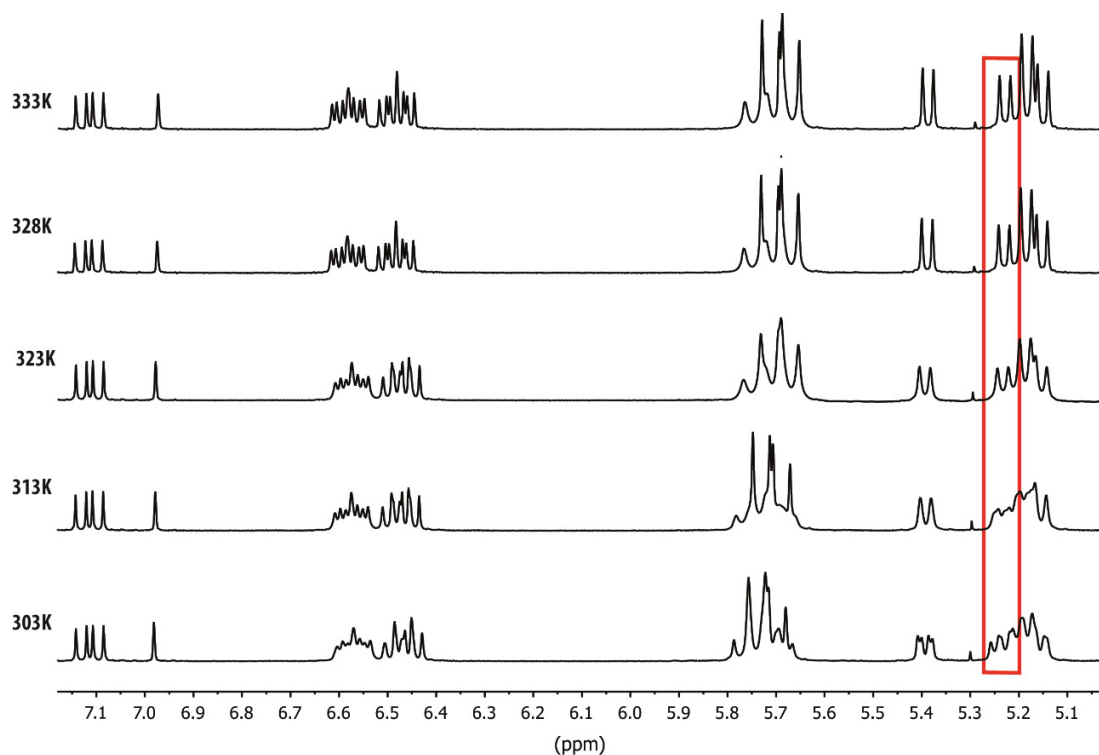


Figure D.3. Partial variable temperature ^1H NMR of **5**.

D. 3. Optimization of Miyaura Borylation

Screened conditions for Miyaura borylation are summarized in **Table D.2**. The standard Miyaura borylation condition afforded the desired product in only 30% yield with difficult purification (**Entry 4**). It appears that vinyl functional groups participate in the coupling reaction to make very complex products. When Pd_2dba_3 with SPhos was used, the yield was increased to 61% with much easier purification (**Entry 13**). It is noteworthy that the introduction of the boronic ester was not achievable through lithium-halogen exchange at $-78\text{ }^\circ\text{C}$ due to the competing styrene polymerization.

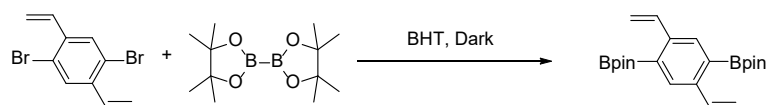


Table D.2. The optimization of Miyaura borylation.

Entry	Catalyst ^a	Ligand ^b	Base	Solvent	Temp. (°C)	Time (h)	Yield (%) ^c
1	Pd(dppf)Cl ₂	PPh ₃	KOAc	DMF	90	12	- ^d
2	Pd(dppf)Cl ₂	-	KOAc	DMF	90	12	- ^d
3	Pd(dppf)Cl ₂	-	KOAc	Dioxane	90	12	12
4	Pd(dppf)Cl ₂	-	KOAc	Dioxane	80	24	30
5	Pd(PPh ₃) ₂ Cl ₂	PPh ₃	KOPh	PhMe	50	12	- ^d
6	Pd(PPh ₃) ₂ Cl ₂	XPhos	KOAc	Dioxane	80	24	32
7	Pd(OAc) ₂	XPhos	KOAc	Dioxane	80	24	20
8	Pd(OAc) ₂	SPhos	K ₃ PO ₄	Dioxane	50	48	30
9	Pd(PPh ₃) ₄	-	KOAc	Dioxane	80	24	- ^d
10	Pd(PPh ₃) ₄	-	KOAc	DMF	80	24	- ^d
11	Pd ₂ dba ₃	-	KOAc	Dioxane	70	18	
12	Pd ₂ dba ₃	XPhos	KOAc	Dioxane	70	18	36
13	Pd ₂ dba ₃	SPhos	KOAc	Dioxane	70	18	61

^a 5 mol% of catalyst was used. ^b 12.5 mol% of catalyst was used ^c Isolated yield. ^d no desired product was observed.

D. 4. Temperature and Concentration Dependent ^1H NMR Spectra

The observed peak separation of **BTp-11** from diluted solution to concentrated solution is not “splitting” of the same proton. Instead, they were coincidentally overlapped protons in a dilute solution. In a concentrated solution, the chemical shifts of these intrinsically different protons were changes due to stronger intermolecular interaction, leading to the observed multiple sharp peaks.

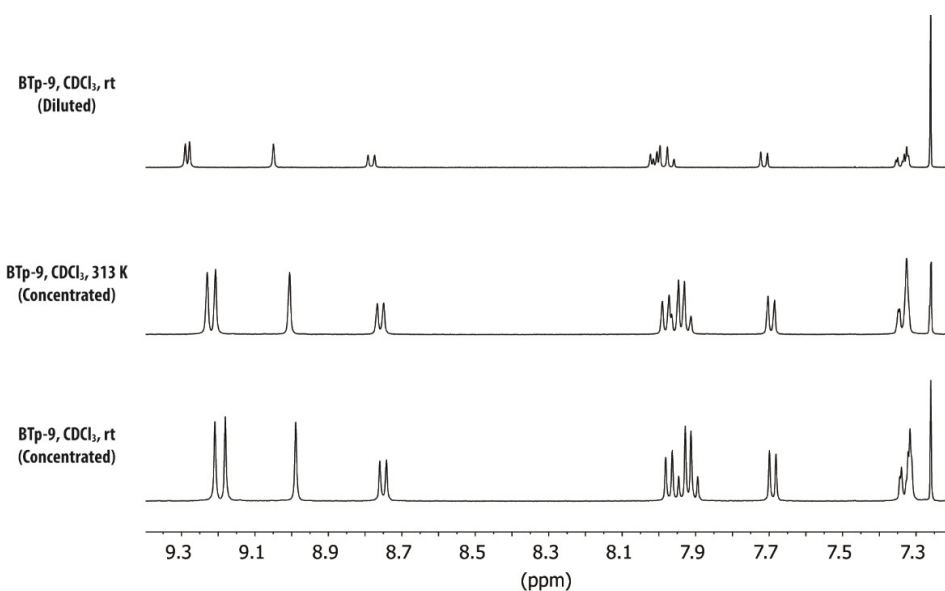


Figure D.4. Partial ^1H NMR spectra of **BTp-9** in aromatic region in diluted, and concentrated solution at room temperature and 313 K.

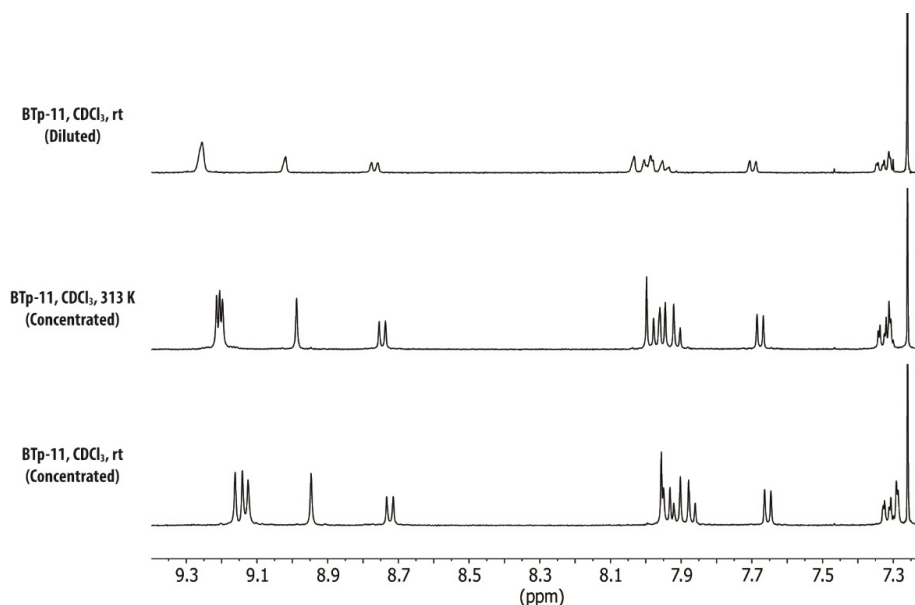


Figure D.5. Partial ^1H NMR spectra of **BTp-11** in aromatic region in diluted, and concentrated solution at room temperature and 313 K.

D. 5. ^1H - ^1H NOESY NMR Spectra of **BTp-5**, **BTp-7**, **BTp-9**, **BTp-11**, and **BTp-13**

In order to fully assign the proton peaks of **BTp-5**, **BTp-7**, **BTp-9**, and **BTp-11**, ^1H - ^1H NOESY was recorded at room temperature in CDCl_3 . The sample solution was degassed by freeze-pump-thaw 3 times before the experiment. The experiment was performed after 90° pulse width calibration. Proton peaks were assigned based on the observed correlation signals. Cross lines in the figures indicate the observed through-space nuclear overhauser effect in the experiment. **BTp-13** was analyzed at 100°C due to its low solubility at room temperature. It is worthy to note that ^1H - ^1H NOESY Spectrum of **BTp-11** was analyzed in concentrated solution due to the clearer splitting patterns of each proton peaks, resulting in upfield shift of aromatic protons due to the aggregation as shown in **Figure D.5**.

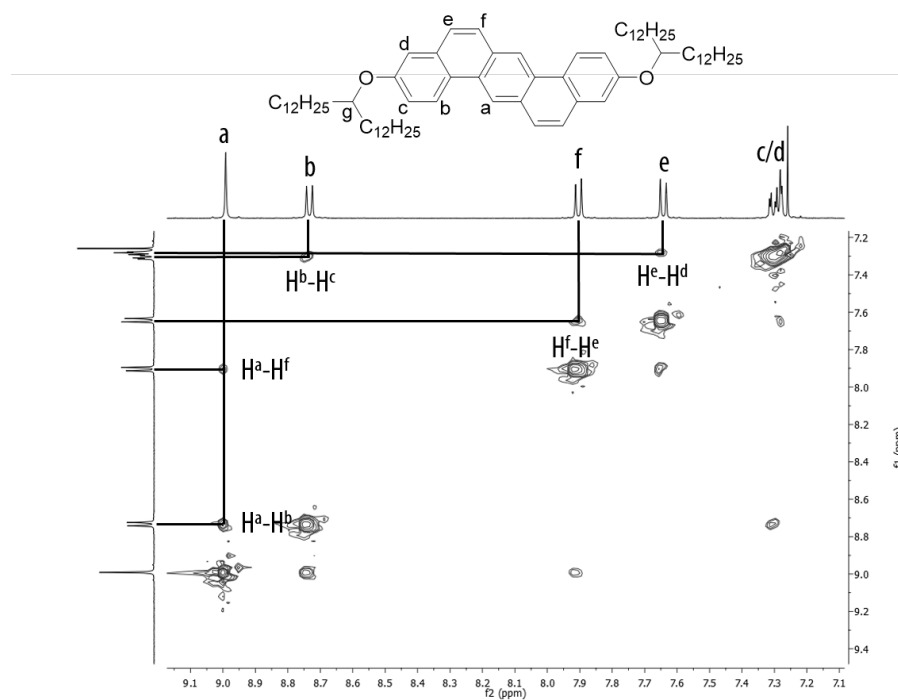


Figure D.6. Partial ^1H - ^1H NOESY spectrum of **BTp-5** (500 MHz, CDCl_3 , RT).

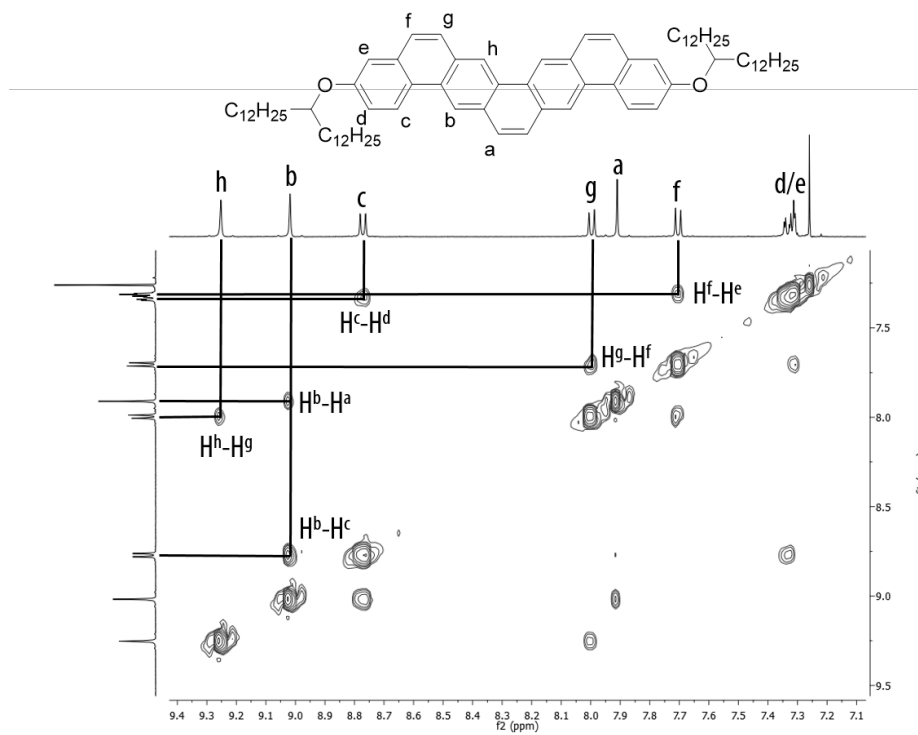


Figure D.7. Partial ^1H - ^1H NOESY spectrum of **BTp-7** (500 MHz, CDCl_3 , RT).

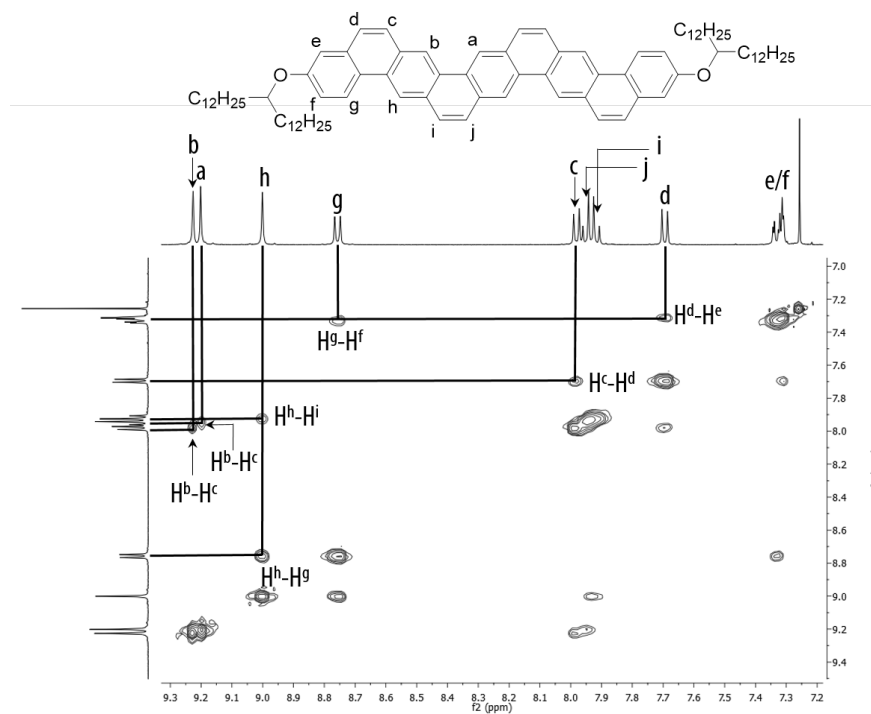


Figure D.8. Partial ^1H - ^1H NOESY spectrum of **BTp-9** (500 MHz, CDCl_3 , RT).

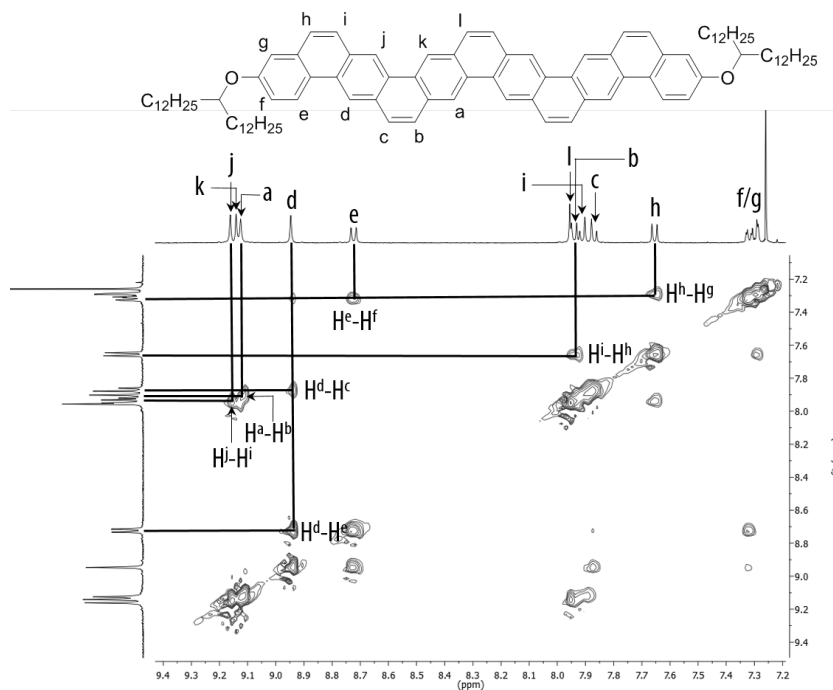


Figure D.9. Partial ^1H - ^1H NOESY spectrum of **BTp-11** (500 MHz, CDCl_3 , RT).

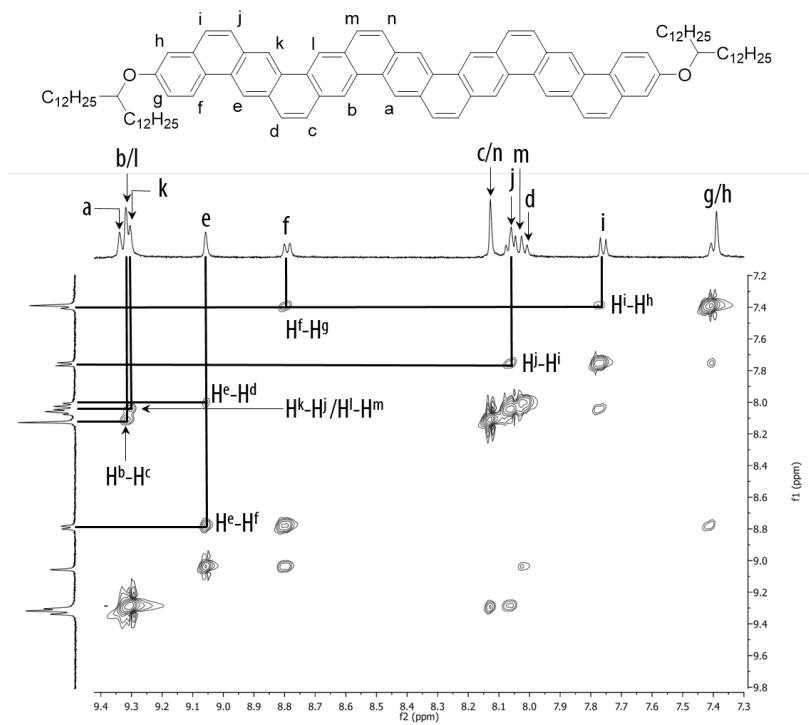


Figure D.10. Partial ¹H-¹H NOESY spectrum of **BTp-13** (500 MHz, C₂D₂Cl₄, 100 °C).

D. 6. Optical Properties

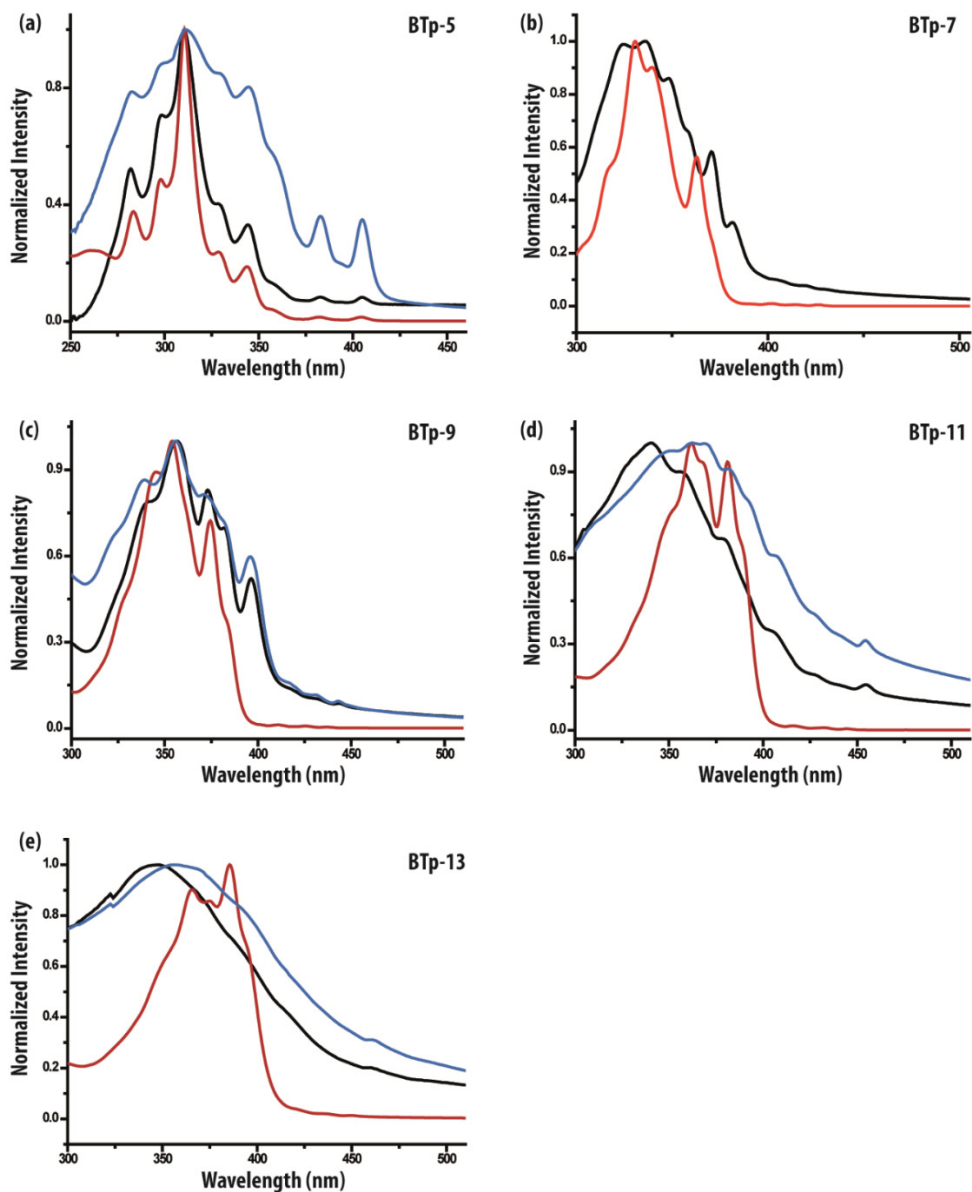


Figure D.11. UV-vis spectra of **BTp-5**, **BTp-7**, **BTp-9**, **BTp-11**, and **BTp-13** in CHCl_3 (red), as-cast thin film (black), and annealed thin film at 250 °C (blue). **BTp-7** showed good crystallinity even before annealing, but it was not able to observe a good quality UV-vis absorption after annealing due to the small grain size of the crystals and phase segregation on the substrate.

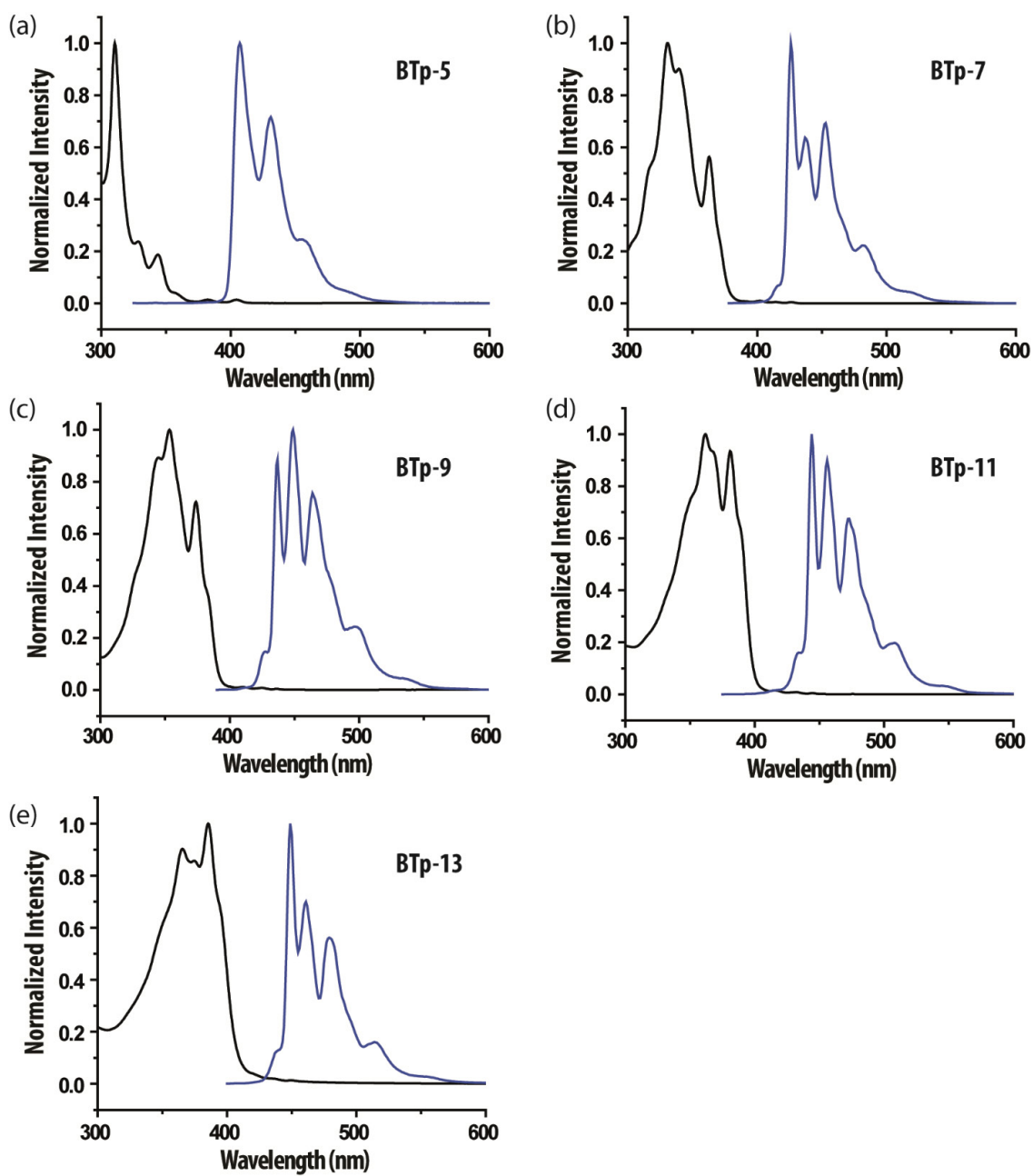


Figure D.12. UV-vis absorption (black) and fluorescent emission spectra (blue) of **BTp-5**, **BTp-7**, **BTp-9**, **BTp-11**, and **BTp-13** in CHCl₃.

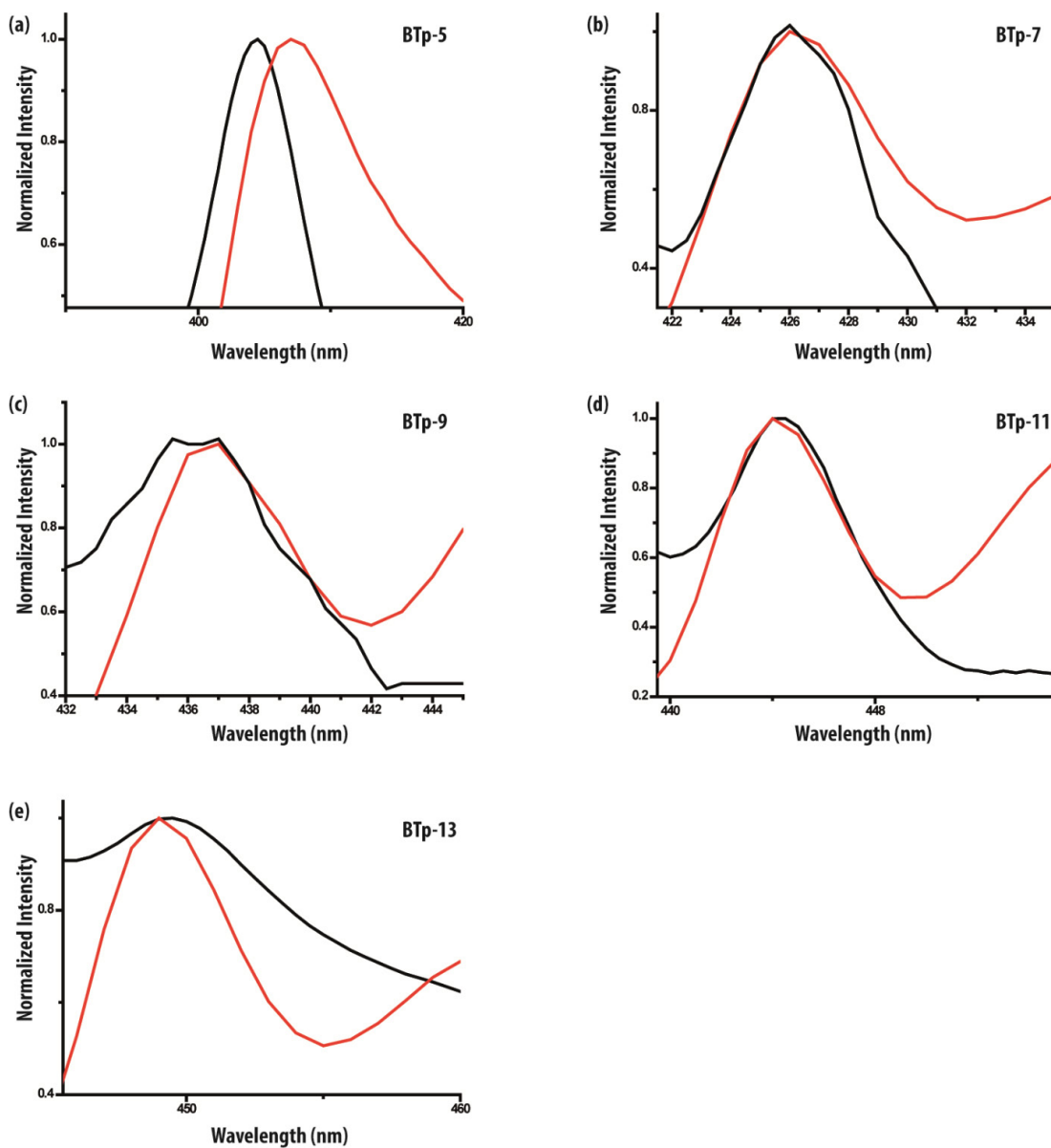


Figure D.13. Partial normalized UV-vis (the longest absorption, black) and fluorescence (emission maxima, red) spectra of **BTp-5**, **BTp-7**, **BTp-9**, **BTp-11**, and **BTp-13**. The difference between the weak α -band and emission maxima (Stokes shift) was measured to be ~ 2.6 nm for **BTp-5** and 0 nm for **BTp-7**, **BTp-9**, **BTp-11**, and **BTp-13**.

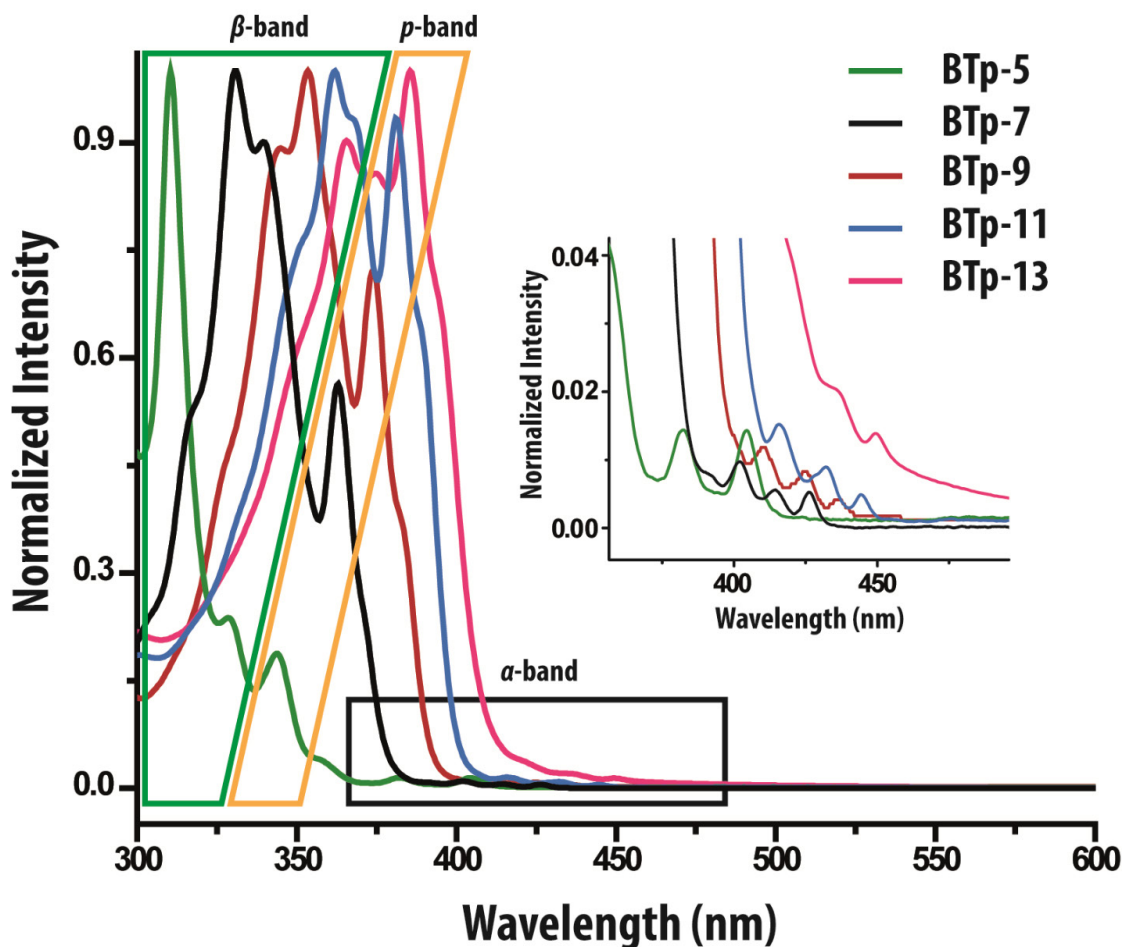


Figure D.14. Normalized UV-vis spectra of BTp-5, BTp-7, BTp-9, BTp-11, and BTp-13. Inset is the zoomed-in spectra of the black box displaying optically weak α -bands. α - (the longest wavelength), β - (the shortest wavelength), and p -bands (the intermediate wavelength) are indicated with black, green, and yellow boxes, respectively.

D. 7. Grazing-Incidence Wide-Angle X-ray Scattering (GIWAXS)

Grazing-incidence Wide-Angle X-ray Scattering was measured on the thin films which were deposited on UV-Ozone cleaned silicon wafers by spin-casting with the solutions (2 mg/mL in CHCl_3) at a spin rate of 1000 rpm. It was worth noting that

formation of thin film of **BTp-13** was not successful due to the poor solubility. Representative GIWAXS images of **BTp-7** and **BTp-11** were further analyzed to estimate the packing structures on the substrate (angle between a substrate and molecules were not considered).

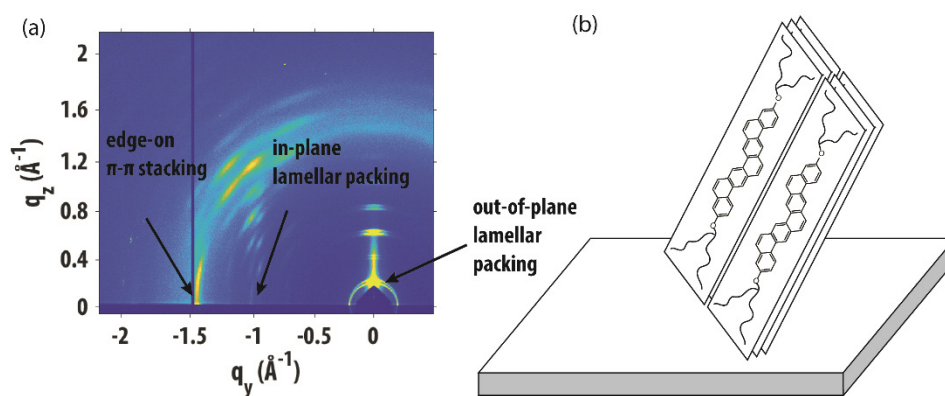


Figure D.15. (a) GIWAXS image of **BTp-7** and (b) estimated packing structure on a substrate.

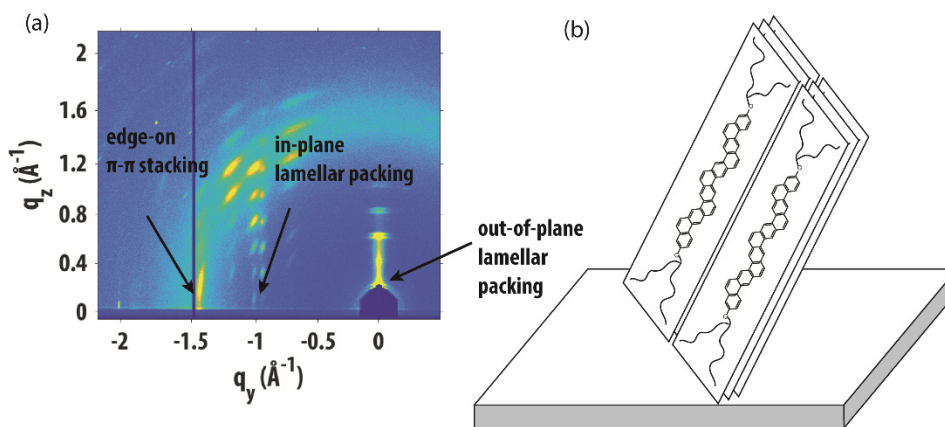


Figure D.16. (a) GIWAXS image of **BTp-11** and (b) estimated packing structure on a substrate.

D. 8. Optical Microscope Images

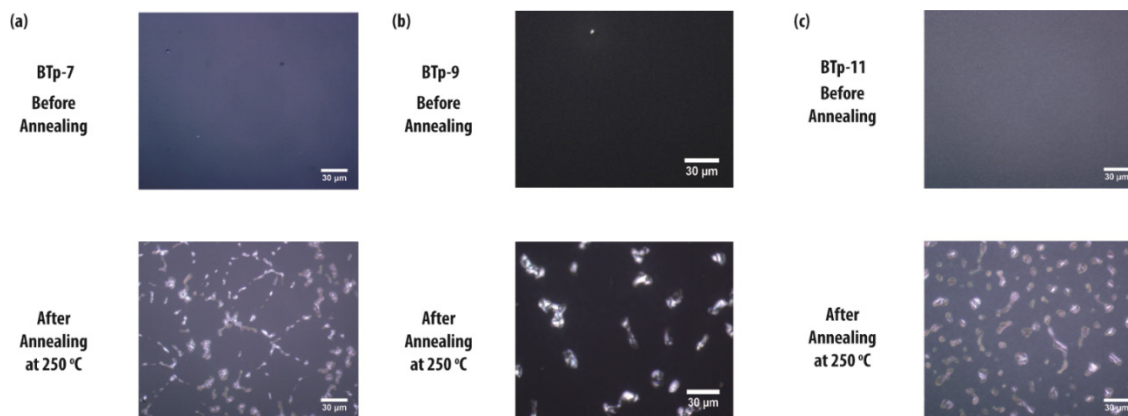


Figure D.17. Optical microscopic images of (a) **BTp-7**, (b) **BTp-9**, and (c) **BTp-11** on silicon wafer before and after annealing at 250 °C.

D. 9. Effective Conjugation Length Analysis

UV-vis absorption and fluorescence emission against the number of benzene rings were plotted by eq. 1 using the p -bands in the UV-vis spectra ($\lambda_{a, \max}$) and fluorescence emission maxima ($\lambda_{e, \max}$), where n is the number of benzene rings, λ_1 and λ_∞ are the wavelengths of the monomer and infinite polymer, respectively, and b is the rate of convergence. Effective conjugation length (ECL) where the absorption is within 1 nm of the infinite polymer was estimated to be 21 by eq. 2. In addition, optical band gap of BTp-based polymer was plotted (**Figure D.11**) by eq. 3 using weak α -bands in the UV-vis spectra and estimated to be 2.73 eV, where E_1 and E_∞ are the optical band gaps of the monomer and infinite polymer, and b is the rates of convergence. The absorption and emission wavelength and optical band gap for each oligomer were summarized in **Table D3**.

$$\lambda_n = \lambda_\infty - (\lambda_\infty - \lambda_1)e^{-b(n-1)} \quad (\text{eq. 1})$$

$$n_{\text{ecl}} = \frac{\lambda_\infty - \lambda_1}{b} + 1 \quad (\text{eq. 2})$$

$$E_n = E_\infty + (E_1 - E_\infty)e^{-a(n-1)} \quad (\text{eq. 3})$$

Table D3. Summary of absorption, emission, and optical band gap data points.

Compound	$\lambda_{a, \text{max}}$ (nm)	$\lambda_{e, \text{max}}$ (nm)	Optical band gap (eV)
BTp-5	344	407	3.07
BTp-7	363	426	2.92
BTp-9	374	437	2.85
BTp-11	381	444	2.80
BTp-13	386	449	2.76

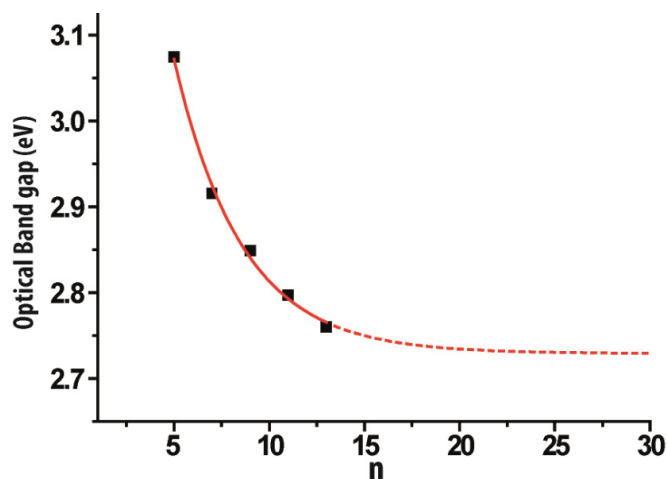


Figure D.18. Correlation plot of **BTp** derivatives between optical band gap (eV) vs number of benzene rings (n).

D. 10. Cyclic Voltammetry

Cyclic voltammograms of **BTp-5**, **BTp-7**, **BTp-9**, and **BTp-11** were measured in 0.1 M solution of [*n*-Bu₄N]PF₆ in dichloromethane at a scan rate of 50 mV s⁻¹. It is worthy to note that the cyclic voltammogram of **BTp-13** was difficult to measure due to its low solubility. Highest occupied molecular orbitals (HOMOs) were obtained from the first oxidation potentials of cyclic voltammograms and lowest unoccupied molecular orbital (LUMO) were calculated by HOMO – absorption onset (*p*-bands). HOMO and LUMO were also calculated at B3LYP/6-311G(d,p) level of theory.

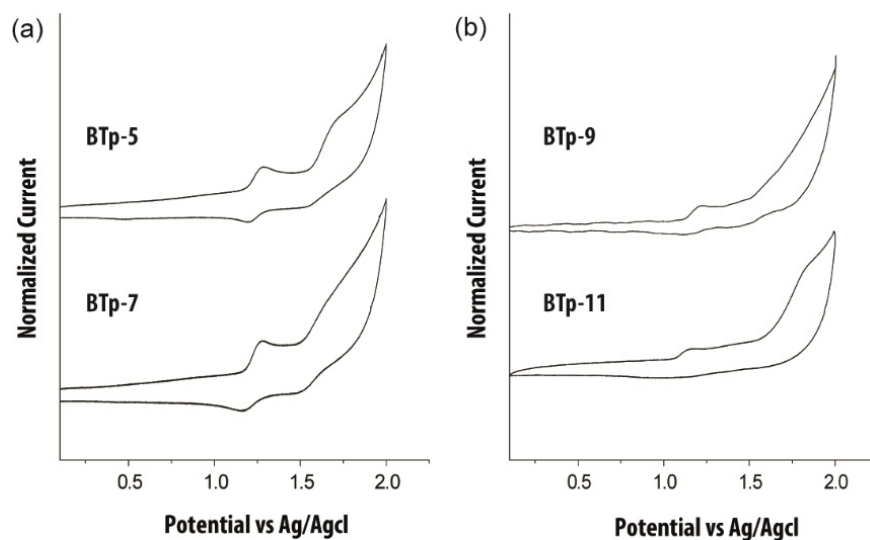


Figure D.19. Cyclic voltammograms of (a) **BTp-5** and **BTp-7** and (b) **BTp-9** and **BTp-11**.

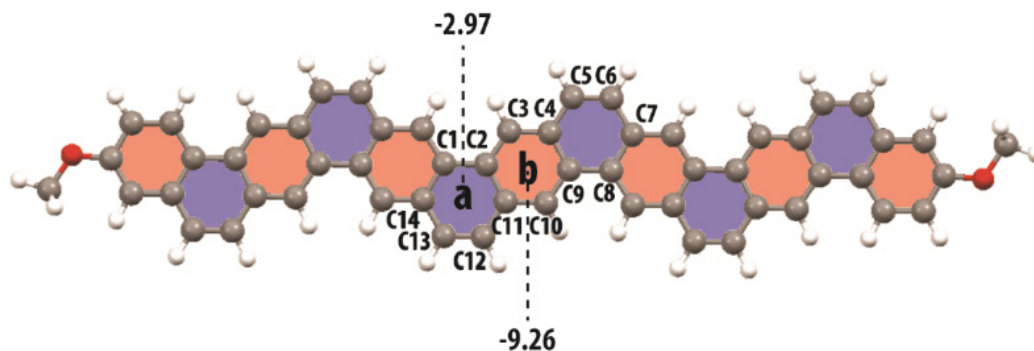
Table D.4. HOMO and LUMO levels of **BTp-5~13**.

Compound	HOMO (eV)^{exp}	LUMO (eV)^{exp}	HOMO (eV)^{cal}	LUMO (eV)^{cal}
BTp-5	-5.57	-2.06	-5.41	-1.62
BTp-7	-5.56	-2.31	-5.43	-1.76
BTp-9	-5.50	-2.36	-5.39	-1.86
BTp-11	-5.45	-2.38	-5.36	-1.93
BTp-13	-	-	-5.35	-1.98

D. 11. DFT Calculation

Atomic structures of **BTp-5**, **BTp-7**, **BTp-9**, **BTp-11**, and **BTp-13** were optimized with density functional theory (DFT) calculations at B3LYP/6-311G(d,p) level of theory. Molecular orbital shapes and energies were calculated at the optimized geometries. The

alkyl chains are replaced with methyl groups for computational simplicity. Orbital pictures were generated with Gaussview 5.08. NICS(0) values were calculated at the B3LYP/6-311+G(d,p) level of theory. All quantum-chemical calculations were performed with the Gaussian09 package.⁸



Bond	Length (Å)	Bond	Length (Å)
C1-C2	1.462	C2-C11	1.431
C8-C9	1.431	C4-C9	1.429
C5-C6	1.354	C1-C14	1.439
C12-C13	1.399	C7-C8	1.439
C3-C4	1.394	C4-C5	1.439
C10-C11	1.394	C11-C12	1.439
C2-C3	1.439	C6-C7	1.439
C9-C10	1.439	C13-C14	1.439

Figure D.20. Bond length analysis of **BTp-13** with NICS(0) values. C5-C6 and C12-C13 shows more double bond character than C1-C2 and C8-C9, indicating that ring **a** (blue) has weaker aromatic character than ring **b** (red), in agreement with NICS(0) values.

D. 12. X-ray Crystallography

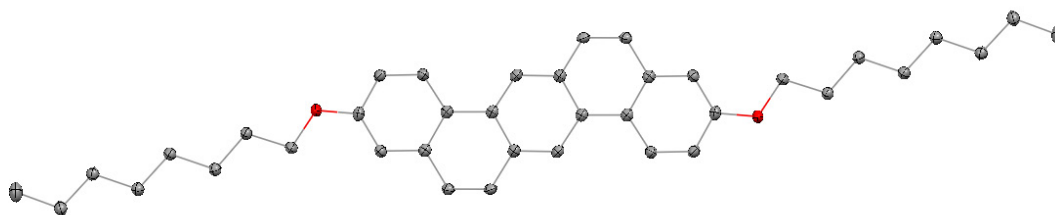
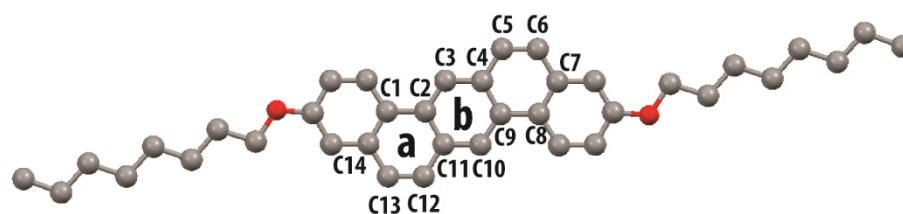


Figure D.21. Single-crystal X-ray structure of **BTp-5_C8** (*n*-octyl side chain) with probability ellipsoids set at 50% level. Hydrogen atoms have been omitted for clarity.



Bond	Length (Å)	Bond	Length (Å)
C1-C2	1.455	C2-C11	1.428
C8-C9	1.455	C4-C9	1.428
C5-C6	1.353	C1-C14	1.413
C12-C13	1.353	C7-C8	1.413
C3-C4	1.399	C4-C5	1.437
C10-C11	1.399	C11-C12	1.437
C2-C3	1.396	C6-C7	1.441
C9-C10	1.396	C13-C14	1.441

Figure D.22. Bond length analysis of **BTp-5_C8**. C5-C6 and C12-C13 shows more double bond character than C1-C2 and C8-C9, indicating that ring **a** has weaker aromatic character than ring **b**.

BTp-5_C8: CIF file can be obtained from the supplementary information. **CCDC-1573016** contains the supplementary crystallographic data for this paper. These data can be obtained free of charge from The Cambridge Crystallographic Data Centre via www.ccdc.cam.ac.uk/data_request/cif. A colorless crystal of **BTp-5_C8** having approximate dimensions of (max, intermediate, and min) 0.245 mm x 0.098 mm x 0.067 mm was mounted on a nylon loop. Cell constants and an orientation matrix for data collection corresponded to a Triclinic cell with dimensions:

$$a = 5.2371(3) \text{ \AA} \quad \alpha = 107.557(2)^\circ$$

$$b = 12.0664(8) \text{ \AA} \quad \beta = 97.844(2)^\circ$$

$$c = 12.4410(8) \text{ \AA} \quad \gamma = 98.571(2)^\circ$$

$$V = 739.83(8) \text{ \AA}^3$$

For $Z = 1$ and $F.W. = 534.75$, the calculated density is 1.200 Mg/m^3 . Systematic reflection conditions and statistical tests of the data suggested the space group $P-1$. The data were collected at a temperature of 100 K with a theta range for the data collection of 3.797 to 70.081° .

D. 13. ^1H and ^{13}C NMR Spectra

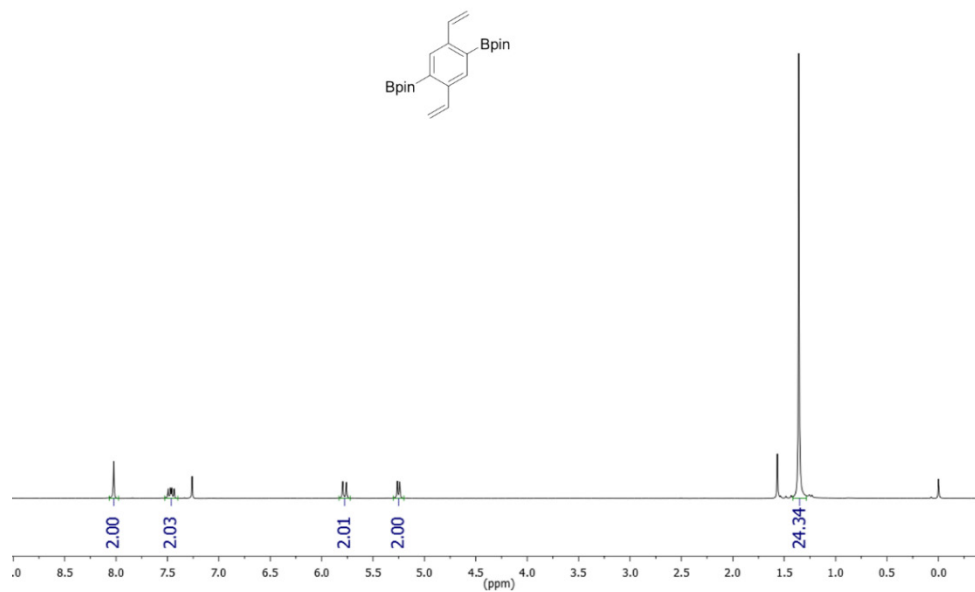


Figure D.23. ^1H NMR of B1 (500 MHz, CDCl_3 , RT).

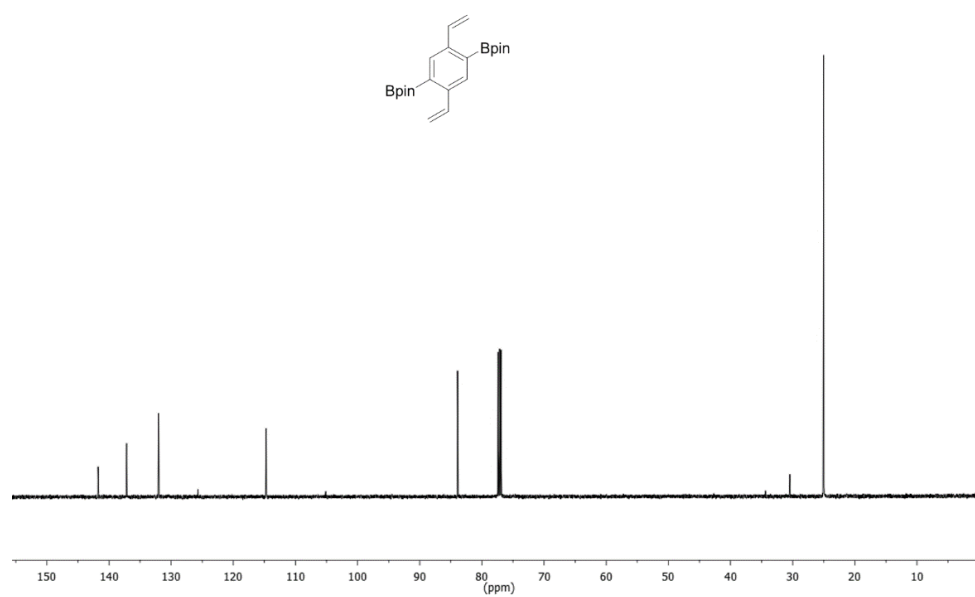


Figure D.24. ^{13}C NMR of B1 (125 MHz, CDCl_3 , RT).

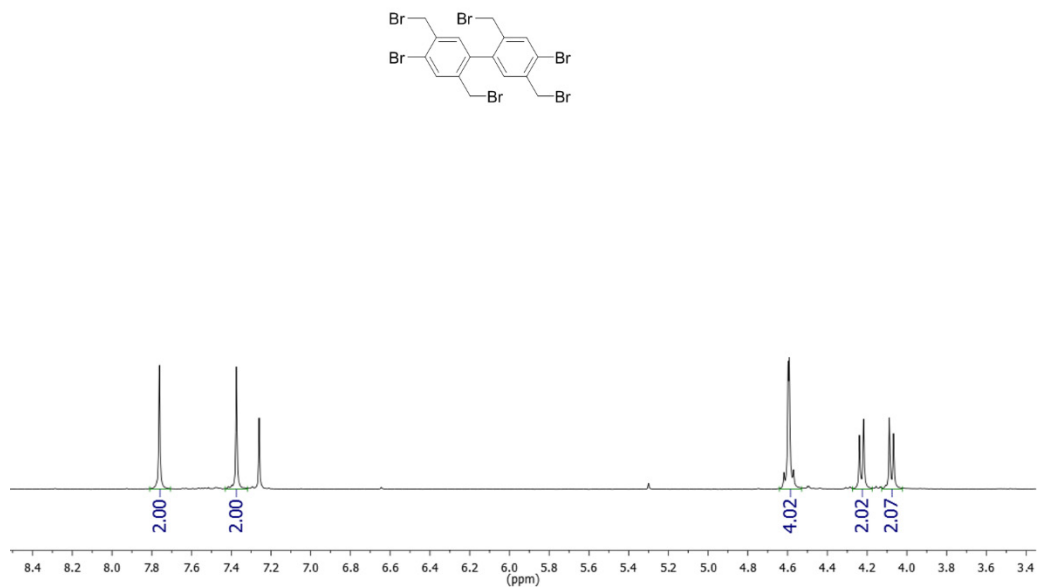


Figure D.25. ¹H NMR of S7 (500 MHz, CDCl₃, RT).

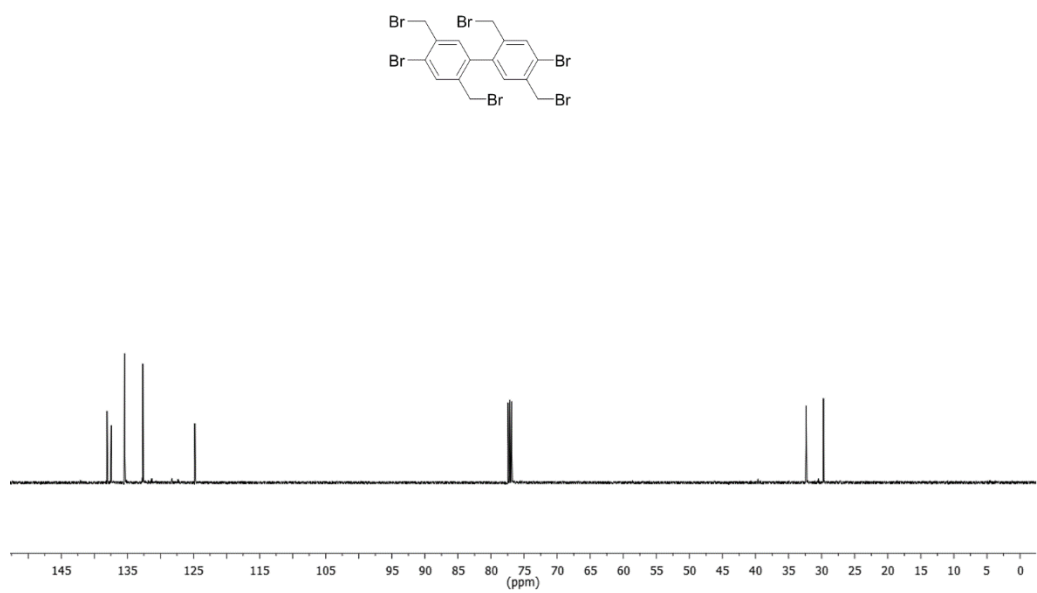


Figure D.26. ¹³C NMR of S7 (125 MHz, CDCl₃, RT).

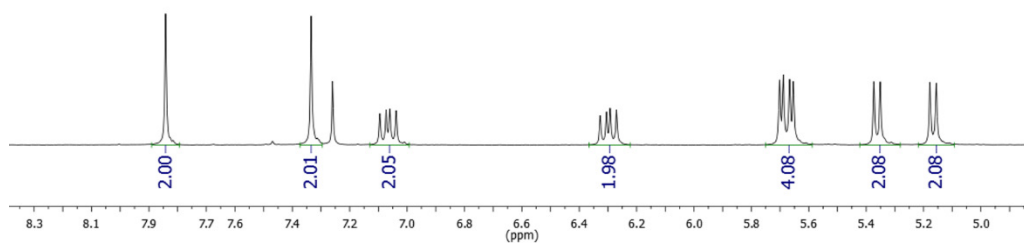
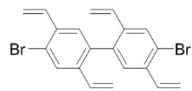


Figure D.27. ^1H NMR of **2** (500 MHz, CDCl_3 , RT).

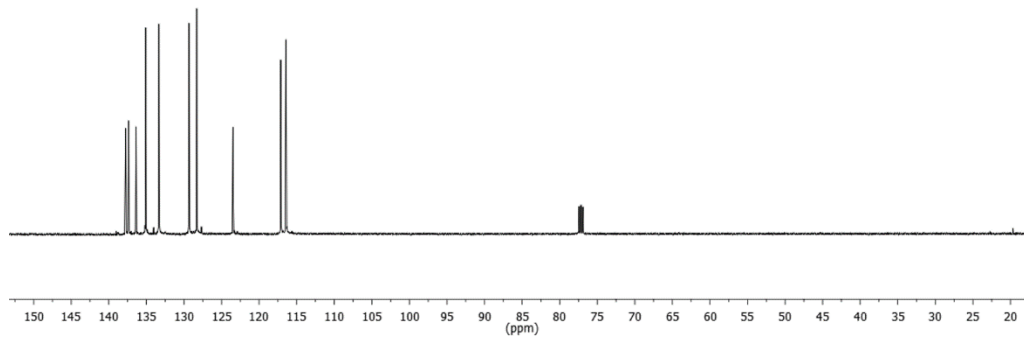
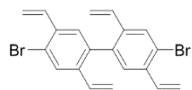


Figure D.28. ^{13}C NMR of **2** (125 MHz, CDCl_3 , RT).

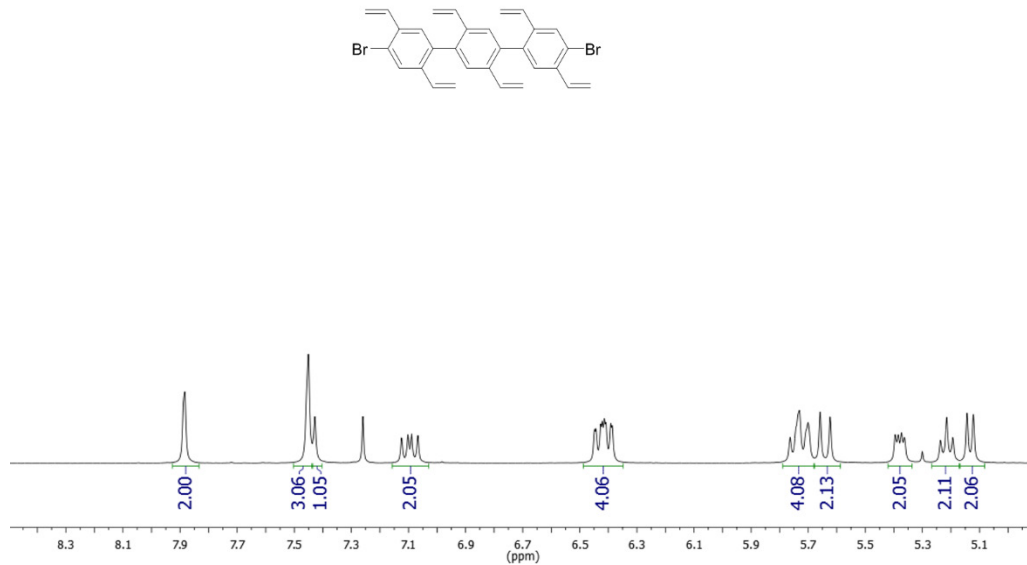


Figure D.29. ^1H NMR of **3** (500 MHz, CDCl_3 , RT).

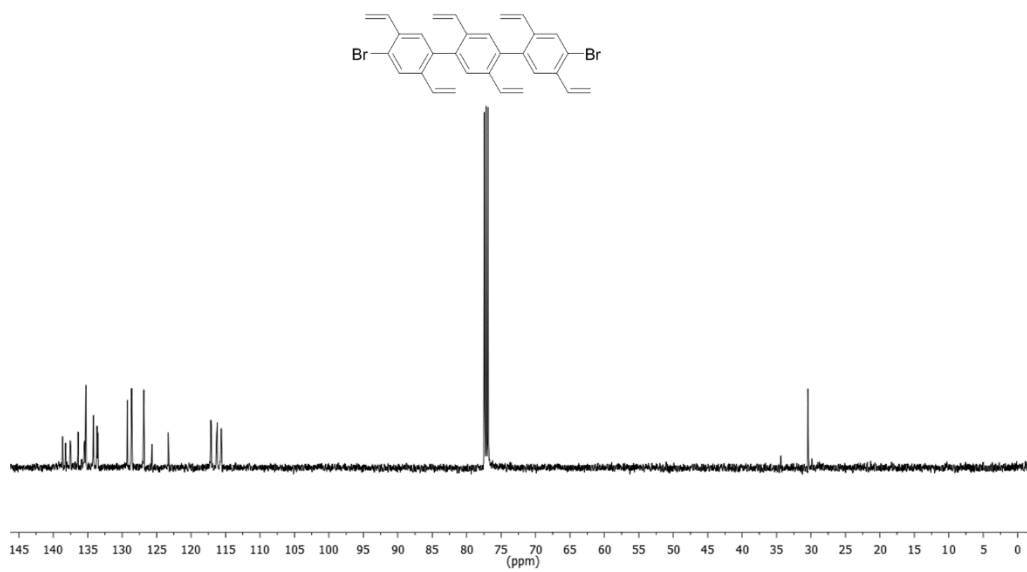


Figure D.30. ^{13}C NMR of **3** (125 MHz, CDCl_3 , RT).

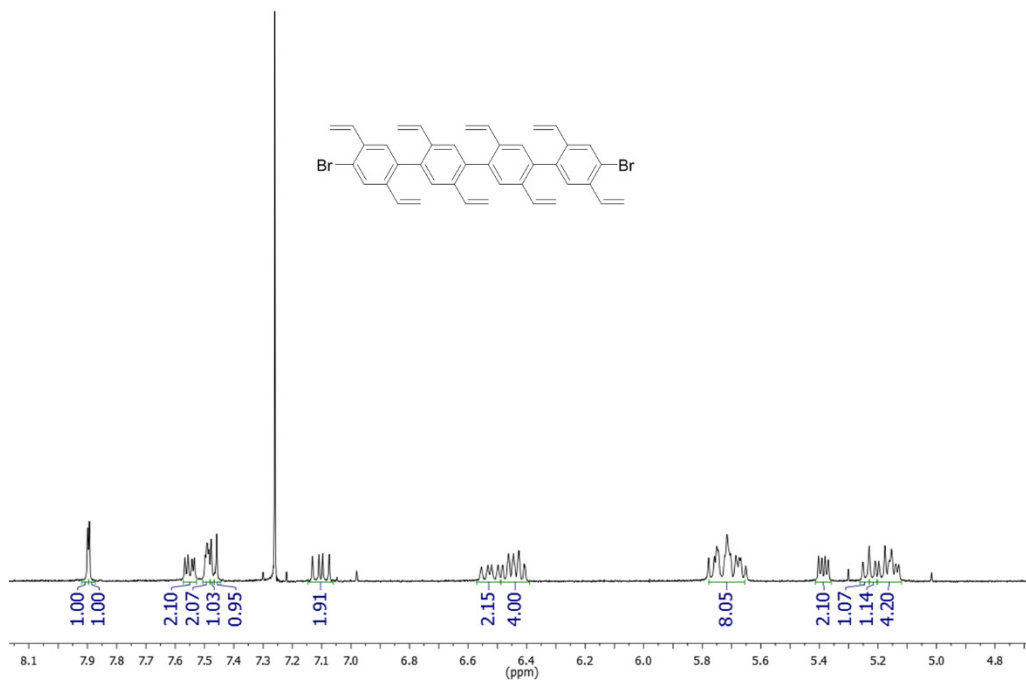


Figure D.33. ^1H NMR of **4** (500 MHz, CDCl_3 , RT).

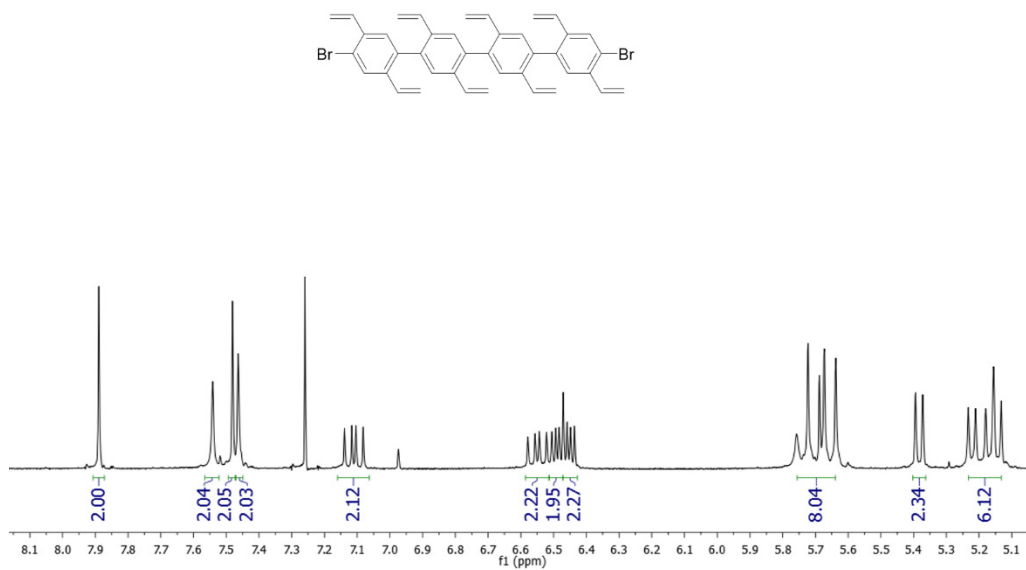


Figure D.34. ^1H NMR of **4** (500 MHz, CDCl_3 , 55 °C).

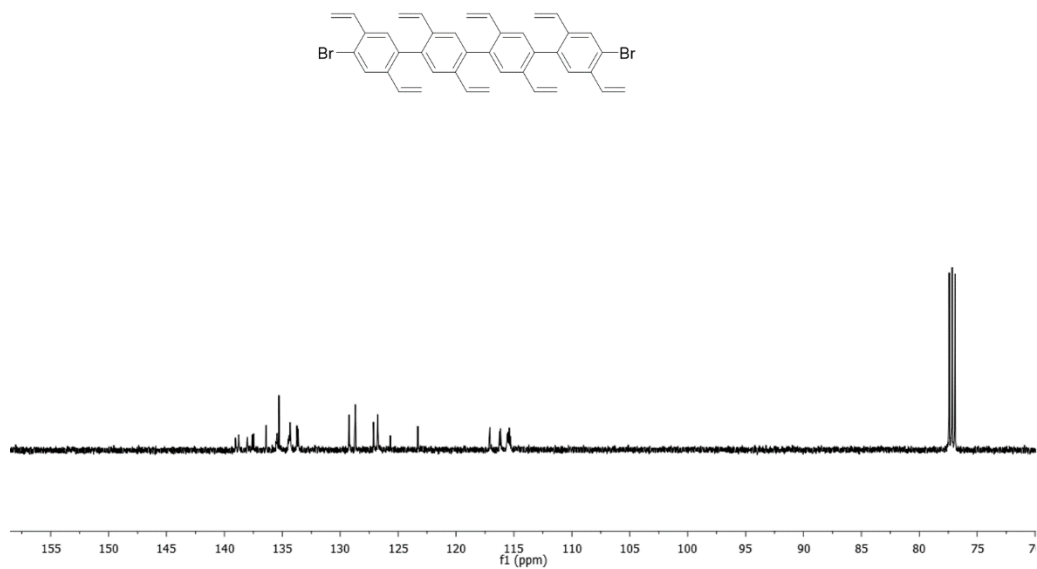


Figure D.35. ^{13}C NMR of **4** (125 MHz, CDCl_3 , RT).

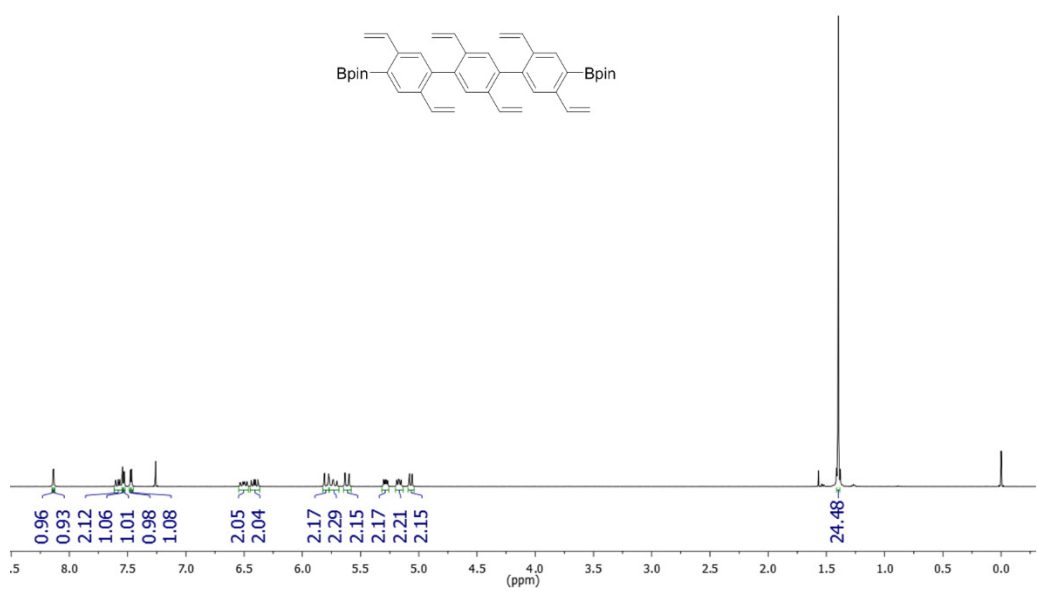


Figure D.36. ^1H NMR of **B3** (500 MHz, CDCl_3 , RT).

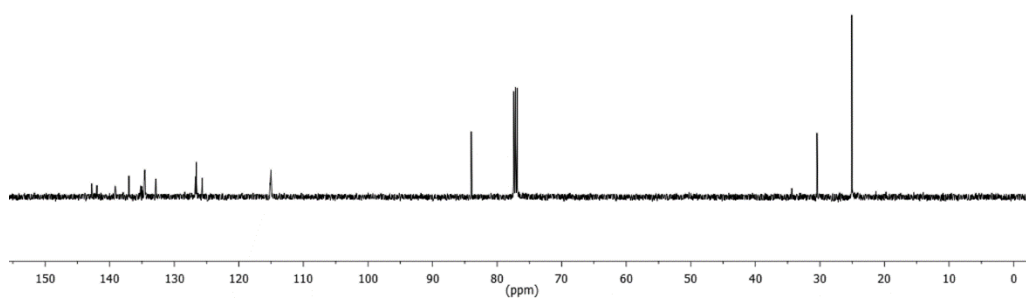
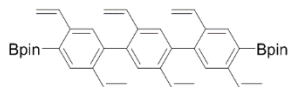


Figure D.37. ^{13}C NMR of **B3** (125 MHz, CDCl_3 , RT).

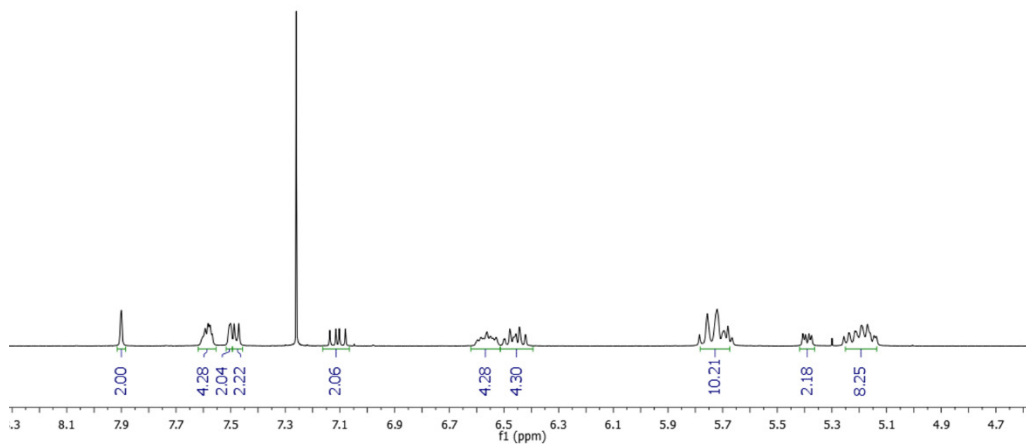


Figure D.38. ^1H NMR of **5** (500 MHz, CDCl_3 , RT).

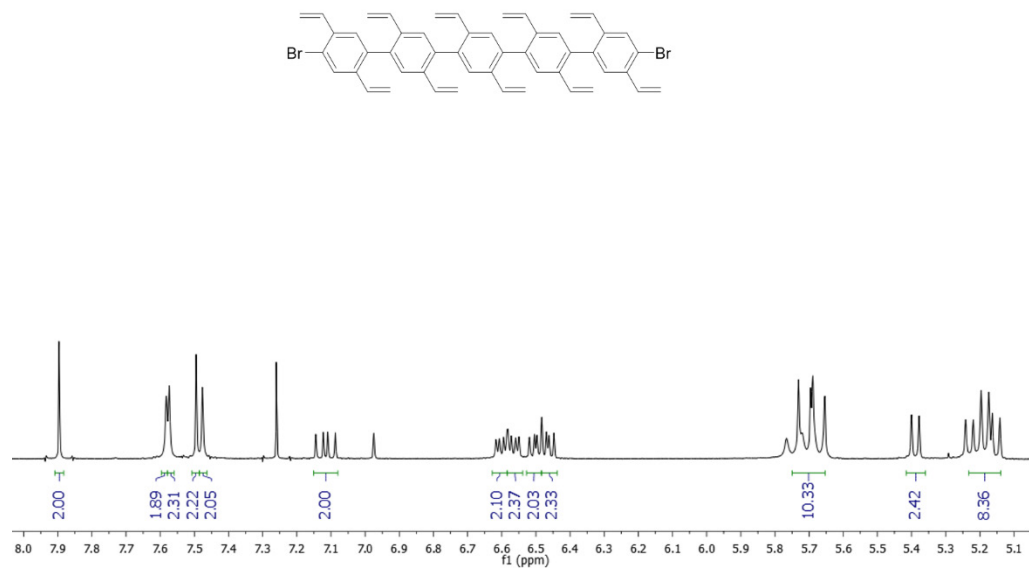


Figure C.39. ¹H NMR of **5** (500 MHz, CDCl₃, 55 °C).

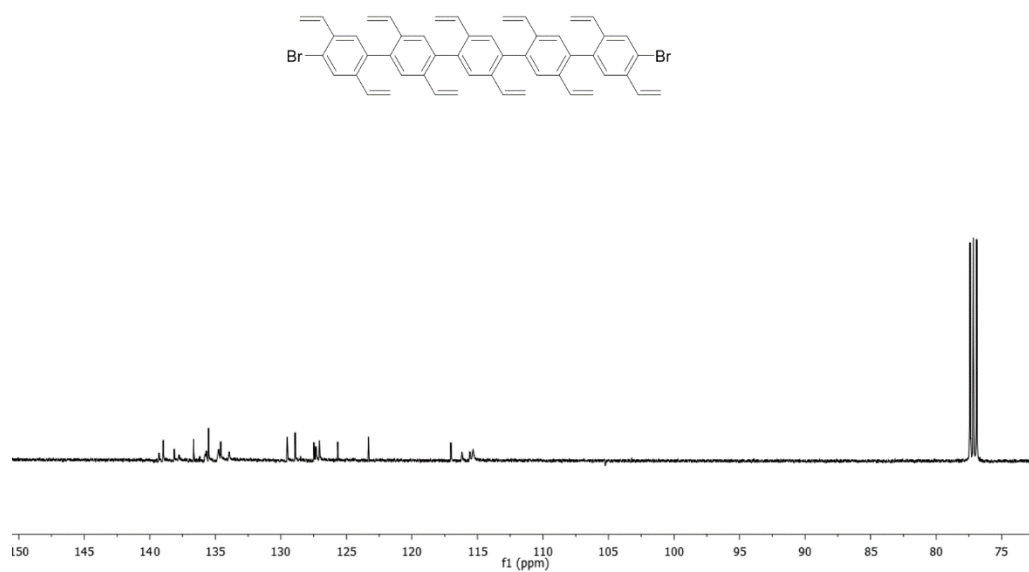


Figure D.40. ¹³C NMR of **5** (125 MHz, CDCl₃, 50 °C).

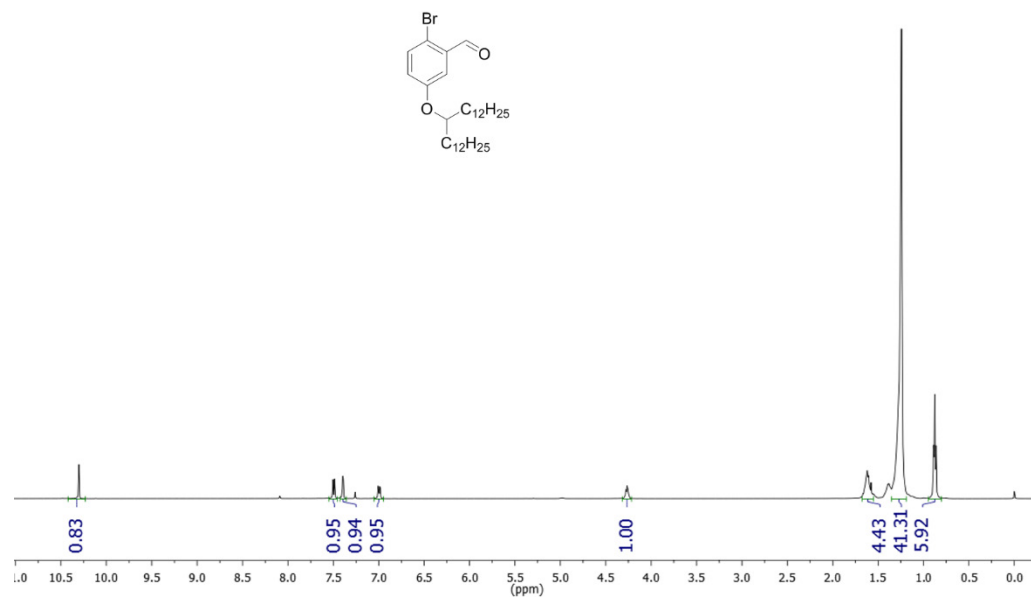


Figure D.41. $^1\text{H NMR}$ of S8 (500 MHz, CDCl_3 , RT).

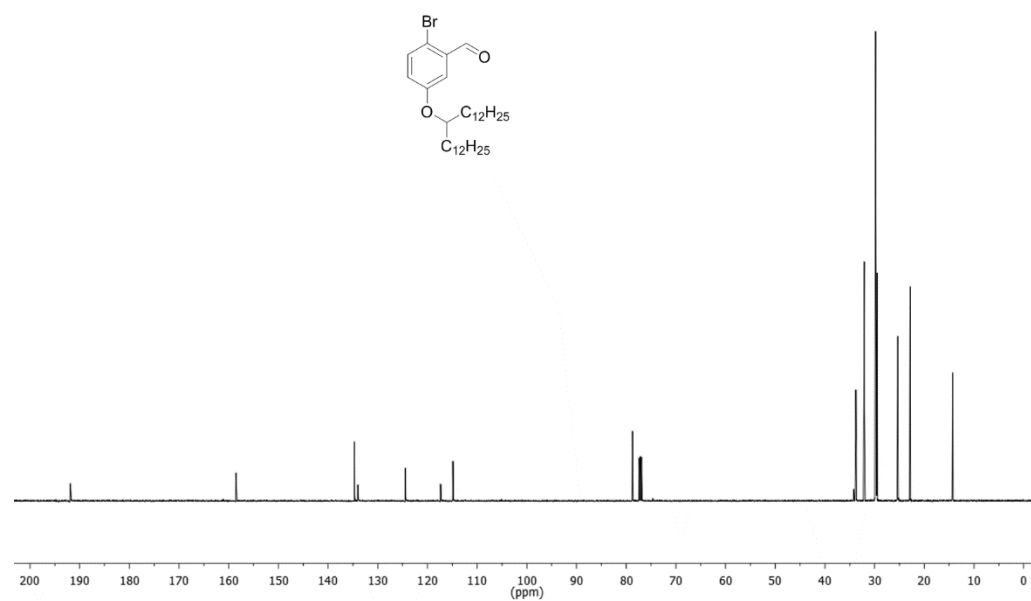


Figure D.42. $^{13}\text{C NMR}$ of S8 (125 MHz, CDCl_3 , RT).

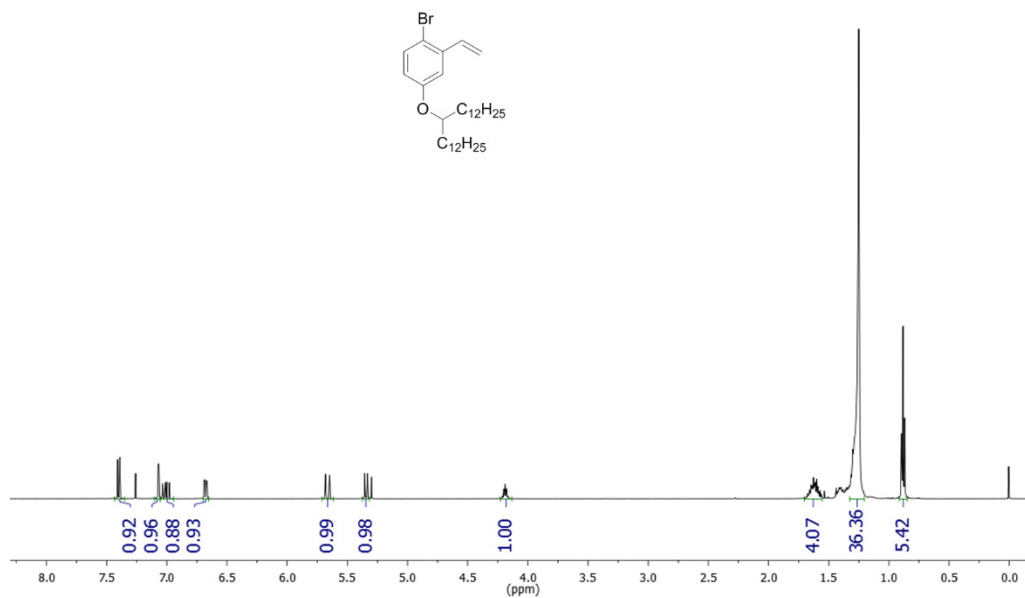


Figure D.43. ^1H NMR of S9 (500 MHz, CDCl_3 , RT).

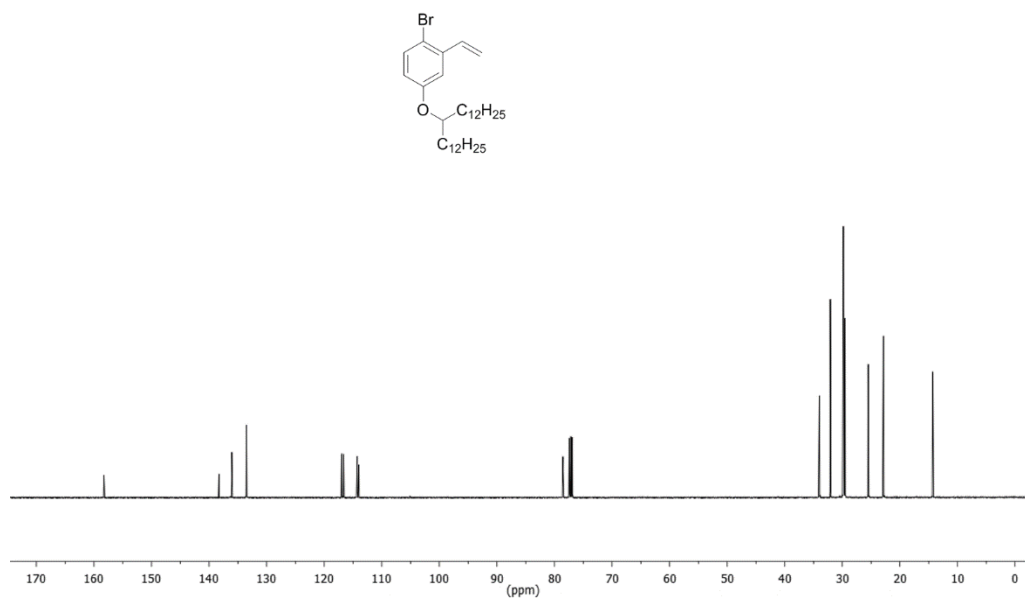


Figure D.44. ^{13}C NMR of S9 (125 MHz, CDCl_3 , RT).

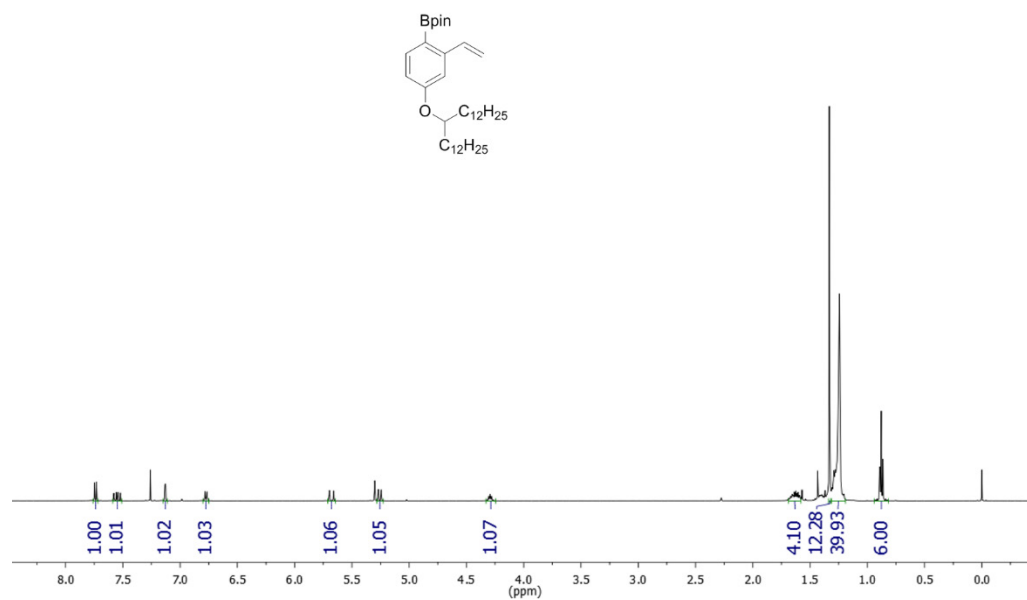


Figure D.45. ^1H NMR of **S10** (500 MHz, CDCl_3 , RT).

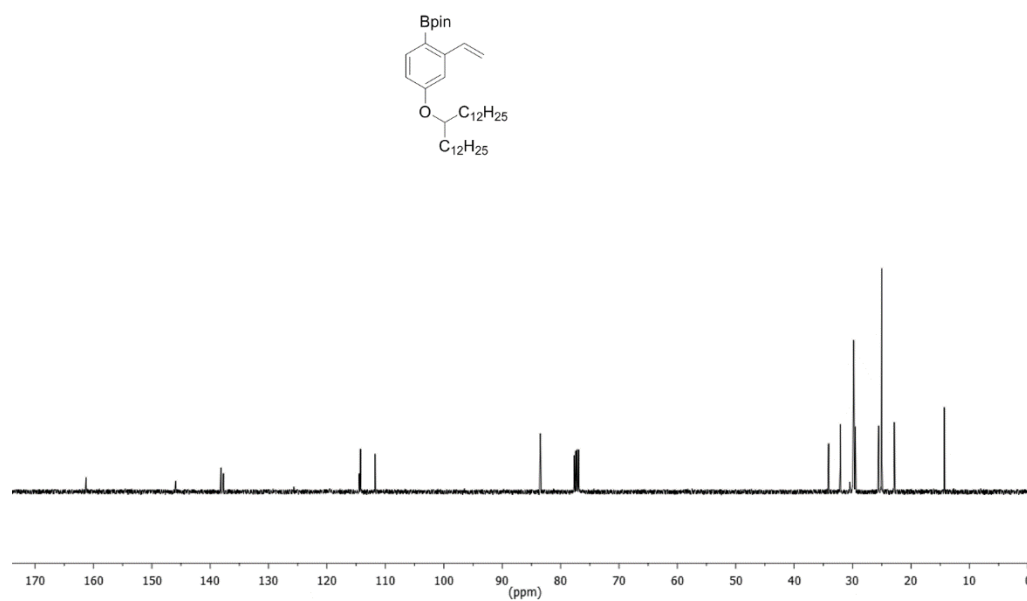


Figure D.46. ^{13}C NMR of **S10** (125 MHz, CDCl_3 , RT).

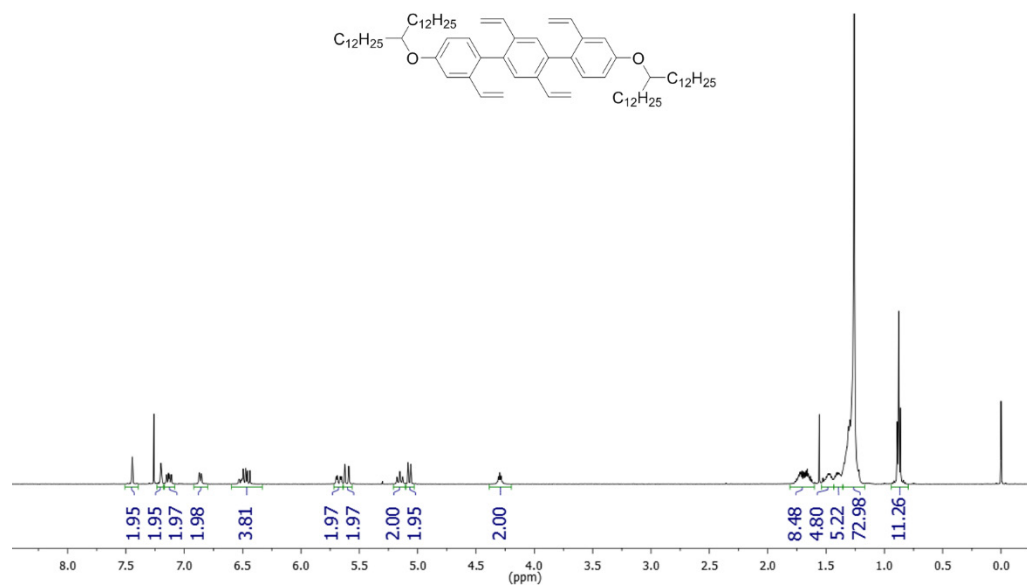


Figure D.47. ^1H NMR of VPP3 (500 MHz, CDCl_3 , RT).

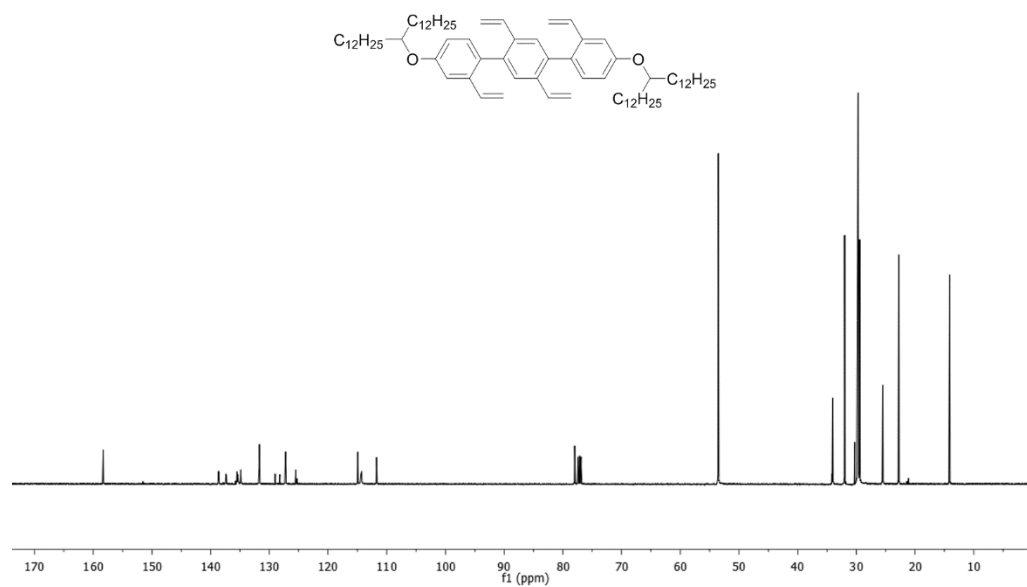


Figure D.48. ^{13}C NMR of VPP3 (125 MHz, CDCl_3 , RT).

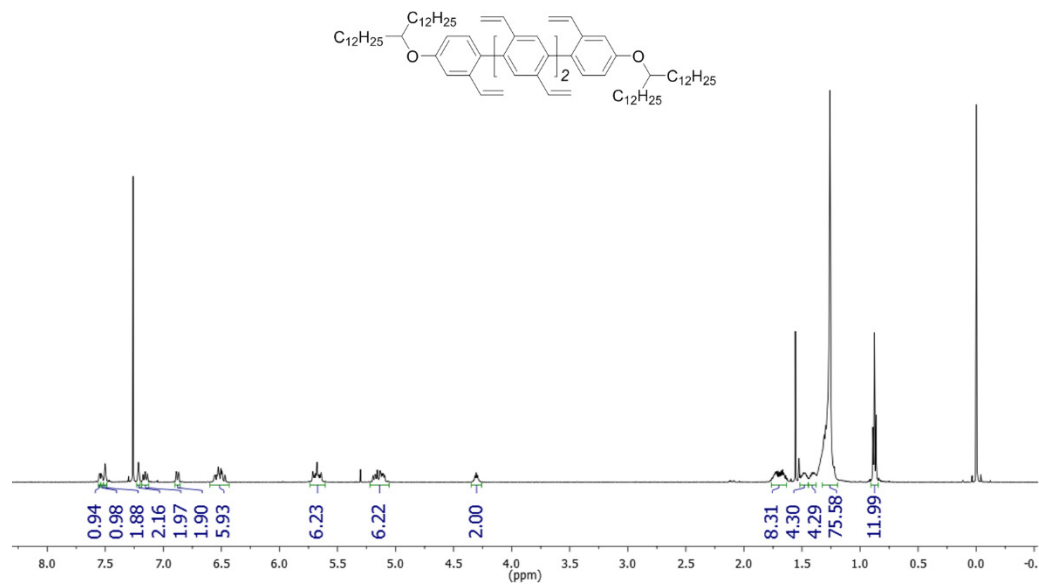


Figure D.49. ¹H NMR of VPP4 (500 MHz, CDCl₃, RT).

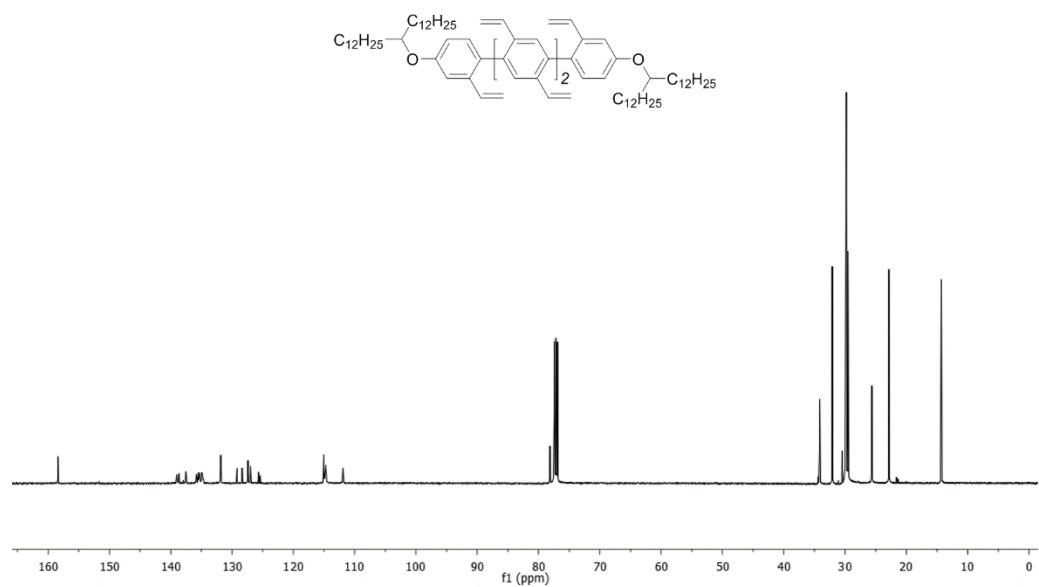


Figure D.50. ¹³C NMR of VPP4 (125 MHz, CDCl₃, RT).

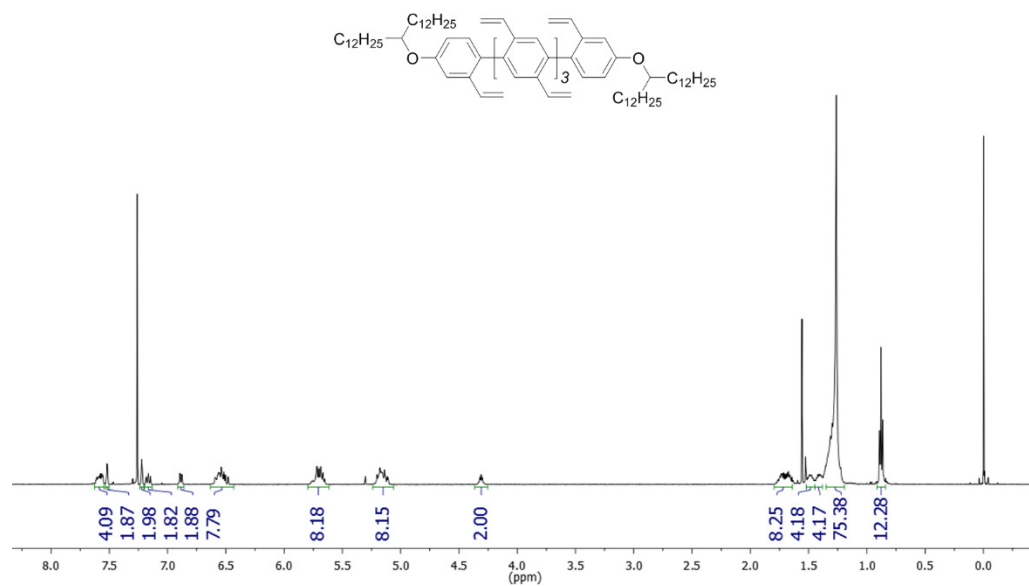


Figure D.51. ^1H NMR of VPP5 (500 MHz, CDCl_3 , RT).

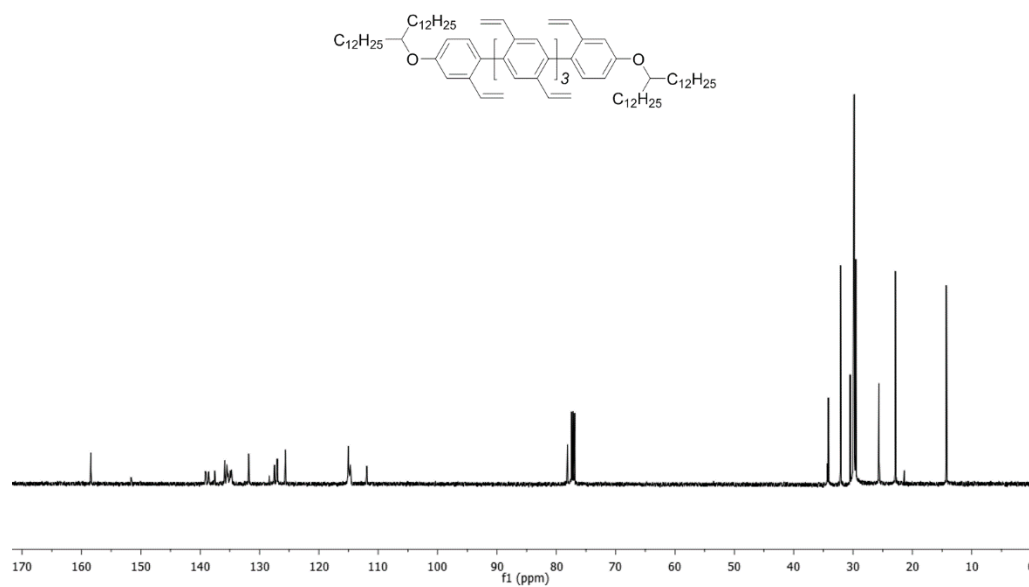


Figure D.52. ^{13}C NMR of VPP5 (125 MHz, CDCl_3 , RT).

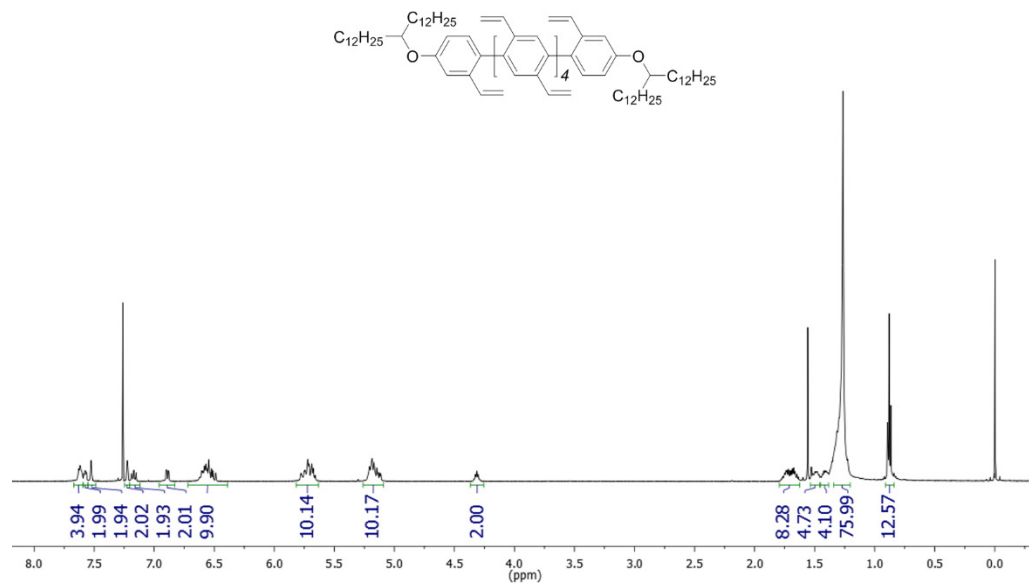


Figure D.53. ^1H NMR of VPP6 (500 MHz, CDCl_3 , RT).

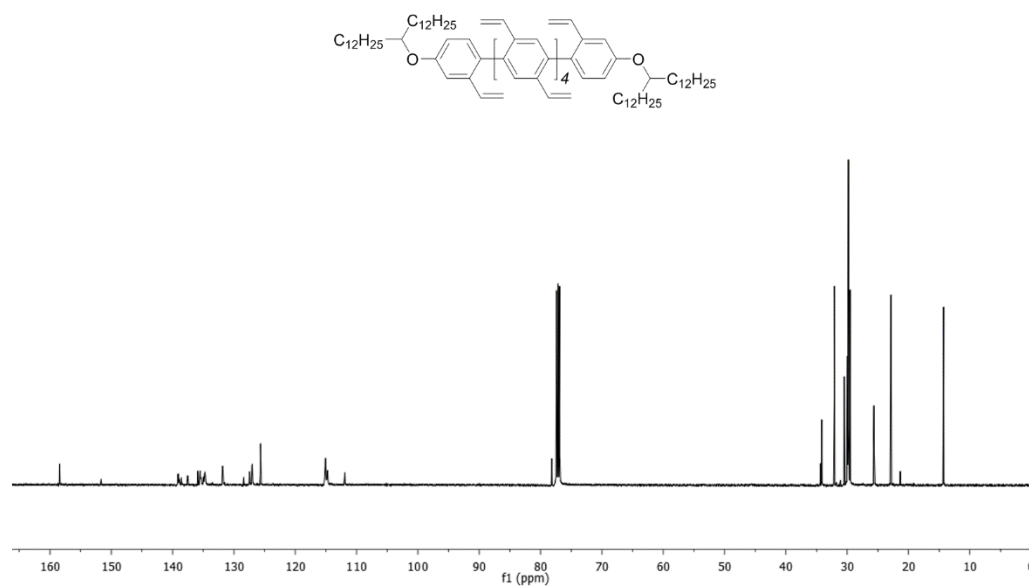


Figure D.54. ^{13}C NMR of VPP6 (125 MHz, CDCl_3 , RT).

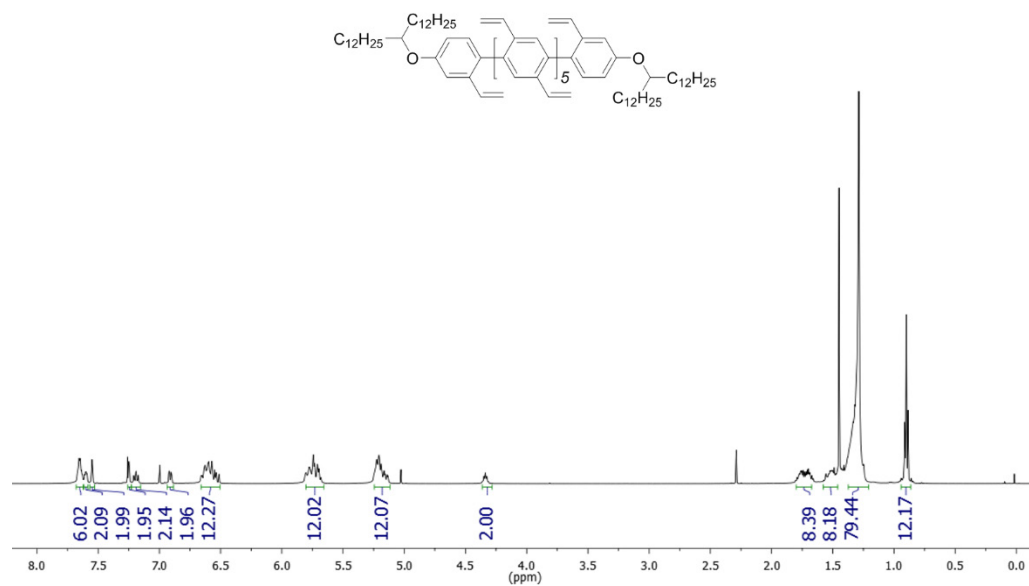


Figure D.55. ^1H NMR of VPP7 (500 MHz, CDCl_3 , RT).

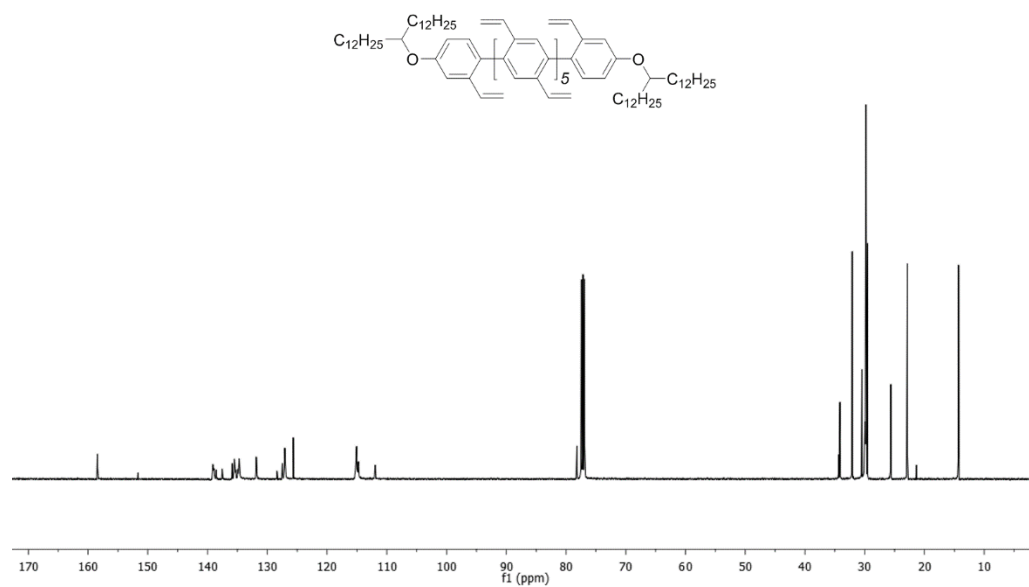


Figure D.56. ^{13}C NMR of VPP7 (125 MHz, CDCl_3 , RT).

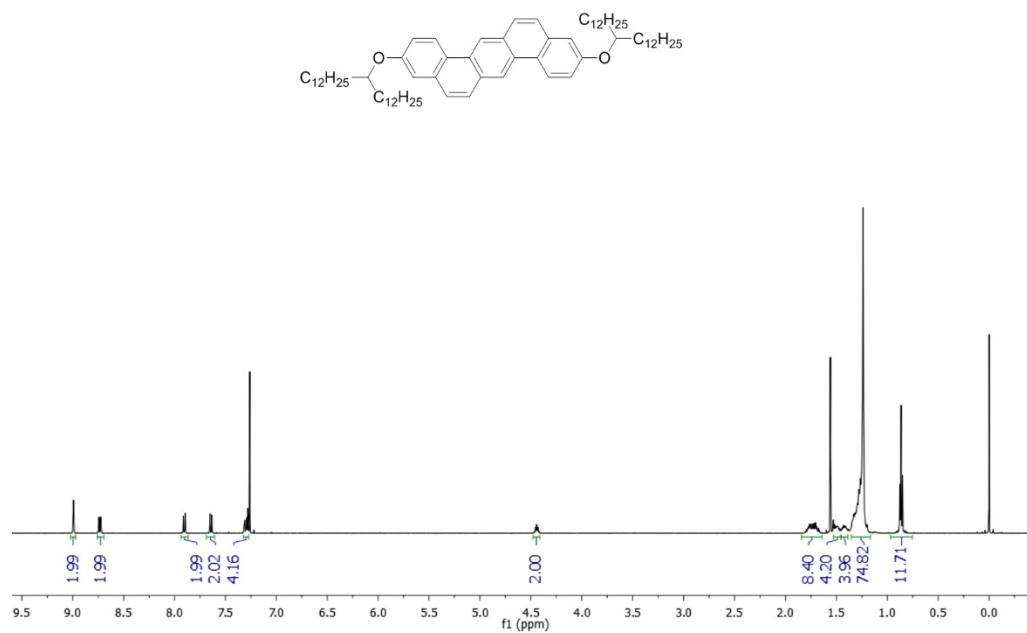


Figure D.57. ^1H NMR of BTp-5 (500 MHz, CDCl_3 , RT).

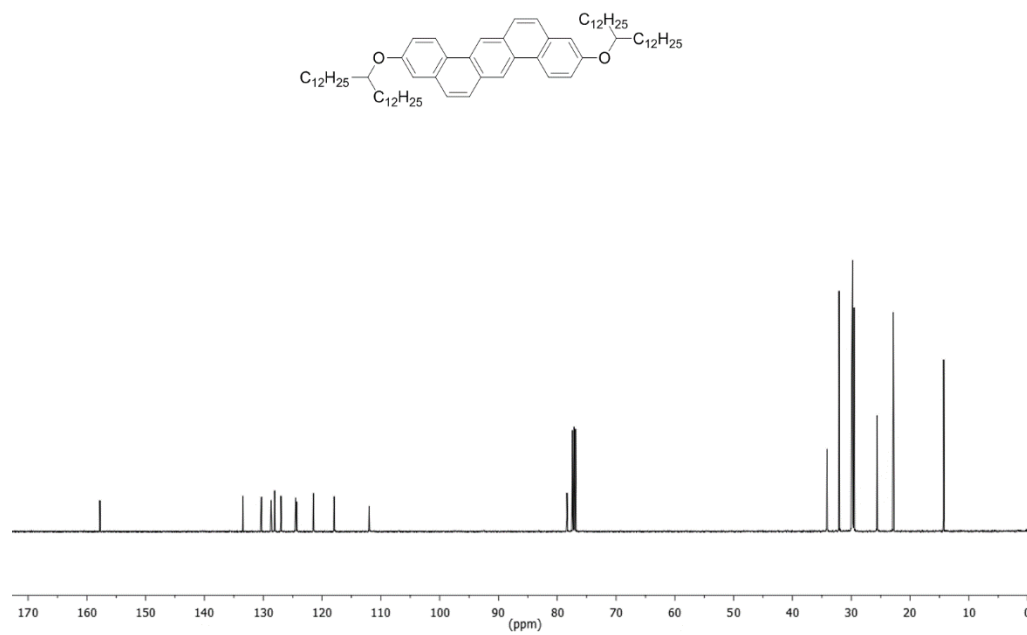


Figure D.58. ^{13}C NMR of BTp-5 (125 MHz, CDCl_3 , RT).

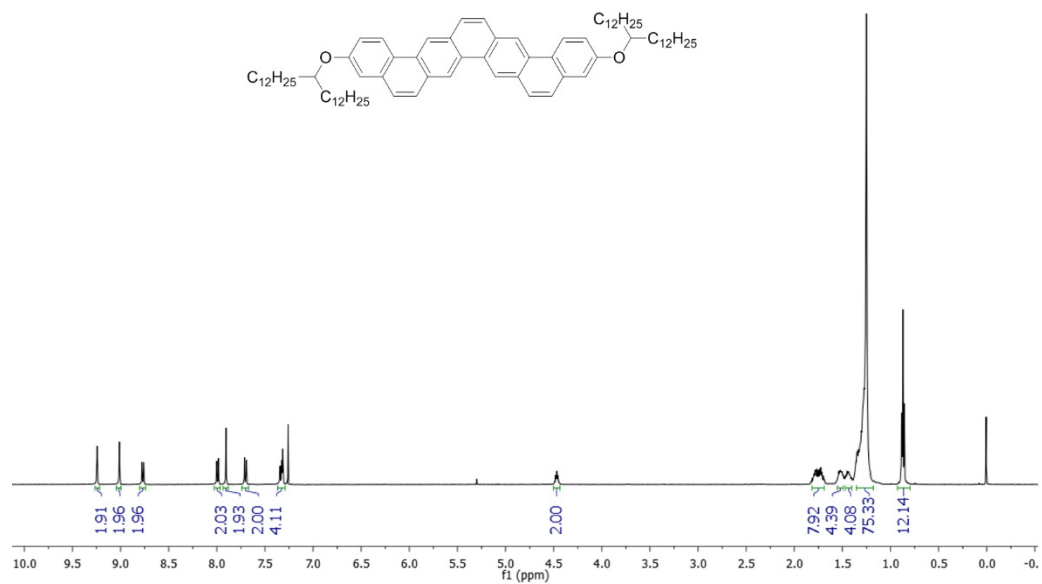


Figure D.59. ^1H NMR of BTp-7 (500 MHz, CDCl_3 , RT).

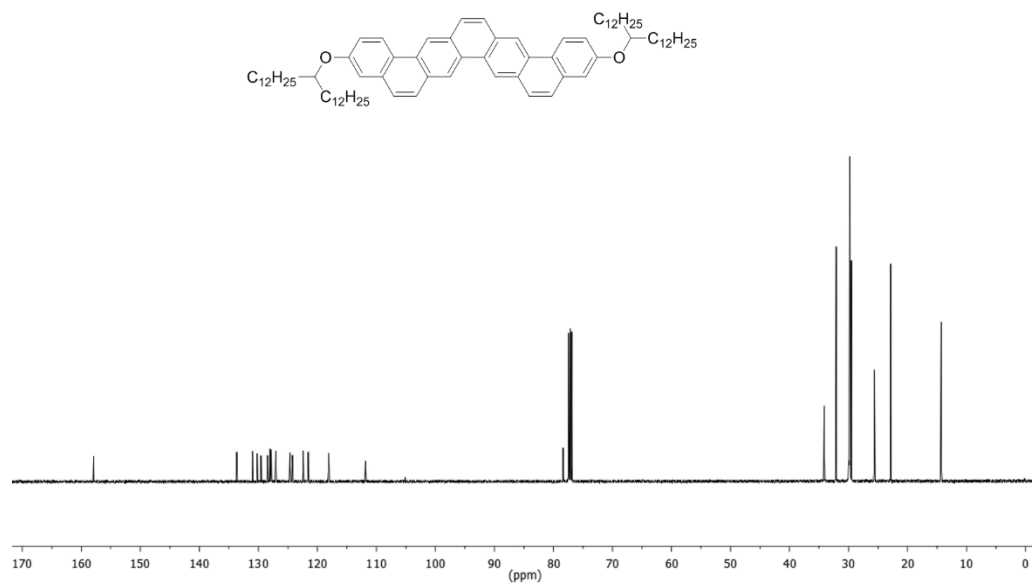


Figure D.60. ^{13}C NMR of BTp-7 (125 MHz, CDCl_3 , RT).

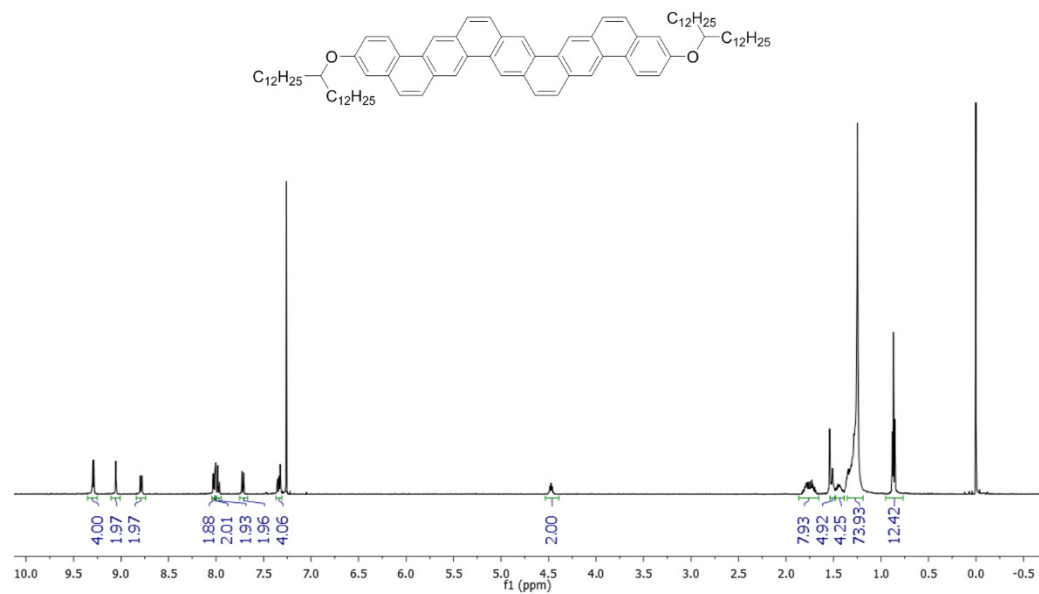


Figure D.61. ¹H NMR of BTp-9 (500 MHz, CDCl₃, RT).

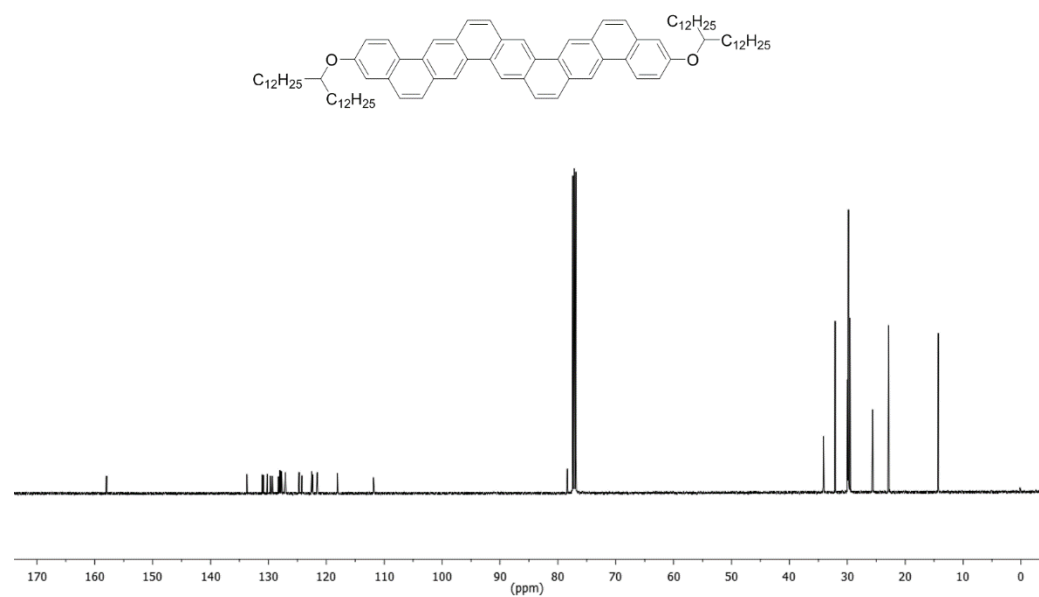


Figure D.62. ¹³C NMR of BTp-9 (125 MHz, CDCl₃, RT).

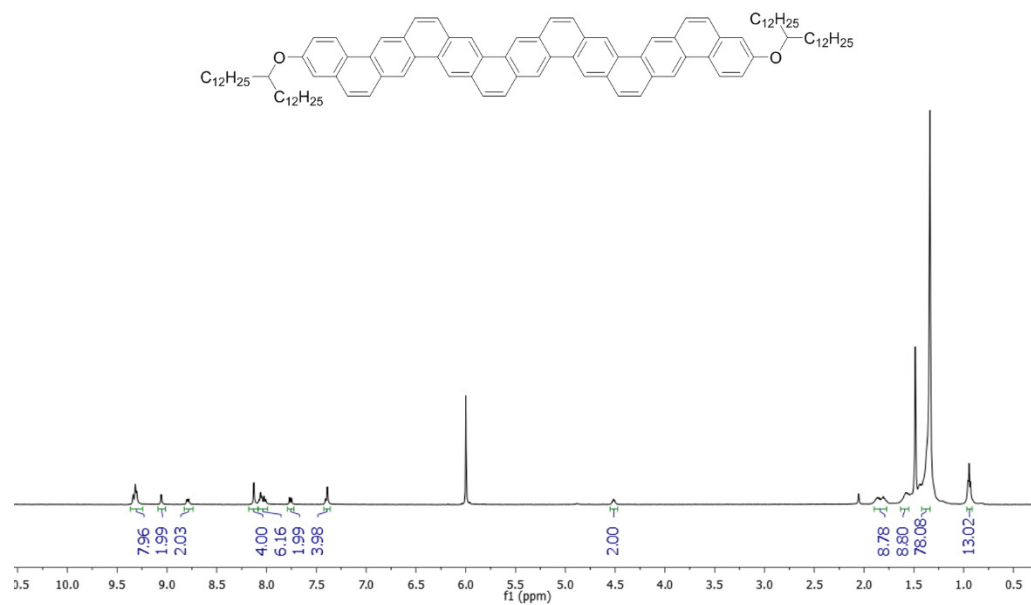


Figure D.65. ^1H NMR of BTp-13 (500 MHz, $\text{C}_2\text{D}_2\text{Cl}_4$, 100 °C).

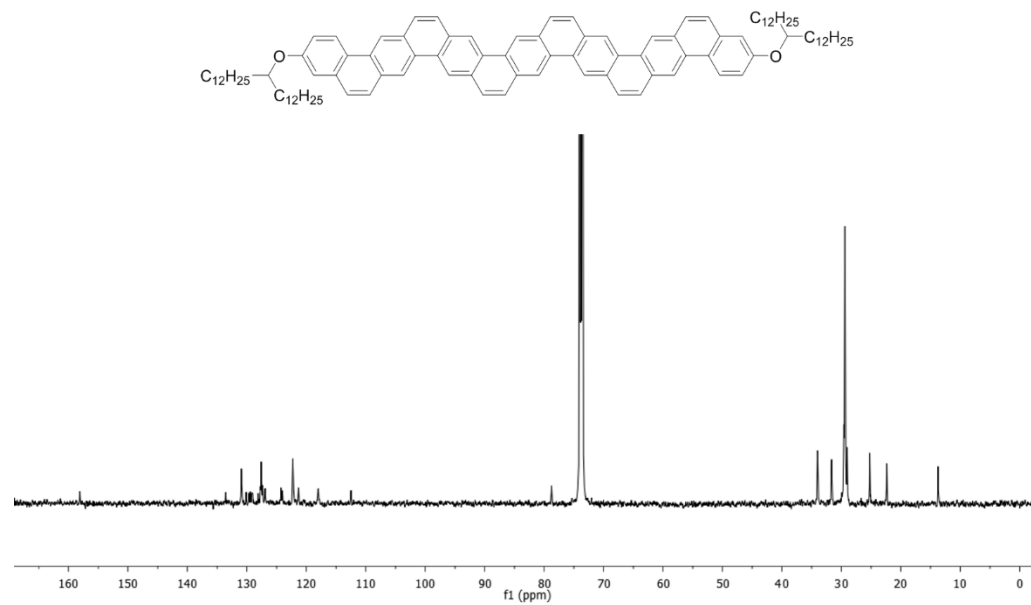


Figure D.66. ^{13}C NMR of BTp-13 (125 MHz, $\text{C}_2\text{D}_2\text{Cl}_4$, 100 °C).